Spatially distributed Wind and Turbulence Measurements with a Fleet of Unmanned Aerial Systems

DISSERTATION

der Mathematisch-Naturwissenschaftlichen Fakultät
der Eberhard Karls Universität Tübingen
zur Erlangung des Grades eines
Doktors der Naturwissenschaften
(Dr. rer. nat.)

vorgelegt von
TAMINO WETZ
aus Lich

Tübingen
2023

Contents

Abbreviations

ABL	atmospheric boundary layer
a.g.l.	above ground level
CABL	convective atmospheric boundary layer
DLR	Deutsches Zentrum für Luft- und Raumfahrt
DWD	Deutscher Wetterdienst (German Meteorological Service)
DWL	Doppler wind lidar
GNSS	global navigation satellite systems
GPS	global position system
IEA	International Energy Agency
ILS	integral length scale
IMU	inertial measurement unit
LES	large-eddy simulation
Lidar	light detection and ranging
NABL	neutral atmospheric boundary layer
RMS	root mean square
SABL	stable atmospheric boundary layer
SWUF-3D	Simultaneous Wind measurements with Unmanned Flight systems
TKE	turbulent kinetic energy
UAS	unmanned aerial systems
UAV	unmanned aerial vehicle
UTC	coordinated universal time
WT	wind turbine
WEA	Windenergieanlage
WMO	World Meteorological Organization

Acknowledgements

I want to thank all the people who contributed to the work in this thesis. In particular I would like to acknowledge:

Zusammenfassung

Die vorliegende Arbeit befasst sich mit der Entwicklung eines neuartigen Messsystems zur Windfeldmessung in der atmosphärischen Grenzschicht und deren Anwendung sowohl hinsichtlich der Analyse von räumlichen turbulenten Strukturen im heterogenen Gelände als auch Strömungsmessungen um eine Windenergieanlage.

Das innovative Messsystem besteht aus einer Flotte von 35 Quadrotoren UAS (unmanned aerial systems), wovon maximal 20 simultan eingesetzt wurden. Dieses Messsystem ermöglicht flexible simultane räumlich verteilte Messungen des Windvektors in der Grenzschicht. Zur Messung des Windes wurde ein Algorithmus entwickelt, welcher auf den Lage- und Beschleunigungssensoren des UAS basiert und ohne zusätzliche externe Windsensoren auskommt. Der Algorithmus setzt die Sensordaten ins Verhältnis zu den angreifenden Windkräften und wird mit Hilfe von Referenzmessungen an einem 99-m meteorologischen Mast kalibriert und validiert. Das Potential der UAS-Flotte für Windfeld- und Turbulenzmessungen zeigen Vergleiche zu Doppler-Wind-Lidar- und Ultraschallanemometer-Messdaten.

Des Weiteren wurde ein spezielles Flugmuster, bestehend aus räumlich horizontal verteilten Messungen, kreiert, mit dem horizontale Turbulenzstrukturen untersucht werden können. Dabei wird zum einen die Grenze der Gültigkeit der Taylor-Hypothese der eingefrorenen Turbulenz untersucht. Zum anderen konnte die unterschiedliche horizontale räumliche Ausprägung von Turbulenzstrukturen unter unterschiedlichen atmosphärischen Bedingungen gezeigt werden. Weiterführend wird die Korrelation von unterschiedlichen Skalen im Frequenzraum mittels Kohärenz untersucht. Dabei zeigt sich im Vergleich zu Kohärenzverfallsmodellen eine auf neutrale Schichtung begrenzte Gültigkeit der Modelle. Insgesamt stellt sich eine geringere Kohärenz für laterale als für longitudinale Separationsdistanz ein.

In einer abschließenden Messkampagne wurden die gewonnenen Erkenntnisse und ein verbesserter Windalgorithmus zur Analyse der Umströmung einer Windenergieanlage (WEA) eingesetzt. Dabei wurden gleichzeitig Messungen im Nachlauf und in der Zuströmung der WEA durchgeführt. Räumlich verteilte Messungen im nahen Nachlauf einer 2 MW WEA zeigen deutlich das erwartete Windgeschwindigkeitsdefizit. Dabei deuten lateral verteilte Messungen im Nachlauf unter stabiler und nah neutraler Schichtung auf eine Doppelgauß-Verteilung des lateralen Geschwindigkeitsverlaufs hin. Unter konvektiven Bedingungen wird die turbulente Mischung verstärkt, was bereits im nahen Nachlauf zu einer Messung einer einfachen Gaußverteilung führt. Weiterhin zeigen horizontale turbulente Flussmessungen den erwartbaren Energieeintrag von außerhalb des Nachlaufs in die Randbereiche des Nachlaufs. Darüber hinaus konnte herausgearbeitet werden, dass zusätzlich in stabiler und nah neutraler Schichtung ein turbulenter Fluss vom Zentrum des Nachlaufs hin zu den Randbereichen des Nachlaufs messbar ist. Außerdem wurde das Auftreten von Wirbeln, resultierend aus den Druckunterschieden an den Rotorblattspitzen, untersucht.

Abstract

This thesis deals with the development of a unique measuring device for wind field measurement in the atmospheric boundary layer and its application to examine spatial turbulence structures in heterogeneous terrain as well as flow measurements around a wind turbine.

The innovative measuring system consists of a fleet of 35 quadrotors UAS (unmanned aerial systems), of which a maximum of 20 were used simultaneously. This measuring system enables flexible, simultaneous, spatially distributed measurements of the wind vector in the boundary layer. An algorithm was developed to measure the wind that is based on the position and acceleration sensors of the UAS and does not require additional external wind sensors. The algorithm puts the sensor data in relation to the acting wind forces and is calibrated and validated with the help of reference measurements on a 99-m meteorological mast. The potential of the UAS fleet for wind field and turbulence measurements is shown by comparisons with Doppler wind lidar and ultrasonic anemometer measurement data.

Furthermore, a special flight pattern with spatially horizontally distributed measurements was developed to allow for the examination of horizontal turbulence structures. On the one hand, the limit of validity of the Taylor hypothesis of frozen turbulence is tested. On the other hand, it is demonstrated how turbulence structures differ in their horizontal spatial characteristics depending on the atmospheric conditions. Additionally, the correlation of different scales in the frequency domain is examined using coherence. In comparison to models of the decay of coherence, the validity of the models is limited to neutral stratification. Overall, the coherence is smaller for the lateral separation distance than for the longitudinal one.

In a final measurement campaign, the knowledge gained and an improved wind algorithm were used to analyze the flow around a wind turbine (WT). At the same time, measurements were carried out in the wake and in the inflow of the WT. Spatially distributed measurements in the near wake of a 2 MW WT clearly show the expected wind speed deficit. Laterally distributed measurements in the wake under stable and near-neutral stratification indicate a double-Gaussian distribution of the lateral velocity profile. Under convective conditions, the turbulent mixing is enhanced, which leads to a measurement of a simple Gaussian distribution already in the near wake. Furthermore, horizontal turbulent flow measurements show the expected energy input from outside the wake into the edge areas of the wake. In addition, it could be shown that a turbulent flow from the center of the wake to the edge areas can also be measured in stable and near-neutral stratification. Also, the occurrence of vortices resulting from the pressure differences at the rotor blade tips was investigated.

List of Publications

Peer-reviewed publications, first author

- **Wetz, T.**, **Wildmann, N.** and **Beyrich, F.**, **2021**: Distributed wind measurements with multiple quadrotor unmanned aerial vehicles in the atmospheric boundary layer. *Atmos. Meas. Tech.*, **14**, 3795–3814, `https://doi.org/10.5194/amt-14-3795-2021`.

- **Wetz, T.** and **Wildmann, N.**, **2022**: Spatially distributed and simultaneous wind measurements with a fleet of small quadrotor UAS. *J. Phys.: Conf. Ser.*, **2265**, 022086, `https://doi.org/10.1088/1742-6596/2265/2/022086`.

- **Wetz, T.**, **Zink, J.**, **Bange, J.** and **Wildmann, N.**, **2023**: Analyses of Spatial Correlation and Coherence in ABL flow with a Fleet of UAS. *Boundary-Layer Meteorol*, Online First, 1–29, `https://doi.org/10.1007/s10546-023-00791-4`.

- **Wetz, T.** and **Wildmann, N.**, **2023**: Multi-point in situ measurements of turbulent flow in a wind turbine wake and inflow with a fleet of uncrewed aerial systems. *Wind Energ. Sci.*, **8**, 515–534, `https://doi.org/10.5194/wes-8-515-2023`.

Peer-reviewed publications, co-author

- **Wildmann, N.** and **Wetz, T.**, **2022**: Towards vertical wind and turbulent flux estimation with multicopter uncrewed aircraft systems, *Atmos. Meas. Tech.*, **15**, 5465–5477, `https://doi.org/10.5194/amt-15-5465-2022`.

Conference contributions

- **Wetz, T. and Wildmann, N.**: Simultaneous Wind Field Measurement with a swarm of multicopter UAV. In *16th EAWE PhD Seminar 2020*, Porto, Portugal, 14-16 December, **2020**.

- **Wetz, T. and Wildmann, N.**: Simultaneous Wind Field Measurement with a swarm of multicopter UAV. In *AGU Fall Meeting 2020*, 11-17 December, **2020**. URL `https://agu.confex.com/agu/fm20/meetingapp.cgi/Paper/750188` last access 20.04.2023.

- **Wetz, T., Wildmann, N., and Beyrich, F.**: Distributed wind measurements with multiple quadrotor UAVs in the atmospheric boundary layer. In *EGU General Assembly 2021*, Online, 19–30 Apr, **2021**. URL `https://doi.org/10.5194/egusphere-egu21-10239` last access 20.04.2023

- **Wetz, T., Wildmann, N. and Zink, J.**: Ertüchtigung und Validierung einer UAS Flotte zur Messung von turbulenter Strömung in der atmosphärischen Grenzschicht. In *DACH Meteorologie Tagung*, Leiptzig, Germany, 21-25 March, **2022**. URL `https://meetingorganizer.copernicus.org/DACH2022/DACH2022-75.html?pdf` last access 20.04.2023.

- **Wetz, T., Wildmann, N. and Zink, J.**: Spatially distributed and simultaneous wind measurements with a fleet of small quadrotor UAS. In *Torque 2022*, Delft, Netherlands, 1-3 June, **2022**. URL `https://iopscience.iop.org/article/10.1088/1742-6596/2265/2/022086/meta` last access 20.04.2023.

- **Wetz, T., Wildmann, N. and Zink, J.**: Spatial Correlation and Coherence Measurements in ABL flow with a Fleet of UAS. In *103th AMS 2023, 24th BLT*, Denver, USA, 8-12 January, **2023**. URL `https://ams.confex.com/ams/103ANNUAL/meetingapp.cgi/Paper/412278lastaccess20.04.2023`

Chapter 1

Introduction

The lowest layer of the atmosphere, up to an altitude of about 1-2 km over land and about 0.7 km over the ocean during daytime, is known as the atmospheric boundary layer (ABL) (Foken, 2021). Due to surface friction, variations in moisture content, and heat transfer to the air during the day and in the reverse direction during the night, the Earth's surface has an impact on the ABL. In offshore situations however, the diurnal circle typically has a minor effect. As the weather and climate on the Earth's surface are determined by the ABL, it is crucial to study and understand the mechanisms involved in this layer.

In addition to the significance of having a broad understanding of the ABL's processes, the ABL has a direct impact on a wide range of applications, including the production of renewable energy, particularly wind energy, the loads on large buildings, and agriculture. The wind in the lower part of the ABL close to the surface (also referred to as the surface layer < 200 m) is of major interest to wind energy science. In particular, turbulent structure and coherence analysis are crucial in wind energy science (Saranyasoontorn et al., 2004) and industrial aerodynamics (Midjiyawa et al., 2021). However, while a multitude of wind measurements exist in atmospheric science, none of them enable flexible, spatially distributed simultaneous turbulence measurements. The aim of the novel developed measurement system is to evaluate wind fields and turbulent structures simultaneously with numerous UAS. This allows spatial correlations and coherence measurements in almost fully flexible arrangements to analyze various phenomena in the ABL. The wind and turbulence structures in the ABL under various conditions and for varied objectives are the main focus of this study.

This section first explains the ABL and its turbulence structure, including correlation and coherence studies. The theoretical background of ABL flows is then applied to wind energy research. The flow around wind turbines (WT) is examined in detail and an overview of experimental studies on WT is given. Subsequently, existing wind measurement methods in the ABL are pointed out, followed by a detailed review of UAS (unmanned aerial systems) used for wind measurements in the ABL. The section ends with the introduction of the SWUF-3D fleet (Simultaneous Wind measurements with Unmanned Flight systems) and the objectives for the present study.

1.1 Atmospheric Boundary Layer

The layer that is directly affected by the Earth's surface at timescales shorter than an hour is known as the ABL. In general, in fair weather conditions and over land, the ABL experiences a diurnal cycle. When the cycle starts at midnight, the ABL is typically stable with an ABL depth of less than 200 m. In a stable boundary layer, the potential temperature increases with height due to radiative cooling at the surface and the turbulence level is typically low. The unstable mixed layer begins to evolve at sunrise (a sunny day is assumed) and grows taller as the day progresses. On a sunny day, the potential temperature usually decreases with height due to the solar heating of the surface, which results in buoyancy forces. Due to that, additional turbulence is produced, which typically leads to higher turbulence levels in convective ABLs. Between stable and convective conditions, neutral conditions are characterized by little cooling or heating from the surface, for example, in overcast situations Stull (2016). Since the current thesis is primarily focused on wind measurements in ABL, only the wind and turbulence of the atmospheric flow is examined in detail.

1.1.1 Turbulence Structure of ABL flows

In the ABL, the wind is mainly driven by large-scale pressure distribution and is additionally affected by surface parameters such as roughness, topography and obstacles near the Earth's surface. In near-neutral stratification, the mean velocity over height is typically approximated using the logarithmic wind profile, which starts at zero velocity at the bottom and grows logarithmically with increasing height. The mean velocity profile alone does not fully characterize the total flow situation since atmospheric flows, particularly under convective conditions, are highly turbulent. In order to analyze the turbulence, the wind speed u can be divided into a mean part $\bar{u}$ and a fluctuation part u' according to Reynold's decomposition

$$u \;=\; \bar{u} + u' \quad . \tag{1.1}$$

In atmospheric measurements the average interval is typically 10, 30 or 60 min (Foken, 2021). The turbulent motion itself can be described as a quasi-random, nonlinear 3D phenomenon with a duration of seconds to minutes, according to Stull (2016).

In atmospheric flows, turbulence can be generated either mechanically (shear) from surface drag or by buoyancy forces in convective ABL. The characterization of turbulence is a crucial part of understanding the processes within the ABL. The size of the turbulence eddies (swirl of a fluid) is one aspect that characterizes the turbulence. However, in ABL flows, they range from millimeters to kilometers, as illustrated in Fig. 1.1a, which poses a challenge for the measurement setup.

The energy spectrum of atmospheric motions from synoptic scales (> 2000 km) to microscales (< 1 km) is depicted in Figure 1.1. This spectrum shows how the various scales contribute to the overall energy of the velocity fluctuations. The low energy region, also called the spectral gap, in the mesoscales (2 - 200 km) distinguishes between local turbulent 3D motions and 2D (sub-)mesoscale non-stationary motions (Liang et al., 2014; Mahrt, 2009). The peak in the large scales in Fig. 1.1a is associated with the 4-day synoptic peak; the following peak is associated with the diurnal cycle; and the significant increase in energy in the microscales is defined as the turbulent peak.

The existence of a spectral gap is also confirmed by earlier studies (Lumley and Panofsky, 1964; Kaimal and Finnigan, 1994). However, according to Larsén et al.

(2016), the gap may or may not be visible, depending on the relative contribution of the microscale and mesoscale to the spectrum. In the presence of flow features such as rolls, low-level jets, and open cells, the spectral gap is not observable (Smedman, 1991; Smedman et al., 1995; Heggem et al., 1998; Larsén et al., 2019). Larsén et al. (2016) showed that the gap region in the spectrum can be superimposed by the meso- and microscale spectra (in offshore and flat terrain near the coast). As the height increases, the depth of the gap in the spectrum decreases.
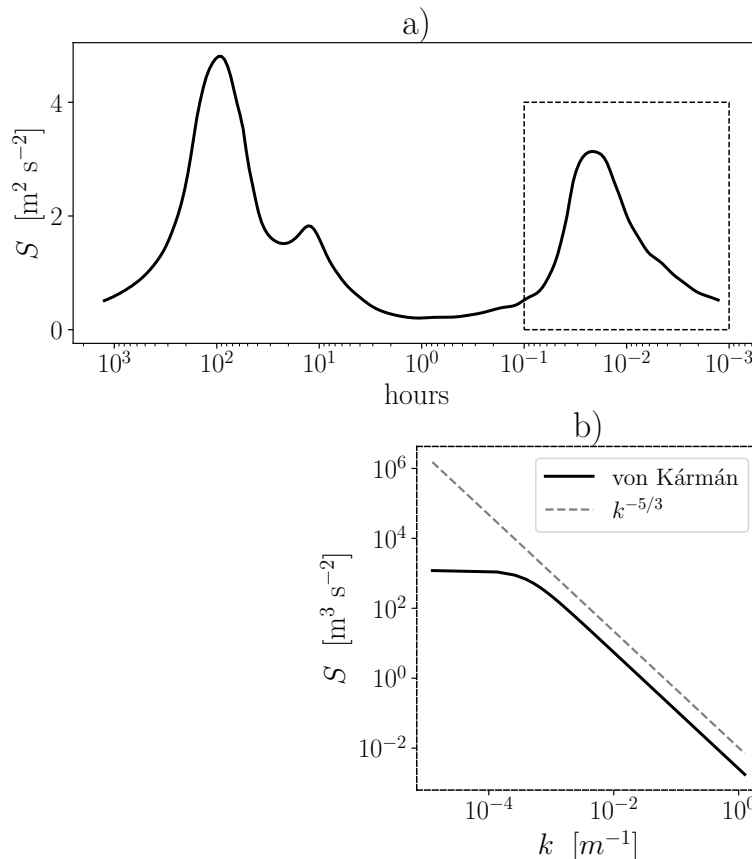
Figure 1.1: Energy spectrum from microscales to synoptic scales re-plotted from Van der Hoven (1957) a) and turbulent spectra from von Kármán (1948) in b).

The marked region in the overview spectrum in Fig. 1.1a) is defined as the turbulence spectrum and ranges from small mesoscales ($> 10^{-3}$ Hz), including the turbulent peak, to the microscales. This spectrum is divided into three parts (from large to small scales): the production zone, the inertial subrange and the dissipation range (Pope, 2000). The production zone is also known as the energy-containing range, implying that most of the turbulence energy is based in this region. From this production zone, the eddies break up into smaller ones and energy is transported to smaller scales until it is dissipated into heat by molecular viscosity at the Kolmogorov scales. This transport of energy is called the turbulent energy cascade. Following Kolmogorov, the inertial subrange and the dissipation range can be referred to as the universal equilibrium range. In this range, the turbulence has a universal isotropic character and the decay of the turbulent energy over the scales follows a clear relationship. Through dimensional analysis, Kolmogorov (1941) found the law of $-5/3$ for the decay of the turbulent energy distribution over the scales (see Fig. 1.1b), which was already stated empirically by Richardson (1920). In Fig. 1.1b the von Kármán spectra (von Kármán, 1948) is shown as representative of the turbulent spectra. This figure describes the theoretical

3

energy distribution across the scales at one position, including the production zone in the larger scales and the inertia subrange with the corresponding $-5/3$ law. This knowledge about the theoretical behavior of the turbulence spectrum can be used to validate the turbulence measurements. However, this spectrum only describes the distribution of the turbulence energy over the scales at one position. In this study, the focus is on the examination of spatial turbulence structure under various conditions and for different objectives, which is performed with spatial cross-correlation analyses.

In atmospheric science, various systems are used to measure turbulent flows. Direct point measurements are derived from ultrasonic measurements (Rajewski et al., 2013; Mauder and Zeeman, 2018), and spatial averages of turbulence parameters can be measured with Doppler wind lidars (DWL) (Smalikho et al., 2005; Wildmann et al., 2020b). These techniques are limited in their spatial resolution for studying the spatial extent of turbulence structures and their temporal evolution. Additionally, assumptions about the state of the atmosphere are necessary for the application of DWL. For the calculation of spatial information from point measurements, Taylor's frozen turbulence assumption is used (Taylor, 1938). This hypothesis states that the turbulence remains unchanged for a certain time while, for example, being advected through a measurement device. This assumption enables the translation from a time domain to a spatial domain using the mean advection velocity.

Taylor's assumption of frozen turbulence has been examined in multiple experiments using arrays of sonic anemometers (Horst et al., 2004) and DWL (Schlipf et al., 2010; Higgins et al., 2012). The validity of Taylor's hypothesis is theoretically examined by Mizuno and Panofsky (1975). They proposed that the validity of the hypothesis depends on two conditions. First, the similarity of the turbulent flow expressed by the coherence in the longitudinal direction should remain unity. Second, the local velocity should equal the advection velocity of the eddies (also called the translation speed of the eddies (Panofsky, 1962)). This study focuses manly on the first condition using coherence measurements but also examines the second one with spatial cross-correlations within the UAS fleet (see Sect. 2.2 and A3).

Correlation functions are often used to estimate the scales of turbulence. Additionally, cross-correlations can be used to compare temporal autocorrelations of single-point measurements with 'true' spatial correlations of two-point measurements separated in flow direction (Panofsky, 1962). An indicator for the horizontal shape of turbulence structures can be derived from the comparison of longitudinal and lateral spatial cross-correlations. The literature also frequently analyzes the structure's inclination angle, which is derived from a two-point correlation map of vertically separated measurements representing the vertical shape of turbulent structures (Hutchins and Marusic, 2007; Chauhan et al., 2012).

Coherence

The correlation functions consider the time series as a whole, including all scales. On the other hand, the similarity of flow structures at different scales can be studied by the coherence between spatially distributed measurements. The coherence can be thought of as a correlation in the frequency space (Ropelewski et al., 1973). The mathematical definition of coherence is the normalized cross-spectrum. On the one hand, assuming frozen turbulence, the time series of two spatially separated measurements would be identical and thus the coherence across all scales would be unity. On the other hand, for example, small-scale motions with a large separation distance show weak cross-correlations, which lead to coherence values close to zero. A

typical curve of coherence in the ABL as a function of frequency (see Fig. 2.10) shows high coherence at the large scales with a decay towards the small scales until nearly zero coherence (Davenport, 1961). Experimentally, the coherence is examined by two spatially separated measurements.

A first model of coherence in ABL flows, formulated by Davenport (1961) in the early 1960s and still widely used, proposed an exponential decay function of the coherence with increasing frequency f (decreasing eddy size). This model is based on observations of vertically separated measurements. The Davenport model predicts a decrease in coherence with increasing distance Δz and decreasing mean velocity $\bar{u}$. The exponential function of the model is scaled with a dimensionless decay parameter a

$$\gamma_z(f) \quad = \quad \mathrm{e}^{-a\dfrac{\Delta z}{\bar{u}}f} \quad . \tag{1.2}$$

The exponential characteristic of the coherence decay is confirmed by Pielke and Panofsky (1970) with observations from vertically separated measurements. They also found a decrease in coherence with increasing atmospheric stability.

Horizontal coherence over sea and on land is examined by Ropelewski et al. (1973) in different heights and for various horizontal separations. Their measurements outline higher decay parameters for lateral than longitudinal separations. Furthermore, the dependency on atmospheric stability is lower for longitudinal coherence than for lateral coherence. The lateral decay parameter tends to increase in unstable conditions.

Since the coherence is crucial in wind energy science in terms of aerodynamic loads and energy production, Saranyasoontorn et al. (2004) studied the longitudinal and lateral coherence in the Longterm Inflow and Structural Test (LIST) field campaign with sonic anemometers. The experiment outlines an increasing decay parameter with increasing vertical and lateral distances for the streamwise velocity fluctuations, based on the Davenport model. Additionally, reasonable agreements were shown with the isotropic turbulence model of von Kármán (1948). Comparisons with the von Kármán model outline a slight overestimation of coherence.

In the COTUR project, offshore turbulence is studied using remote sensing techniques. The lateral coherence is measured with multiple DWL for many different separation distances depending on the incoming flow direction, including a detailed study on coherence for separation distances around $\Delta y = 21$ m (Cheynet et al., 2021). The authors extended the Davenport model by taking two directions into account, the lateral and the longitudinal coherence. Furthermore, large eddy simulations (LES) are used by Simley and Pao (2015) to examine longitudinal coherence in the inflow of a WT. From these simulations, lidar-based scan strategies are derived for inflow coherence measurements at a WT. A theoretical turbulence model for spatial coherence is evaluated by Mann (1994) in extensive experiments.

1.2   Wind Measurements in the ABL

In atmospheric science, a multitude of measurement systems exist for analyzing the wind in the atmospheric boundary layer. Established and reliable wind measurement devices are sonic anemometers. Mounted on a meteorological mast, they are a powerful tool for long-term high-frequency studies at a fixed location in the ABL. Sonic anemometer measurements on meteorological masts are often supplemented by cup anemometers, which have a limited temporal resolution but are robust and

inexpensive. These masts, which can be up to 300 m high, are used for fundamental research, for example in heterogeneous terrain in Lindenberg (Beyrich and Adam, 2007), in a cluster for analyzing complex terrain flows in the context of wind energy research Fernando et al. (2019) or also for long-term observations and wind assessments for WTs Gryning et al. (2013). For more than a decade, Doppler wind lidars (DWL) have extend the remote sensing possibilities of wind in the atmosphere for a variety of applications, for example in wind energy research (Wildmann et al., 2018b) or fundamental turbulence structure analysis (Cheynet et al., 2016). Flexible in situ measurements are achieved with airborne measurements (Platis et al., 2018).

The measurement results of the mentioned methods and systems are reliable and valuable. However, these systems cannot be used very flexibly and typically involve a high level of logistical effort. Precisely because of these disadvantages, unmanned aerial systems (UASs) are becoming increasingly important to support or augment conventional atmospheric measurement techniques. The possible flight paths and thus the flight patterns with these vehicles are almost unlimited. In addition, the simultaneous use of several UAS in a campaign has the potential to measure atmospheric quantities in situ at flexible positions simultaneously. This enables new measurement strategies which are not possible with conventional measurement systems.

1.2.1 Unnmaned Arial Systems

Two possible but fundamentally different architectures exist for UAS. One has fixed wings and the other one is comparable with helicopters, in which only the thrust of the rotors provides lift for the vehicle (so-called rotary-wing UAS). The advantages of fixed-wing UAS are their long range and long flight times, which allow for studies at high altitudes. Various research groups use this approach for atmospheric research (van den Kroonenberg et al., 2008; Wildmann et al., 2015; Reuder et al., 2016; Mauz et al., 2019; Hamilton et al., 2022). The rotary-wing approach has the advantage that the vehicle can be used flexibly without the need for a runway. The vehicle can be placed flexibly at the point of interest in the atmosphere and measure the flow at this specific position while hovering. Additionally, this approach enables the use of multiple vehicles simultaneously in order to resolve 2D or even 3D wind fields. Since the aim of the present study is to measure wind fields and turbulent flows at multiple positions, only the multirotor approach is pursued.

Various approaches to measuring wind speed with multirotors are described in the literature. The obvious approach is to mount an external wind sensor such as hot wire probes (Cuxart et al., 2019; Molter and Cheng, 2020) or sonic anemometers (Shimura et al., 2018; Reuter et al., 2020; Thielicke et al., 2021; Nolan et al., 2018). Another approach is to use the motion of the UAS itself as a sensor without additional external sensors. Therefore, the onboard sensors of the avionic system of a multirotor are used to derive the wind vector (Palomaki et al., 2017; Brosy et al., 2017; Neumann et al., 2012; Neumann and Bartholmai, 2015; Gonzalez-Rocha et al., 2017; González-Rocha et al., 2019; Wang et al., 2018; Bartholmai and Neumann, 2011; Bell et al., 2020). The overall goal of the project is to achieve a fleet of up to 100 individual UAS; due to this high number, the complexity should be as low as possible to ensure robust methods and comparatively cost-effective solutions. For this reason, I focus on the approach that only uses the onboard sensors without the need for additional wind sensors (see Sect. 2.1 and A1, A2).

In general, this approach relates the orientation and acceleration measured by the UAS's Inertial Measurement Unit (IMU) to wind forces. Most of the approaches cited

6

assume the vehicle is hovering, which is reached on the basis of the GNSS (Global Navigation Satellite System), such that the remaining movements can be attributed to reactions to external wind forces. Neumann et al. (2012) took the inclination angle of the UAS and related the obtained drag forces by the Rayleigh drag equation to the wind speed. The drag coefficient and the projected area were estimated using analytic tools and wind tunnel experiments. However, the experiments were performed with fixed rotors, which neglect the major part of the aerodynamic drag of a multirotor (Schiano et al., 2014). For this reason, Neumann et al. (2012) calibrate a direct relation between the inclination angle and wind speed, resulting in a second-order polynomial fit. The velocity based on GNSS data is used by Brosy et al. (2017) as a reference to calibrate a regression function in flight experiments between wind speed and inclination angle. The result was a root-function with limited validation of $< 6 \, \mathrm{m \, s^{-1}}$. Based on wind tunnel experiments, González-Rocha et al. (2019) claim a linear relationship between the angle of inclination and wind speed for their UAS. The wind algorithm developed in this study is described in detail in Sect. 2.1.1.

1.3   Flow Field around Wind Turbines

Besides the more generalized theoretical analyses of turbulent flow structures in the ABL, the understanding of the flow around WTs and their optimization is highly relevant for the society. To achieve the International Energy Agency's (IEA) net-zero emissions targets by 2050, renewable energy generation capacity must increase dramatically. Veers et al. (2019) named the atmospheric flow one of the grand challenges for future wind energy research.

The performance and mechanical loads of WTs are primarily driven by the atmospheric flow, particularly the turbulence. Also, the wake of a WT is affected by atmospheric conditions. Larger WTs with high power generation or additional, closer staggered WTs in wind farms will be necessary in the future to fulfill the increasing demand for wind energy in the limited available space. The efficiency of wind farms is mainly determined by whether additional wake losses, which are caused by upstream wind turbines, can be reduced. Due to the energy extraction of a WT, a wake develops downstream of the WT and is characterized by a low velocity region. If this region encounters a downstream turbine, its efficiency is significantly reduced. The wake also increases loads and fatigue on the downstream turbine due to the induction of turbulence. Therefore, smaller relative separation distances of WTs, due to repowering, and larger WTs, which cause more prominent wakes, make understanding WT wakes crucial for wind farm optimization.

The flow around a WT follows a generalizable pattern with characteristic short-term flow features and mean velocity distributions. This universal and rather theoretical flow field around a wind turbine is described below to allow a better understanding of the velocity measurement carried out on a wind turbine in operation.

In Fig. 1.2, the flow field around a WT is illustrated, including the different zones. The WT affects the ambient atmospheric flow downstream and upstream. The area upstream of the WT where the blockage effects of the WT reduced the wind velocity is described as the induction zone. Simley et al. (2016) proposed an estimation for the reduced wind velocity based on the induction factor.

As illustrated in Fig. 1.2 and proposed by Vermeer et al. (2003) the downstream regime of a WT can be classified into a near wake and a far wake. Complex and highly heterogeneous flow distributions characterize the near wake. This zone is influenced

by the current conditions and operation of the WT as well as their design. The extent of the zone is shown in Fig. 1.2 and defined by Wu and Porté-Agel (2012) with a distance of two to four rotor diameters D. One dominant flow feature in the wake is the tip vortex, which develops at the tip of the rotors due to the pressure differences between the suction and the pressure side. These tip vortices form a helical vortex that wraps around the wake and separates the wake from the freestream, as shown in Fig. 1.2. In contrast to the near wake, the regime further downstream, defined as the far wake, is more uniform. No specific flow features are present and the velocity distribution depends only slightly on the operation and the specific design of the WT. Therefore, the velocity distribution is more uniform and can be assumed to be of universal character. The recovery of the velocity deficit, also called wake recovery, is completed at 8 D downstream of the WT (Porté-Agel et al., 2019). This distance can increase multiple diameters further downstream under stable atmospheric conditions and for increased sizes of WTs (Fuertes et al., 2018).
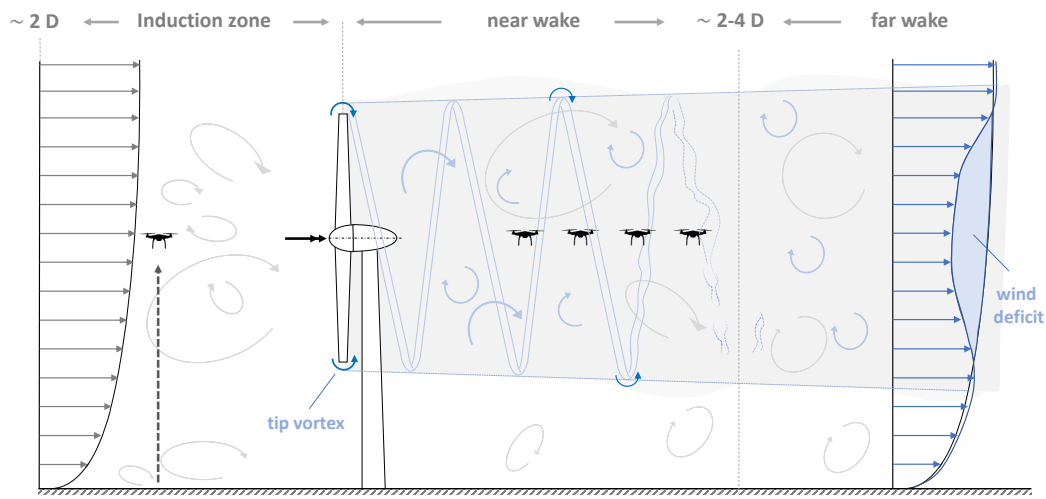
Figure 1.2: Schematic flow field around a WT. Blue eddies result from interactions with WT and grey origin in the ABL. Potential inflow and wake measurements with the SWUF-3D fleet are illustrated with drone icons.

1.3.1   Measurements at WTs

Since modern WTs have existed for decades, their operation and wake have been widely examined with numerical methods.Jensen (1983) developed a basic analytic model that is still implemented in current fast computing wake models of single turbines. More advanced wake models designed for fast optimization of entire wind farm operations and design were developed by (Bastankhah and Porté-Agel, 2014). Nowadays, for detailed studies of the WT wake, large-eddy simulations (LES) with high-resolutions are state-of-the-art (Mehta et al., 2014; Englberger et al., 2020).

Besides numerical simulation, WTs have been studied in numerous experiments in wind tunnels and field campaigns. In the examination of laboratory flows, the particle image velocimetry (PIV) method has contributed a great deal to a better understanding of wake flows of WT in the last decade (Sherry et al., 2013; Bastankhah and Porté-Agel, 2017). In field campaigns with full-size WTs, mostly remote sensing systems are deployed to measure the flow field. In recent years, often DWLs are used, which are deployed at the ground to study the development and characteristics of the wake, for example, in complex terrain (Menke et al., 2018; Wildmann et al., 2020a). Further

wake analysis can be performed using DWLs, such as the influence of atmospheric stability on the wake length (Wildmann et al., 2018a) and the wake-center localization (Wildmann et al., 2018b). Besides ground-based lidars, they are also deployed on the nacelle for flow measurements which are used for LES validation (Doubrawa et al., 2020) and for detailed WT wake studies (Aitken and Lundquist, 2014; Machefaux et al., 2015; Fuertes et al., 2018). Additionally, in the optimization of active yaw control, spinner-integrated lidars provide valuable measurements (Mikkelsen et al., 2012).

As a supplement or also for independent experiments, in situ measurements are becoming more prominent in flow analysis in wind energy research. In this research field, different airborne systems are used. Analysis of entire offshore wind parks are carried out with crewed research aircraft (Platis et al., 2021) and for measurements around single WTs UAS rotary-wing (Thielicke et al., 2021; Li et al., 2022; Wetz and Wildmann, 2023) and fixed-wing configurations are used (Kocer et al., 2011; Wildmann et al., 2014; Reuder et al., 2016; Mauz et al., 2019; Alaoui-Sosse et al., 2022). Due to the fact that only one system is used in the listed measurements, no simultaneous measurement of a flow field is possible. Multicopters enable only one spatial position, while fixed wings only provide a single time step at certain positions. However, by using multiple or even a fleet of quadrotors, multiple time series can be measured at different spatial positions, which enables the simultaneous measurement of a wind field with high temporal resolution. For the application of wind energy research, with this measurement system detailed wake analyses are possible while simultaneous even observations in the inflow can be carried out. The results of the measurement are analyzed in Sect. 2.3.

1.4 Measurement System

In this study, a novel measurement system is developed to measure the wind at different spatial positions simultaneously. Various flight systems were tested for this purpose. As mentioned previously, the goal is to resolve a 3D wind field with high-resolution turbulence measurements; only multicopters fulfill this requirement. Since accessibility of the sensor data from the IMU (inertial measurement unit) is mandatory for the wind algorithm, only a multirotor with the open-source Pixhawk autopilot, which allows both accessibility and adjustments, is pursued. Adjustability is important for the integration of additional sensors such as temperature and humidity or, for example, external systems for position control in indoor environments without GNSS, which is necessary for wind tunnel experiments.

Due to its simple architecture and possible small dimensions, a multicopter with four propellers, a so-called quadrotor, is selected for this study. Two different quadrotor sizes are extensively tested, namely the HolyBro S500 with 500 mm diagonal spacing between the rotor axis and the HolyBro QAV250 with 250 mm diagonal spacing. The experiments were carried out both in the field and in a wind tunnel. The tests reveal better dynamic behavior and higher resistance to high wind speeds for the small quadrotor. Additionally, the smaller size enables the resolution of smaller turbulence structures. A drawback is the lower potential payload and shorter flight time compared to the larger quadrotor. However, the HolyBro QAV250 (shown in Fig. 1.3) is chosen due to its better dynamic behavior in turbulent wind conditions.

To reduce the complexity of the wind algorithm the quadrotor is operated in the 'weather-vane' mode. That operation mode controls the yaw angle such that the roll angle is minimized and the UAS is therefore oriented towards the wind direction.

The maximal total flight time with a battery capacity of 3500 mAh is approximately 17 min. A temperature and humidity sensor (HYT271) is additionally mounted on the UAS. The weight of the complete system is 0.645 kg.

Figure 1.3: Picture of the quadrotor 'HolyBro QAV250' in front of the meteorological mast at Falkenberg. Photo by Bernd Lammel. This picture and description are taken from Wetz et al. (2021).

The fleet consists of a total of 35 UAS, of which a maximum of 20 quadrotors are operated simultaneously. Since the entire fleet cannot be controlled manually, they are monitored by the ground station © QGroundControl, which allows multiple vehicles to be controlled. The fleet communicates via an external Wi-Fi router. In most of the experiments, the measurements of the UAS were performed at a fixed position. To create the individual flight paths, a tool is developed that enables semi-automatic flight planning, including approach and landing from the target measurement position of the specific measurement patterns. Special attention was paid to the intersection of the trajectories when 20 UAS are flying at the same time.

1.5   Research Objectives

One of the main goals of this thesis is the development of a measurement system that enables high-temporal-resolution measurements of turbulent wind fields. For the turbulence wind measurements, a wind algorithm is developed and calibrated for the fleet of UAS and validated against various references. With this calibrated SWUF-3D fleet, turbulence structures and their horizontal extent in heterogeneous terrain are analyzed with horizontally distributed measurements. The potential of the SWUF-3D fleet for research application in the flow field around wind turbines is investigated in a field campaign. In particular, the velocity profile in the near wake of an operating WT is examined in detail together with turbulence analysis and the tip-vortex. For each of the subject areas, the following specific research questions can be derived.

1.5.1   Wind Algorithm of the UAS

- Can a clear relationship between the pitch angle and the wind speed be formulated for the chosen hardware?

- Does the 'weather-vane' mode and thus only the orientation of the UAS, reveal accurate wind direction measurements?

- How accurate are the mean wind speed measurements?

- Is the aerodynamic behavior within the entire fleet comparable, so that the wind algorithm can be applied to the entire fleet?

- Which turbulence scales/resolutions are possible and does additional data from the IMU, for example accelerometer data, improve the dynamic behaviour?

- Does the SWUF-3D fleet deliver reasonable wind field measurements in comparison to lidar and meteorological tower observations?

1.5.2 Examination of Turbulence Structures of the ABL

- Are the separation distances observable in the phase spectrum of two spatially separated UAS measurements?

- Does the two-point cross-correlation of streamwise separated measurements agree with the temporal autocorrelation under different atmospheric conditions?

- How does the horizontal shape of turbulent structures vary with atmospheric stability, regarding the cross-correlations in the lateral and longitudinal directions?

- Are exponential decay models from Davenport and Schlez appropriate to model the coherence under different conditions?

- How does the coherence change with atmospheric stability?

- What are the limits of the validity of Taylor's frozen turbulence assumptions?

1.5.3 In Situ Measurements at a 2 MW Wind Turbine

These research questions are adapted from the 4th publication of this thesis (Wetz and Wildmann, 2023).

- Can a fleet of UASs measure a double-Gaussian velocity deficit and turbulence intensity profile in the near wake of a WT?

- Do the horizontal momentum fluxes point towards the inner wake at the edge of the wake?

- It is possible to capture the tip vortex with multicopter measurements at the edge of the wake?

- Do the near-wake characteristics significantly change at different downstream distances ($< 2D$)?

- What are the influences of atmospheric stability on the near wake regarding the velocity deficit and the turbulence intensity?

Chapter 2

Results

2.1 Wind Algorithm Calibration and Validation

The results presented in this section are based on the two publications Wetz et al. (2021) and Wetz and Wildmann (2022) (see Appendix A1, A2). The introduced SWUF-3D fleet, consisting of 35 quadrotors, is intended to measure the wind vector without additional sensors. For wind measurements without external sensors, different approaches were discussed in Sect. 1.2.1. The goal of developing a 1D wind algorithm is to create a robust method that can be applied to the entire UAS fleet with only small individual offset calibrations. The idea for this robust calibration is based on the relation between the motion of the UAS and the wind forces. The wind speed can be derived from the wind forces using the established Rayleigh drag equation (Eq. 2.2). The data from nine UASs are calibrated with tower measurements and also validated against lidar data. In the next step, an advanced 2D wind algorithm, based on the accelerometer data, with improved dynamic behavior, is calibrated for the entire UAS fleet of 35 quadrotors.

2.1.1 Wind Algorithm

Taking the force equation of a ridged body model into account, the inertial forces are balanced by the gravity forces and the external forces acting on the UAS. Only the x-direction of the body system is considered, since the UAS is always aligned in the wind direction due to the activated 'weather-vane' mode. The autopilot compensates for wind forces mainly by increasing the pitch angle to keep the UAS in a fixed position. For this approach, idealized hover flight conditions are assumed; that means that the inertial forces can be neglected, which results in the simple equation for the wind forces in the x-direction

$$F_{w,x} \quad = \quad mg \sin \theta \quad , \tag{2.1}$$

where θ is the pitch angle of the UAS, g the gravity and m the mass of the UAS. Taking the aerodynamic Rayleigh-equation into account

$$\mathbf{F_w} \quad = \quad \frac{\rho}{2} \, c_d \, A \, \mathbf{V}_w^2 \quad , \tag{2.2}$$

the wind velocity in the x-direction of the UAS can be calculated

$$V_{w,x} \quad = \quad \sqrt{\frac{2 \, F_{w,x}}{c_d \, A \, \rho}} \tag{2.3}$$

12

with the drag coefficient c_d, the projected area A and the density ρ. In this equation, the term $c_d\,A$ remains unknown and could either be estimated or calibrated. Due to the complex aerodynamics and shape of a quadrotor, this term is calibrated in this work. The dependency of the projected area and the drag coefficient on the attitude of the UAS is considered with an additional term $f(\theta)$

$$c_dA \;=\; c_{d,0}A_0 + f(\theta) \quad, \tag{2.4}$$

where $c_{d,0}A_0$ is the drag coefficient and the area at zero pitch angle and in this study, it is assumed that the function $f(\theta)$ is a linear function.

2.1.2 Measurement Site

In order to calibrate and validate the wind algorithm, the site of the German Meteorological Service (Deutscher Wetterdienst, DWD) at the Boundary Layer Field Site (Grenzschichtmessfeld, GM) Falkenberg of the Lindenberg Meteorological Observatory was chosen, where we participated in the FESST@MOL campaign for two weeks (July 21-31, 2020). Central to the present study at GM Falkenberg is the 99 m tower, which is instrumented with sonic and cup anemometers at multiple levels. In this campaign, 76 single UAS-fleet flights were realized, resulting in 4800 minutes of flight data. Different flight patterns were deployed with the purpose of calibrating and validating the UAS fleet. The results were compared with reference measurements from the tower in the 'drone tower' flight pattern (see Fig. 2.1) where eight quadrotors fly at the same horizontal position but at different altitudes within a horizontal safety distance of 20 m to the tower. On the map in Fig. 2.1, the tower is illustrated, as well as the different flight patterns. Additionally, a Doppler wind lidar of the type Leosphere Windcube 200S is installed at the side and used for validation of the UAS fleet. First, in the 'lidar-line-pattern', the UASs are aligned in a fixed lidar beam. In a second pattern, 'drone 3x3 lidar', the drones are oriented in a 3x3 vertical grid in order to compare 2D wind field measurements with the lidar data.

2.1.3 Calibration

The parameters from Eq. 2.4 are calibrated agianst the reference measurements on the tower. The aim of the calibration is to find a parameter set ($c_{d,0}A_0$ and c_p) for all UASs that reflects the general behavior of the UAS to the wind. For this purpose, a UAS is selected that has been used in a large wind speed range. In addition to the general parameter set, an individual pitch offset $\Delta\theta$ is calibrated, to account for small deviations in the misalignment of the installation of the IMU and slightly different mass distributions of the individual systems. This drone-specific parameter can be calibrated with only a single flight.

In a first step, a benchmark calibration with individual calibrations of all parameters for each UAS is performed in order to compare them with the following calibrations. In the second step, one parameter set is used for all UAS. The comparison to the benchmark calibration shows that a universal parameter set can be found within the fleet, which only leads to a small loss of accuracy with a root-mean-square (rms) deviation of $\bar{\epsilon}_u = 0.25$ m s^{-1} in comparison to the benchmark calibration $\bar{\epsilon}_u = 0.23$ m s^{-1}. This calibration leads to the universal parameters

$$c_dA \;=\; 0.03 - 0.047\cdot\theta \quad. \tag{2.5}$$
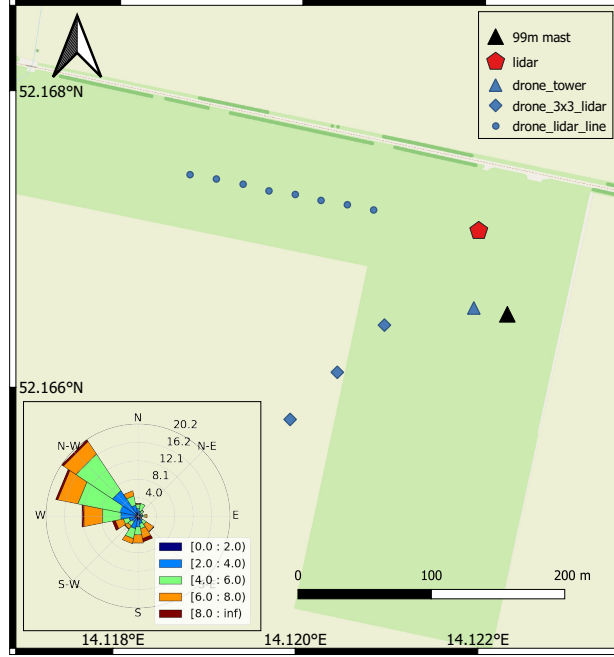
Figure 2.1: Map of the experiment site, including the locations of UAS fleet measurements. ©OpenStreetMap contributors 2020. Distributed under a Creative Commons BY-SA License. The wind rose in the bottom left shows the wind conditions during the campaign period (21-30 July 2020). Figure and description from Wetz et al. (2021).

In a next step, the pitch offset $\Delta\theta$ is calibrated with only one flight for each UAS. This calibration leads to an accuracy of $\bar{\epsilon}_u = 0.27$ m s^{-1} within the entire fleet, which again deviates only slightly from the benchmark calibration. The validation plots of the calibration for all UAS involved can be found in Appendix A1. For a fair validation, an independent data set from the calibration is chosen. Therefore, the calibration will only be performed on flights from the first week, while the validation is executed with data from the second week.

Besides the wind speed, the wind direction can also be derived from the UAS data. Since the UASs operate in the 'weather-vane' mode, the yaw-angle measured by the IMU gives a good first estimate of the wind direction. However, an additional offset calibration of the yaw angle is performed since optimal orientation of the magnetometer towards the north cannot always be guaranteed. Therefore, a calibration is conducted with the reference wind direction of the tower measurements. This calibration results in a mean accuracy of $\bar{\epsilon}_\Phi = 7.5$ °

2.1.4 Comparisons with Lidar Data

For further validation and the ability to resolve flow structures in the ABL, measurement data are compared with DWL data. Two different scenarios were carried out during that campaign. First, eight quatrotors were distributed along in a fixed lidar beam. They were placed in equal distance (20 m) in the line-of-sight as the range gate separation distance of the DWL as illustrated in Fig. 2.1 in the 'lidar-line' pattern. Figure 2.2 shows the comparison of the time series, which were interpolated to form a continuous horizontal spatial line, over the measurement time. This figure outlines the agreement in the measurement of the wind speed variation. For example, at 13:27 UTC, there was a clear gust that was observed with both systems.
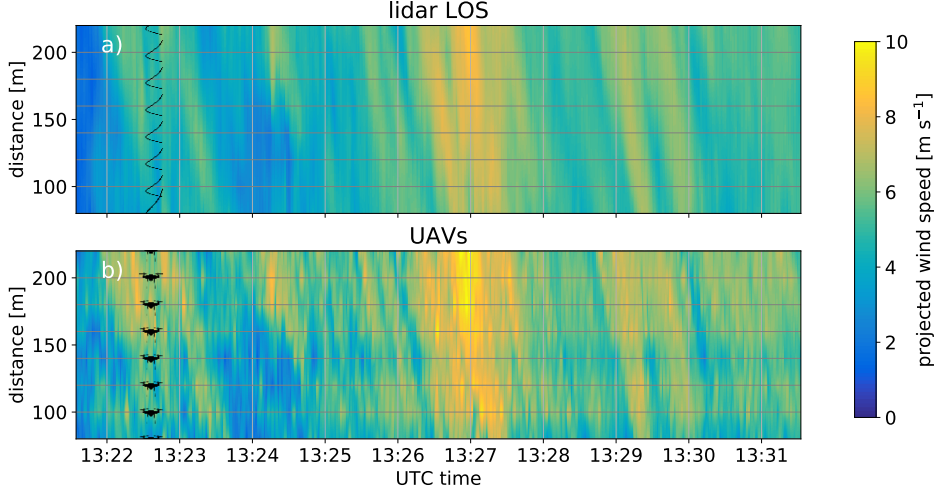
Figure 2.2: Time series of spatial wind measurements with a lidar (a) and eight UAS (b) along a lidar line-of-sight. The y-axis grid represents the horizontal location of the range gate centers of the lidar and the UASs respectively. Figure and description from Wetz et al. (2021).

In a second scenario, a vertical plane with nine UAS is spanned in 'drone 3x3 lidar' pattern (see Fig. 2.1). This pattern is compared with lidar data in that plane, which were derived from lidar RHI (range-height indicator) scans, in order to validate the 2D wind field measurements. The main features of the flow are observed with the UAS and the DWL (see Appendix A1).

These two comparisons reveal that the SWUF-3D fleet is able to capture spatial structures, even though direct comparison to the reference instruments is extremely challenging under convective conditions that were present during these comparisons.

2.1.5   Advanced Wind Algorithm

For the basic 1D wind algorithm, only the pitch angle was used as an input variable to calculate the wind speed. In a second approach, the acceleration data from the IMU is now used directly, both in longitudinal and lateral directions, in order to achieve better dynamic behavior and a 2D wind algorithm. In addition, since the aerodynamics of the quadrotors are more complex than those of a solid body, the relationship between wind speed and forces previously described with the Rayleigh drag equation is not used since most of the drag is caused by the rotors. Therefore, a general approach to the calibration equation with a variable exponent is chosen.

In this approach, the dynamic part of the equation of motion is additionally taken into account, which was neglected for the 1D algorithm due to the assumption of idealized hovering. This means that the acceleration of the UAS is considered when calculating the horizontal wind force. The additional gyroscopic terms contained in the equation of motion are negligibly small and therefore the equations for the forces result in

$$F_{\mathrm{w,x}} = m[g\sin(\theta) + \ddot{x}] \tag{2.6}$$

$$F_{\mathrm{w,y}} = m[g\cos(\theta)\sin(\phi) + \ddot{y}] \tag{2.7}$$

In Figure 2.3 the different input data for the wind algorithm are compared. There, it is clearly shown that the dynamic behavior at small scales can be improved with the

15

accelerometer data as input data. With this approach, the turbulence scales can be resolved until 1 Hz. At even smaller scales, sensor noise dominates the measurements, as shown in the figure.
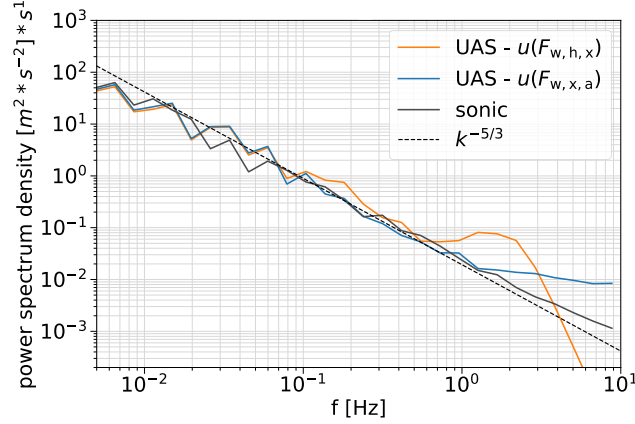
Figure 2.3: Power spectra in longitudinal direction - of the wind velocity spectra derived from the wind forces: $F_{w,h,x}$ hover state assumption, $F_{w,x,a}$ including acceleration data from the accelerometer of UAS measurements in comparison with sonic anemometer data. Figure and description from Wetz and Wildmann (2022).

The advantage of a variable exponent in comparison with the root-function (Rayleigh drag equation) for the relation between wind speed and wind forces is that the calibration curve can better represent the actual transfer function. Additionally to the adjusted function, the wind velocity is corrected with the ground speed of the UAS obtained from the GNSS, which theoretically enables measurements even during forward flights and not only in the hovering state. The equations for the longitudinal u and lateral v wind velocity result in

$$\mathbf{V} = \begin{pmatrix} u \\ v \end{pmatrix} = \begin{pmatrix} c_x \cdot F_{w,x}^{b_x} \\ c_y \cdot F_{w,y}^{b_y} \end{pmatrix} - \begin{pmatrix} \dot{x}_{gps} \\ \dot{y}_{gps} \end{pmatrix} \quad . \tag{2.8}$$

Since the UASs are operating in the 'weather-vane' mode, the side wind component is small. Therefore, the variance σ_v^2 is used as the target variable for the calibration of the crosswind component. The additional lateral wind component particularly increases the dynamic behavior of the wind direction measurements, as not only the yaw angle of the UAS is taken into account but also the tangent of the longitudinal and lateral wind components. The target values for the calibration of the along-wind component are taken from the sonic measurements. In order to increase the dynamic behavior and the statistic for wind variance measurements, only 2 s time averages are taken as targets in comparison to 10 min time averages for the 1D algorithm.

The experiment was conducted during the FESSTVaL (Field Experiment on Sub-Mesoscale Spatio-Temporal Variability in Lindenberg) campaign at GM Falkenberg in June/July 2021 with the entire SWUF-3D fleet of 35 quadrotors. During the experiment, 119 calibration flights (see the 'calibration pattern' in Fig. 2.5) were performed with wind speeds ranging from 0 to 8 m s^{-1} and turbulent kinetic energies (TKE) from 0.03 to 2.5 m^2 s^{-2}. The resulting calibration parameters for the longitudinal and lateral horizontal directions of the wind algorithm (Eq. 2.8) are listed in Table 2.1.

Table 2.1: Specification of wind algorithm parameters for Eq. 2.8 (proportional parameter c and exponent b). Table and description from Wetz and Wildmann (2022).

direction	c	b
longitudinal (x)	7.775	0.845
lateral (y)	6.373	0.898

The calibration results for the advanced wind algorithm are shown in Fig. 2.4. A single data point in this figure shows the time average of the corresponding flight in comparison with the reference sonic measurement. In order to ensure independent input data for the validation, the data used for the calibration of the UAS fleet are excluded from the validation. In Fig. 2.4a, the mean longitudinal velocity measurements agree well with the sonic data, with a mean RMS deviation of $\epsilon_u = 0.25$ m s^{-1}. The accuracy of the wind speed variance (Fig. 2.4b) with an RMS deviation of $\epsilon_{\sigma^2,\mathrm{u}} = 0.16$ m^2 s^{-2} is significantly improved. The additional correction of the wind direction measurement using the lateral velocity component results in an average RMS deviation of less than $\epsilon_\Phi < 5°$ (Fig. 2.4d).
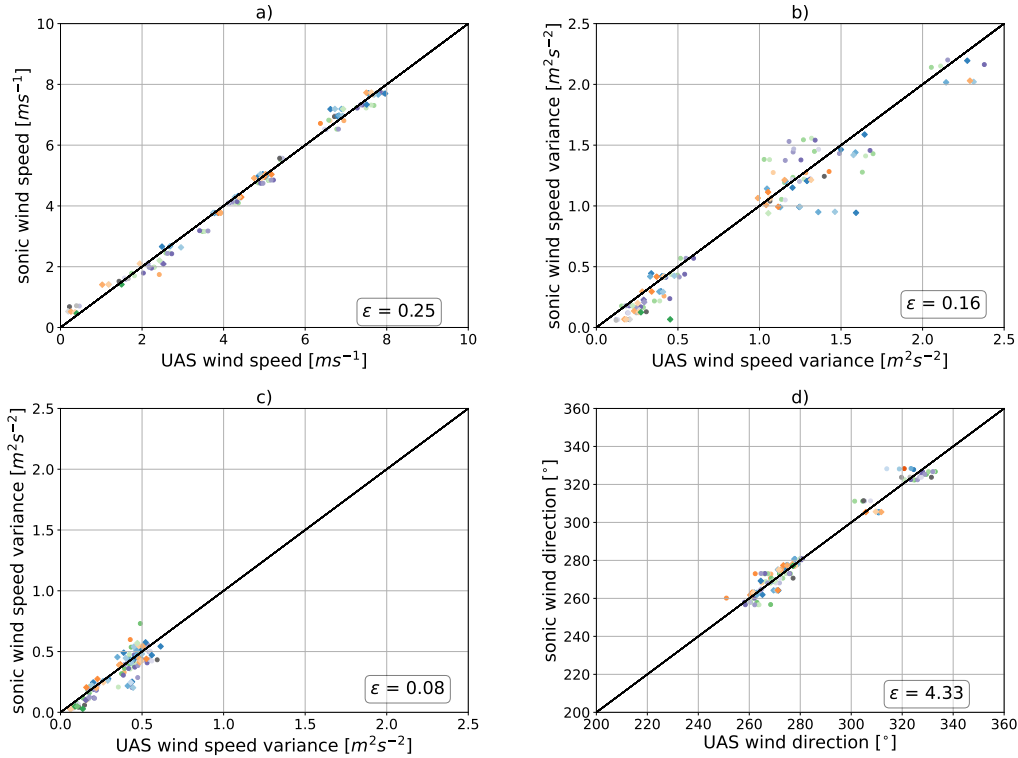
Figure 2.4: Flight averaged data for all calibration flights, different colors and markers representing different UAS (no. 2-35) measurements in comparison to sonic anemometer wind measurements including the RMS deviation ϵ : a) longitudinal wind speed, b) longitudinal wind speed variance, c) lateral wind speed variance, d) wind direction. Figure and description from Wetz and Wildmann (2022).

The turbulence spectra measurements for different flight cases were also analyzed during this campaign (see Appendix A2). These show that in cases of high turbulence, the UAS measurements follow the sonic measurements and the Kolmogorov slope up to approximately 2 Hz. For smaller scales, there is an almost constant noise level of

0.01 m^2 s^{-1}. Due to that, in low turbulence conditions, already at lower frequencies, the noise of the sensor is significant and disturbs the turbulence measurement due to the low signal-to-noise ratio.

2.2 Horizontal Correlations of Spatially Distributed Measurements

Building on the extensively calibrated and validated wind measurements of the SWUF-3D fleet, horizontal correlations and coherence of turbulence are examined using spatially distributed UAS measurements. The results of this study were published in the journal *Boundary-Layer Meteorology* (Wetz et al., 2023) (see Appendix A3).

2.2.1 Experiment

At the same field site as in the previous campaign, the GM Falkenberg, spatially horizontally distributed measurements were carried out simultaneously with 10 quadrotors during the FESSTVaL campaign (illustrated in the map in Fig. 2.5).
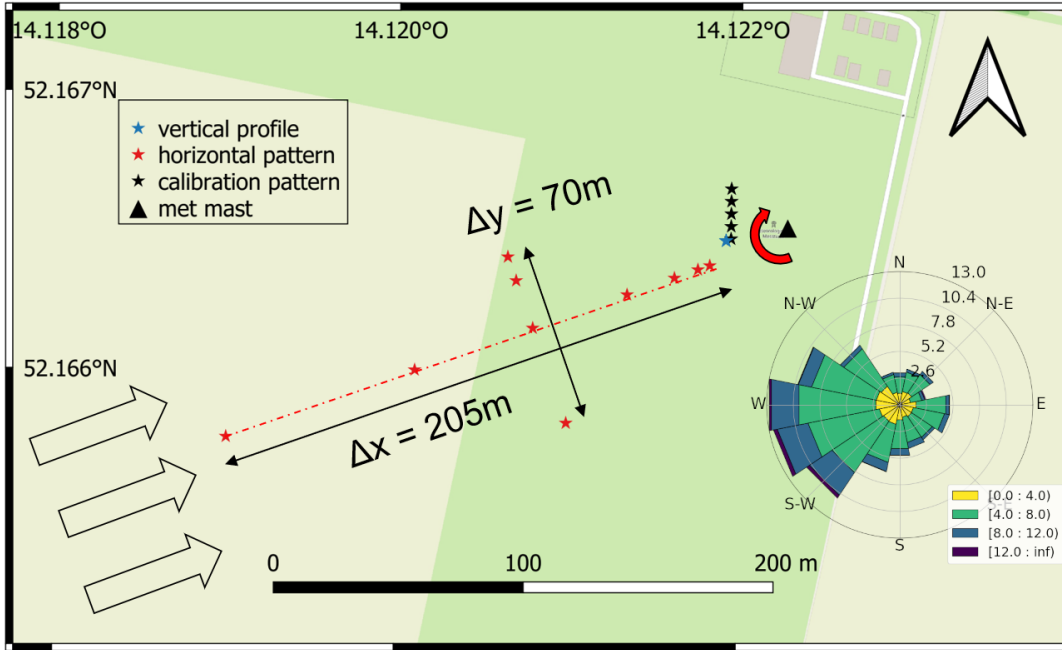
Figure 2.5: Map of the field site of GM Falkenberg, including the 99 m meteorological mast and different flight patterns of the UAS fleet. Each star represents an individual UAS at its measurement position. The dark green area is short cut grass, whereas the light green area was a cornfield in 2021. The arrows on the left side represent the wind direction and the corresponding orientation of the 'horizontal pattern'. Background map ©OpenStreetMap contributors 2022. Distributed under a Creative Commons BY-SA License. The wind rose is extracted from the meteorological mast at 98 m a.g.l. Figure and description from Wetz et al. (2023).

For examining turbulence structures in the ABL, the focus is on the 'horizontal pattern'. In this pattern, multiple UAS are spatially distributed at different distances longitudinally and laterally to the mean wind direction. In order to adjust the orientation of the pattern to the current wind direction (illustrated by the red curved arrow in Fig. 2.5), the flight plans are generated and uploaded semi-automatically. Logarithmic horizontal separation distances were chosen for the 'horizontal pattern' to generate maximal diversity in the potential separation distances for the evaluation where all UAS are combined with each other. The lateral spacings (Δy) are between 10 m to 70 m, while the longitudinal spacings (Δx) are between 5 m and 205 m. In order to ensure comparable results, this particular pattern was not modified during

19

the campaign but was applied under different atmospheric conditions and at different altitudes.

2.2.2 Validation of Turbulence Measurements

Since coherence and turbulence analysis will be part of this study, in this section the turbulence spectra of the UAS measurements are checked for plausibility and compared with reference measurements. In Fig. 2.6a the amplitude spectra of the along-wind component of two UAS are compared to the corresponding single-point power spectrum of the reference measurements. Also, the power spectrum of a single UAS is provided for a fair comparison to the power spectrum of the sonic anemometer. This figure demonstrates the ability of the UAS to measure turbulence spectra under these neutral atmospheric conditions. The agreement of the measurements is good even though the horizontal distance between the UAS and the reference measurement is 30 m.
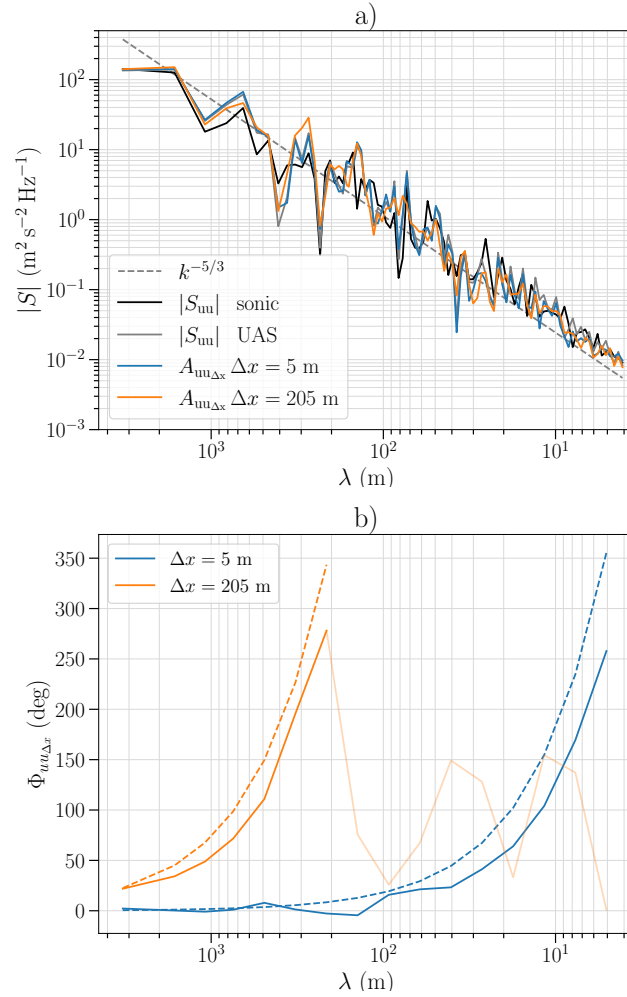
Figure 2.6: Power spectrum density $|S_{uu}|$ of sonic anemometer measurements in comparison to UAS measurements a) power spectrum $|S_{uu}|$ and amplitude spectra $A_{uu_{\Delta x}}$ and b) phase spectra $\Phi_{uu_{\Delta x}}$ with longitudinal separation of $\Delta x = 5$ m and $\Delta x = 205$ m. The thin orange line represents the measured phase for $\lambda < \Delta x$. Dashed lines indicate the theoretical phase resulting from the separation distance Δx and the advection velocity $\bar{u}$ as calculated from Eq. 2.10. Figure and description from Wetz et al. (2023).

In Fig. 2.6b the phase spectra of two longitudinally separated UAS measurements ($\Delta x = 5$ m and $\Delta x = 205$ m) are shown. Assuming that the turbulence is frozen, eddies are transported with the mean local velocity $\bar{u}$. Based on this assumption, the wavelength is defined as

$$\lambda \;\; = \;\; \frac{\bar{u}}{f} \;\; . \tag{2.9}$$

The separation distance of the measurement Δx is expected at the position of the first maximum of the phase spectrum (360°) so that $\lambda(\Phi = 360°) = \Delta x$. The theoretical phase spectra for larger wavelengths, expressed in degrees, can be calculated as

$$\Phi_{\mathrm{uu}_{\Delta_{\mathrm{x}}}} \;\; = \;\; \frac{\Delta x}{\lambda} \; 360° \;\; . \tag{2.10}$$

These comparisons reveal that the phase spectra measured by the UAS is in agreement with the theoretical phase and the maxima are observed at the wavelength that corresponds to the separation distances. However, between the theoretical phase and the phase spectra small deviations are present in the range of shorter wavelengths. These deviations could either originate from deviations from the 'true' separation distance or from smaller mean local velocities compared to the translation speed of the eddies.

2.2.3 Spatial Cross-Correlations

The objective of the horizontal pattern (illustrated in Fig. 2.5) is to analyze horizontal correlation in streamwise and lateral directions. First, the cross-correlation functions of streamwise separated measurements are shown in Fig. 2.7. For this purpose, the seven UAS wind velocity measurements at different positions are cross correlated with the most easterly UAS in this flight (as illustrated on top of Fig. 2.7). It is plausible that the time shifts of the correlation maxima increase and the magnitude of the correlation maxima decrease with increasing separation distance. From this figure, the separation distances can be derived by the time delay from the maxima of the single cross-correlations. In idealized frozen turbulence conditions, this delay would be concurrent with the theoretical time delay calculated with the local velocity and the separation distances. Also, the amplitude of the maxima would be unity if the frozen turbulence assumption were completely valid. In this particular flight case, in a neutral boundary layer, both the position and the amplitude are close to the frozen turbulence assumptions.

Typically, the autocorrelation function of single-point velocity measurement is used to calculate the turbulent integral length scale. From the integral of the temporal autocorrelation function, the integral time scale (Lenschow and Stankov, 1986) is obtained and from this the length scale can be calculated using Taylor's hypothesis. However, the present longitudinally separated measurements allow a spatial cross-correlation at different separation distances from which a 'true' spatial correlation function for the wind velocity can be derived. The temporal autocorrelation is compared with the two-point spatial cross-correlation (which corresponds to the marked points on the y-axis in Fig. 2.7) of all possible cross-correlation combinations in the longitudinal direction $\binom{7}{2}=21$ in Fig. 2.8a. In this particular flight of a neutral atmospheric boundary layer (NABL), the spatial cross-correlation is well represented by the autocorrelation, thus the assumption of Taylor can be considered to be applicable.

In Fig. 2.8b different atmospheric stabilities are compared. The deviation between the curves of the different correlations increases for stable and convective conditions
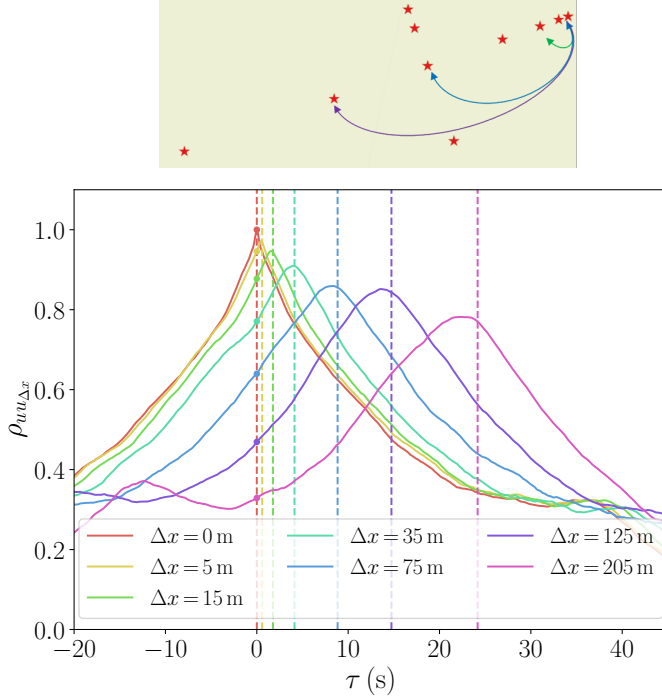
Figure 2.7: Cross-correlation functions of streamwise velocity between the longitudinally separated UAS (separation distance Δx). Dashed vertical lines are the theoretical time lags of the correlation maxima calculated with Taylor's hypothesis. Colored points mark the intersection between the correlation functions and $\tau = 0$. Figure and description adapted from Wetz et al. (2023). The sketch illustrates the cross-correlation between the measurement positions of the UASs.

(and for lower altitudes, which are not explicitly shown here but are described in Appendix A3). The significant drop in cross-correlations under convective conditions at $\Delta x = 80$ m and $\Delta x > 125$ m is related to the UAS in the far west. Technical errors in the correlation measurements of the specific UAS can be ruled out by very good agreement with reference measurements of flights before and after the flight under consideration. Therefore, the difference originates in the atmospheric flow. At the specific position of this UAS the land use (corn fields) deviates from the other UAS locations (grassland), which could be a plausible explanation. The different land uses result in different surface roughness and could also lead to different surface heat fluxes, particularly in convective conditions. Both effects will affect the shape of turbulent structures. This outcome of multiple spatially distributed measurements shows additional observations that would not be visible in an individual measurement.

In Fig. 2.7 the theoretical travel time, equal to the time shift, of the turbulence using Taylor's hypothesis with the mean local velocity is illustrated by the horizontal lines and should perfectly agree with the time shift τ of the spatial cross-correlation if the turbulence were frozen. Instead of the time shift, we can also compare the local mean velocity $\bar{u}$ with the eddy transport velocity u_e calculated from the time shift and the separation distances ($u_e = \tau \, \Delta x$). If the two velocities would be equal, one of the validity requirements for the frozen turbulence assumption, according to Panofsky (1962) would be fulfilled. In this particular case, the agreement between the time shifts (different velocities) is good, with a slightly faster eddy transport velocity than the local velocity ($u_e > \bar{u}$). In the underlying publication (see Appendix A3) the comparison of the time lags under different atmospheric conditions is explicitly shown.
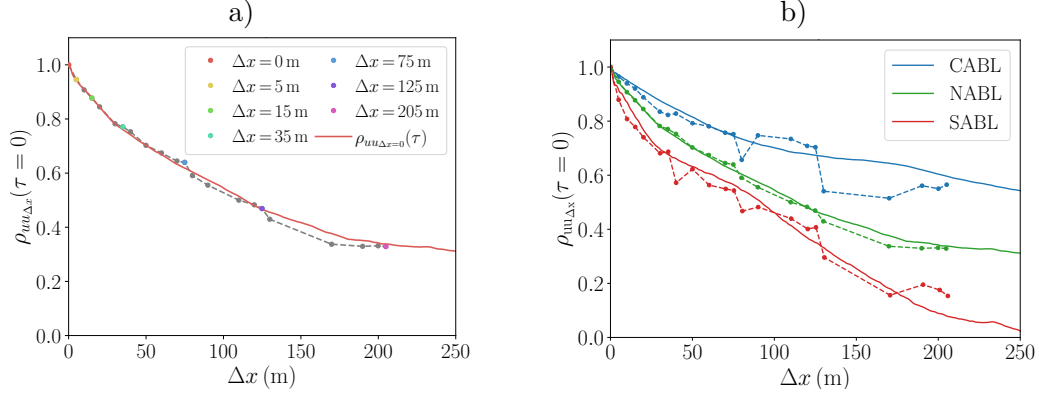
Figure 2.8: a) Autocorrelation function $\rho_{uu_{\Delta x=0}}(\tau)$ of single UAS, solid line, in comparison to direct spatial cross-correlations, dots and dashed line, using the intersection of the cross-correlation function $\rho_{uu_{\Delta x}}$ and $\tau = 0$, marked as dots in Fig. 2.7. b) Same comparison as in a) but for additional flights under different atmospheric conditions (convective - CABL, neutral - NABL and stable - SABL) in 90 m a.g.l. Figure and description adapted from Wetz et al. (2023).

Since the spatial cross-correlation gives an indicator of the size of turbulent structures, the longitudinal extent can be compared with the lateral extent by analyzing the longitudinal and lateral spatial cross-correlations. The maxima of cross-correlation functions in dependency of the separation distances (lateral Δy and longitudinal Δx) for different atmospheric stratifications are shown in Fig. 2.9. From the small ratio between lateral and longitudinal cross-correlations under CABL, no preferential direction can be derived. Therefore, turbulence structures are expected to be of a nearly circular shape. Due to the significantly larger ratios under SABL and NABL, the shape of the turbulence structure will be more narrow. Due to the higher correlations in the longitudinal direction compared to the lateral direction, the structures are stretched in wind direction.
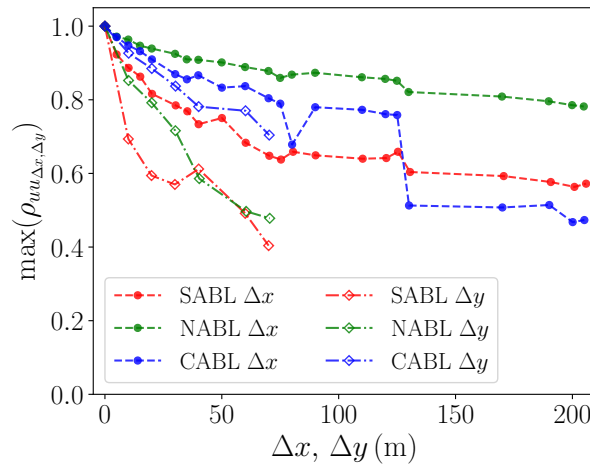
Figure 2.9: Cross-correlation maxima for longitudinal and lateral distributed measurement against the separation distances Δx and Δy in 90 m a.g.l. Figure and description adapted from Wetz et al. (2023).

2.2.4 Coherence

The relationship between different UAS time series is depicted by the cross-correlation function. One step further, the similarity of flow structures in the frequency domain is characterized by the coherence. In this section, the horizontal pattern of the SWUF-3D fleet is used to calculate the coherence of the atmospheric flow. These measurements are performed under different atmospheric conditions and are compared with basic coherence models.

Mathematically, the coherence is defined as the amplitude spectrum $A_{uu_{\Delta x}}(f)$ normalized by the product of the individual power spectra $S_{uu_{\Delta x}}$. Additionally, the root-coherence and co-coherence are used in atmospheric science (Cheynet et al., 2016). However, the magnitude-squared coherence is exclusively considered in this study.

$$\gamma^2_{uu_{\Delta x}}(f) \;=\; \frac{A_{uu_{\Delta x}}(f)^2}{S_{uu}(f)S_{u_{\Delta x}u_{\Delta x}}(f)} \quad . \tag{2.11}$$

Following (Lumley and Panofsky, 1964) unity of the coherence is reached if the individual Fourier components of the considered time series have proportional amplitudes for the entire ensemble. The coherence is zero if no correlation exists between the amplitudes.

The results of the coherence measurement of the 'horizontal pattern' in longitudinal a) and lateral direction b) are shown in figure 2.10. In this section and also in the following, only the coherence of the streamwise velocity fluctuations is considered. The coherence is typically plotted as a function of the frequency (f). In Figure 2.10 different separation distances are shown for longitudinal (Δx) and lateral directions (Δy). Consistent with the literature, the coherence measurements increase with decreasing frequency and decreasing distance. The coherence of lateral separated measurements is smaller compared to the longitudinal coherence (see Fig. 2.10). A pronounced decay of coherence implies only a narrow frequency domain (at low frequencies) where flow similarity is valid.

Coherence Models

The coherence approximation using an exponential decay model is already illustrated by the dashed lines in Fig. 2.10. The Davenport model is studied for lateral and longitudinal separations in the present study under various atmospheric conditions. For longitudinal separations, also the hypothesized dependence on the separation distance in this model is investigated. Since the decay model from Schlez and Infield (1998) does not show any significant improvements compared to the model from Davenport (1961), it is not taken into consideration in this thesis, but is examined in the underlying publication (see Appendix A3).

The decay parameter c, which is used to scale the coherence decay model of Davenport, is calculated from the curve fit of the coherence for separation distances of $\Delta x = 5$ m and $\Delta y = 10$ m. The comparison of the parameters in Fig. 2.11 reveal that the decay parameter for lateral separations is much larger than for longitudinal separations, leading to less correlation of the turbulent structures in the frequency domain in lateral than in longitudinal directions. The classification of the decay parameters in Fig. 2.11 is based on the dynamic stability, which is derived from the bulk Richardson number (Ri_b). With regard to the mean decay parameters, for the lateral direction, a decrease in coherence is visible with increasing stability. The results for the longitudinal direction show low coherence for stable and unstable conditions, while under neutral
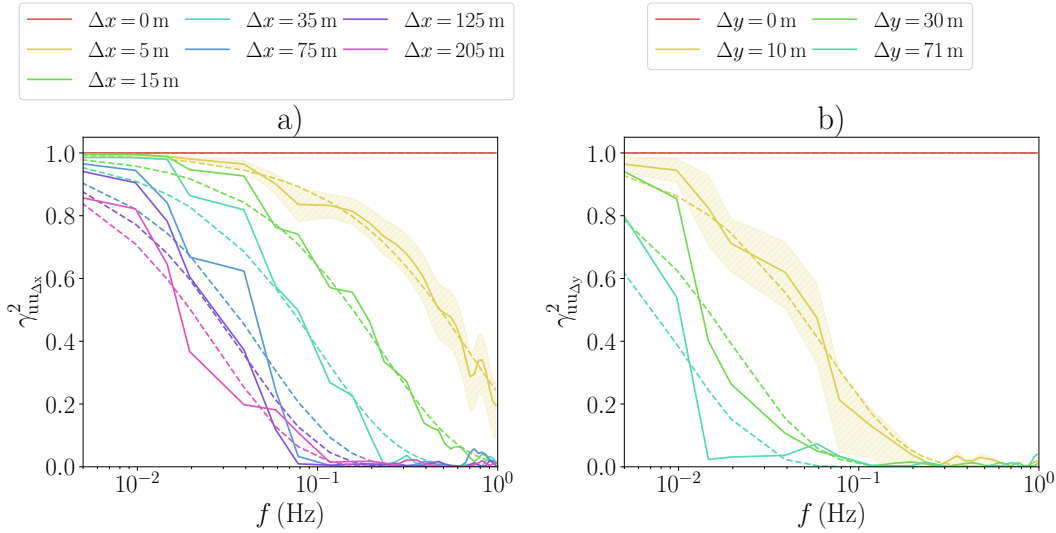
Figure 2.10: Coherence of streamwise velocity fluctuations of a) longitudinally separated UAS measurements and b) laterally separated measurements. In dashed lines, corresponding approximations with exponential decay function (Eq. 1.2) using individual decay parameters are shown. Uncertainties of the coherence estimation are indicated by the yellow shadow for one separation distance in each direction. Figure and description adapted from Wetz et al. (2023).

conditions the coherence increases. Overall, the decay parameter shows a wide scatter over different atmospheric stabilities and a constant value for the decay parameter is not sufficient to describe the coherence for different atmospheric conditions.

As previously mentioned, coherence is a function of separation distance. Davenport includes this dependency in his model. With the different separation distances between the UAS measurements of the 'horizontal pattern' it is possible to evaluate this dependency for multiple distances. In neutral conditions, the decay parameter in the longitudinal direction only slightly varies for different separation distances (see Appendix A3). In stable conditions, the decay parameter decreases with increasing distance, which is contrary to the assumption of the coherence model since the separation distance is already included as a parameter. The spread of the parameter is wider and a clear trend cannot be seen under convective conditions. Consequently, the dependence on distances is only adequately represented by the Davenport model under neutral conditions since the parameter should theoretically be constant over distance.

2.2.5 Discussion

The Davenport coherence model shows reasonable results only under the neutral stratification conditions for which it was originally formulated. Under convective and stable conditions, the scatter is wide and not consistent over the postulated dependence on separation distances. However, estimating the coherence decay parameter with the Davenport model allows comparison with other studies because it has been widely used.

The results of the decay parameter in the current study are in the range of $c_y = 9 \ldots 16$ for lateral separations and of $c_x = 2 \ldots 5$ for longitudinal separations. A range of $c_y = 10.4 \ldots 13.6$ for lateral separation distances of 40 m is calculated by Shiotani and Iwatani (1980) without consideration of atmospheric conditions. Multiple studies
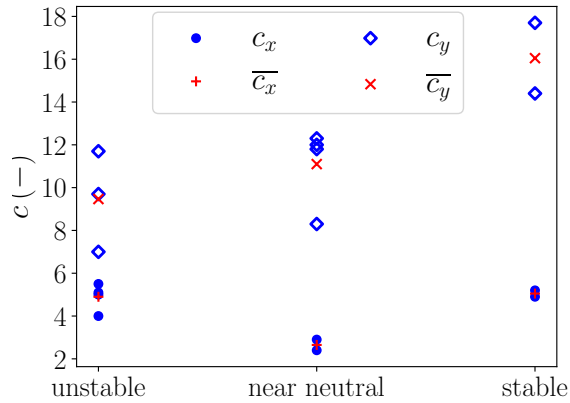
Figure 2.11: Coherence decay parameter for the Davenport approach c_x, c_y for longitudinal x and lateral direction y in dependency of the dynamic stability classes based on Ri_b, with separation distances of $\Delta x = 5$ m and $\Delta y = 10$ m. Figure and description adapted from Wetz et al. (2023).

from various research groups on lateral and longitudinal coherence were listed by Schlez and Infield (1998). The resulting parameters vary in the range of $c_x = 3 \dots 8$ in the longitudinal direction and $c_y = 19 \dots 40$ in the lateral direction. Due to low measurement heights and large separation distances, as well as different surface types, the results are not unconditionally comparable with the present study. Another experiment by Jensen and Kristensen (1979) at the Sotra bridge results in a lateral decay parameter of $c_y = 14$ for neutral stratification, which is more comparable to the present results. The increase in the lateral decay parameter with increasing stability found in Fig. 2.11 is consistent with the results of Ropelewski et al. (1973). Altogether, the decay parameters in the literature are found to be in the range of $c_x = 3 \dots 10$ and $c_y = 9 \dots 30$. These decay parameters are based on different atmospheric stabilities and different experiments. However, the results are in general agreement with the results of this study.

The evaluation of the coherence of large separations, particularly in the lateral direction, reveals that for reliable coherence measurements of separation distances in the range of integral length scale, measurement times of more than 20 min are necessary in order to provide accurate coherence estimation for the large-scale structures.

According to Mizuno and Panofsky (1975) the spatial validity of Taylor's frozen turbulence hypothesis can be evaluated based on the coherence decay parameter and the integral length scale. This estimate is possible with the present measurements and results in a validity length of 120 m for a flight under stable conditions and a length of approx. 380 m for unstable conditions, for which frozen turbulence could be assumed.

The results of the cross-correlation analysis of longitudinal separated measurements show that deviations from the theoretical behavior of frozen turbulence conditions are small for neutral stabilities. For the considered measurement time under these conditions, only a small development of the turbulence over the covered measurement space is observed. Therefore, the frozen turbulence assumption under these conditions is valid. This assumption is further supported by the coherence measurements of low decay parameters (for NABL), which indicate a high coherence and thus a large scale range where the turbulent structures show a large correlation.

2.3 In Situ WT-Wake and Inflow Measurements

Understanding the flow around WTs is crucial for optimizing WTs and their leading role in future energy production. Detailed and high resolution measurements of the wind field are decisive for this understanding. However, only few high resolution observations, especially in the near wake exist. The SWUF-3D fleet can provide valuable measurement data in this area. In the present study, a field campaign at a 2-MW-WT is used to examine multi-point in situ inflow and wake observations. These results have been published in the *Wind Energy Science* journal (Wetz and Wildmann, 2023) (see Appendix A4).

2.3.1 Experiment

Located on a high plateau, the field site is dominated by a river valley to the west and can be described as complex terrain (detailed description and map included in Appendix A4). The WT of the type Enercon E-82 E2 has a rated power of 2 MW at a wind speed of 12.5 m s^{-1}. The comparatively large hub height of 138 m with a rotor diameter of only $D = 82$ m is due to the fact that the WT was built in complex terrain.

For reference purposes, the inflow is measured at an upstream distance of 2 D simultaneously with the wake. The thermal stratification of the inflow is determined by calculating the lapse rate during the ascent to the measuring height of 120 m a.g.l. The wake is studied with two different flight patterns. First, the UASs are aligned across the wind direction and second, the UASs are distributed longitudinally to the inflow, as illustrated in Fig. 2.12. Both patterns are conducted at constant altitudes. The lateral flight pattern is carried out at hub height of the WT and the longitudinal flight pattern at 120 m a.g.l. due to operations in the open category of the EASA regulations. Those regulations also only allow the simultaneous flight of five UASs with dedicated remote pilots during this campaign.

The aim of the 'lateral pattern' is to measure the horizontal profiles of the wake. For this purpose, one UAS is placed outside the wake at $y = 1$ D and the other UASs are positioned inside the wake in order to resolve the profile with high spatial resolution. The UAS are distributed across the inflow wind direction and the orientation of the WT. This orientation is adjusted a priori for every single flight according to the current conditions.
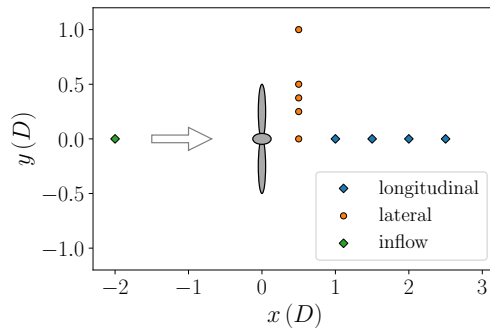
Figure 2.12: Different flight patterns of the UAS fleet from the top view. The arrow represents the wind direction towards the WT. Figure and description adapted from Wetz and Wildmann (2023).

An overview of the conducted measurements is shown in Fig. 2.13 by the normalized

wind velocity at the UAS measurement positions. The orientation of the coordinate system in this figure is based on the inflow and is not aligned with the WT orientation. The reduced wind speed (also called wind deficit) downstream of the WT is clearly visible in Fig. 2.13. Also, laterally outside the wake, the freestream velocity can be seen. The visible deviations in the alignments of the UAS in Fig. 2.13 result from the consistently observable yaw misalignment of the WT and the consideration of this orientation for the positioning of the pattern (details can be found in Appendix A4).
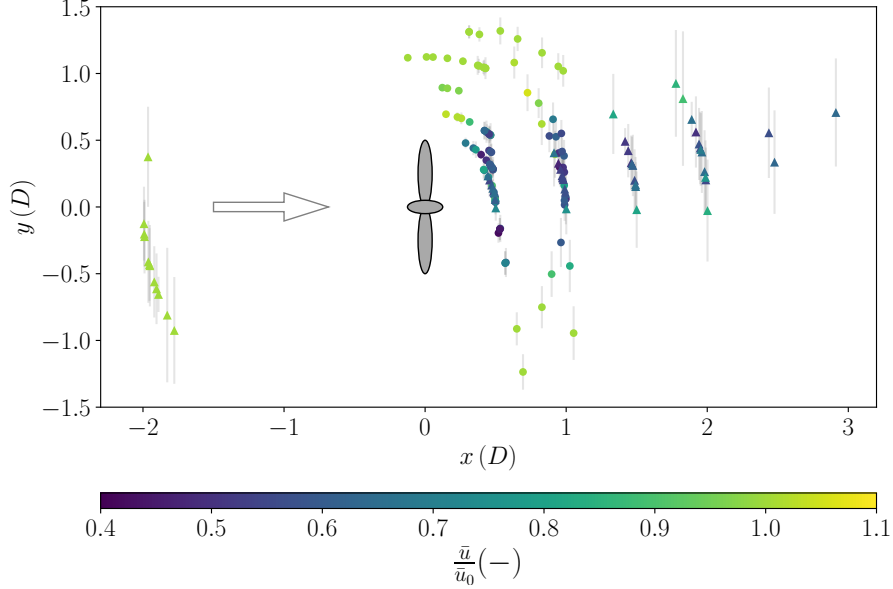
Figure 2.13: Normalized wind velocity of UAS measurements $\bar{u}/\bar{u}_0$ at locations relative to the reference wind direction. The illustration of the WT defines the position and the lateral dimensions of the WT rotor. Triangle markers represent the longitudinal flight pattern while circle markers define the lateral flight pattern. The arrow indicates the inflow wind direction. The standard deviation in lateral position is illustrated by the grey vertical lines and is calculated from the standard deviation of the inflow wind direction. Figure and description adapted from Wetz and Wildmann (2023).

2.3.2 Analyse of Single Flight Case

For a detailed case study, the time series of a single flight of the lateral pattern is examined. The flight, shown in Fig. 2.14, was conducted during the early morning hours (04:53 UTC, 12 May 2022) in the presence of the nighttime stable boundary layer. The velocity series in Fig. 2.14a shows that the UAS at $y = 1.05\,D$ is located in freestream with high velocities. The lower velocities and high fluctuations measurements of the remaining UAS indicate measurements within the wake. Significantly higher fluctuation amplitudes are observed for the UAS at $y = 0.55\,D$, which is measuring at the edge of the WT.

The variability of the freestream wind direction, shown in Fig. 2.14b, varies the relative lateral position of UAS, as illustrated in Fig. 2.14c). Small changes in the relative position at the edge of the wake can cause a significant difference in the velocity measurement since measurements inside (5:03 UTC) and outside (04:56 UTC) of the wake can occur. This correlation between the relative position and the velocity measurement is supported by a correlation coefficient of $R = 0.5$. Evidently, this highly fluctuating and meandering position of the wake causes high turbulence levels at

that measurement position, as will be shown in the following sections. Overall, these results of the time series emphasize the challenge of single-point measurements in a continuously changing environment in field measurements at WTs and the sensitivity of the results to the exact relative location of the measurements.
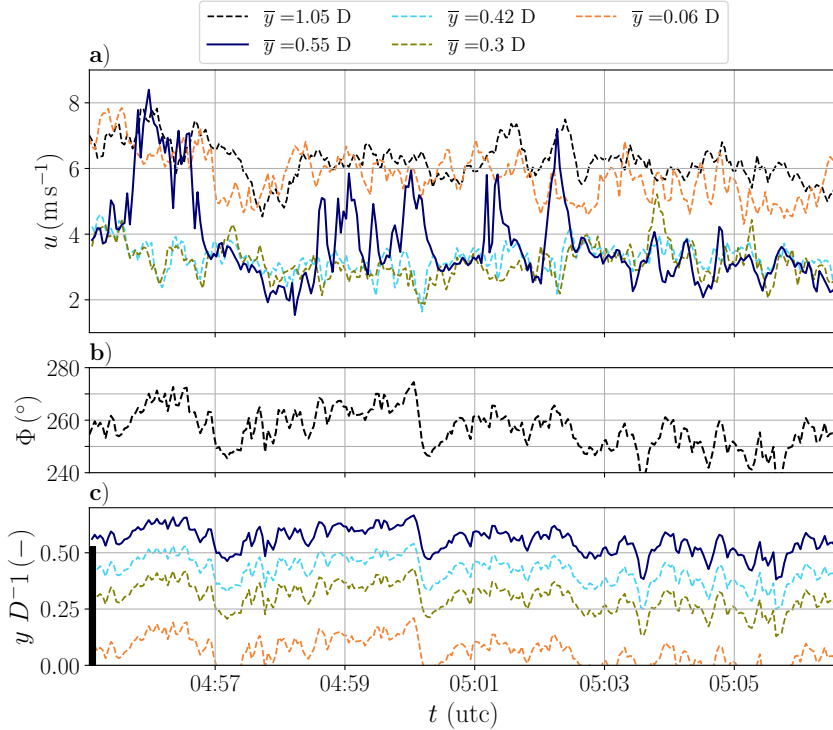
Figure 2.14: Time series of wind velocity a), wind direction b) and lateral position c) of a lateral flight pattern in stable conditions. The lateral positions are calculated using the wind direction of the reference UAS measurement, which is shown in the middle figure. The black bar in c) indicates the lateral position of the WT rotor. Figure and description adapted from Wetz and Wildmann (2023).

The possibility of measuring the tip vortex with the UAS located at the edge of the wake is discussed on the basis of the turbulent spectrum in Appendix A4. From the rotational speed of the WT the so-called blade-passing frequency can be calculated. A slight increase in the spectrum can be observed in the range of this corresponding frequency. In principle, no clear peaks are to be expected in the spectra due to the comparatively large distance to the wind turbine and the constantly changing position of the wake due to wake meandering and unsteady inflows to the WT.

In this part, it is specifically discussed whether the signature of the tip vortex may be observed, at least in the time series. Since the signature largely varies with the relative position with respect to the center of the vortices, it is generally challenging to measure the tip vortices at a single fixed position. Despite these uncertainties, the tip vortex is visible in the time series of the lateral velocity v. In Fig. 2.15 one segment of the times of the relevant UAS clearly emphasizes the tip vortex. At this particular location (hub height, north of the WT) and under the conditions (westerly wind) of the measurement, the vortex first appears as a strong increase of the cross-wind component, followed by an almost instantaneous turn into the reverse direction as the vortex center passes. Finally, the velocity decays to the ambient velocity while the

29

vortex is transported further downstream. This signature can be recognized clearly in the time series. Detailed theoretical analyses on the direction of rotation of the vortex and the expected detailed velocity profile at the measurement position have been performed and are in line with the measurements (details can be found in Appendix A4).
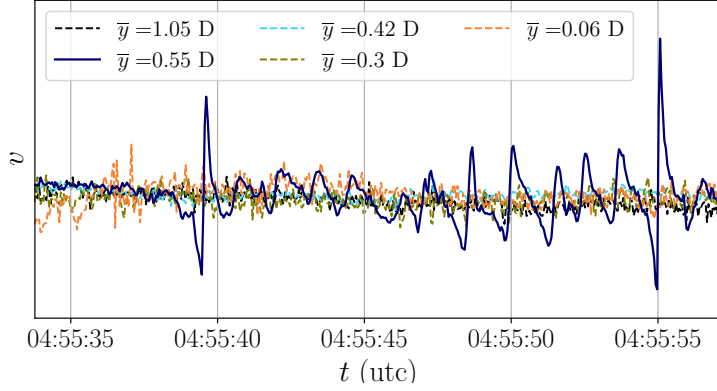
Figure 2.15: Time series of the lateral velocity component v of the lateral flight pattern.

2.3.3 WT Wake Profiles

The 'lateral pattern', already shown for a single flight in Fig. 2.14, is used to derive lateral horizontal profiles of the velocity distribution in the wake. Since the WT extracts energy from the flow, a significant reduction of the velocity is expected behind the rotor plane. The profiles of the mean velocity deficit in the (far) wake are often modeled as a Gaussian distribution. In the near wake, different results can be found for the velocity profile. In this study, lateral profiles of the normalized wind velocity and of the added turbulence intensity ($\Delta I = \sqrt{I^2 - I_0^2}$, see Fradsen, 2007) are examined under different atmospheric conditions and for different downstream distances x in the near wake of the WT. At a downstream distance of 0.5 D in stable to near-neutral conditions, a double-Gaussian-like distribution of the velocity is visible in Fig. 2.16a with a large velocity deficit at the edge and a small deficit in the wake center. Under more unstable conditions, the profile follows a single-Gaussian distribution without the low deficit region in the wake center. Further downstream, at a distance of 1 D, also under near-neutral to stable conditions, the double-Gaussian shape is less pronounced, indicating that turbulent mixing inside the wake center balances out the velocity differences.

In order to analyze and compare the distribution of turbulence in the wake, the added turbulence intensity ΔI is plotted in Figure 2.16b in the same manner as the velocity deficit. As expected, at the edge of the wake, the peak of the turbulence intensity can be identified. The increase in turbulence in this area is caused by the tip vortex, wake meandering, and shear layer. Comparable to the velocity distribution, the turbulence decreases in the inner wake, and therefore the profile could also be approximated with a double-Gaussian distribution for near-neutral to stable conditions. However, in unstable conditions, the distribution is more uniform and can be described as a single-Gaussian distribution. The higher fluctuation of the wind direction and the higher turbulence in the unstable conditions enhance the turbulence mixing, which smears out the peaks and supports the breakdown of the tip vortices.

30
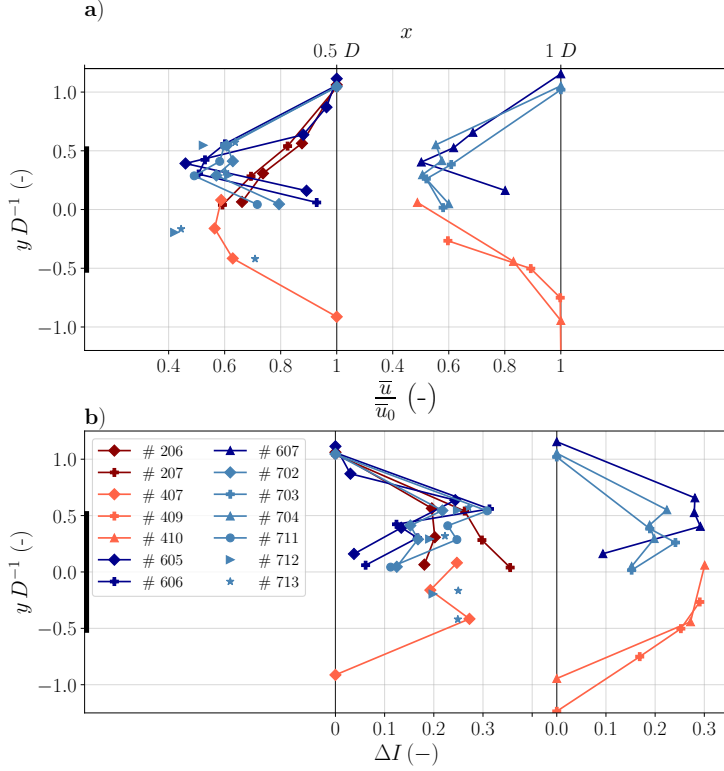
Figure 2.16: a) Lateral profile of normalized wind speed $\bar{u}/\bar{u}_0$ in the WT wake at different downstream distances ($x = 0.5\ D$ and $1\ D$). b) Lateral profile of added turbulence intensity ΔI at the bottom figure. Different colors indicate different flight days. The blue color represents stable to near-neutral atmospheric conditions, while the red color indicates unstable convective conditions (dark red for highly unstable and light red for less unstable cases). Details about the flight cases are listed in Appendix A4. Figure and description adapted from Wetz and Wildmann (2023).

Another important physical variable that influences the wake decay, which is particularly important for estimating the efficiency of wind farms, are turbulent fluxes. Since turbulent fluxes drive the energy transport into the wake, they significantly affect the wake recovery. The distributions of the horizontal turbulent fluxes in Fig. 2.17 are shown in the same manner as the velocity distributions previously. In accordance with Bastankhah and Porté-Agel (2017) the nondimensionalization of the fluxes is performed with $\bar{u}_0^2$ (freestream velocity). As expected, the fluxes at the edge of the wake point towards the wake center, indicating energy entrainment into the low-energy region. As the fluxes point towards the wake center at both wake edges, the signs of the fluxes have to be opposite on both sides in Fig. 2.17. Remarkable are the additional fluxes inside the wake that are pointing from the inner wake towards the outer wake. These fluxes could be explained by the double-Gaussian velocity distribution and the energy transport from the high-velocity zones in the wake center towards the outer wake with low-velocity regions.

However, these additional fluxes inside the wake are only observable in near-neutral to stable conditions, whereas in unstable conditions, due to the absence of the double-Gaussian distribution, which drives these fluxes, the fluxes from the inner wake towards the outer wake are not visible. The prominent fluxes from the freestream towards the wake at the edge of the wake are also visible in unsteady conditions, with slightly

increased amplitude compared to steady conditions.
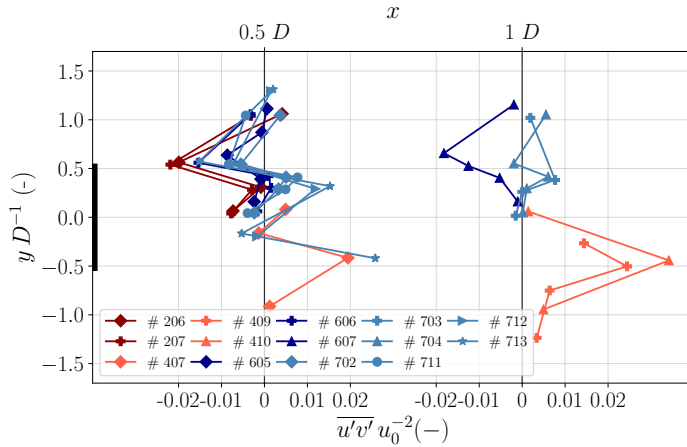
Figure 2.17: Lateral profile of normalized horizontal momentum fluxes $\overline{u'v'}/\bar{u}_0^2$ in the WT wake at different downstream distances ($x = 0.5\ D$ and $1\ D$). Different colors indicate different flight days. The blue color represents stable to near-neutral atmospheric conditions, while the red color indicates unstable convective conditions. Figure and description adapted from Wetz and Wildmann (2023).

Additionally, at the campaign, the development of the wake is studied with longitudinally distributed measurements in the wake center. A decrease in velocity due to the conversion from double-Gaussian to single-Gaussian lateral profiles is observed at close distances to the wind turbine, followed by an increase in velocity at longer distances, leading to an already incipient wake recovery and increased turbulent mixing. More details can be found in Appendix A4.

2.3.4 Discussion of the Wake Measurements

In the literature, mostly measurements and velocity profiles are examined at larger downstream distances than $> 1\ D$. Only a few publications about observations in this area exist. However, the double-Gaussian distribution of the velocity profile is also described by Abraham et al. (2019) in the vertical direction near the tower region, based on field experiments with PIV using snowflakes. In the complex terrain at the field site in Perdigão, Menke et al. (2018) showed a double-Gaussian velocity profile in one rotor diameter downstream distance based on lidar measurements.

Based on wind tunnel experiments, Krogstad and Adaramola (2011) showed that the tip speed ratio (TSR) highly affects the velocity distribution in the near wake. In particular, high TSR leads to a double-Gaussian distribution, while for lower TSRs closer to the design point, the profile becomes more uniform and approaches a single-Gaussian distribution. These findings can also partially explain the velocity distributions in the present cases (more details in Appendix A4). The influence of atmospheric stability on the wake is studied by Machefaux et al. (2015). Based on LES and nacelle-based lidar, they found that under stable conditions the velocity profile takes on a double-Gaussian distribution, whereas under unstable conditions the distribution is more uniform, which is in accordance with the present study.

The observed turbulent fluxes at the edge of the wake, which point from the freestream to the wake, as shown in Fig. 2.17, are consistent with studies from Bastankhah and Porté-Agel (2017). Also, the magnitudes of the normalized momentum fluxes are in accordance with this study. Their results are based on wind tunnel experiments using

PIV measurements. In these results, only the fluxes from the freestream to the wake could be observed but not the additional fluxes at the center of the wake, which could be measured with the SWUF-3D fleet. Also, in their velocity profile measurements, no high-velocity region could be observed in the wake center (more of a single-Gaussian distribution). This would explain the absence of turbulent fluxes from the wake center since no large velocity differences are found between the wake center and the edge of the wake that would drive the turbulent fluxes in this area.

Chapter 3

Conclusion

In the present thesis, a novel measurement system was successfully established. The SWUF-3D fleet was calibrated and validated during two measurement campaigns, demonstrating that it is possible to achieve accurate wind measurements with a fleet of quadrotors by relating the multicopter motions to the wind forces without the need for additional wind sensors.

In the first campaign, a robust 1D wind algorithm based on the Rayleigh drag equation and the pitch angle was calibrated against data from a meteorological tower. This calibration shows that similar aerodynamic behavior can be assumed within the entire fleet. The validation of the 1D wind algorithm resulted in precise mean wind speed and wind direction measurements.

Comparisons with lidar data highlight the possibility for turbulent wind field measurements as well as the UAS's advantage over lidars in terms of higher temporal resolution.

In the second campaign, an advanced wind algorithm for 2D horizontal measurements with a more flexible calibration approach was conducted for 35 UAS. Additionally, the condition of hover flight was weakened, and raw accelerometer data were taken into consideration. The novel approach improved the dynamic behavior of the wind measurements, allowing turbulence to be measured with a temporal resolution of 1 Hz. The mean wind speed measurements are accurate within $\epsilon_u = 0.25$ m s^{-1}. The variance in both streamwise and lateral directions can be resolved with high accuracy. Furthermore, by accounting for the lateral wind component in addition to the UAS's orientation in 'weather vane' mode, the dynamic behavior of wind direction readings can be enhanced. The accuracy of the mean wind direction is $\epsilon_\Phi < 5°$.

Overall, the calibrated UAS fleet and chosen strategy demonstrate the desired precision. Nevertheless, there's still potential for development in terms of campaign logistics, hardware reliability, automation, and fleet communication.

For the purpose of analyzing turbulent structures in heterogeneous terrain, the advanced 2D wind algorithm was employed. Various comparisons of turbulent spectra with sonic anemometer data demonstrate the potential for precise turbulence measurements. The plausibility of the measurements was further supported by the observable separation distances in the phase spectra. Spatial cross-correlations along a horizontal line of spatially distributed UAS enable the examination of Taylor's frozen turbulence assumption. In neutral atmospheric conditions, the application of the frozen turbulence assumption appears to be valid, since the temporal autocorrelation functions of

single-point measurements are in line with spatial multi-point cross-correlations. In addition, under neutral conditions, the coherence for streamwise separations shows the largest correlation over the scales compared to convective and stable cases. An estimation of the validity length of Taylor's hypothesis is discussed for various atmospheric conditions, which can be beneficial for future planning of ABL experiments.

However, in convective conditions the heterogeneous terrain influences the spatial cross-correlations, showing a drop in correlation for UAS measurements over different land uses. These heterogeneities are not visible in the autocorrelation and would be ignored if Taylor's hypotheses were used to calculate the turbulent length scale.

The horizontal extent of turbulent structures was discussed based on the comparison of lateral and longitudinal spatial correlations. This comparison shows that horizontal turbulent structures are anisotropic and extended in the longitudinal direction under neutral and stable conditions, whereas they have a more circular shape under convective conditions. This different shape in convective conditions is driven by higher turbulence mixing, which uniforms the turbulence structures. The tendency to isotropic structure of the turbulence throughout the measured scales in CABL is supported by the fact that the ratio between lateral and longitudinal coherence is highest for NABL and SABL, as shown in Fig. 2.11, whereas it is small under unstable conditions.

The ability to measure coherence with the SWUF-3D is extensively shown in this study. With these measurements, coherence models, in particular those after Davenport, are examined. The calculated decay parameter and the behavior under different conditions are consistent with previous researches. However, the comparisons with the present measurements outline that the Davenport model only shows reasonable results in neutral conditions for various separation distances, while in stable and convective conditions the validity is limited.

In conclusion, the examination of horizontal correlations and coherence demonstrates the huge potential of the SWUF-3D fleet for this kind of study. However, due to the limited flight time, coherence measurements at large separations cannot be delivered with high accuracy. The coherence decays particularly quickly for lateral and vertical separations, which emphasizes the significance of the measurement duration and coherence estimation accuracy. Furthermore, turbulent length scales and correlations can only be estimated for the specified time period, which, depending on the atmospheric conditions, cannot capture the complete turbulent spectrum.

In this study, at another campaign, a fleet of UAS was successfully used for the first time to measure the wind flow around a WT. Even without any additional field instrumentation, the simultaneous up- and down-stream measurements demonstrate their considerable potential for comprehensive WT wake research. The results of the single case study demonstrate that the expected signature of tip vortices can be measured with UAS using the velocity time series near the wake's edge. Profiles of the mean velocity deficit in the near wake are studied with laterally distributed measurements. At a downstream distance of $y = 0.5\ D$, the measurements of the velocity profile under near-neutral to stable conditions show a double-Gaussian-like distribution. Due to faster turbulent mixing under unstable conditions, the high velocity zone at the wake center of the double-Gaussian distribution is mixed out into a single-Gaussian distribution of the velocity deficit profile.

Momentum fluxes, which drive the decay of the wake, could be measured at the edge of the wake in the direction from the freestream towards the wake in both stable and unstable conditions. Additionally, only under stable and near-neutral conditions can

turbulent momentum fluxes be measured in the opposite direction from the wake center towards the edges of the wakes.

During experiments at WTs, the relative positioning of the UASs in the wake with continuously varying inflows is challenging, especially in this complex terrain where the wake might be diverted both vertically and horizontally. In this study, it is shown that the relative position in the wake can be accurately predicted with simultaneous inflow measurements. However, for larger distances, it would be favorable to capture the entire wake at its position in more detail. The present study of the flow around WT demonstrates the SWUF-3D fleet's potential for novel measurements such as horizontal fluxes and high temporal resolution wind measurements at multiple positions; for more detailed investigations, further flights with additional UAS involved would be required.

Chapter 4

Future Perspectives

Due to the previously mentioned encouraging results, the overall research with the SWUF-3D fleet will be continued in future work. The state of the wind algorithm presented in this thesis has already been extended by the vertical component and thus to a complete 3D wind vector by Wildmann and Wetz (2022). The algorithm for the vertical wind component is based on the motor thrust data and still relies on the assumption of a mean vertical velocity of zero throughout the flight time. The calibrations in these studies are based on reference measurements of sonic anemometers at a meteorological tower.

In an ongoing study, the wind algorithm is tested and calibrated in an extensive experiment in an open-channel wind tunnel. This wind tunnel allows for reproducible turbulent flow scenarios, including gust fronts, sinus waves, or statistical turbulence, by using an active grid consisting of several flaps. With this, particularly at large wind speeds, the understanding and performance of the dynamic behavior of the quadrotors will be enhanced.

Extending the flight time is still a crucial issue for the further development of the fleet. Both the efficiency of the flight system with regard to the propulsion unit and the capacity of the batteries show some promising improvement potential, making measurement times of 20 minutes feasible in the near future. Longer measurement times would significantly improve the potential for coherence measurements over large distances and cross-wind correlations. Future research could also incorporate the vertical coherence along with the lateral and longitudinal coherence by using vertically distributed measurements. Particularly in wind energy science, the lateral and vertical coherence of the inflow are crucial for the aerodynamic loads. Wind energy norms provide a general estimation of coherence, but these estimations could be challenged with future extended measurement campaigns.

Extensive experiments are planned at the Krummendeich Research Wind Farm (WiValdi) owned by the German Aerospace Center (DLR) (Wildmann et al., 2022) (https://windenergy-researchfarm.com). In addition to, two extensively instrumented 3 MW WTs, various meteorological measurement systems will be installed at the site, including Windlidar (ground-based and on the nacelle) and meteorological mast arrays. This field site will improve the understanding of the interaction of the atmospheric flow with the WT and how the WT wake affects the downstream turbines. The entire fleet of > 20 UASs together with the various measurement systems at the site, will enable a new quality for the whole dataset and possible studies of the flow around WTs. The lidar data can be used to capture the larger picture of the wake, along with

the magnitude and varying position of the wake due to meandering. As previously mentioned, the coherence of the inflow of the WT with the fleet could be examined. In the wake, different profiles can be measured simultaneously with multiple UASs at different distances. In addition, the algorithm also enables measurements during forward flights, creating additional opportunities for examining the wake. The analysis of the tip vortices shown, could be carried out further with closely staggered UAS. Several UAS could then simultaneously measure different areas of the vortex, and from these measurements, the precise position and strength of the vortex might be possible to determine.

Besides the experiments on the heterogeneous but mainly flat terrain in Falkenberg and the investigations of the flow around a WT, more applications can be thought of for the SWUF-3D fleet. The UAS fleet is already utilized in a mountain region near the Inn-valley to analyze slope winds and temperature profiles in the context of mountain meteorology. Due to its versatility, the UAS fleet can be particularly useful in areas where permanent measurement equipment is logistically difficult to deploy. In the upcoming years, further campaigns are planned as part of the TEAMx project. The SWUF-3D fleet could also be practically applied in other areas, such as delivering in-depth wind assessments at airports upon request or supporting regional wind and weather predictions using spatially distributed observations and vertical profiles in conjunction with the WMO.

Bibliography

Abraham, A., Dasari, T., and Hong, J. (2019). Effect of turbine nacelle and tower on the near wake of a utility-scale wind turbine. *Journal of Wind Engineering and Industrial Aerodynamics*, 193:103981.

Aitken, M. L. and Lundquist, J. K. (2014). Utility-scale wind turbine wake characterization using nacelle-based long-range scanning lidar. *Journal of Atmospheric and Oceanic Technology*, 31(7):1529–1539.

Alaoui-Sosse, S., Durand, P., and Médina, P. (2022). In situ observations of wind turbines wakes with unmanned aerial vehicle BOREAL within the MOMEMTA project. *Atmosphere*, 13(5):775.

Bartholmai, M. and Neumann, P. P. (2011). Adaptive ortsaufgelöste Gaskonzentrationsmessung mit einer Mikrodrohne. *Technisches Messen*, 78(10):470–478.

Bastankhah, M. and Porté-Agel, F. (2014). A new analytical model for wind-turbine wakes. *Renewable Energy*, 70:116–123.

Bastankhah, M. and Porté-Agel, F. (2017). Wind tunnel study of the wind turbine interaction with a boundary-layer flow: Upwind region, turbine performance, and wake region. *Physics of Fluids*, 29(6):065105.

Bell, T. M., Greene, B. R., Klein, P. M., Carney, M., and Chilson, P. B. (2020). Confronting the boundary layer data gap: evaluating new and existing methodologies of probing the lower atmosphere. *Atmospheric Measurement Techniques*, 13(7):3855–3872.

Beyrich, F. and Adam, W. (2007). Site and Data Report for the Lindenberg Reference Site in CEOP – Phase i. *Offenbach a.M. - Selbstverlag des Deutschen Wetterdienstes: Berichte des Deutschen Wetterdienstes*, (230):55pp.

Brosy, C., Krampf, K., Zeeman, M., Wolf, B., Junkermann, W., Schäfer, K., Emeis, S., and Kunstmann, H. (2017). Simultaneous multicopter-based air sampling and sensing of meteorological variables. *Atmospheric Measurement Techniques*, 10(8):2773–2784.

Chauhan, K., Hutchins, N., Monty, J., and Marusic, I. (2012). Structure inclination angles in the convective atmospheric surface layer. *Boundary-Layer Meteorology*, 147(1):41–50.

Cheynet, E., Flügge, M., Reuder, J., Jakobsen, J. B., Heggelund, Y., Svardal, B., Saavedra Garfias, P., Obhrai, C., Daniotti, N., Berge, J., Duscha, C., Wildmann, N., Onarheim, I. H., and Godvik, M. (2021). The COTUR project: remote sensing of offshore turbulence for wind energy application. *Atmospheric Measurement Techniques*, 14(9):6137–6157.

Cheynet, E., Jakobsen, J. B., Snæbjörnsson, J., Mikkelsen, T., Sjöholm, M., Mann, J., Hansen, P., Angelou, N., and Svardal, B. (2016). Application of short-range dual-Doppler lidars to evaluate the coherence of turbulence. *Experiments in Fluids*, 57(12):184.

Cuxart, J., Wrenger, B., Matjacic, B., and Mahrt, L. (2019). Spatial Variability of the Lower Atmospheric Boundary Layer over Hilly Terrain as Observed with an RPAS. *Atmosphere*, 10(11):715.

Davenport, A. G. (1961). The spectrum of horizontal gustiness near the ground in high winds. *Quarterly Journal of the Royal Meteorological Society*, 87:194–211.

Doubrawa, P., Quon, E. W., Martinez-Tossas, L. A., Shaler, K., Debnath, M., Hamilton, N., Herges, T. G., Maniaci, D., Kelley, C. L., Hsieh, A. S., Blaylock, M. L., Laan, P., Andersen, S. J., Krueger, S., Cathelain, M., Schlez, W., Jonkman, J., Branlard, E., Steinfeld, G., Schmidt, S., Blondel, F., Lukassen, L. J., and Moriarty, P. (2020). Multimodel validation of single wakes in neutral and stratified atmospheric conditions. *Wind Energy*, 23(11):2027–2055.

Englberger, A., Dörnbrack, A., and Lundquist, J. K. (2020). Does the rotational direction of a wind turbine impact the wake in a stably stratified atmospheric boundary layer? *Wind Energy Science*, 5(4):1359–1374.

Fernando, H. J. S., Mann, J., Palma, J. M. L. M., Lundquist, J. K., Barthelmie, R. J., Belo-Pereira, M., Brown, W. O. J., Chow, F. K., Gerz, T., Hocut, C. M., Klein, P. M., Leo, L. S., Matos, J. C., Oncley, S. P., Pryor, S. C., Bariteau, L., Bell, T. M., Bodini, N., Carney, M. B., Courtney, M. S., Creegan, E. D., Dimitrova, R., Gomes, S., Hagen, M., Hyde, J. O., Kigle, S., Krishnamurthy, R., Lopes, J. C., Mazzaro, L., Neher, J. M. T., Menke, R., Murphy, P., Oswald, L., Otarola-Bustos, S., Pattantyus, A. K., Rodrigues, C. V., Schady, A., Sirin, N., Spuler, S., Svensson, E., Tomaszewski, J., Turner, D. D., van Veen, L., Vasiljević, N., Vassallo, D., Voss, S., Wildmann, N., and Wang, Y. (2019). The perdigão: Peering into microscale details of mountain winds. *Bulletin of the American Meteorological Society*, 100(5):799–819.

Foken, T. (2021). *Springer Handbook of Atmospheric Measurements*. 2522-8706. Springer.

Fradsen, S. (2007). *Turbulence and turbulence-generated structural loading in wind turbine clusters*. PhD thesis, Technical University of Denmark.

Fuertes, F. C., Markfort, C., and Porté-Agel, F. (2018). Wind turbine wake characterization with nacelle-mounted wind lidars for analytical wake model validation. *Remote Sensing*, 10(5):668.

Gonzalez-Rocha, J., Woolsey, C. A., Sultan, C., de Wekker, S., and Rose, N. (2017). Measuring atmospheric winds from quadrotor motion. In *AIAA Atmospheric Flight Mechanics Conference*. American Institute of Aeronautics and Astronautics.

González-Rocha, J., Woolsey, C. A., Sultan, C., and Wekker, S. F. J. D. (2019). Sensing wind from quadrotor motion. *Journal of Guidance, Control, and Dynamics*, 42(4):836–852.

Gryning, S.-E., Batchvarova, E., Floors, R., Peña, A., Brümmer, B., Hahmann, A. N., and Mikkelsen, T. (2013). Long-term profiles of wind and weibull distribution parameters up to 600 m in a rural coastal and an inland suburban area. *Boundary-Layer Meteorology*, 150(2):167–184.

Hamilton, J., de Boer, G., Doddi, A., and Lawrence, D. A. (2022). The DataHawk2 uncrewed aircraft system for atmospheric research. *Atmospheric Measurement Techniques*, 15(22):6789–6806.

Heggem, T., Lende, R., and Løvseth, J. (1998). Analysis of long time series of coastal wind. *Journal of the Atmospheric Sciences*, 55(18):2907 – 2917.

Higgins, C. W., Froidevaux, M., Simeonov, V., Vercauteren, N., Barry, C., and Parlange, M. B. (2012). The effect of scale on the applicability of Taylor's frozen turbulence hypothesis in the atmospheric boundary layer. *Boundary-Layer Meteorology*, 143(2):379–391.

Horst, T. W., Kleissl, J., Lenschow, D. H., Meneveau, C., Moeng, C.-H., Parlange, M. B., Sullivan, P. P., and Weil, J. C. (2004). HATS: Field observations to obtain spatially filtered turbulence fields from crosswind arrays of sonic anemometers in the atmospheric surface layer. *Journal of the Atmospheric Sciences*, 61(13):1566 – 1581.

Hutchins, N. and Marusic, I. (2007). Evidence of very long meandering features in the logarithmic region of turbulent boundary layers. *Journal of Fluid Mechanics*, 579:1–28.

Jensen, N. (1983). *A note on wind generator interaction*. Number 2411 in Risø-M. Risø National Laboratory.

Jensen, N. and Kristensen, L. (1979). Lateral coherence in isotropic turbulence and in the natural wind. *Boundary-Layer Meteorology*, 17(3):353–373.

Kaimal, J. C. and Finnigan, J. J. (1994). *Atmospheric Boundary Layer Flows*. Oxford University Press, USA.

Kocer, G., Mansour, M., Chokani, N., Abhari, R., and Müller, M. (2011). Full-scale wind turbine near-wake measurements using an instrumented uninhabited aerial vehicle. *Journal of Solar Energy Engineering*, 133(4).

Kolmogorov, A. N. (1941). Local structure of turbulence in an incompressible viscous fluid at very large Reynolds numbers. *Dokl. Akad. Nauk SSSR*, 30(4):299–301.

Krogstad, P.-Å. and Adaramola, M. S. (2011). Performance and near wake measurements of a model horizontal axis wind turbine. *Wind Energy*, 15(5):743–756.

Larsén, X. G., Larsen, S. E., and Petersen, E. L. (2016). Full-scale spectrum of boundary-layer winds. *Boundary-Layer Meteorology*, 159(2):349–371.

Larsén, X. G., Larsen, S. E., Petersen, E. L., and Mikkelsen, T. K. (2019). Turbulence characteristics of wind-speed fluctuations in the presence of open cells: A case study. *Boundary-Layer Meteorology*, 171(2):191–212.

Lenschow, D. H. and Stankov, B. B. (1986). Length scales in the convective boundary layer. *Journal of Atmospheric Sciences*, 43(12):1198 – 1209.

Li, Z., Pu, O., Pan, Y., Huang, B., Zhao, Z., and Wu, H. (2022). A study on measuring wind turbine wake based on UAV anemometry system. *Sustainable Energy Technologies and Assessments*, 53:102537.

Liang, J., Zhang, L., Wang, Y., Cao, X., Zhang, Q., Wang, H., and Zhang, B. (2014). Turbulence regimes and the validity of similarity theory in the stable boundary layer over complex terrain of the Loess Plateau, China. *Journal of Geophysical Research: Atmospheres*, 119(10):6009–6021.

Lumley, J. L. and Panofsky, H. A. (1964). *The Structure of Atmospheric Turbulence, Monographs and Texts in Physics and Astronomy Vol. XII*. John Wiley & Sons Inc.

Machefaux, E., Larsen, G. C., Koblitz, T., Troldborg, N., Kelly, M. C., Chougule, A., Hansen, K. S., and Rodrigo, J. S. (2015). An experimental and numerical study of the atmospheric stability impact on wind turbine wakes. *Wind Energy*, 19(10):1785–1805.

Mahrt, L. (2009). Variability and maintenance of turbulence in the very stable boundary layer. *Boundary-Layer Meteorology*, 135(1):1–18.

Mann, J. (1994). The spatial structure of neutral atmospheric surface-layer turbulence. *Journal of Fluid Mechanics*, 273:141–168.

Mauder, M. and Zeeman, M. J. (2018). Field intercomparison of prevailing sonic anemometers. *Atmospheric Measurement Techniques*, 11(1):249–263.

Mauz, M., Rautenberg, A., Platis, A., Cormier, M., and Bange, J. (2019). First identification and quantification of detached-tip vortices behind a wind energy converter using fixed-wing unmanned aircraft system. *Wind Energy Science*, 4(3):451–463.

Mehta, D., van Zuijlen, A., Koren, B., Holierhoek, J., and Bijl, H. (2014). Large eddy simulation of wind farm aerodynamics: A review. *Journal of Wind Engineering and Industrial Aerodynamics*, 133:1–17.

Menke, R., Vasiljević, N., Hansen, K. S., Hahmann, A. N., and Mann, J. (2018). Does the wind turbine wake follow the topography? a multi-lidar study in complex terrain. *Wind Energy Science*, 3(2):681–691.

Midjiyawa, Z., Cheynet, E., Reuder, J., Ágústsson, H., and Kvamsdal, T. (2021). Potential and challenges of wind measurements using met-masts in complex topography for bridge design: Part II – Spectral flow characteristics. *Journal of Wind Engineering and Industrial Aerodynamics*, 211:104585.

Mikkelsen, T., Angelou, N., Hansen, K., Sjöholm, M., Harris, M., Slinger, C., Hadley, P., Scullion, R., Ellis, G., and Vives, G. (2012). A spinner-integrated wind lidar for enhanced wind turbine control. *Wind Energy*, 16(4):625–643.

Mizuno, T. and Panofsky, H. A. (1975). The validity of Taylor's hypothesis in the atmospheric surface layer. *Boundary-Layer Meteorology*, 9(4):375–380.

Molter, C. and Cheng, P. W. (2020). ANDroMeDA - A Novel Flying Wind Measurement System. *Journal of Physics: Conference Series*, 1618:032049.

Neumann, P. P., Asadi, S., Lilienthal, A., Bartholmai, M., and Schiller, J. (2012). Autonomous gas-sensitive microdrone: Wind vector estimation and gas distribution mapping. *IEEE Robotics & Automation Magazine*, 19(1):50–61.

Neumann, P. P. and Bartholmai, M. (2015). Real-time wind estimation on a micro unmanned aerial vehicle using its inertial measurement unit. *Sensors and Actuators A: Physical*, 235:300–310.

Nolan, P., Pinto, J., González-Rocha, J., Jensen, A., Vezzi, C., Bailey, S., de Boer, G., Diehl, C., Laurence, R., Powers, C., and et al. (2018). Coordinated Unmanned Aircraft System (UAS) and Ground-Based Weather Measurements to Predict Lagrangian Coherent Structures (LCSs). *Sensors*, 18(12):4448.

Palomaki, R. T., Rose, N. T., van den Bossche, M., Sherman, T. J., and Wekker, S. F. J. D. (2017). Wind estimation in the lower atmosphere using multirotor aircraft. *Journal of Atmospheric and Oceanic Technology*, 34(5):1183–1191.

Panofsky, H. A. (1962). Scale analysis of atmospheric turbulence at 2 m. *Quarterly Journal of the Royal Meteorological Society*, 88(375):57–69.

Pielke, R. A. and Panofsky, H. A. (1970). Turbulence characteristics along several towers. *Boundary-Layer Meteorology*, 1(2):115–130.

Platis, A., Hundhausen, M., Lampert, A., Emeis, S., and Bange, J. (2021). The Role of Atmospheric Stability and Turbulence in Offshore Wind-Farm Wakes in the German Bight. *Boundary-Layer Meteorology*, 182(3):441–469.

Platis, A., Siedersleben, S. K., Bange, J., Lampert, A., Bärfuss, K., Hankers, R., Cañadillas, B., Foreman, R., Schulz-Stellenfleth, J., Djath, B., Neumann, T., and Emeis, S. (2018). First in situ evidence of wakes in the far field behind offshore wind farms. *Scientific Reports*, 8(2163).

Pope, S. B. (2000). *Turbulent Flows*. Cambridge University Press.

Porté-Agel, F., Bastankhah, M., and Shamsoddin, S. (2019). Wind-Turbine and Wind-Farm Flows: A Review. *Boundary-Layer Meteorology*, 174(1):1–59.

Rajewski, D. A., Takle, E. S., Lundquist, J. K., Oncley, S., Prueger, J. H., Horst, T. W., Rhodes, M. E., Pfeiffer, R., Hatfield, J. L., Spoth, K. K., and Doorenbos, R. K. (2013). Crop Wind Energy Experiment (CWEX): Observations of Surface-Layer, Boundary Layer, and Mesoscale Interactions with a Wind Farm. *Bulletin of the American Meteorological Society*, 94(5):655–672.

Reuder, J., Båserud, L., Kral, S., Kumer, V., Wagenaar, J. W., and Knauer, A. (2016). Proof of concept for wind turbine wake investigations with the RPAS SUMO. *Energy Procedia*, 94:452–461.

Reuter, M., Bovensmann, H., Buchwitz, M., Borchardt, J., Krautwurst, S., Gerilowski, K., Lindauer, M., Kubistin, D., and Burrows, J. P. (2020). Development of a small unmanned aircraft system to derive CO_2 emissions of anthropogenic point sources. *Atmospheric Measurement Techniques Discussions*, 2020:1–27.

Richardson, L. F. (1920). The supply of energy from and to atmospheric eddies. *Proceedings of the Royal Society of London. Series A, Containing Papers of a Mathematical and Physical Character*, 97(686):354–373.

Ropelewski, C. F., Tennekes, H., and Panofsky, H. A. (1973). Horizontal coherence of wind fluctuations. *Boundary-Layer Meteorology*, 5:353 – 363.

Saranyasoontorn, K., Manuel, L., and Veers, P. S. (2004). A Comparison of Standard Coherence Models for Inflow Turbulence With Estimates from Field Measurements. *Journal of Solar Energy Engineering*, 126(4):1069–1082.

Schiano, F., Alonso-Mora, J., Rudin, K., Beardsley, P., Siegwart, R., and Sicilianok, B. (2014). Towards Estimation and Correction of Wind Effects on a Quadrotor UAV. In *IMAV 2014 : International Micro Air Vehicle Conference and Competition 2014*, pages 134 – 141.

Schlez, W. and Infield, D. (1998). Horizontal, two point coherence for separations greater than the measurement height. *Boundary-Layer Meteorology*, 87:459–480.

Schlipf, D., Trabucchi, D., Bischoff, O., Hofsäss, M., Mann, J., Mikkelsen, T., Rettenmeier, A., Trujillo, J., and Kühn, M. (2010). Testing of Frozen Turbulence Hypothesis for Wind Turbine Applications with a Scanning LIDAR System. In *Detailed Program*. ISARS. 15th International Symposium for the Advancement of Boundary Layer Remote Sensing, ISARS 2010 ; Conference date: 28-06-2010 Through 30-06-2010.

Sherry, M., Nemes, A., Jacono, D. L., Blackburn, H. M., and Sheridan, J. (2013). The interaction of helical tip and root vortices in a wind turbine wake. *Physics of Fluids*, 25(11):117102.

Shimura, T., Inoue, M., Tsujimoto, H., Sasaki, K., and Iguchi, M. (2018). Estimation of Wind Vector Profile Using a Hexarotor Unmanned Aerial Vehicle and Its Application to Meteorological Observation up to 1000 m above Surface. *Journal of Atmospheric and Oceanic Technology*, 35(8):1621–1631.

Shiotani, M. and Iwatani, Y. (1980). Gust structures over flat terrains and their modification by a barrier. In *Wind Engineering*, pages 203–214. Elsevier.

Simley, E., Angelou, N., Mikkelsen, T., Sjöholm, M., Mann, J., and Pao, L. Y. (2016). Characterization of wind velocities in the upstream induction zone of a wind turbine using scanning continuous-wave lidars. *Journal of Renewable and Sustainable Energy*, 8(1):013301.

Simley, E. and Pao, L. Y. (2015). A longitudinal spatial coherence model for wind evolution based on large-eddy simulation. In *2015 American Control Conference (ACC)*, pages 3708–3714.

Smalikho, I., Köpp, F., and Rahm, S. (2005). Measurement of atmospheric turbulence by 2-μm doppler lidar. *Journal of Atmospheric and Oceanic Technology*, 22(11):1733–1747.

Smedman, A.-S. (1991). Occurrence of roll circulations in a shallow boundary layer. *Boundary-Layer Meteorology*, 57(4):343–358.

Smedman, A.-S., Bergström, H., and Högström, U. (1995). Spectra, variances and length scales in a marine stable boundary layer dominated by a low level jet. *Boundary-Layer Meteorology*, 76(3):211–232.

Stull, R. (2016). *Practical Meteorology: An Algebra-based Survey of Atmospheric Science*. AVP International, University of British Columbia.

Taylor, G. I. (1938). The spectrum of turbulence. *Proceedings of the Royal Society of London Series*, 164(919):476–490.

Thielicke, W., Hübert, W., Müller, U., Eggert, M., and Wilhelm, P. (2021). Towards accurate and practical drone-based wind measurements with an ultrasonic anemometer. *Atmospheric Measurement Techniques*, 14(2):1303–1318.

van den Kroonenberg, A., Martin, T., Buschmann, M., Bange, J., and Vörsmann, P. (2008). Measuring the Wind Vector Using the Autonomous Mini Aerial Vehicle M2AV. *Journal of Atmospheric and Oceanic Technology*, 25(11):1969–1982.

Van der Hoven, I. (1957). Power spectrum of horizontal wind speed in the frequency range from 0.0007 to 900 cycles per hour. *Journal of Atmospheric Sciences*, 14(2):160–164.

Veers, P., Dykes, K., Lantz, E., Barth, S., Bottasso, C. L., Carlson, O., Clifton, A., Green, J., Green, P., Holttinen, H., Laird, D., Lehtomäki, V., Lundquist, J. K., Manwell, J., Marquis, M., Meneveau, C., Moriarty, P., Munduate, X., Muskulus, M., Naughton, J., Pao, L., Paquette, J., Peinke, J., Robertson, A., Sanz Rodrigo, J., Sempreviva, A. M., Smith, J. C., Tuohy, A., and Wiser, R. (2019). Grand challenges in the science of wind energy. *Science*, 366(6464):eaau2027.

Vermeer, L., Sørensen, J., and Crespo, A. (2003). Wind turbine wake aerodynamics. *Progress in Aerospace Sciences*, 39(6-7):467–510.

von Kármán, T. (1948). Progress in the Statistical Theory of Turbulence. *Proceedings of the National Academy of Sciences*, 34(11):530–539.

Wang, J.-Y., Luo, B., Zeng, M., and Meng, Q.-H. (2018). A Wind Estimation Method with an Unmanned Rotorcraft for Environmental Monitoring Tasks. *Sensors*, 18(12):4504.

Wetz, T. and Wildmann, N. (2022). Spatially distributed and simultaneous wind measurements with a fleet of small quadrotor UAS. *Journal of Physics: Conference Series*, 2265(2):022086.

Wetz, T. and Wildmann, N. (2023). Multi-point in situ measurements of turbulent flow in a wind turbine wake and inflow with a fleet of uncrewed aerial systems. *Wind Energy Science*, 8(4):515–534.

Wetz, T., Wildmann, N., and Beyrich, F. (2021). Distributed wind measurements with multiple quadrotor unmanned aerial vehicles in the atmospheric boundary layer. *Atmospheric Measurement Techniques*, 14(5):3795–3814.

Wetz, T., Zink, J., Bange, J., and Wildmann, N. (2023). Analyses of Spatial Correlation and Coherence in ABL Flow with a Fleet of UAS. *Boundary-Layer Meteorology*. Online First, 1–29.

Wildmann, N., Gerz, T., and Lundquist, J. K. (2020a). Long-range Doppler lidar measurements of wind turbine wakes and their interaction with turbulent atmospheric boundary-layer flow at Perdigao 2017. *Journal of Physics: Conference Series*, 1618(3):032034.

Wildmann, N., Hagen, M., and Gerz, T. (2022). Enhanced resource assessment and atmospheric monitoring of the research wind farm WiValdi. *Journal of Physics: Conference Series*, 2265(2):022029.

Wildmann, N., Hofsäß, M., Weimer, F., Joos, A., and Bange, J. (2014). MASC – a small remotely piloted aircraft (RPA) for wind energy research. *Advances in Science and Research*, 11(1):55–61.

Wildmann, N., Kigle, S., and Gerz, T. (2018a). Coplanar lidar measurement of a single wind energy converter wake in distinct atmospheric stability regimes at the Perdigão 2017 experiment. *J. Phys.: Conf. Ser.*, 1037(5):052006.

Wildmann, N., Päschke, E., Roiger, A., and Mallaun, C. (2020b). Towards improved turbulence estimation with Doppler wind lidar velocity-azimuth display (VAD) scans. *Atmospheric Measurement Techniques*, 13(8):4141–4158.

Wildmann, N., Rau, G. A., and Bange, J. (2015). Observations of the Early Morning Boundary-Layer Transition with Small Remotely-Piloted Aircraft. *Boundary-Layer Meteorology*, 157(3):345–373.

Wildmann, N., Vasiljevic, N., and Gerz, T. (2018b). Wind turbine wake measurements with automatically adjusting scanning trajectories in a multi-Doppler lidar setup. *Atmospheric Measurement Techniques*, 11(6):3801–3814.

Wildmann, N. and Wetz, T. (2022). Towards vertical wind and turbulent flux estimation with multicopter uncrewed aircraft systems. *Atmospheric Measurement Techniques*, 15(18):5465–5477.

Wu, Y.-T. and Porté-Agel, F. (2012). Atmospheric Turbulence Effects on Wind-Turbine Wakes: An LES Study. *Energies*, 5(12):5340–5362.

Appendix A

Peer-Reviewed First-Author Publications

A.1 Distributed wind measurements with multiple quadrotor unmanned aerial vehicles in the atmospheric boundary layer

Atmospheric
Measurement
Techniques

Distributed wind measurements with multiple quadrotor unmanned aerial vehicles in the atmospheric boundary layer

Tamino Wetz[1], Norman Wildmann[1], and Frank Beyrich[2]

[1]Deutsches Zentrum für Luft- und Raumfahrt e.V., Institut für Physik der Atmosphäre, Oberpfaffenhofen, Germany
[2]Deutscher Wetterdienst, Meteorologisches Observatorium Lindenberg – Richard-Aßmann-Observatorium, Lindenberg, Germany

Correspondence: Tamino Wetz (tamino.wetz@dlr.de)

Abstract. In this study, a fleet of quadrotor unmanned aerial vehicles (UAVs) is presented as a system to measure the spatial distribution of atmospheric boundary layer flow. The big advantage of this approach is that multiple and flexible measurement points in space can be sampled synchronously. The algorithm to obtain horizontal wind speed and direction is designed for hovering flight phases and is based on the principle of aerodynamic drag and the related quadrotor dynamics. During the FESST@MOL campaign at the boundary layer field site (Grenzschichtmessfeld, GM) Falkenberg of the Lindenberg Meteorological Observatory – Richard Assmann Observatory (MOL-RAO), 76 calibration and validation flights were performed. The 99 m tower equipped with cup and sonic anemometers at the site is used as the reference for the calibration of the wind measurements. The validation with an independent dataset against the tower anemometers reveals that an average accuracy of $\sigma_{\mathrm{rms}} < 0.3\,\mathrm{m\,s^{-1}}$ for the wind speed and $\sigma_{\mathrm{rms},\psi} < 8°$ for the wind direction was achieved. Furthermore, we compare the spatial distribution of wind measurements with the fleet of quadrotors to the tower vertical profiles and Doppler wind lidar scans. We show that the observed shear in the vertical profiles matches well with the tower and the fluctuations on short timescales agree between the systems. Flow structures that appear in the time series of a line-of-sight measurement and a two-dimensional vertical scan of the lidar can be observed with the fleet of quadrotors and are even sampled with a higher resolution than the deployed lidar can provide.

1 Introduction

Wind patterns and flow structures in the atmospheric boundary layer (ABL) are diverse and complex, depending on the synoptic conditions, mesoscale forcings and local effects (e.g., changes in land use or topographic changes). Examples for such flow structures are convective elements (Kaimal et al., 1976), coherent structures due to canopy flows (Dupont and Brunet, 2009), recirculation zones in mountainous terrain (Menke et al., 2019), or even a mix of convective and terrain-driven flows (Brötz et al., 2014). Turbulent structures also occur in the interaction of the ABL with wind turbines. Following the review of Veers et al. (2019) one of the major challenges in the science of wind energy is the understanding of the microscale wind conditions around a wind plant – this means the inflow conditions as well as the complex wake pattern behind individual turbines and their interaction in wind parks. The goal of the project presented in this study is to provide a tool for flexible measurements in this field.

A variety of measurement campaigns were performed in the past, studying the wind around wind plants using different measurement techniques (Rajewski et al., 2013; Fernando et al., 2019; Wilczak et al., 2019) including meteorological masts, lidar (Wildmann et al., 2018) or airborne in situ measurements (Platis et al., 2018). These methods provide valuable results but are associated with a significant logistical effort and are not very flexible in their deployment. Against these drawbacks, unmanned aerial vehicles (UAVs) are getting more relevant in supporting or expanding conventional atmospheric measurement techniques. The flexibility in flight patterns is almost unlimited. Furthermore, by apply-

ing multiple UAVs simultaneously at a campaign, there is the potential of measuring atmospheric quantities simultaneously and in situ at flexible positions that were not possible before.

In general, there are two different types of UAVs, one with fixed-wing configuration and one that uses only the power of the rotor to provide the lift for flying the vehicle (known as rotary-wing UAVs). Both types of UAVs were already applied for measuring the wind speed in the lower atmosphere (see for example Wildmann et al., 2015, for fixed-wing UAVs; Cuxart et al., 2019, for rotary-wing; or Kral et al., 2020, for a combination of both). The purpose of the present project is to measure the wind simultaneously at different positions in predefined patterns. For this purpose, UAV rotary-wing systems are chosen over those with fixed wings. Multirotors are able to hover at fixed positions and need only small space for takeoff and landing.

For measuring both wind speed and direction using rotary-wing UAVs, different methods have been described in literature. There are two major concepts. The first approach measures wind with an additional external wind sensor, e.g., sonic anemometers (Shimura et al., 2018; Reuter et al., 2021; Thielicke et al., 2021; Nolan et al., 2018) or hot wire/element probes (Cuxart et al., 2019; Molter and Cheng, 2020). The second approach uses only onboard sensors of the avionic system of a multirotor; e.g., the orientation angles measured by an inertial measurement unit (IMU) are used for wind measurement (Palomaki et al., 2017; Brosy et al., 2017; Neumann et al., 2012; Neumann and Bartholmai, 2015; Gonzalez-Rocha et al., 2017; González-Rocha et al., 2019; Wang et al., 2018; Bartholmai and Neumann, 2011; Bell et al., 2020). Furthermore there are commercial solutions for measuring the wind of the lower atmosphere with multirotors (Greene et al., 2019). A comparison of UAVs used in atmospheric science is exercised by Barbieri et al. (2019). Abichandani et al. (2020) compare different approaches described in the literature and demonstrate that with their best approach for using only onboard sensors a root-mean-square (rms) deviation of $\epsilon_{rms} = 0.6\,\mathrm{m\,s^{-1}}$ in wind speed is determined.

Regarding the method for measuring the wind with multirotors using only onboard sensors, Neumann and Bartholmai (2015) tried to link the wind speed with the inclination angle of the multirotor by taking the well-known Rayleigh drag equation into account. They tried to estimate the unknown drag coefficient and projected area of the multirotor by wind-tunnel tests and analytical approaches. The wind-tunnel tests were performed with still rotors. They concluded that neglecting the rotor movement is not a valid approach for estimating the drag coefficient. This is confirmed by wind-tunnel tests of Schiano et al. (2014). In their experiment they investigated the drag coefficient for different yaw and pitch angles of the multirotor. However, the experiments were performed with still rotors, which had a significant influence on the results, compared to real flight environments with moving ro-

tors. Therefore, Neumann and Bartholmai (2015) calibrated the wind speed directly against the inclination angle without estimating a drag coefficient and came up with a polynomial fit of second order. Brosy et al. (2017) use the GPS velocity as reference speed for obtaining a regression function between wind speed and inclination angle. They performed flights with different constant velocities in calm wind conditions. The obtained relation is a root function which is only valid to the limit of $6\,\mathrm{m\,s^{-1}}$. Further, González-Rocha et al. (2019) claim a linear relation between wind speed and inclination angle for their multirotor as demonstrated by wind-tunnel experiments.

In the present study we introduce a method to derive the wind using a similar approach, which we describe in detail in Sect. 4. The hardware and software of the quadrotors are introduced in Sect. 2. The experiment in which the fleet, consisting of up to 10 UAVs, is operated simultaneously is described in Sect. 3. Both wind speed and direction are calibrated against sonic anemometers for the 10 quadrotors, and the accuracies of different calibration datasets are validated with independent validation datasets (Sect. 5). Measured wind data from the fleet of multirotors are compared to cup and sonic anemometer measurements as well as Doppler wind lidar measurements to evaluate the capabilities to resolve microscale structures in the ABL (Sect. 6).

2 System description

This section describes the measurement system including the hardware and necessary software for performing simultaneous wind field measurements with rotary-wing UAVs.

2.1 UAV hardware

In general, commercial UAVs have some essential sensors implemented for their avionics. These is at least an IMU, i.e., gyroscopes, accelerometers and magnetometers to measure the attitude, as well as a GNSS system to determine the position. The flight controller (or autopilot) processes the measured data for either stabilizing the UAV to hold the position in hover state (together with the data from the GNSS) or flying predefined trajectories. Actuator outputs of the autopilot are the rotor speeds.

For our purpose of wind field measurements with a fleet of UAVs in the ABL, we chose the Holybro QAV250 quadrotor frame in combination with the Pixhawk® 4 Mini flight controller as shown in Fig. 1. This system has multiple advantages and meets most of the requirements that were defined.

- All raw output data of the IMU should be accessible, which requires an open-source solution such as the Pixhawk flight controller and the PX4 software. With the PX4 software, the raw sensor data are available at 100 Hz. For wind measurement, we average the data to 1 Hz in this study. The selection of an open-source so-

lution has the further advantage that the system allows software adjustment and the possibility of implementing additional sensors.

- The system should be as simple as possible regarding the flight kinematics, for calculating and calibrating wind speed measurement. Thus, a suitable type is a multirotor consisting of only four rotors, i.e., a quadrotor. In the kinematic model of the quadrotor only four forces due to the four rotors are acting on the quadrotor. The defined arrangement of the rotors in a square, viewed from the bird perspective, simplifies the model. Multirotors with more than four rotors have more forces included in the kinematic model. Due to the higher number of rotors, different geometric arrangements of the rotors are necessary, which results in a more complex kinematic model. In general, four rotors are the minimum number of rotors to maintain a stable flight in a multirotor setup. This configuration as a consequence yields the most simple kinematic model.

- The UAV should endure strong winds and high turbulence with a good stability of the hover position. In order to sustain the hover position in these conditions, a system with a highly dynamic flight controller and sufficient high actuator performance is required. These requirements are fulfilled with standard settings of commercial racing drones by design. This type has the potential to react fast against small disturbances, and we thus expect it to be able to resolve small scales of the flow. Since it is desirable to resolve structures as small as possible, the small class of racing drones with a distance between the rotor axes of 0.25 m was chosen.

- A long flight duration is desirable to capture all relevant turbulent scales in the ABL. A typical averaging period for turbulence retrievals is 30 min. This flight time can not be reached with the current combination of battery, airframe and controller parameters, but the 12 min that is currently possible with a battery capacity of 2.600 mAh can likely be increased with optimization of hardware and software in the future.

- Taking the goal of a fleet of UAVs into account, the single quadrotor should be off the shelf.

- With a weight of $m = 0.65\,\text{kg}$, the quadrotor is below the weight of 2 kg, which defines the threshold in the EU for classification in the open category with subcategory A2 until January 2023.

Choosing a quadrotor before multirotors with more than four rotors has several advantages such as easy kinematics, smaller frame sizes and price. Nevertheless, there are disadvantages such as the safety issues in case of motor failure, as flying with three remaining rotors is not possible. Furthermore, the ability to respond to side wind could be

Figure 1. Picture of quadrotor Holybro QAV250 in front of the mast at Falkenberg. Photo by Bernd Lammel.

Table 1. System description of quadrotor Holybro QAV250.

Parameter	Description
UAV type	quadrotor
weight (including battery)	0.65 kg
dimension (axis to axis)	0.25 m
autopilot	Pixhawk 4 Mini*
temperature and humidity sensor	HYT271*
frequency of sensor data logging	up to 100 Hz
mission flight speed	$< 15\,\text{m s}^{-1}$
flight time	$< 12\,\text{min}$

* Sensor specifications are listed in Appendix B.

smoother and more defined for hexa- or octocopters. Furthermore, the potential payload is typically higher for multirotors with more than four rotors, but since we are not planning to add heavy payloads to the system, we do not consider that relevant for our purpose.

In addition to the onboard sensors of the flight controller, a temperature and humidity sensor of type HYT271 is integrated in every quadrotor. Specifications of the sensors are listed in Table B1 in the Appendix. Fleet communication is realized by a Wi-Fi router to which all quadrotors and the ground station computer are connected. The important system parameters are listed in Table 1.

We will refer to the fleet of Holybro QAV250 quadrotors as the SWUF-3D (Simultaneous Wind measurement with Unmanned Flight Systems in 3D) fleet corresponding to the name of the project.

2.2 Software

The Pixhawk 4 Mini autopilot features the PX4 software. Specific parameter settings for the quadrotor are set to optimize flight behavior and to realize fleet flights. In order to align the quadrotor to the wind direction, the "weather-vane" mode is enabled. In that mode, the yaw angle is used as a control variable to minimize the roll angle amplitude, and hence the quadrotor will always face in upwind direction. The minimum roll angle for weather-vane controller to demand a yaw rate is set to $1°$.

Control of the fleet is realized by the software © QGround-Control. QGroundControl is an open-source software developed by the Dronecode Foundation (Gagne et al., 2020). The current release of the software allows us to control 15 drones simultaneously; however, with minor changes in the source code this number can be increased. This ground station software is used to launch and monitor the fleet. The flight paths are planned a priori in global coordinates and are uploaded to the single quadrotors. This allows complete freedom in the design of possible flight patterns. However, it has to be guaranteed by design that flight paths do not cross and thus no collision of UAVs is possible. All flight data that are logged by the autopilot to the internal SD card can be transferred to the ground station through an interface in QGroundControl.

## 3 The FESST@MOL experiment

Originally, calibration and validation flights with the SWUF-3D were planned to be performed during the FESSTVaL (Field Experiment on submesoscale spatio-temporal variability in Lindenberg) campaign that was initiated by the Hans-Ertel-Zentrum für Wetterforschung (HErZ) of the German Meteorological Service (Deutscher Wetterdienst, DWD). Due to the SARS-CoV-2 pandemic, this campaign could not be realized as planned but had to be significantly reduced in the number of participants and divided into smaller sub-campaigns (so-called "FESST@home" experiments). From May to August 2020, the campaign FESST@MOL was organized at the boundary layer field site (Grenzschichtmessfeld, GM) Falkenberg of the Lindenberg Meteorological Observatory – Richard Assmann Observatory (MOL-RAO). GM Falkenberg is located about 80 km to the southeast of the center of Berlin. Here, DWD runs a comprehensive operational measurement program of micrometeorological and boundary layer measurements including the use of a variety of wind sensors and measurement systems (cup and sonic anemometers at towers, Doppler sodar, Doppler lidar; see, e.g., Neisser et al., 2002; Beyrich and Adam, 2007). During FESST@MOL, this measurement program was extended by the operation of six Doppler lidar systems provided by DLR and KIT (Karlsruhe Institute of Technology). It was a major goal of this campaign to test and to compare different scanning configurations to derive both wind and turbulence infor-

mation from Doppler lidar measurements and to elaborate on strategies for the validation of the Doppler lidar retrievals by airborne measurements.

The central measurement facility at GM Falkenberg is a 99 m tower instrumented with sonic and cup anemometers at multiple levels. Cup anemometers (Thies wind transmitter type 4.3303.022.000) are installed at heights of 10, 20, 40, 60, 80 and 98 m above ground. At each level, there are three anemometers which are mounted at the tips of three booms pointing towards 11, 191 and 281°, respectively. Wind direction is measured with wind vanes (Thies wind direction transmitter type 4.3121.32.000/4.3124.30.002) at the 40 m and at 98 m levels. As for the wind speed, one vane is mounted on each of the three booms. Wind speed and wind direction data are measured with 1 Hz sampling frequency and aggregated in the data loggers to 1 min resolution time series (mean values, standard deviation, maximum wind speed). For the final wind dataset, the measurements are taken from those sensors which are not situated in the upstream or downstream region of the tower, depending on the actual wind direction.

Three-dimensional sonic anemometers (Metek USA-1) are mounted on the booms pointing towards south (191°) at the 50 and 90 m levels; these measurements are distorted through the tower for wind directions between 345 and 50° via north, but this wind direction was not observed during the present flight campaign.

The quadrotor flights were realized during the period 21–31 July 2020 at GM Falkenberg. In total 76 SWUF-3D flights were performed with 2 to 10 quadrotors accumulating in a flight duration of 4800 min (counting every minute of individual quadrotor flights). A protocol of all flights and their basic characteristics (flight time, flight pattern, number of quadrotors, mean wind conditions) is given in Appendix E. In general, the experiments were performed by flying individual predefined flight paths of multiple quadrotors simultaneously to discrete positions. At these discrete positions, the quadrotors were hovering for a certain time before flying back to the takeoff location. At the campaign the hovering time ranges between 9 and 11 min. Different fleet flight patterns were implemented. All of the pattern were targeting the goal to calibrate and validate the wind measurement algorithm of the quadrotors and of whole the fleet. The flight pattern "drone tower" consisted of up to eight quadrotors hovering at the altitudes of the tower wind measurements. The quadrotors were flown simultaneously at the same horizontal position marked in Fig. 2 but at different altitudes. The horizontal position was defined close to the tower in upwind direction, in order to have free inflow towards the quadrotor and no disturbance from the tower. A safety distance of 20 m to the tower was chosen. For a second flight pattern, one of the Doppler wind lidars was used for inter-comparison with SWUF-3D measurements. The location of the lidar is indicated in Fig. 2. The lidar is a Leosphere Windcube 200S, and it was operated at a physical resolution of 50 m with range–height indicator (RHI) scans and in staring mode. The staring mode at an ele-
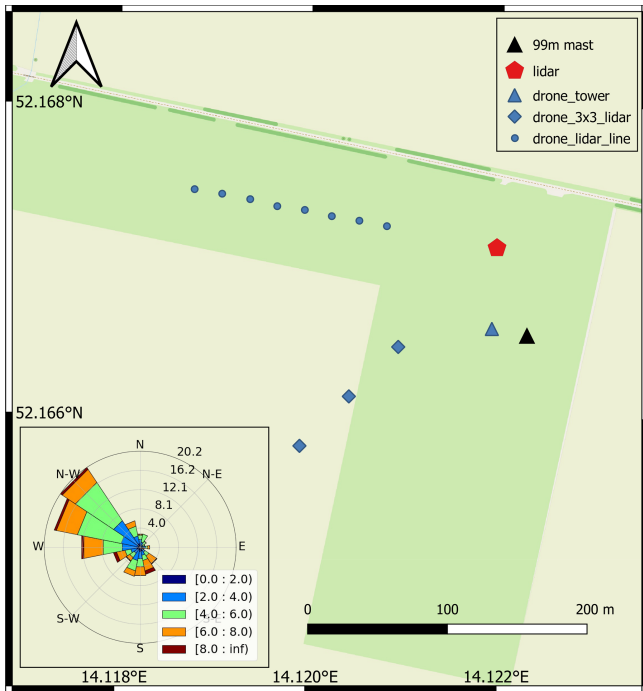
Figure 2. Map of the experiment site, including the locations of UAV fleet measurements. © OpenStreetMap contributors 2020. Distributed under a Creative Commons BY-SA License. The wind rose in the bottom left shows the wind conditions during the campaign period (21–30 July 2020).

vation angle of 7.1° allowed us to place all quadrotors within the lidar beam to measure the same flow field continuously ("lidar line"). The pattern "3 × 3 lidar" spanned an array of 3 × 3 quadrotors to represent a 2-D field within the RHI plane of the lidar scan. The mesh width of the SWUF-3D grid in this configuration was 100 m in the horizontal and 40 m in the vertical. Another pattern that appears in the protocol, called "drone line", was not used in the present analysis, since the distance to the 99 m tower is larger than for the drone tower. However, this pattern can get relevant in future data analysis.

4 Methods

4.1 System equation

The motion of the quadrotor can be described by the fundamental mechanic equation of force and moment equilibrium. For the definition of the motion of the system, the frames of reference need to be introduced.

4.1.1 Coordinate systems

The inertial frame, or also called earth frame, is fixed on the earth with the z component pointing orthogonally away from the earth surface. The second frame, the body frame, moves with the system and has its origin in the center of gravity of

the quadrotor (see also Palomaki et al., 2017). The inertial frame is distinguished by the indices $\boldsymbol{i}_n$ with $n(1, 2, 3)$ for the three dimensions, and similarly the body frame is defined by the indices $\boldsymbol{b}_n$. The position vector $\boldsymbol{X}_{\mathrm{i}}$ and the angular vector $\boldsymbol{\Phi}_{\mathrm{i}}$ are defined in the inertial frame. Furthermore, $\boldsymbol{V}_{\mathrm{b}}$ is the vector of translation speeds and $\boldsymbol{\omega}_{\mathrm{b}}$ the angular velocity vector in the body frame.

$$\boldsymbol{X}_{\mathrm{i}} = \begin{bmatrix} x & y & z \end{bmatrix}^T \tag{1}$$

$$\boldsymbol{\Phi}_{\mathrm{i}} = \begin{bmatrix} \phi & \theta & \psi \end{bmatrix}^T \tag{2}$$

$$\boldsymbol{V}_{\mathrm{b}} = \begin{bmatrix} u & v & w \end{bmatrix}^T \tag{3}$$

$$\boldsymbol{\omega}_{\mathrm{b}} = \begin{bmatrix} p & q & r \end{bmatrix}^T \tag{4}$$

In order to transform the motions from one frame to another a rotation matrix $\mathbf{R}$ is needed. For detailed definition see Appendix D. The time derivative of the position vector $\dot{\boldsymbol{X}}_{\mathrm{i}}$ represents the velocity vector in inertial frame.

$$\dot{\boldsymbol{X}}_{\mathrm{i}} = \mathbf{R}(\boldsymbol{\Phi}_{\mathrm{i}})\boldsymbol{V}_{\mathrm{b}} \tag{5}$$

4.1.2 Mechanical model

Regarding the quadrotor as a rigid body, its motion in space can be described by the basic mechanical equation dividing the motion in translation and rotation. The translation motion is balanced by the gravity force $\boldsymbol{F}_{\mathrm{g}}$, control forces $\boldsymbol{F}_{\mathrm{c}}$ and external forces $\boldsymbol{F}_{\mathrm{e}}$. The inertial forces are defined by the product of mass m and acceleration $\ddot{\boldsymbol{X}}_{\mathrm{i}}$.

$$m\ddot{\boldsymbol{X}}_{\mathrm{i}} = \boldsymbol{F}_{\mathrm{g}} + \boldsymbol{F}_{\mathrm{c}} + \boldsymbol{F}_{\mathrm{e}} \tag{6}$$

The angular momentum is driven by control moments $\boldsymbol{M}_{\mathrm{c}}$ and external moments $\boldsymbol{M}_{\mathrm{e}}$. Further, the angular inertia $\mathbf{I}$ and the angular acceleration vector $\ddot{\boldsymbol{\Phi}}_{\mathrm{i}}$ are needed to define the momentum equation.

$$\mathbf{I}\ddot{\boldsymbol{\Phi}}_{\mathrm{i}} = \boldsymbol{M}_{\mathrm{c}} + \boldsymbol{M}_{\mathrm{e}} \tag{7}$$

Transforming the equations of motion in the body frame leads to additional gyroscopic terms (with i_3 and b_3 representing unit vectors in inertial and body frame respectively):

$$m\ddot{\boldsymbol{X}}_{\mathrm{i}} = m\dot{\boldsymbol{V}}_{\mathrm{b}} + m\boldsymbol{V}_{\mathrm{b}} \times \boldsymbol{\omega}_{\mathrm{b}} = mg\mathbf{R}^T i_3 - \boldsymbol{F}_{\mathrm{c}}b_3 + \boldsymbol{F}_{\mathrm{e}}. \tag{8}$$

In the following step, only the linear motions were regarded for calculating the wind speed. Further the only external forces F_{e} are in this case the wind forces F_{w}. For the linear motions in body frame the following equations are obtained:

$$m(\dot{u} + qw - rv) = -mg[\sin(\theta)] + F_{\mathrm{w},x} \tag{9}$$

$$m(\dot{v} + pw - ru) = -mg[\cos(\theta)\sin(\phi)] + F_{\mathrm{w},y} \tag{10}$$

$$m(\dot{w} + pv - qu) = mg[\cos(\theta)\cos(\phi)] + F_{\mathrm{w},z}$$
$$- d\left(n_1^2 + n_2^2 + n_3^2 + n_4^2\right), \tag{11}$$

where g is the acceleration of gravity, n_i represents the rotational speeds of the motors and d is the thrust coefficient.

For our wind estimation in hover state with a weather-vane mode that ensures that the quadrotor points in the main wind direction, we proceed with only Eq. (9).

4.2 Wind estimation in hover state

The well-known aerodynamic Rayleigh equation for calculating aerodynamic forces from the wind velocity V_w takes the projected front area A and the dimensionless drag coefficient c_d into account. The variation of the density of air can be neglected for the low vertical extent of the flight profiles; it is assumed to be constant ($\rho = 1.2\,\mathrm{kg\,m^{-3}}$).

$$\boldsymbol{F}_w = \frac{\rho}{2} c_d A V_w^2 \qquad (12)$$

In a stable hover state, we assume that inertial forces on the left-hand side of Eq. (9) can be neglected and thus

$$F_{w,x} = mg\sin\theta. \qquad (13)$$

By taking Eq. (12) into account, Eq. (13) leads to the following equation for wind speed in the direction the quadrotor is facing:

$$\frac{\rho}{2} c_d A V_{w,x}^2 = F_{w,x} \qquad (14)$$

$$V_{w,x} = \sqrt{\frac{2F_{w,x}}{c_d A \rho}}. \qquad (15)$$

The term $c_d A$ is unknown and requires calibration. The drag coefficient and the projected area vary with the attitude of the quadrotor.

$$c_d A = c_{d,0} A_0 + f(\theta), \qquad (16)$$

where $c_{d,0} A_0$ is the drag coefficient and area at zero pitch angle. In this study we assume that the function $f(\theta)$ is a linear function.

4.3 Hover state accuracy

In order to calculate the wind velocity with the introduced method, the UAVs have to maintain a hover state. In order to evaluate the validity of the assumption of negligible linear and angular motion, we can look at the variance of the measured positions from GNSS data. The mean horizontal standard deviation of horizontal movement over all 76 flights of the campaign for all quadrotors results in $\sigma_{p,h} = 0.19\,\mathrm{m}$. The vertical stability appears to be slightly lower with $\sigma_{p,v} = 0.85\,\mathrm{m}$. These measured standard deviations are within the accuracy of the GNSS measurement, which is estimated to be of the order of $\epsilon_h = 0.6\,\mathrm{m}$ in the horizontal direction and $\epsilon_v = 0.8\,\mathrm{m}$ in the vertical direction by the avionic system. This means that actual movements can be slightly larger than the measured standard deviations but are still very small. These findings are also confirmed by visual inspection of the flights.

5 Calibration of wind measurement

As mentioned in Sect. 4.2, the parameter $c_d A$ can not be estimated from system specifications alone. In order to calculate this parameter, calibration flights were performed at the GM Falkenberg during the FESST@MOL campaign as described in Sect. 3. In the following comparison the meteorological mast provides the reference for the wind measurements of the quadrotors. For the calibration only drone tower pattern flights were used. In total 34 flights with multiple quadrotors were performed in this pattern. As established previously in Eq. (16) the parameter $c_d A$ is approximated by a constant and a linear term depending on the pitch angle with the proportional parameter c_p (Eq. 17).

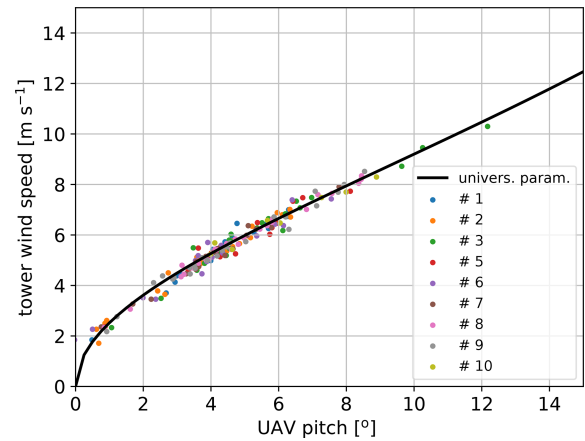$$c_d A = c_{d,0} A_0 + c_p \times \theta \qquad (17)$$

One flight consists of approx. 10 min of hovering, and data were averaged over this time period for the following calibration steps in order to compare the data with corresponding 10 min averaged wind speeds of the anemometers on the mast. Thus, the calibration is based on 10 min averaged data.

5.1 Individual quadrotor wind calibration

In the first step, each quadrotor is calibrated individually against the reference with all drone tower flights. Besides the determination of the parameters $c_{d,0} A_0$ and c_p, an offset for the pitch angle is introduced as $\Delta\theta$. This is necessary because of misalignment in the installation of the IMU in the quadrotor frame and slight differences in the mass distribution of the individual systems. Once the offset is calibrated it is applied to the measured pitch angle before any further processing. The pitch offset is obtained from the following calibration of the wind speed with the reference anemometer measurements. The optimal calibration function is obtained by solving a defined nonlinear least-squares problem. In particular, bounds were defined and the minimization was performed by the trust region reflective algorithm (Branch et al., 1999). The bounds were chosen in order to guide the minimization in physical plausible values. The resulting wind speed for this calibration is plotted in Fig. 3. One single data point represents the time-averaged wind speed of a single flight of one quadrotor in comparison to the corresponding average of the tower reference measurement. Due to some technical issues with quadrotor no. 4, it is not taken into consideration in the further calibration procedure. The root-mean-square deviations (σ_{rms}) of the calculated wind speed against the reference as well as a bias (ΔV_w) are determined from all single flights for the individual quadrotors and listed in the left column of Table 2. In the present case the calibration dataset is equal to the validation data; therefore, the deviation is expected to be relatively small, and remaining differences include the atmospheric variability in mostly convective ABLs. For this calibration, the averaged bias between quadrotor wind speed measurements and the reference

53
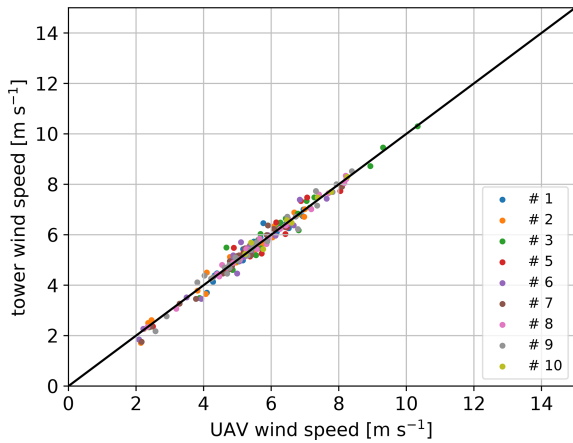
Figure 3. Ten-minute averaged wind speed for $n = 34$ flights drone vs. tower using the individual parameter calibration from the same 34 flights.

Table 2. Accuracy of wind speed measurement in meters per second $(m\,s^{-1})$ for a dataset of 34 flights (used for calibration and validation) **(a)** for calibration with all three parameters and **(b)** using only pitch offset for calibration with universal parameter values for c_p and $c_{d,0}A_0$.

No.	Individual (Fig. 3)		Universal	
	ΔV_w	σ_{rms}	ΔV_w	σ_{rms}
1	0.01	0.24	0.01	0.26
2	0.00	0.20	0.00	0.22
3	0.00	0.27	−0.01	0.29
5	0.00	0.33	0.00	0.33
6	0.01	0.28	0.03	0.29
7	0.02	0.21	0.07	0.27
8	0.00	0.12	0.00	0.13
9	0.00	0.22	0.01	0.22
10	0.00	0.17	0.01	0.21
Mean		0.23		0.25

wind speed is $\Delta V_w < 0.01\,m\,s^{-1}$. The random deviation for time-averaged data is $\sigma_{rms} = 0.23\,m\,s^{-1}$ on average over all flights. The accuracies of each UAV are listed in Table 2. This kind of calibration with many flights in different conditions and individual coefficients for each UAV is considered the best possible calibration and the benchmark for more simplified calibration procedures with reduced calibration datasets and calibration parameters that are common for the whole fleet.

5.2 Aerodynamic calibration

The aim of the study is to implement a robust calibration for a large number of UAVs in a fleet. In a large number of drones it will not always be possible to obtain as many

Figure 4. Regression function used for determining one universal set of parameters for c_p, $c_{d,0}A_0$.

calibration flights. Quadrotors of the same build should however have very similar aerodynamic characteristics. In order to achieve this requirement, one common set of parameters $c_{d,0}A_0$ and c_p with sufficiently reasonable accuracy for all regarded quadrotors shall therefore be determined in this section. Only the pitch offset remains as an individual calibration parameter for each quadrotor. By using the dataset of 34 flights the following function is obtained by taking the mean of the parameters of all quadrotors to minimize the overall error (Eq. 18).

$$c_d A = 0.03 - 0.047 \times \theta \qquad (18)$$

Figure 4 demonstrates that the obtained curve fits well with the individual data points of all quadrotors. The result of the calibration with common parameters is shown in the right column of Table 2. In comparison to the individual calibration, the accuracy is still reasonably high ($\sigma_{rms} = 0.25\,m\,s^{-1}$). The obtained value for $c_{d,0}A_0$ is in the range of the expected value as it would be calculated from an approximated surface area $A \approx 0.25 \cdot 0.05\,m^2$ and the drag coefficient of a long flat plate $c_d = 2$. Estimation of the constant parameter $c_{d,0}A_0$ from these parameters leads to a value of $0.025\,m^2$. Of course, the drag coefficient and surface area of the quadrotor with running rotors can not be measured this simply, which is why the calibration is considered necessary. Comparing this result with the mentioned studies in literature (see Introduction), different functions were obtained for the relation between wind speed and quadrotor attitude. In our study the relation is more complex but could roughly be described as a root function.
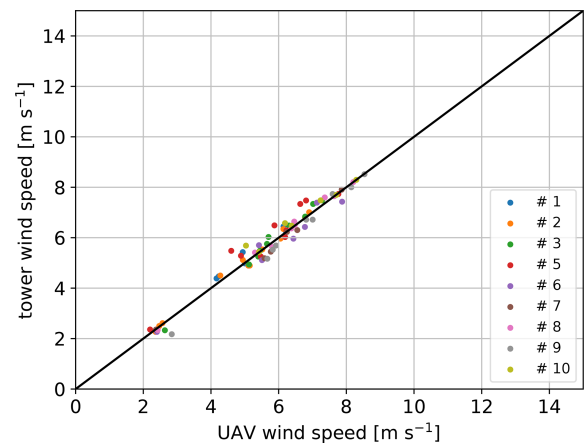
5.3 Pitch offset calibration

Having established aerodynamic parameters which appear to be universally applicable to the SWUF-3D fleet, it is still necessary to calibrate the pitch offset $\Delta\theta$ for each individual quadrotor. In this section, we evaluate how many calibration

flights are necessary and how stable the calibration is, i.e., how large the errors grow if only fewer calibration flights are used. First, the full dataset of 34 flights is used to determine $\Delta\theta$. Then, different calibration scenarios are performed with the present dataset, and the related rms deviations in comparison to the tower measurements are calculated. In order to use a common validation dataset, only drone tower flights of the second week (see Table E2) are used to calculate rms deviations and wind speed bias. Four different calibration scenarios were performed.

a. All 34 drone tower flights are used to estimate individual values of $\Delta\theta$. This should yield the best results for the accuracy estimation.

b. Only the first week of flights is used for calibration, i.e., 22 drone tower flights as listed in Table E1. In this scenario, the calibration dataset is completely independent of the validation dataset but still quite large, with a variety of wind conditions.

c. In order to simplify the calibration and evaluate if $\Delta\theta$ is stable throughout the whole campaign, only one flight is considered for calibration. Flight no. 31 is selected as the calibration flight, with an average wind speed of $6\,\mathrm{m\,s^{-1}}$. The idea is to choose a flight with arbitrary wind conditions for the calibration of the pitch offset. The goal is to show that it is possible to calibrate the system in frequently occurring wind conditions and still get accurate results in a wide range of different wind conditions. The pattern drone tower is only performed with eight quadrotors, which is why UAV no. 10 is not included in this calibration.

d. For the calibration of all quadrotors in the fleet, a second calibration flight is required. Flight no. 31 and no. 56 are used as base data in the following sections for calculating the wind speed (Fig. 5).

The accuracy estimates of the respective calibration scenarios are listed in Table 3. It is found that reducing the number of calibration flights yields lower accuracy, as expected. Using only the first week as the calibration dataset increases the averaged σ_{rms} from 0.23 to $0.25\,\mathrm{m\,s^{-1}}$, and using only a single flight increases it further to $0.28\,\mathrm{m\,s^{-1}}$. Both bias and rms deviation increase if fewer flights are used to estimate $\Delta\theta$, which suggests that the offset is not completely stable throughout the campaign. However, even the largest deviation estimate of quadrotor no. 5 is still below $0.5\,\mathrm{m\,s^{-1}}$, which is considered acceptable for this study, but it will be a goal to improve this in the future. The calibrated pitch offset parameter ranges between $\pm4.3°$. Additionally to the 10 min time-averaged wind speed validation, another evaluation of the same data with 2 min time average wind speed measurements is performed. Setting the time average to 2 min leads to an increase in the number of validation points and

Figure 5. Average wind speed for $n = 12$ flights from the second week drone vs. tower using the universal parameter – only individual pitch offset is calibrated from flight number 31 and 56 (scenario d).

greater independence of the flight time of one single validation flight. However, the synchronization of the UAV measurements with the tower measurements due to the horizontal distance becomes an issue the smaller the time average chosen is. The results of 2 min time-averaged data are showing comparable trends to the 10 min average evaluation concerning the mean accuracies for the different calibration scenarios. Nevertheless, the mean rms deviation for the single flight pitch offset calibration increases to $0.38\,\mathrm{m\,s^{-1}}$ due to higher uncertainties of the wind measurements in smaller scales. Detailed results about the 2 min average evaluation are shown in Appendix C.

5.4 Yaw-offset determination

Additionally to the magnitude of the wind speed, the wind direction is obtained from the quadrotors. As mentioned in Sect. 2, the quadrotors were operated in weather-vane mode. Hence, the quadrotor is automatically yawed in the direction of the wind. Therefore, the corresponding wind direction can directly be obtained from the yaw angle ψ. Nevertheless, the magnetometer is not always perfectly oriented towards north and calibration deviations can occur, which makes an offset calibration of the yaw angle necessary. For this purpose, the same two flights as for the wind speed calibration are used (i.e., flight no. 31 and no. 56). The offset yaw angle ranges between $\Delta\psi = -2°$ and $\Delta\psi = 22°$. The calibrated average wind direction for the drone tower flights of the second week is plotted in Fig. 6. The mean rms deviation results in $\sigma_{\mathrm{rms},\psi} = 7.5°$. The few outliers can be explained by low wind speed conditions, when roll angles above $1°$ are hardly reached and the weather-vane mode does not always correct the yaw angle fully into the wind direction.

Table 3. Accuracy of wind speed measurements in meters per second (m s^{-1}) for different calibration data using only pitch offset applied to the validation dataset of 12 flights from the second week. Data used for calibration: **(a)** all possible drone tower flight patterns (34 flights); **(b)** only flights from the first week (12 flights); **(c)** only one single flight with flight number 31; **(d)** two flights with flight number 31 and 56.

	(a) n34 all		**(b) n12 first week**		**(c) n1 fl.31**		**(d) n2 fl.31+56 (Fig. 5)**	
No.	ΔV_{w}	σ_{rms}	ΔV_{w}	σ_{rms}	ΔV_{w}	σ_{rms}	ΔV_{w}	σ_{rms}
1	0.00	0.16	0.00	0.16	−0.21	0.27	−0.21	0.27
2	−0.13	0.20	−0.25	0.30	−0.24	0.29	−0.01	0.15
3	−0.12	0.23	−0.19	0.27	−0.11	0.22	−0.06	0.21
5	−0.04	0.37	−0.19	0.41	−0.28	0.47	−0.31	0.48
6	−0.08	0.32	−0.12	0.33	0.18	0.35	0.18	0.35
7	0.09	0.19	0.11	0.20	0.13	0.21	0.16	0.23
8	−0.02	0.12	−0.03	0.12	−0.03	0.12	−0.03	0.12
9	−0.05	0.22	−0.06	0.22	0.25	0.34	0.23	0.33
10	0.03	0.23	0.13	0.26	–	–	−0.20	0.30
Mean		0.23		0.25		0.28		0.27
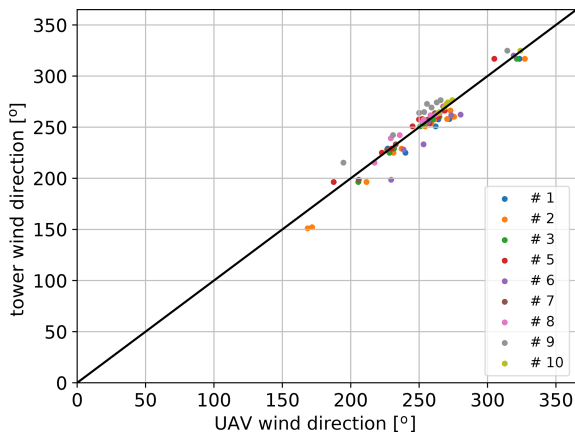
Figure 6. Average wind direction for $n = 12$ flights from the second week drone vs. tower including offset calibration.

## 6 Validation of synchronous fleet measurements

The goal of the SWUF-3D fleet is to capture small-scale to mesoscale flow structures in the ABL. Having calibrated the quadrotors for good wind measurement accuracy, we now evaluate how the synchronous measurements of multiple drones compare to synchronous measurements of multiple anemometers on the 99 m mast and with Doppler lidar wind measurements.

6.1 Vertical profiles

The drone tower flight pattern which was also used for calibration is suitable for measurements of vertical profiles with the quadrotors. As an example, we present flights no. 61 and no. 62 (without UAV no. 4) of the campaign since they feature shear and some gustiness in the wind field and were per-

formed in close succession. In Fig. 7a, only the quadrotor at 90 m is compared to the corresponding sonic measurement at the same height. It is evident from this plot that not only the 10 min averaged values are in good agreement with the reference instruments, but also the resolved time series of wind speed matches the sonic anemometer data very well. The variance of the velocity fluctuation of the 1 Hz data of the quadrotor $\sigma_{\mathrm{v,q}}^2 = 1.76\,\mathrm{m^2\,s^{-2}}$ is thus in good agreement with the sonic data $\sigma_{\mathrm{v,s}}^2 = 1.65\,\mathrm{m^2\,s^{-2}}$ for this particular case. However, some outliers occur in the time series plot in Fig. 7a. In this particular case at 13:40 UTC, the sonic anemometer data show high vertical wind up to $3.5\,\mathrm{m\,s^{-1}}$ that causes lift at the UAV, which leads to an increased altitude. In order to sustain the vertical position, the motor thrust is reduced to descend the UAV to the target altitude. To stabilize the descent, the pitch angle is controlled to a more horizontal position. This causes an underestimation of the wind speed due to small pitch angle. The same situation applies at 13:16 UTC, where UAV measurements also underestimate the reference wind speed. Figure 7b and c show the time series of the vertical profile for cup anemometers on the mast and seven quadrotors respectively. The data from the cup anemometers are only available as 1 min average values, which is why the complete met-mast data are shown in the contour plot with a resolution of 1 min and thus significantly less structure in the flow field is seen compared to the SWUF-3D fleet. Nevertheless, periods of higher wind speeds and stronger shear are present and match well between SWUF-3D and mast. To show the shear profile more clearly, Fig. 8 gives the averaged vertical profiles for the two 10 min periods. The differences between UAVs and mast measurements are of the same order as the previously determined rms deviations.
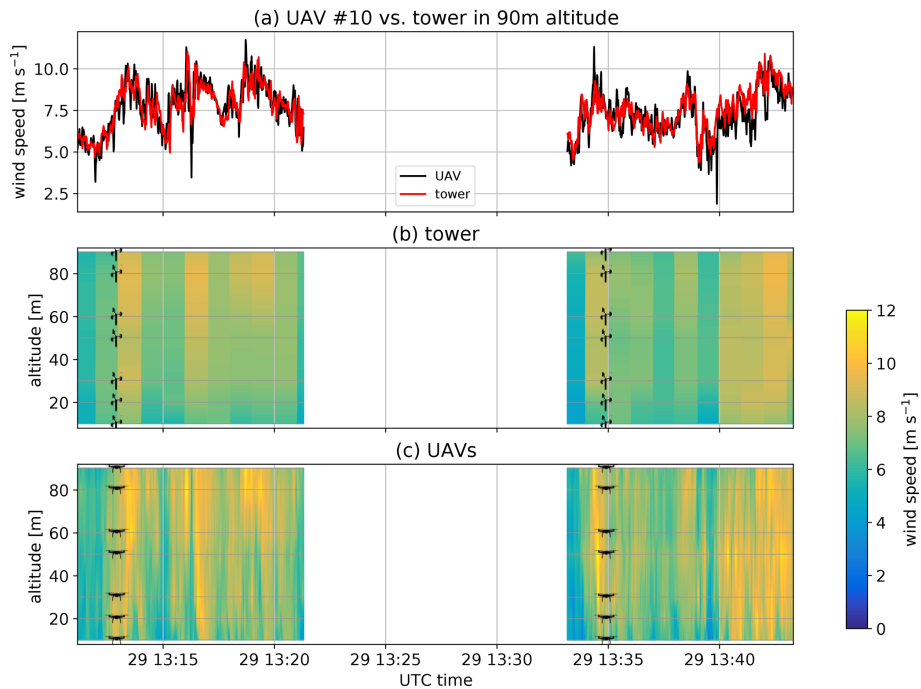
Figure 7. Comparison of drone tower to reference data from the tower for flight no. 61 and no. 62: **(a)** one single UAV at 90 m altitude vs. sonic measurements, **(b)** time series of tower measurements at different altitudes, and **(c)** corresponding UAV time series of seven quadrotors at different altitudes.
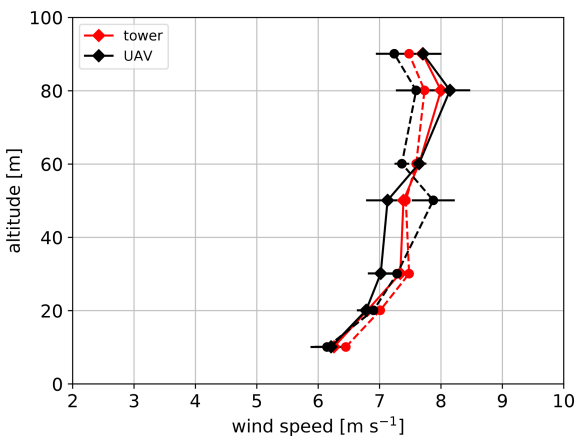
Figure 8. Comparison of drone tower to reference data from the tower for flight no. 61 (solid line) and no. 62 (dashed line). The error bars represent the rms deviation that was determined for each individual quadrotor in Sect. 5.3.

6.2 Variance

With the 1 Hz resolution of the quadrotor measurements, a significant part of the turbulent fluctuations can theoretically be resolved. In order to evaluate the capability to measure wind speed variance, we compare all flights at 50 and 90 m with the corresponding sonic anemometers. Figure 9 shows the scatterplot of this comparison. The mean rms deviation
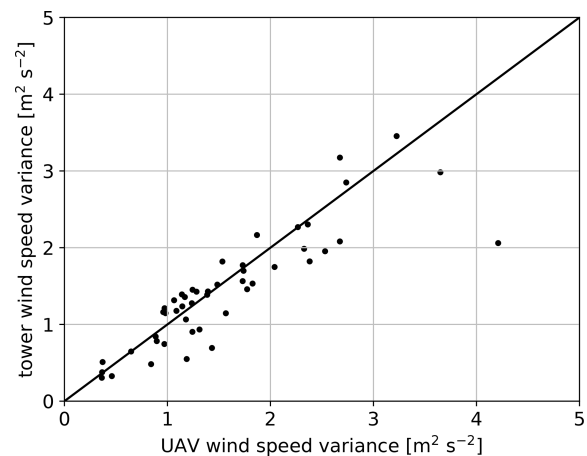
Figure 9. Variance of the wind speed for $n = 34$ flights in comparison to sonic measurements at 50 and 90 m altitude.

of the variance is $\sigma_{\mathrm{rms},\sigma^2} = 0.37\,\mathrm{m^2\,s^{-2}}$. Given the convective nature of the ABL in which most of the flights were performed, we consider the agreement satisfactory. Further detailed analyses of the scales that are resolved with the quadrotor are out of the scope of this study and will be handled in a separate study.

6.3 Horizontal line

The long-range lidar was used for further validation of the possibility to resolve horizontal structures in the atmospheric boundary layer with the SWUF-3D fleet. In one scenario, the lidar was set to measure continuously at a fixed elevation (7°) and azimuth angle (280°). Eight quadrotors were placed along the line of sight in the same spacing as the range gate separation of the lidar, which was set to 20 m with the closest range gate 80 m from the lidar (see also Fig. 2). As the lidar is measuring with a nonzero elevation angle, there is a height difference of 18 m between the position of the first range gate at 10 m a.g.l. (meters above ground level) and the last range gate at 28 m a.g.l. Figure 10 shows the comparison of the time series of the interpolated horizontal line. It is evident how both measurement systems measure the same variations in wind speed. A significant gust occurred at 13:27 UTC for example, which is observed with both systems. The lidar measurements show smoother gradients in wind speed variations along the line of sight which can be attributed to the volume averaging effect that is inherent to the method and can also explain the lower maximum values of the lidar measurements.

6.4 Vertical plane

In order to evaluate the performance of the UAV fleet to measure wind fields and their spatial distribution, flights were performed in a 3×3 grid, in the measurement plane of a lidar RHI (range–height indicator) scan. Figure 11 shows the resulting time series of one 10 min flight. The lidar data are linearly interpolated to the quadrotor location, and the horizontal wind component is reconstructed by division through the cosine of the elevation angle ($v_h = \frac{v_r}{\cos\phi}$). The 1 Hz quadrotor data points are centered at the time when the lidar beam crossed the quadrotor location and the wind component in line with the RHI plane was calculated from quadrotor wind speed and wind direction. It shows that the main features of the flow are captured similarly with a quadrotor and lidar. At the location of the central quadrotor, the lidar showed some hard target reflections that were probably caused by the quadrotor and lead to some gaps in the data for this location. As for the previous validation measurements, a good agreement with the reference system is found with deviations between quadrotor and lidar that are of the order of the previously determined accuracies. This example gives some confidence that spatial structures can be well captured with the SWUF-3D fleet even though the convective nature of the ABL in this experiment is extremely challenging for a direct comparison to the reference instruments.

7 Conclusions

Atmospheric measurements with multirotor UAVs are of increasing interest to the scientific community because of the

many new possibilities for flexible measurements with a quick and low-cost deployment. In order to establish the technology and classify the quality of the measurements, a transparent description of the algorithms and a traceable validation is important. In this study we described an algorithm for wind measurements that is based on the physical principle of aerodynamic drag and the related quadrotor dynamics. With the goal to enable fleet measurements that can capture small-scale structures in the ABL, nine quadrotors were calibrated against wind measurements of sonic and cup anemometers installed on the 99 m mast at the GM Falkenberg. An overall accuracy of $\sigma_{\rm rms} < 0.3\,{\rm m\,s^{-1}}$ for the wind speed and $\sigma_{\rm rms, \psi} < 8°$ for wind direction measurement was found. The SWUF-3D fleet is then successfully validated using lidar and mast measurements. The major achievements of the study can be summarized as follows.

– A commercial racing drone was utilized as a measurement system. The choice of this kind of UAV proved to be very beneficial, since the dynamics of the small quadrotors allow for a sensitive calibration curve. Also, the stability of the hover position is important for the measurement of turbulent winds, and the systems can operate in high wind speeds.

– The algorithm is successfully calibrated for individual quadrotors, resulting in an average accuracy of $\sigma_{\rm rms} = 0.23\,{\rm m\,s^{-1}}$ if a large number of calibration flights is used.

– One universal set of aerodynamic parameters is determined for the whole fleet. An accuracy of wind measurements as high as $\sigma_{\rm rms} = 0.27\,{\rm m\,s^{-1}}$ is achieved although only two flights were taken into account for the calibration of pitch misalignment offsets. This leads to the possibility of fast fleet calibration by using only few flights, which should however be chosen to be performed in medium to high wind speeds. The rms deviation includes the uncertainty due to the location offset between quadrotors and sonic anemometers, which was comparably large ($\approx 20\,{\rm m}$) in this study. The atmospheric variability can be especially large since all flights were performed during daytime, mostly in a well-developed convective ABL.

– The application of a weather-vane mode simplifies both the measurement of wind speeds and wind direction. The wind speed measurement algorithm can thus be reduced to a pitch angle relationship, and wind direction measurements can be directly read from the yaw angle of the UAV.

– Lidar and tower comparison shows that detailed flow structures both in time and in space could be resolved with the quadrotors. In the given configuration, the quadrotor data have a higher spatial resolution than the
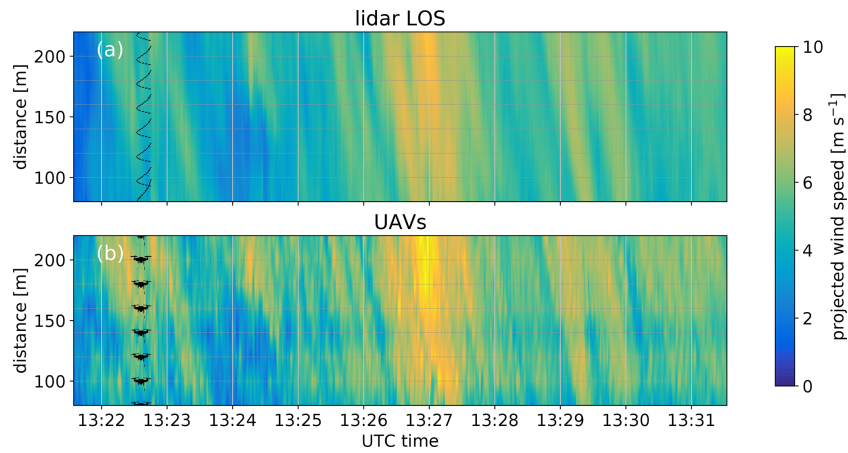
Figure 10. Time series of spatial wind measurements with a lidar **(a)** and eight drone **(b)** along a lidar line of sight. The *y*-axis grid represents the location of the range gate centers of the lidar and the drones respectively.
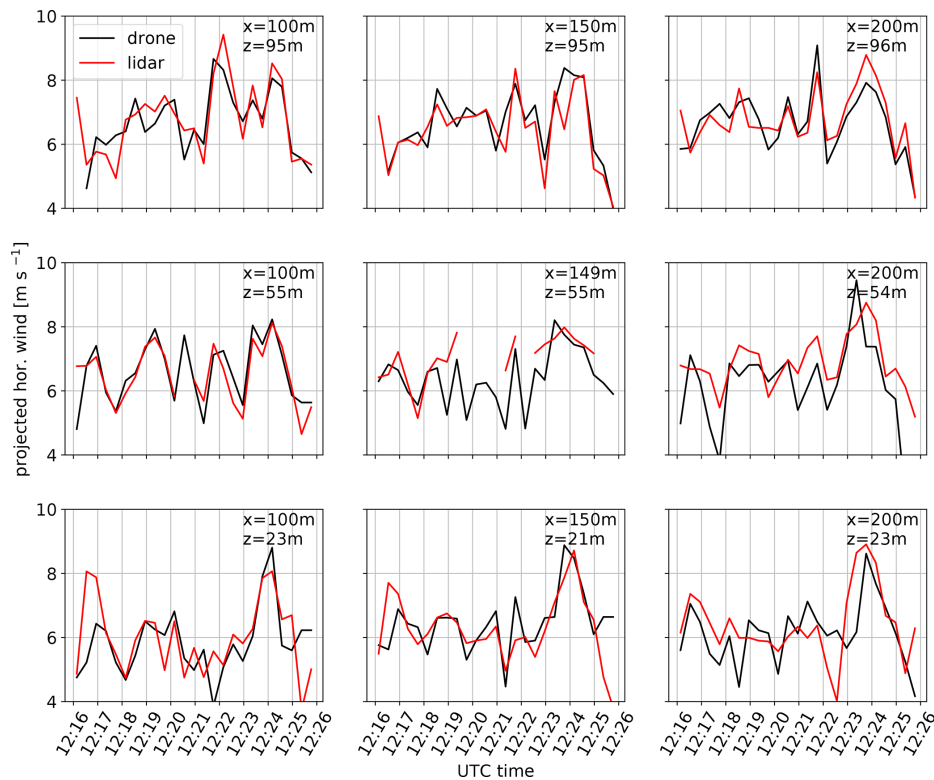
Figure 11. Time series of wind measurements of nine quadrotors compared to corresponding lidar measurements at the same locations on 24 July 2020.

long-range lidar data and allow us to detect turbulent structures like wind gusts.

8 Outlook

In the future, further analysis of the data and improvement of the wind algorithm will be considered. Some of the major fields of future research and development are the following.

– *Improving the algorithm of wind measurement by increasing the level of complexity, i.e., for example to dissolve the assumptions that were made for the hover state by taking gyroscopic terms into account.* Also, the roll angle could be included to resolve small-scale disturbances which are not in line with the main wind direction. Making use of the available information of motor output could potentially allow even finer resolution and

vertical wind measurements but needs significantly improved system identification and calibration.

– *Analyzing measurement data towards turbulence intensity, correlation between multiple UAVs, coherence and turbulent structures in general.* A big advantage and goal of the SWUF-3D fleet is to analyze turbulence without the assumption of Taylor's hypothesis of frozen turbulence as it is usually necessary with airborne measurements or stationary mast measurements. The fleet with multiple measurements in space can potentially directly measure cross-correlation and structure functions in space.

– *Acquiring simultaneous data of the SWUF-3D fleet, which can be a very valuable tool for validation of numerical simulations such as large-eddy simulations.* In the future, comparisons to such models will be pursued.

– *Improvement of flight time with higher battery capacity and controller optimization.* Flight times of 17 min were reached in some test flights with the presented quadrotors under best conditions. Significantly longer flight times would however require larger UAVs.

– *Expanding the SWUF-3D fleet up to 100 quadrotors for a larger grid of wind measurements.* It is the goal for SWUF-3D to measure turbulent structures in the wake of wind turbines. With the results of this study, it will be the next step to fly in close vicinity to wind turbines.

– *Improving the temperature and humidity measurements of the quadrotors.* It was found, although not presented in this study, that the sensors were installed too close to the body of the quadrotor and suffered from radiative heating of the system itself. An improved installation will solve this problem in the future.

Appendix A: Nomenclature

ϵ_h	horizontal accuracy of the GNSS measurement (m)
ϵ_v	vertical accuracy of the GNSS measurement (m)
ρ	density of air (kg m^{-3})
$\sigma_{p,h}$	standard deviation of the measured horizontal position (m)
$\sigma_{p,v}$	standard deviation of the measured vertical position (m)
$\sigma_{v,q}^2$	variance of the velocity fluctuation for the quadrotor measurement (m^2 s^{-2})
$\sigma_{v,s}^2$	variance of the velocity fluctuation for the sonic measurement (m^2 s^{-2})
σ_{rms}	root-mean-square deviations of wind speed calculation (m s^{-1})
σ_{rms,σ^2}	root-mean-square deviations of the variance measurement (m^2 s^{-2})
$\sigma_{rms,\psi}$	root-mean-square deviations of wind direction calculation (–)
$\boldsymbol{\omega}_b$	angular velocity vector in body frame (s^{-1})
$\Delta\theta$	pitch angle offset of quadrotor measurement (°)
ΔV_w	bias of wind speed calculation (m s^{-1})
$\boldsymbol{\Phi}_i$	angular vector in inertial frame (rad)
ϕ	roll angle of quadrotor (rad)
θ	pitch angle of quadrotor (rad)
ψ	yaw angle of quadrotor (rad)
c_d	drag coefficient (–)
$c_{d,0}$	drag coefficient for zero pitch angle (–)
c_p	proportional parameter for aerodynamic drag calibration (m^2)
d	thrust coefficient (m kg)
g	acceleration due to gravity (m s^{-2})
m	mass (kg)
n_i	rotational speeds of motors (s^{-1})
A	projected front area (m^2)
A_0	projected front area for zero pitch angle (m^2)
$\boldsymbol{F}_c$	control forces (N)
$\boldsymbol{F}_e$	external forces (N)
$\boldsymbol{F}_g$	gravity forces (N)
$F_{w,x}$	wind forces in x direction (N)
$\mathbf{I}$	rotational inertia (kg m^2)
$\boldsymbol{M}_c$	control moments (N m)
$\boldsymbol{M}_e$	external moments (N m)
$\mathbf{R}$	rotation matrix (–)
$\boldsymbol{V}_b$	translation velocity vector in body frame (m s^{-1})
V_w	wind velocity (m s^{-1})
$\boldsymbol{X}_i$	position vector in inertial frame (m)

Appendix B: Sensor specification

Table B1. Data sheet of the sensors. Accuracies representing the raw data output of the sensor without any processing of the Pixhawk autopilot.

Sensor	Type	Accuracy
accelerometer	(ICM-20689)/BMI055	$\pm 70\,\mathrm{m}g$
gyroscope	(ICM-20689)/BMI055	$\pm 5°\,\mathrm{s}^{-1}$
magnetometer	IST8310	± 0.3
barometer	MS5611	$\pm 1.5\,\mathrm{mbar}$
GPS	u-blox NEO-M8N	$2.5\,\mathrm{m}$ (horizontal position) $0.05\,\mathrm{m\,s}^{-1}$ (velocity)
temperature	HYT271	$\pm 0.2\,\mathrm{K}$ (0 to $+60\,°\mathrm{C}$)
humidity	HYT271	$\pm 1.8\,\%$ RH at $+23\,°\mathrm{C}$ ($0\,\%$ RH to $90\,\%$ RH)

Appendix C: Additional evaluation of validation data using 2 min averaged data
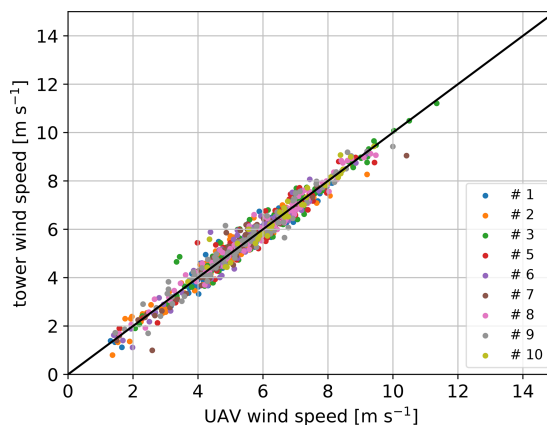

Figure C1. Two-minute averaged wind speed for $n = 34$ flights drone vs. tower using the individual parameter calibration from the same 34 flights.
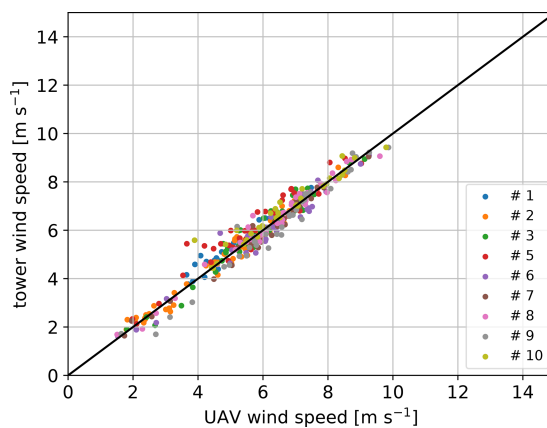

Figure C2. Two-minute averaged wind speed for $n = 12$ flights from the second week drone vs. tower using the universal parameter – only individual pitch offset is calibrated from flight number 31 and 56 (scenario d).

Table C1. Accuracy of wind speed measurement in meters per second $(\mathrm{m\,s^{-1}})$ for a dataset of 34 flights (used for calibration and validation) (a) for calibration with all three parameters and (b) using only pitch offset for calibration with universal parameter values for c_{p} and $c_{\mathrm{d},0}A_0$. The wind speed accuracy is based on 2 min time-averaged data.

No.	Individual (Fig. C1)		Universal	
	ΔV_{w}	σ_{rms}	ΔV_{w}	σ_{rms}
1	0.04	0.32	0.04	0.33
2	0.01	0.33	0.01	0.32
3	0.00	0.36	−0.01	0.36
5	−0.03	0.44	−0.03	0.43
6	0.00	0.38	0.03	0.40
7	0.02	0.36	0.08	0.42
8	0.00	0.25	−0.01	0.25
9	−0.02	0.33	−0.01	0.33
10	0.00	0.33	0.01	0.35
Mean		0.34		0.35

Table C2. Accuracy of wind speed measurements in meters per second $(\mathrm{m\,s^{-1}})$ for different calibration data using only pitch offset applied to the validation dataset of 12 flights from the second week. The wind speed accuracy is based on 2 min time-averaged data. Data used for calibration: **(a)** all possible drone tower flight patterns (34 flights); **(b)** only flights from the first week (12 flights); **(c)** only one single flight with flight number 31; **(d)** two flights with flight number 31 and 56.

No.	(a) n34 all		(b) n12 first week		(c) n1 fl.31		(d) n2 fl.31+56 (Fig. C2)	
	ΔV_{w}	σ_{rms}	ΔV_{w}	σ_{rms}	ΔV_{w}	σ_{rms}	ΔV_{w}	σ_{rms}
1	0.01	0.28	0.01	0.28	−0.20	0.35	−0.20	0.35
2	−0.12	0.30	−0.24	0.37	−0.23	0.36	−0.01	0.28
3	−0.13	0.35	−0.19	0.37	−0.11	0.34	−0.06	0.33
5	−0.07	0.45	−0.22	0.50	−0.31	0.55	−0.34	0.57
6	−0.10	0.41	−0.14	0.43	0.15	0.42	0.15	0.42
7	0.10	0.27	0.12	0.28	0.14	0.29	0.17	0.30
8	−0.02	0.28	−0.02	0.28	−0.03	0.28	−0.03	0.28
9	−0.05	0.37	−0.06	0.37	0.24	0.44	0.23	0.43
10	0.02	0.36	0.13	0.38	–	–	−0.20	0.42
Mean		0.34		0.36		0.38		0.38

Appendix D: Transformation matrix

The rotation matrix $\mathbf{R}(\mathbf{\Phi}_{\mathrm{i}})$ is

$$\mathbf{R}(\mathbf{\Phi}_{\mathrm{i}}) = \begin{bmatrix} \cos\theta\cos\psi & \cos\psi\sin\theta\sin\phi - \cos\phi\sin\psi & \cos\psi\sin\theta\cos\phi + \sin\phi\sin\psi \\ \cos\theta\sin\psi & \cos\phi\cos\psi + \sin\theta\sin\phi\sin\psi & -\sin\phi\cos\psi + \sin\theta\cos\phi\sin\psi \\ -\sin\theta & \cos\theta\sin\phi & \cos\theta\cos\phi \end{bmatrix}. \quad \text{(D1)}$$

Appendix E: Flight protocol

Table E1. Flight protocol of the first week of the FESST@MOL campaign.

Date (dd.m)	No.	Time start UTC	Time end UTC	QAV no. 1	2	3	4	5	6	7	8	9	10	Flight pattern	Wind speed 98 m (m s^{-1})	Wind dir. 98 m (°)	Temp 98 m (°C)	Hum 98 m (%)
20.7	1	09:14:50	09:23:50	×	×				×	×				drone tower	1.14	216	22.2	77.3
20.7	2	10:02:30	10:11:40	×	×				×	×				drone tower	5.57	314	22.95	69.8
20.7	3	10:18:30	10:27:50	×	×				×	×				drone tower	5.23	320	23.15	67.3
20.7	4	11:30:10	11:39:20	×	×				×	×				drone tower	5.58	335	23.46	63.9
20.7	5	11:45:10	11:54:10	×	×				×	×				drone tower	5.94	337	23.54	61.9
20.7	6	13:47:00	13:56:00			×	×				×	×		drone tower	9.98	305	22.54	55.2
20.7	7	14:01:40	14:10:50			×	×				×	×		drone tower	9.32	313	22.42	58.3
20.7	8	14:19:40	14:28:50			×	×				×	×		drone tower	9.89	315	22.51	57.9
21.7	9	08:49:10	08:58:00			×	×				×	×		drone tower	4.49	289	17.23	58.9
21.7	10	09:56:20	10:05:10			×	×				×	×		drone tower	4.88	280	17.97	50.5
21.7	11	10:11:20	10:20:00			×	×				×	×		drone tower	5.87	300	17.78	47.5
21.7	12	12:35:30	12:41:45			×	×				×	×		drone tower	6.79	305	19.04	37.8
21.7	13	13:07:00	13:13:20			×	×				×	×		drone tower	6.81	290	19.5	32.2
21.7	14	13:20:30	13:29:20			×	×				×	×		drone tower	5.91	299	19.77	32.1
21.7	15	14:31:40	14:41:00	×	×	×	×		×	×	×	×		drone tower	6.28	307	19.97	31.5
21.7	16	14:56:40	15:04:00	×	×	×	×		×	×	×	×		drone tower	6.81	298	20.19	32
22.7	17	09:06:30	09:15:30	×	×	×	×		×	×	×	×		drone tower	5.66	289	16.7	49.6
22.7	18	09:22:30	09:31:00	×	×	×	×		×	×	×	×		drone tower	6.72	288	16.85	47
22.7	19	11:04:40	11:13:30			×	×				×	×		1 × 4 lidar	5.28	303	17.81	39.4
22.7	20	11:18:10	11:27:30			×	×				×	×		1 × 4 lidar	5.05	298	18.06	39.2
22.7	21	12:14:40	12:22:00	×	×	×	×		×	×	×	×		2 × 4 lidar	5.59	300	18.7	36.9
22.7	22	12:40:50	12:49:10	×	×	×	×		×	×	×	×		2 × 4 lidar	5.01	294	18.8	35.9
22.7	23	14:57:00	15:05:30	×	×	×	×	×	×	×	×	×	×	DLR logo	5.12	307	19.58	35.3
23.7	24	10:35:20	10:43:50	×	×	×	×		×	×	×			drone tower	2.72	311	17.5	53.5
23.7	25	11:21:00	11:28:30	×	×	×	×		×	×		×	×	drone line	1.81	257	17.56	52.5
23.7	26	13:03:40	13:12:00	×	×	×	×		×	×		×	×	2 × 4 lidar	3.42	253	18.81	44.7
23.7	27	13:24:40	13:33:20	×	×	×	×		×	×		×	×	2 × 4 lidar	4.04	254	19.12	41.3
24.7	28	07:45:40	07:55:00	×	×	×	×		×	×		×	×	2 × 4 lidar	4.36	210	20.12	47.6
24.7	29	08:04:50	08:08:20	×	×	×	×		×	×		×	×	2 × 4 lidar	4.84	221	20.42	45.5
24.7	30	09:59:20	10:09:30	×	×	×		×	×	×	×	×		drone tower	5.42	251	22.76	35.5
24.7	31	10:19:30	10:29:10	×	×	×		×	×	×	×			drone tower	6.51	209	23.05	34.4
24.7	32	11:52:20	12:01:50	×	×	×		×	×	×	×	×	×	3 × 3 lidar	5.83	235	24.03	33.7
24.7	33	12:15:50	12:25:30	×	×	×		×	×	×	×	×	×	3 × 3 lidar	6.07	230	24.37	34.1
24.7	34	13:18:20	13:27:50	×	×	×		×	×	×	×	×	×	3 × 3 lidar	5.96	261	24.87	31.9
24.7	35	14:14:00	14:24:00	×	×	×		×	×	×	×	×	×	3 × 3 lidar	7.91	252	25.83	28.7
24.7	36	15:06:10	15:15:50	×	×	×		×	×	×	×	×	×	3 × 3 lidar	7.21	272	25.9	28.4
24.7	37	15:53:50	16:03:50	×	×	×			×	×	×		×	drone tower	5.07	279	26.02	29.8

Table E2. Flight protocol of the second week of the FESST@MOL campaign.

Date (dd.m)	No.	Time start UTC	Time end UTC	1	2	3	4	5	6	7	8	9	10	Flight pattern	Wind speed 98 m (m s^{-1})	Wind dir. 98 m (°)	Temp 98 m (°C)	Hum 98 m (%)
27.7	38	07:33:40	07:44:30		×		×							drone tower	2.23	137	18.66	78.3
27.7	39	07:49:20	08:00:00		×		×							drone tower	2.5	134	19.32	75.3
27.7	40	09:20:30	09:30:30		×	×	×	×	×	×	×	×		drone tower	3.04	186	21.17	63
27.7	41	13:24:30	13:33:30					×	×					drone line	2.26	182	23.82	41.2
27.7	42	13:45:10	13:55:00	×	×	×	×	×	×	×	×	×	×	drone line	2.76	198	23.88	42.7
28.7	43	07:21:40	07:31:20	×	×	×		×	×	×	×	×		drone tower	5.1	216	23.12	52.8
28.7	44	07:57:30	08:07:20	×	×	×		×	×	×	×	×		drone tower	5.86	235	23.79	52.3
28.7	45	08:41:20	08:48:50	×	×	×		×	×	×	×	×		2 × 4 lidar	6.25	285	24.07	49.1
28.7	46	09:14:40	09:24:40	×	×	×		×	×	×	×	×		2 × 4 lidar	4.88	291	23.73	50.4
28.7	47	11:07:10	11:16:30	×	×	×	×	×	×	×	×	×	×	drone line	4.77	222	25.46	44.4
28.7	48	11:24:30	11:33:30	×	×	×	×	×	×	×	×	×	×	drone line	6.07	248	25.56	43.4
28.7	49	13:03:10	13:12:20	×	×	×	×	×	×	×	×	×	×	drone line	8.73	291	25.14	44
28.7	50	13:24:40	13:34:30	×	×	×	×	×	×	×	×	×	×	drone line	5.94	291	25.1	44.8
28.7	51	14:45:50	14:54:30	×	×	×	×	×	×	×	×	×	×	drone line	6.71	266	25.94	39.4
28.7	52	15:14:30	15:23:30	×	×	×	×	×	×	×	×	×	×	drone line	6.43	295	25.38	41.8
29.7	53	07:16:50	07:26:20	×	×	×	×	×	×	×	×	×	×	drone line	5.96	291	16.7	56.2
29.7	54	07:41:50	07:51:10	×	×	×	×	×	×	×	×	×	×	drone line	5.74	291	16.63	56.9
29.7	55	08:45:40	08:55:10		×	×	×	×		×	×	×	×	drone tower	6.02	268	17.34	54.9
29.7	56	09:16:30	09:26:30		×	×	×	×		×	×	×	×	drone tower	7.18	259	17.96	50.9
29.7	57	09:46:00	09:56:20		×	×	×	×		×	×	×	×	drone tower	6.55	260	18.32	45.2
29.7	58	11:16:30	11:26:10	×	×	×		×	×	×	×	×	×	3 × 3 lidar	5.65	271	19.43	39.9
29.7	59	11:35:20	11:45:20	×	×	×		×	×	×	×	×	×	3 × 3 lidar	6.3	268	19.87	40.2
29.7	60	12:34:30	12:44:40	×	×	×	×		×		×	×	×	drone tower	8.32	287	20.07	40
29.7	61	13:11:10	13:21:30	×	×	×	×		×		×	×	×	drone tower	7.41	268	20.78	36.7
29.7	62	13:33:10	13:43:20	×	×	×	×		×		×	×	×	drone tower	9.03	268	20.99	36.1
29.7	63	14:34:00	14:44:00	×	×	×		×	×	×	×	×	×	3 × 3 lidar	7.12	261	21.42	35.2
29.7	64	15:09:20	15:19:10	×	×	×	×	×	×	×	×	×	×	drone line	7.12	276	21.38	34.3
30.7	65	07:33:20	07:43:30	×	×	×		×	×	×	×	×	×	3 × 3 lidar	4.23	282	15.99	56.9
30.7	66	07:55:50	08:05:40	×	×	×		×	×	×	×	×	×	3 × 3 lidar	4.46	279	16.3	55.3
30.7	67	09:43:20	09:53:00	×	×	×	×	×	×	×	×	×	×	drone line	5.6	266	18.04	48.5
30.7	68	10:03:10	10:12:50	×	×	×	×	×	×	×	×	×	×	drone line	5.51	252	18.12	48
30.7	69	11:45:10	11:55:10	×	×	×	×	×	×	×	×	×	×	drone line	4.74	279	20.02	40.4
30.7	70	12:12:20	12:22:20	×	×	×	×	×	×	×	×	×	×	drone line	4.75	307	20.25	39.4
30.7	71	13:21:20	13:31:50	×	×	×		×		×	×	×	×	lidar line	4.77	292	21.27	33.9
30.7	72	13:39:00	13:49:30	×	×	×		×		×	×	×	×	lidar line	5.44	301	21.44	33.8
30.7	73	15:02:30	15:13:00	×	×	×		×	×		×	×	×	drone tower	5.77	330	21.42	34.4
31.7	74	07:40:40	07:47:00	×	×	×		×	×	×	×	×	×	drone line	4.8	317	17.15	57.3
31.7	75	09:20:31	09:30:00	×	×	×		×	×	×	×	×	×	drone line	5.02	312	19.14	50.5
31.7	76	09:57:30	10:07:10	×	×	×		×	×	×	×	×	×	drone line	5.64	309	19.83	48.7

References

Abichandani, P., Lobo, D., Ford, G., Bucci, D., and Kam, M.: Wind Measurement and Simulation Techniques in Multi-Rotor Small Unmanned Aerial Vehicles, IEEE Access, 8, 54910–54927, 2020.

Barbieri, L., Kral, S., Bailey, S., Frazier, A., Jacob, J., Reuder, J., Brus, D., Chilson, P., Crick, C., Detweiler, C., Doddi, A., Elston, J., Foroutan, H., González-Rocha, J., Greene, B., Guzman, M., Houston, A., Islam, A., Kemppinen, O., Lawrence, D., Pillar-Little, E., Ross, S., Sama, M., Schmale, D., Schuyler, T., Shankar, A., Smith, S., Waugh, S., Dixon, C., Borenstein, S., and de Boer, G.: Intercomparison of Small Unmanned Aircraft System (sUAS) Measurements for Atmospheric Science during the LAPSE-RATE Campaign, Sensors, 19, 2179, https://doi.org/10.3390/s19092179, 2019.

Bartholmai, M. and Neumann, P. P.: Adaptive ortsaufgelöste Gaskonzentrationsmessung mit einer Mikrodrohne, Tech. Mess., 78, 470–478, https://doi.org/10.1524/teme.2011.0158, 2011.

Bell, T. M., Greene, B. R., Klein, P. M., Carney, M., and Chilson, P. B.: Confronting the boundary layer data gap: evaluating new and existing methodologies of probing the lower atmosphere, Atmos. Meas. Tech., 13, 3855–3872, https://doi.org/10.5194/amt-13-3855-2020, 2020.

Beyrich, F. and Adam, W.: Site and Data Report for the Lindenberg Reference Site in CEOP – Phase I, Selbstverlag des Deutschen Wetterdienstes: Berichte des Deutschen Wetterdienstes, Offenbach a. M., Germany, 55 pp., 2007.

Branch, M. A., Coleman, T. F., and Li, Y.: A Subspace, Interior, and Conjugate Gradient Method for Large-Scale Bound-Constrained Minimization Problems, SIAM J. Sci. Comput., 21, 1–23, 1999.

Brosy, C., Krampf, K., Zeeman, M., Wolf, B., Junkermann, W., Schäfer, K., Emeis, S., and Kunstmann, H.: Simultaneous multicopter-based air sampling and sensing of meteorological variables, Atmos. Meas. Tech., 10, 2773–2784, https://doi.org/10.5194/amt-10-2773-2017, 2017.

Brötz, B., Eigenmann, R., Dörnbrack, A., Foken, T., and Wirth, V.: Early-Morning Flow Transition in a Valley in Low-Mountain Terrain Under Clear-Sky Conditions, Bound.-Lay. Meteorol., 152, 45–63, https://doi.org/10.1007/s10546-014-9921-7, 2014.

Cuxart, J., Wrenger, B., Matjacic, B., and Mahrt, L.: Spatial Variability of the Lower Atmospheric Boundary Layer over Hilly Terrain as Observed with an RPAS, Atmosphere, 10, 715, https://doi.org/10.3390/atmos10110715, 2019.

Dupont, S. and Brunet, Y.: Coherent structures in canopy edge flow: a large-eddy simulation study, J. Fluid Mech., 630, 93–128, https://doi.org/10.1017/S0022112009006739, 2009.

Fernando, H. J. S., Mann, J., Palma, J. M. L. M., Lundquist, J. K., Barthelmie, R. J., Belo-Pereira, M., Brown, W. O. J., Chow, F. K., Gerz, T., Hocut, C. M., Klein, P. M., Leo, L. S., Matos, J. C., Oncley, S. P., Pryor, S. C., Bariteau, L., Bell, T. M., Bodini, N., Carney, M. B., Courtney, M. S., Creegan, E. D., Dimitrova, R., Gomes, S., Hagen, M., Hyde, J. O., Kigle, S., Krishnamurthy, R., Lopes, J. C., Mazzaro, L., Neher, J. M. T., Menke, R., Murphy, P., Oswald, L., Otarola-Bustos, S., Pattantyus, A. K., Rodrigues, C. V., Schady, A., Sirin, N., Spuler, S., Svensson, E., Tomaszewski, J., Turner, D. D., van Veen, L., Vasiljević, N., Vassallo, D., Voss, S., Wildmann, N., and Wang, Y.: The Perdigão: Peering into Microscale Details of Mountain Winds, B. Am. Meteorol. Soc., 100, 799–819, https://doi.org/10.1175/BAMS-D-17-0227.1, 2019.

Gagne, D., Meier, L., Grubba, G., Bot, P. B., Agar, D., Pereira, P. J., Carpenter, M., Stellanova, T., Gubler, T., Walser, J., Canabrava, T., Lizarraga, M., Weibley, N., pixhawk students, Küng, B., Voznytsa, A., Galvani, W., Frančeškin, M., pierre.tilak, Jehangir, R., oberion, tecnosapiens, Bircher, A., Tapsell, J., D, G., Bonney, B., Oes, J., Anthony, N., Ghanghas, P., and Kuula, S.: mavlink/qgroundcontrol v4.0.9, Zenodo [code], https://doi.org/10.5281/zenodo.3937530, 2020.

Gonzalez-Rocha, J., Woolsey, C. A., Sultan, C., de Wekker, S., and Rose, N.: Measuring Atmospheric Winds from Quadrotor Motion, in: AIAA Atmospheric Flight Mechanics Conference, American Institute of Aeronautics and Astronautics, https://doi.org/10.2514/6.2017-1189, 2017.

66

González-Rocha, J., Woolsey, C. A., Sultan, C., and Wekker, S. F. J. D.: Sensing Wind from Quadrotor Motion, J. Guid., Control Dynam., 42, 836–852, https://doi.org/10.2514/1.g003542, 2019.

Greene, B., Segales, A., Bell, T., Pillar-Little, E., and Chilson, P.: Environmental and Sensor Integration Influences on Temperature Measurements by Rotary-Wing Unmanned Aircraft Systems, Sensors, 19, 1470, https://doi.org/10.3390/s19061470, 2019.

Kaimal, J. C., Wyngaard, J. C., Haugen, D. A., Š, O. R. C., Izumi, Y., Caughey, S. J., and Readings, C. J.: Turbulence Structure in the Convective Boundary Layer, J. Atmos. Sci., 33, 2152–2169, https://doi.org/10.1175/1520-0469(1976)033<2152:TSITCB>2.0.CO;2, 1976.

Kral, S. T., Reuder, J., Vihma, T., Suomi, I., Haualand, K. F., Urbancic, G. H., Greene, B. R., Steeneveld, G.-J., Lorenz, T., Maronga, B., Jonassen, M. O., Ajosenpää, H., Båserud, L., Chilson, P. B., Holtslag, A. A. M., Jenkins, A. D., Kouznetsov, R., Mayer, S., Pillar-Little, E. A., Rautenberg, A., Schwenkel, J., Seidl, A. W., and Wrenger, B.: The Innovative Strategies for Observations in the Arctic Atmospheric Boundary Layer Project (ISOBAR) – Unique fine-scale observations under stable and very stable conditions, B. Am. Meteorol. Soc., 102, 1–64, https://doi.org/10.1175/BAMS-D-19-0212.1, 2020.

Menke, R., Vasiljević, N., Mann, J., and Lundquist, J. K.: Characterization of flow recirculation zones at the Perdigão site using multi-lidar measurements, Atmos. Chem. Phys., 19, 2713–2723, https://doi.org/10.5194/acp-19-2713-2019, 2019.

Molter, C. and Cheng, P. W.: ANDroMeDA – A Novel Flying Wind Measurement System, J. Phys. Conf. Ser., 1618, 032049, https://doi.org/10.1088/1742-6596/1618/3/032049, 2020.

Neisser, J., Adam, W., Beyrich, F., Leiterer, U., and Steinhagen, H.: Atmospheric boundary layer monitoring at the Meteorological Observatory Lindenberg as a part of the "Lindenberg Column": Facilities and selected results, Meteorol. Z., 11, 241–253, 2002.

Neumann, P. P. and Bartholmai, M.: Real-time wind estimation on a micro unmanned aerial vehicle using its inertial measurement unit, Sensor. Actuat. A-Phys., 235, 300–310, https://doi.org/10.1016/j.sna.2015.09.036, 2015.

Neumann, P. P., Asadi, S., Lilienthal, A., Bartholmai, M., and Schiller, J.: Autonomous Gas-Sensitive Microdrone: Wind Vector Estimation and Gas Distribution Mapping, IEEE Robot. Autom. Mag., 19, 50–61, https://doi.org/10.1109/mra.2012.2184671, 2012.

Nolan, P., Pinto, J., González-Rocha, J., Jensen, A., Vezzi, C., Bailey, S., de Boer, G., Diehl, C., Laurence, R., Powers, C., Foroutan, H., Ross, S. D., and Schmale, D. G.: Coordinated Unmanned Aircraft System (UAS) and Ground-Based Weather Measurements to Predict Lagrangian Coherent Structures (LCSs), Sensors, 18, 4448, https://doi.org/10.3390/s18124448, 2018.

Palomaki, R. T., Rose, N. T., van den Bossche, M., Sherman, T. J., and Wekker, S. F. J. D.: Wind Estimation in the Lower Atmosphere Using Multirotor Aircraft, J. Atmos. Ocean. Tech., 34, 1183–1191, https://doi.org/10.1175/jtech-d-16-0177.1, 2017.

Platis, A., Siedersleben, S., and Bange, J. E. A.: First in situ evidence of wakes in the far field behind offshore wind farms, Sci. Rep., 8, 2163, https://doi.org/10.1038/s41598-018-20389-y, 2018.

Rajewski, D. A., Takle, E. S., Lundquist, J. K., Oncley, S., Prueger, J. H., Horst, T. W., Rhodes, M. E., Pfeiffer, R., Hatfield, J. L.,

Spoth, K. K., and Doorenbos, R. K.: Crop Wind Energy Experiment (CWEX): Observations of Surface-Layer, Boundary Layer, and Mesoscale Interactions with a Wind Farm, B. Am. Meteorol. Soc., 94, 655–672, https://doi.org/10.1175/BAMS-D-11-00240.1, 2013.

Reuter, M., Bovensmann, H., Buchwitz, M., Borchardt, J., Krautwurst, S., Gerilowski, K., Lindauer, M., Kubistin, D., and Burrows, J. P.: Development of a small unmanned aircraft system to derive CO_2 emissions of anthropogenic point sources, Atmos. Meas. Tech., 14, 153–172, https://doi.org/10.5194/amt-14-153-2021, 2021.

Schiano, F., Alonso-Mora, J., Rudin, K., Beardsley, P., Siegwart, R., and Sicilianok, B.: Towards Estimation and Correction of Wind Effects on a Quadrotor UAV, in: IMAV 2014: International Micro Air Vehicle Conference and Competition 2014, 12–15 August 2014, Delft, the Netherlands, 134–141, https://doi.org/10.3929/ethz-a-010286793, 2014.

Shimura, T., Inoue, M., Tsujimoto, H., Sasaki, K., and Iguchi, M.: Estimation of Wind Vector Profile Using a Hexarotor Unmanned Aerial Vehicle and Its Application to Meteorological Observation up to 1000 m above Surface, J. Atmos. Ocean. Tech., 35, 1621–1631, https://doi.org/10.1175/jtech-d-17-0186.1, 2018.

Thielicke, W., Hübert, W., Müller, U., Eggert, M., and Wilhelm, P.: Towards accurate and practical drone-based wind measurements with an ultrasonic anemometer, Atmos. Meas. Tech., 14, 1303–1318, https://doi.org/10.5194/amt-14-1303-2021, 2021.

Veers, P., Dykes, K., Lantz, E., Barth, S., Bottasso, C. L., Carlson, O., Clifton, A., Green, J., Green, P., Holttinen, H., Laird, D., Lehtomäki, V., Lundquist, J. K., Manwell, J., Marquis, M., Meneveau, C., Moriarty, P., Munduate, X., Muskulus, M., Naughton, J., Pao, L., Paquette, J., Peinke, J., Robertson, A., Sanz Rodrigo, J., Sempreviva, A. M., Smith, J. C., Tuohy, A., and Wiser, R.: Grand challenges in the science of wind energy, Science, 366, 6464, https://doi.org/10.1126/science.aau2027, 2019.

Wang, J.-Y., Luo, B., Zeng, M., and Meng, Q.-H.: A Wind Estimation Method with an Unmanned Rotorcraft for Environmental Monitoring Tasks, Sensors, 18, 4504, https://doi.org/10.3390/s18124504, 2018.

Wilczak, J. M., Stoelinga, M., Berg, L. K., Sharp, J., Draxl, C., McCaffrey, K., Banta, R. M., Bianco, L., Djalalova, I., Lundquist, J. K., Muradyan, P., Choukulkar, A., Leo, L., Bonin, T., Pichugina, Y., Eckman, R., Long, C. N., Lantz, K., Worsnop, R. P., Bickford, J., Bodini, N., Chand, D., Clifton, A., Cline, J., Cook, D. R., Fernando, H. J. S., Friedrich, K., Krishnamurthy, R., Marquis, M., McCaa, J., Olson, J. B., Otarola-Bustos, S., Scott, G., Shaw, W. J., Wharton, S., and White, A. B.: The Second Wind Forecast Improvement Project (WFIP2): Observational Field Campaign, B. Am. Meteorol. Soc., 100, 1701–1723, https://doi.org/10.1175/BAMS-D-18-0035.1, 2019.

Wildmann, N., Rau, G. A., and Bange, J.: Observations of the Early Morning Boundary-Layer Transition with Small Remotely-Piloted Aircraft, Bound.-Lay. Meteorol., 157, 345–373, https://doi.org/10.1007/s10546-015-0059-z, 2015.

Wildmann, N., Vasiljevic, N., and Gerz, T.: Wind turbine wake measurements with automatically adjusting scanning trajectories in a multi-Doppler lidar setup, Atmos. Meas. Tech., 11, 3801–3814, https://doi.org/10.5194/amt-11-3801-2018, 2018.

A.2 Spatially distributed and simultaneous wind measurements with a fleet of small quadrotor UAS

This publication can be found at
`https://iopscience.iop.org/article/10.1088/1742-6596/2265/2/022086/meta`.

Spatially distributed and simultaneous wind measurements with a fleet of small quadrotor UAS

Tamino Wetz [1], Norman Wildmann [1]

[1] Deutsches Zentrum für Luft- und Raumfahrt e.V., Institut für Physik der Atmosphäre, Oberpfaffenhofen, Germany

E-mail: `tamino.wetz@dlr.de`

Abstract. The understanding of micro-scale flow in the atmospheric boundary layer is one major challenge in wind energy research. Besides the broad possibilities of numerical simulations, experimental data are necessary for tests of the flow conditions within a wind farm under real conditions. In wind energy and atmospheric science, a variety of measurement devices exist for measuring the wind speed. We propose a measurement system that enables completely flexible simultaneous wind measurements using a fleet of multirotor unmanned aircraft systems (UAS). This approach is validated through a two-week measurement campaign at the boundary layer field site Falkenberg of the German National Meteorological Service (DWD). The wind speed is calculated from UAS motions in hover state without additional wind sensors. The measurements are calibrated and validated against sonic anemometers mounted at a 99 m mast. The capability of highly accurate spatial distributed wind measurement with an improved wind algorithm is proven by a root mean square error (RMSE) of 0.25 ms^{-1} for the horizontal wind speed and $< 5°$ for the wind direction. Further, turbulence measurements are presented showing valid results up to a frequency of 2 Hz in high turbulence conditions. Additionally, spatially horizontal distributed measurements with multiple UAS are examined in a case study of a gust front event.

1. Introduction

One of the major challenges in the science of wind energy is the understanding of micro-scale flow conditions within a wind farm [1]. A variety of measurement techniques exist, which qualify for studying the wind conditions in the inflow and wake of wind turbines (WT). Among these are meteorological masts [2], Doppler wind lidar (DWL) [3], or manned [4] as well as unmanned [5] airborne in-situ measurements. All of these systems provide wind measurements with good accuracy, but they are all limited in the flexibility to measure at multiple positions at the same time. We established a system to achieve simultaneous spatial measurements with a fleet of multirotor UAS, the so-called SWUF-3D fleet (Simultaneous Wind Measurements with Unmanned Flight systems in 3D). The major benefit of this approach is, that true simultaneous measurements can be achieved without the need of expensive infrastructure, such as masts or multiple DWL. A possible scenario which thus becomes available for wind energy research is the in-situ measurement of 2-D flow fields of the inflow and wake of a wind turbine.

For single UAS multirotor wind measurement, different approaches exist. First, external wind sensors can be installed at the UAS, such as sonic anemometers [6],[7],[8] or hot wire probes [9],[10]. The second approach is based on the on-board avionic sensors of UAS and relates the

motion of the UAS to the wind [11, 12, 13, 14, 15]. The advantage of an additional wind sensor on the UAS is that theoretically, small scales can be resolved more accurately. However, the motion of the UAS and the disturbance of the wind by the induced air flow from the rotors need to be considered. The additional payload also decreases the flight time. The abdication of additional wind sensors reduces the complexity of the system, which becomes relevant by scaling towards a fleet of UAS measurement devices. Therefore, in the present study the second approach is preferred. The developed algorithm to obtain horizontal wind speed and direction is designed for hovering conditions and is based on the principle of aerodynamic drag and the related quadrotor dynamics. In Sect. 2, the experiment, the improved wind algorithm and the strategy for fleet operation are explained. Section 3 shows the results of the validation of the wind algorithm, temporal resolution of measurements with single UAS and a case study of the fleet measurement within a gust front.

2. Methodology

At the boundary layer field site (Grenzschichtmessfeld, GM) Falkenberg of the Meteorological Observatory Lindenberg - Richard Aßmann-Observatory (MOL-RAO), two campaigns were carried out associated to the FESST@MOL 2020 and the FESSTVaL 2021 activities at the MOL-RAO. With data from the FESST@MOL 2020 experiment, we compared the spatial distribution of horizontal wind in main wind direction, as obtained from the UAS fleet to tower vertical profiles and DWL scans before [16]. In order to calculate turbulence parameters which are essential to understand loads and wake dynamics of WT, it is desirable to measure with high temporal resolution in all three dimensions. In the next step of development in this study, we extend the wind algorithm by the lateral wind component. We also focus on second order statistics and improve the accuracy and temporal resolution by taking additional sensor data into account.

2.1. Experiment description

In June/July 2021 the UAS fleet was deployed for two weeks within the FESSTVaL (Field Experiment on submesoscale spatio-temporal variability in Lindenberg) campaign at MOL-RAO. The data presented in this study was collected during this period. Our goal for the campaign was the calibration and validation of the fleet, and additionally the investigation of turbulence structures with spatially distributed measurements. On the map of the field site in Fig. 1, the 99 m met mast and the different flight pattern, consisting of multiple UAS, are marked. In the map, only the designated measurement positions of the UAS in the hovering state are marked, excluding the flight path from take-off and towards landing. In wind directions between $330-50°$ flow distortion from the tower corrupts the sonic measurements. These directions were excluded from the dataset. For more details on the facilities of the measurement site we refer to Neisser et al. (2002) [17]. In order to calibrated and validate the UAS fleet, we operated multiple UAS in the corresponding altitudes of the sonic anemometer measurements in 50 m and 90 m altitude. In the "calibration pattern", as illustrated in the map in Fig. 1, the UAS are horizontally distributed perpendicular to the dominant wind direction which is from the west in this campaign. Due to safety considerations with regard to mast instrumentation and UAS, the horizontal distance of the UAS to the tower is restricted to a minimum of 20 m. Additionally, in this study we will discuss flights from the "horizontal pattern", with the purpose of turbulence structure analysis. During the complete campaign the UAS are operated in the weather vane mode, which controls the yaw angle in order to orientate the quadrotor towards the wind direction. This feature simplifies and increases the accuracy of the wind algorithm, due to more similar relative inflow of the wind towards the quadrotor, resulting in less variability of the aerodynamic drag. The hardware and software have not changed significantly compared to the 2020 campaign so that we refer to Wetz et al. (2021) [16] for more details.
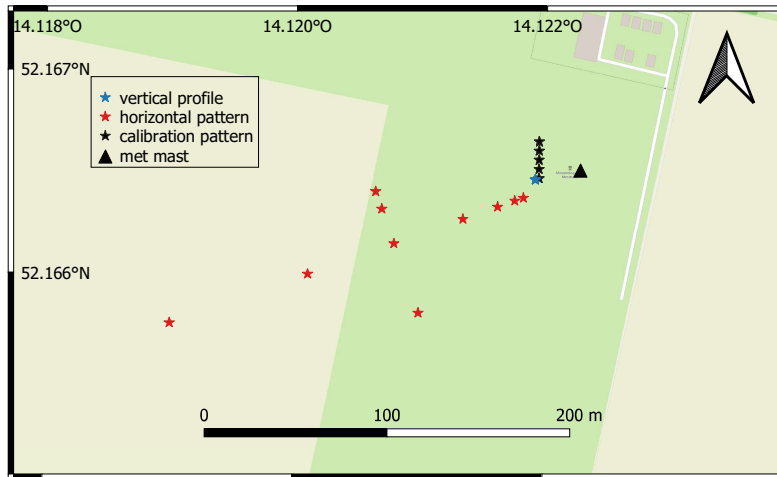
Figure 1. Map of the field site of Falkenberg including the 99 m met mast and different flight patterns of the UAS-fleet. Each star representing an individual UAS at its measurement position. The dark green area is short cut grass, whereas the light green area was a cornfield in 2021. Background map ©OpenStreetMap contributors 2022. Distributed under a Creative Commons BY-SA License.

2.2. Basic equations of quadrotor dynamics

The basis for the calculation of the horizontal wind vector from multicopter data is the equation of motion in longitudinal (x) Eq. (1) and lateral (y) direction Eq. (2) in the body frame of the UAS. Here, g represents the acceleration due to gravity and m the mass of the UAS. The position vector $\mathbf{X_b}$ of the UAS is defined in Eq. (3), the angular velocities $\omega_\mathbf{b}$ and the vector of attitude angles $\mathbf{\Phi_i}$, also known as Euler angles, are defined in Eq. (4) and Eq. (5) respectively. The Euler angles are defined as rotation around the longitudinal axis represented by roll angle ϕ, around the lateral axis as pitch angle θ and around the vertical axis as yaw angle ψ. The wind forces are defined as $\mathbf{F_w}$ in the corresponding directions, x represents the longitudinal and y the lateral direction in the body frame.

$$m(\ddot{x} + q\dot{z} - r\dot{y}) \quad = \quad -mg[\sin(\theta)] + F_{w,x} \tag{1}$$

$$m(\ddot{y} + p\dot{z} - r\dot{x}) \quad = \quad -mg[\cos(\theta)\sin(\phi)] + F_{w,y} \tag{2}$$

$$\mathbf{X_b} \quad = \quad \begin{bmatrix} x & y & z \end{bmatrix}^T \tag{3}$$

$$\omega_\mathbf{b} \quad = \quad \begin{bmatrix} p & q & r \end{bmatrix}^T \tag{4}$$

$$\mathbf{\Phi_i} \quad = \quad \begin{bmatrix} \phi & \theta & \psi \end{bmatrix}^T \tag{5}$$

In a first approach the wind forces were calculated according to Wetz et al. (2021) [16], assuming zero motion of the UAS during hovering (see Eq. (6)). In this case, the wind forces are only a function of the Euler angles. The wind forces lateral to the orientation of the UAS are calculated from the roll angle ϕ and the pitch angle θ (Eq. (7)). We now consider the dynamic part of the equation of motion to not be negligible, even in the hover state, but acceleration of the UAS is taken into account for the calculation of the horizontal wind forces (Eq. (8)). Through this, we attempt to increase the accuracy of the wind algorithm especially in the small scales with a better representation of the dynamic behaviour of the UAS. In particular, the linear acceleration in longitudinal and lateral body direction is considered. The accelerometer of the

inertial measurement unit (IMU) measures the acceleration of motion in the three body axis, including the acceleration due to gravity. Alternatively, the derivative of the UAS velocity in the earth frame, as measured by GPS, can be used as linear acceleration after the transformation to the body frame of the UAS. The contribution of gyroscopic terms in Eq. (1,2) is still negligible, since the variances of those terms are two orders of magnitude smaller than the variance of the linear acceleration.

$$F_{w,h,x} = mg[\sin(\theta)] \tag{6}$$

$$F_{w,h,y} = mg[\cos(\theta)\sin(\phi)] \tag{7}$$

$$F_{w,x} = m[g\sin(\theta) + \ddot{x}] \tag{8}$$

$$F_{w,y} = m[g\cos(\theta)\sin(\phi) + \ddot{y}] \tag{9}$$

The different approaches for the wind forces calculation are compared in Fig. 2a). In this figure the power spectrum density of the forces from the first approach, using only the Euler angles (Eq. 6), are compared with the second approach including linear acceleration (Eq. 8), derived from GPS data ($F_{w,x,g}$) and from the accelerometer ($F_{w,x,a}$). The spectral densities are averaged over frequency bins for better visualisation in the figure. The unfiltered data is shown in light grey. The spectrum shows that the wind forces, calculated from the Euler angles of the internal extended Kalman filter (EKF) attitude estimation, follows the theoretical slope of $k^{-5/3}$ Kolmogorov's-law in the inertial subrange of turbulent flows only until approximately 0.5 Hz. The extended Kalman filter (EKF) of the autopilot estimates the dynamic states of the UAS through sensor fusion of inertial and navigation data. However, in this process there are also filters applied to the data. The shape in smaller scales of the Euler angles indicates prior internal filtering of the sensor data. The spectrum of the accelerometer data are aligned to Kolmogorov's-law until 2 Hz, within higher frequencies the noise level dominates. The GPS data show similar behaviour but deviate from the $k^{-5/3}$-slope at 2 Hz already significantly. Due to this, we focus on sensor data from the accelerometers for further processing.
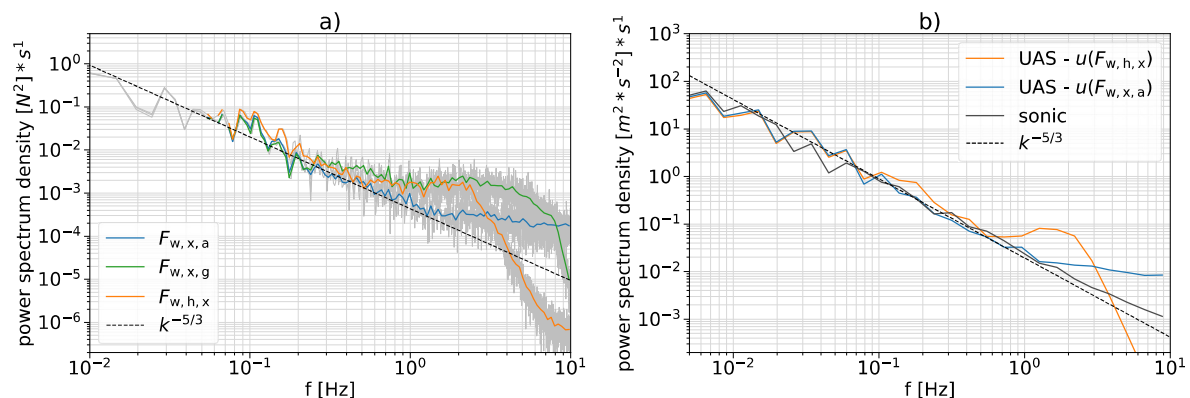
Figure 2. Power spectrum density in longitudinal direction - a) of the wind forces: $F_{w,h,x}$ hover state assumption, $F_{w,x,a}$ including acceleration from the accelerometer, $F_{w,x,g}$ including acceleration from the derived GPS velocity; b) of the wind velocity for different algorithm approaches of UAS measurements in comparison with sonic anemometer data (flight case no. 1 in Table 2).

Table 1. Specification of wind algorithm parameters (proportional parameter c and exponent b).

| direction	c	b
longitudinal (x)	7.775	0.845
lateral (y)	6.373	0.898

2.3. Wind vector calibration

The horizontal wind vector $\mathbf{V}$ in the body frame is calculated from the horizontal wind forces using the relationship as described in Eq. (10). In this work, we choose an approach with an unknown exponent b for calibration in contrast to previous work where the Rayleigh drag equation was chosen, which yields $b = 0.5$. The composition of aerodynamic drag of quadrotors is complex, besides the profile and friction losses of the UAS frame, a dominant part of the drag results from the rotor dynamics [18]. The approximation of the relation between wind forces and wind speed with a variable exponent allows, in this case, a more accurate approximation of the calibration curve than the Rayleigh drag equation.

$$\mathbf{V} = \left(\begin{array}{c} u \\ v \end{array} \right) = \left(\begin{array}{c} c_x \cdot F_{\mathrm{w,x}}^{b_x} \\ c_y \cdot F_{\mathrm{w,y}}^{b_y} \end{array} \right) - \left(\begin{array}{c} \dot{x}_{gps} \\ \dot{y}_{gps} \end{array} \right) \tag{10}$$

The calibration dataset consists of 119 calibration flights from the two weeks of the campaign. This includes wind speed ranges from almost 0 up to 8 ms^{-1} with turbulent kinetic energy (TKE) levels from 0.03 to 2.5 $\mathrm{m^2 s^{-2}}$. As it can be seen from Fig. 2, the data are corrupted by noise in the small scales, so that in post-processing, the measurement data are low-pass filtered at 2 Hz in the frequency domain. For the calibration of the wind speed in the body system, the horizontal wind vector is divided into a longitudinal and lateral component aligned to the orientation of the UAS. The calibration target values for the longitudinal wind component are 2 s average wind speeds of the corresponding sonic anemometer measurements. The short average time compared to Wetz et al. (2021) [16] is chosen for better statistics in the calibration of the velocity variance. First, the proportional parameter c_x and the exponent b_x of Eq. (10) are calculated for one specific UAS with the widest range of calibration flights. Similar to previous work, we assume equivalent aerodynamic behaviour within the UAS fleet, so that the calculated parameters for one UAS are valid for the complete UAS-fleet. The calibrated parameters are listed in Table 1. Additionally, offset values for the input parameter pitch $\Delta\theta$, respectively the acceleration Δa, are individually calculated for each UAS of the fleet with only one flight per UAS. The difference between the approaches assuming hover state on the one hand and taking accelerometer data into account on the other hand is shown in the time series of the longitudinal velocity in Fig. 3. It is noticeable that some peaks, that are pronounced with the hover state assumption, are reduced with the acceleration approach, which thus reproduce the dynamic behavior of the reference measurement more realistically. This behaviour can be confirmed with the power spectrum of the longitudinal velocity in Fig. 2, where an overestimation of the energy level in the small scales is visible.

  For the calibration of the parameter in lateral direction, the variance σ_v^2 of the single flights is chosen as target value. The mean value of the lateral wind component is not expedient because of the weather-vane mode, which orientates the UAS in wind direction and thus leads to only small absolute values of the lateral wind speed v. Identical to the calibration of the longitudinal wind component, the parameters c_y and b_y are first calibrated for a single UAS and individual offsets for the roll angle are determined for each UAS in a further step. For both directions, the wind estimation is corrected with the UAS velocity measured by the GPS-System ($\dot{x}_{gps}, \dot{y}_{gps}$). Due to the hover state, the magnitude of the GPS velocity is small and only has a minor influence
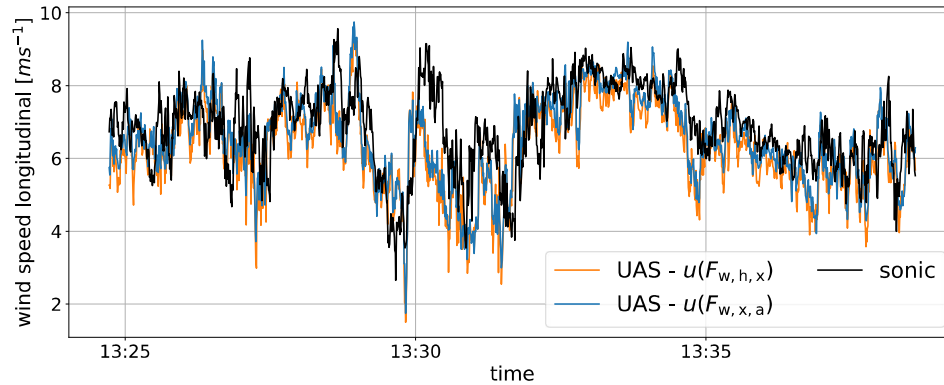
Figure 3. Time series of the longitudinal wind velocity for different algorithm approaches of UAS measurements in comparison with sonic anemometer data - $F_{w,h,x}$ hover state assumption, $F_{w,x,a}$ including acceleration from the accelerometer (flight case no. 1 of Table 2).

on the results in some peaks of the GPS velocity (max $|v_{gps}| = 0.3$ ms^{-1}, $\sigma_{gps} < 0.003$ m^{2}s^{-2}). In order to rotate the body-frame wind speeds into the geodetic coordinate system, the yaw angle ψ of the UAS is crucial and also needs an offset calibration due to possible errors in the initial calibration of the magnetometers on site. An individual yaw angle offset $\Delta\psi$ for each UAS is calculated from the difference to the reference wind direction which is calculated from the sonic anemometers (Eq. 11). The wind direction in the geodetic frame Φ_w is the corrected yaw angle ψ_c plus the misalignment of the UAS towards the wind direction, which can be calculated as the tangent of the lateral v and longitudinal wind component u in the body frame (Eq. 12). In Fig. 4 the results of the different steps of the wind direction calculation are shown in comparison to reference measurements. It is clearly visible that the dynamic behaviour of the final wind direction calculation follows the reference measurement best. For that particular flight the standard deviation σ of the corrected yaw angle results in $\sigma_{\psi,c} = 9.0°$, whereas the corrected wind direction yields $\sigma_{\Phi,w} = 12.1°$, which confirms the improved dynamic behaviour in comparison to the sonic measurements $\sigma_{\Phi,w,sonic} = 12.5°$.

$$\psi_c = \psi + \Delta\psi \tag{11}$$

$$\Phi_w = \psi_c + \tan(v/u) \tag{12}$$

2.4. Fleet operation

During the campaign we managed to operate 20 UAS simultaneously. The fleet is controlled by a ground station, which is connected to the fleet of UAS through Wifi. Besides the monitoring of the fleet, the ground station operator can also initiate contingency and emergency procedures through the software. Two further remote pilots are employed to observe a maximum of 10 UAS and report unusual behaviour. They can also take control of single UAS if necessary. The specific mission flight patterns for each UAS are planned and uploaded prior to operation. The patterns are generated semi-automatically in order to be able to update the pattern on short notice. This allows the adaption of the mission to current atmospheric conditions, as it was practiced with the "horizontal pattern" to study the turbulence at distributed points along and perpendicular to the main wind direction. With the current setup the flight time for a single UAS is approximately limited to 15 minutes and measurement time needs to be adapted according to the distance of the hover positions to the take-off location, which defines the flight time including.
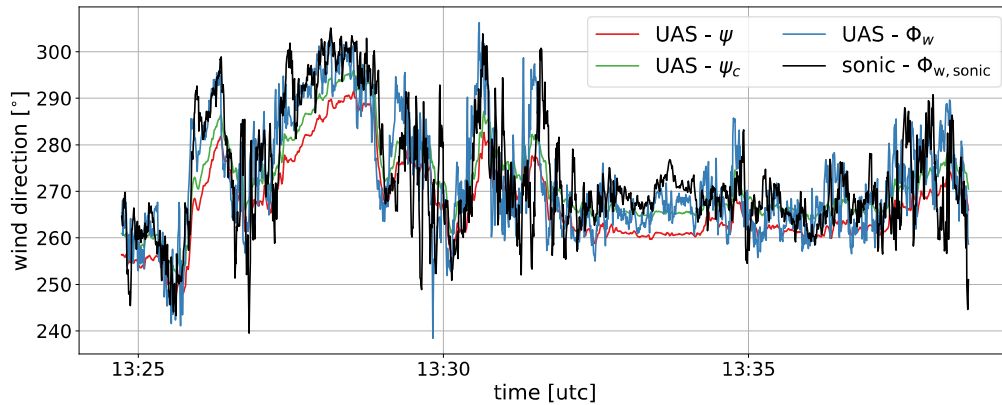
Figure 4. Time series of wind direction for different algorithm approaches of UAS measurements in comparison with sonic anemometer data (flight case no. 1 of Table 2) [ψ: raw yaw angle, ψ_c: calibrated yaw angle, Φ_w: calibrated and with the lateral wind speed corrected wind direction].

However, the measurement time can be significantly increased by replacing the current UAS at the measurement position by a fully charged UAS in flight. If an overlap at the measurement position is guaranteed, continuous measurements at multiple position can be realized. During the campaign, we thus performed vertical profile measurements at five height levels for more than 4 hours continuously during a morning transition of a convective boundary layer. Furthermore, a measurement time of more than 40 min with the "horizontal pattern" was achieved by replacing 10 UAS twice.

3. Results

3.1. Calibration

In order to produce reliable calibrations and quantification of the measurement accuracy, we performed calibration flights with each UAS of the fleet at different atmospheric conditions. The results of 119 single UAS calibration flights are shown in the scatter plots in Fig. 5. The measurement data used for the calibration are excluded in the results to ensure an independent dataset for the validation of the UAS fleet. Each data point represents the time average of one flight versus the sonic anemometer average for the same time. The wind vector is calculated with the improved algorithm including the accelerometer data. In Fig. 5a, the mean longitudinal velocity of the UAS measurement is shown to be in good agreement with the reference in a broad range of wind speeds. A mean RMSE of $\epsilon_u = 0.25$ ms^{-1} is achieved. Compared to the approach with the hover state assumption (RMSE of $\epsilon_u = 0.3$ ms^{-1}), the accelerometer approach could increase the accuracy. In particular, the accuracy of the wind speed variance (Fig. 5b) with an RMSE of $\epsilon_{\sigma^2,u} = 0.16$ m^{2}s^{-2} is improved significantly. Furthermore, the variance of the lateral wind component is reproduced with an RMSE to the reference measurement of $\epsilon_{\sigma^2,v} = 0.08$ m^{2}s^{-2} (Fig. 5c). The additional correction of the wind direction with the lateral and longitudinal wind component results in an average RMSE of less than $\epsilon_{\Phi,w} < 5°$ (Fig. 5 d).

3.2. Turbulence analyses

To evaluate the performance of the UAS measurements in different atmospheric conditions and especially with regards to their capabilities to resolve turbulence, four different flights are examined in more detail. The cases were selected in order to cover a range of possible different atmospheric conditions, from stable to unstable atmospheric stratification, high and low turbulence. Flight no. 1 was performed during convective conditions in the late afternoon.
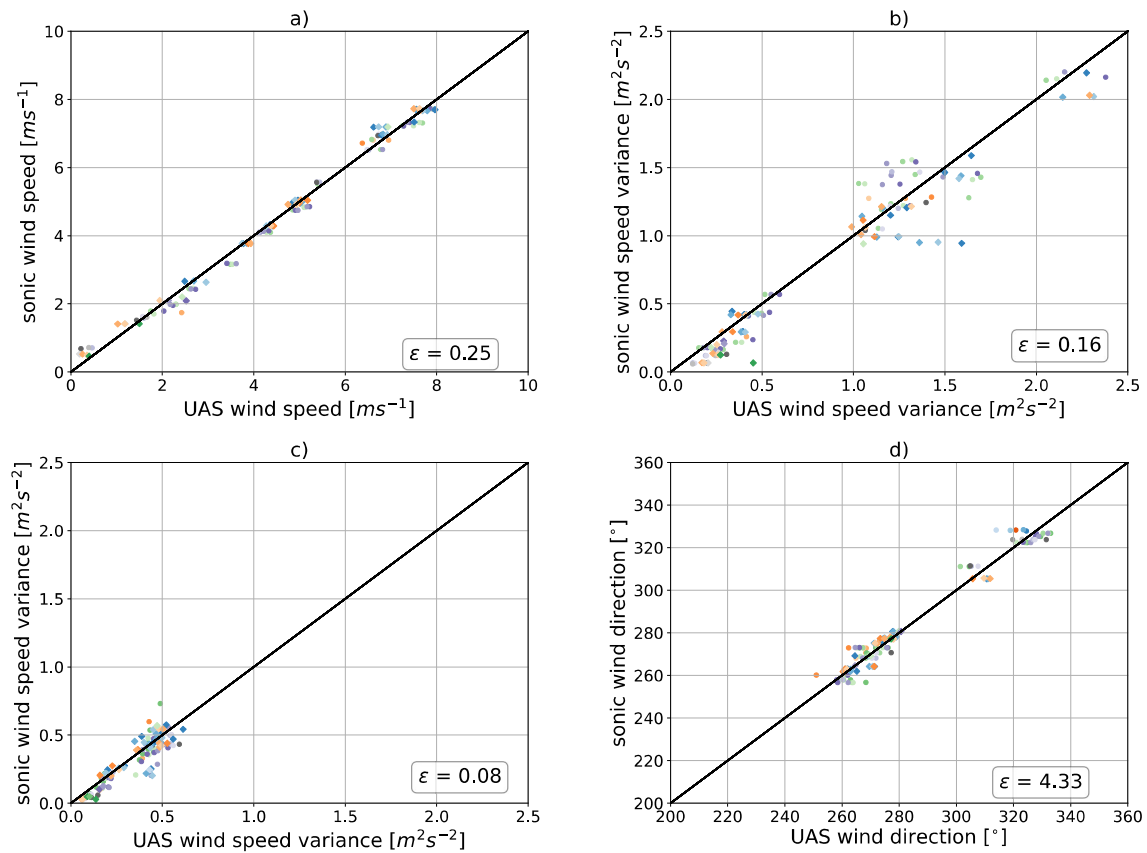
Figure 5. Flight averaged data for all calibration flights, different colors and markers representing different UAS (no. 2-35) measurements in comparison to sonic anemometer wind measurements including the RMSE ϵ : a) longitudinal wind speed, b) longitudinal wind speed variance, c) lateral wind speed variance, d) wind direction.

Table 2. Specification of four case studies (mean horizontal wind speed $\overline{V_w}$, horizontal variance $\sigma_{u,v}^2$).

case no.	date	time [utc]	$\overline{V_w}$ [ms^{-1}]		$\sigma_{u,v}^2$ [m^{2}s^{-2}]		characterisation
			sonic	UAS	sonic	UAS	
1	02/07/2021	13:22	6.88	6.54	2.01	1.89	convective
2	30/06/2021	14:57	7.27	7.21	1.73	1.65	shear turbulence
3	28/06/2021	3:54	6.76	6.49	0.15	0.17	low level jet
4	26/06/2021	9:50	1.64	1.74	0.10	0.24	low wind speed

A high level of turbulence is present in flight no. 2 which is however more shear-driven. The mean wind speed during the morning transition in flight no. 3 was high due to a low level jet event at the top of the nighttime inversion layer, but the turbulence intensity in the LLJ is significant smaller than in case 1 and 2 due to the strong static stability. The last case, flight no. 4, represents a day with very low wind speeds. The different flights and the respective wind speed and turbulence conditions in the form of horizontal wind speed variance $\sigma_{u,v}^2$ are listed in Table 2. The comparison of the power spectrum density of horizontal wind speed between the four flight cases in Fig. 6 demonstrates the different turbulence conditions during the flights.

Case no. 1 and 2 with high turbulence levels show a pronounced inertial subrange that follows the Kolmogorov-law within the regarded scales up to 2 Hz. In contrast, the low turbulence cases no. 3 and 4 show that in such conditions even the sonic anemometer spectra are flatter than $k^{-5/3}$. As emphasized in section 2.3, the UAS sensors are limited in resolving small scales. This limitation is more pronounced in low turbulence conditions, where the energy level of the complete spectrum is lower. The noise level of the UAS data has an almost constant energy density level of about 0.01 $\mathrm{m^2s^{-1}}$, which results in an additional variance of $\sigma^2_{\mathrm{noise}} \approx 0.1$ $\mathrm{m^2s^{-2}}$ assuming a constant noise level in the complete frequency domain. Therefore, in low turbulence condition the noise of the sensor dominates even at lower frequencies and corrupts the turbulence measurement. The case studies outline that in conditions with wind speed variances of the order of 0.3 $\mathrm{m\,s^{-1}}$ or smaller, the resolution of turbulence is not possible with the current system. The temporal resolution in low wind speed could potentially be improved by more accurate accelerometers, or by the reduction of the noise level due to vibration of the system. Additionally, the dimension of the quadrotor limits the resolvable scales, such that even smaller multicopters could lead to improved temporal resolution regarding the small scales.
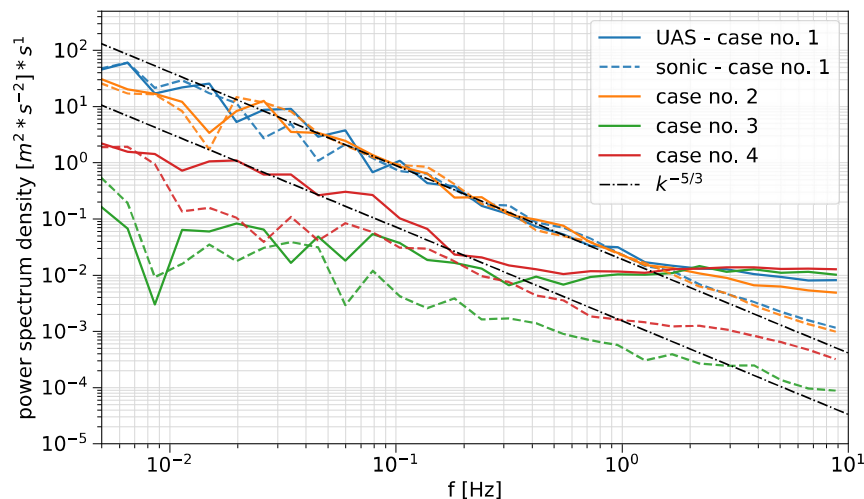
Figure 6. Power spectrum density of the wind velocity measurement from the UAS and the corresponding sonic anemometers for the four defined flight cases. Solid lines represent UAS measurements, dashed lines sonic anemometer measurements.

3.3. Distributed measurements in a gust front

In addition to the calibration flights, one flight of the horizontal pattern is shown in Fig. 7. In that flight, ten UAS hovered at 50 m AGL while a gust front, associated to a convective cell approximately 8 km east of the site, hit the site with wind speeds up to 15 $\mathrm{m^2s^{-2}}$. In the map, each UAS with its measured wind vector is drawn at the time marked in the time series below with the green vertical line. The gust from the east approaches the UAS pattern and appears first at the sonic anemometer (black arrow) and UAS #22 (blue) in the east before it reaches the most western UAS #28 (red) with a delay of almost 20 s. This corresponds to an advection velocity of 10 $\mathrm{m^2s^{-2}}$ for the 200 m distance between the quadrotors. Considering a WT with a rotor diameter of 100 m at the location of UAS #28, the UAS are distributed in wind direction in an area corresponding to two rotor diameters (2 D), and at a distance of 1 D, three more UAS are positioned perpendicular to the wind direction. It is obvious that the flow field is far from uniform during an event like this. This demonstrates the challenges for WT controllers and

the corresponding operational wind measurement systems, e.g. lidars, to provide a meaningful control variable. A more detailed analysis of the flow structure during this event is beyond the scope of this paper, but will be presented in a future publication.
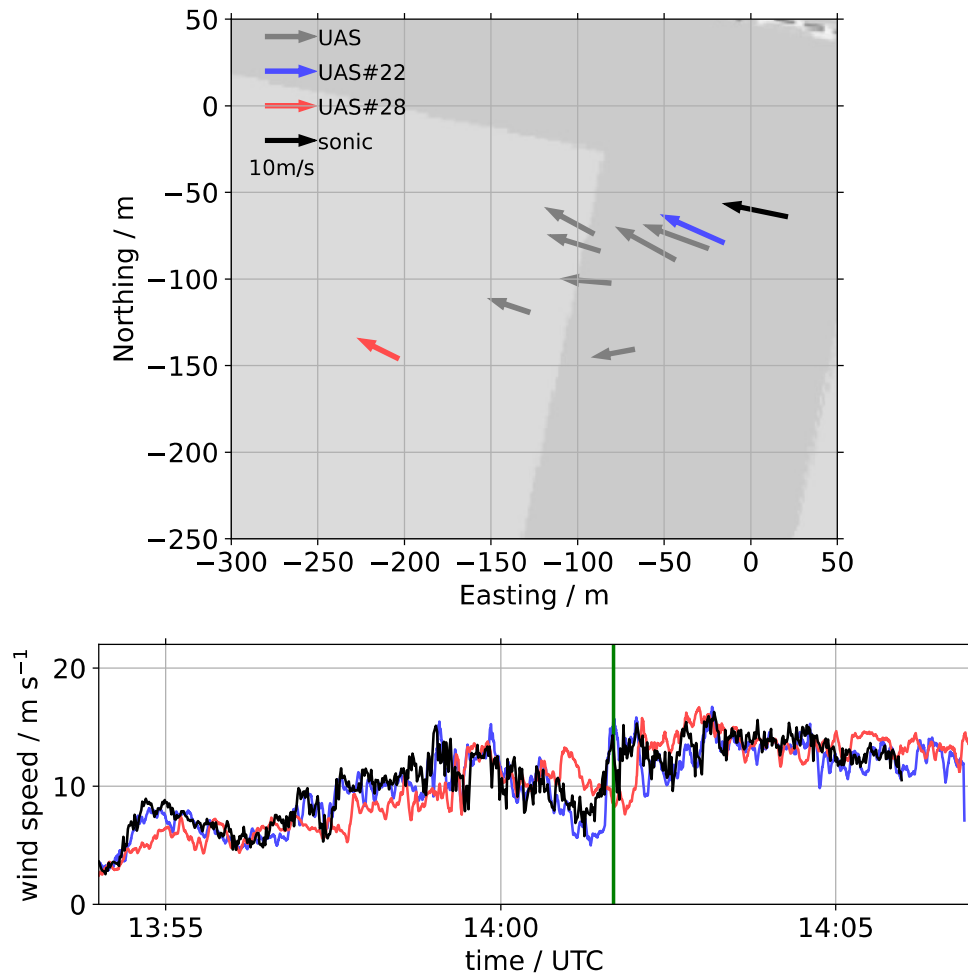
Figure 7. Time series of horizontal wind speed measurements during an incoming gust front of a cold pool event for the horizontal flight pattern. The map shows the distributed measurements of the wind vector of 9 UAS hovering at 50 m (light grey, blue and red). The time series below gives the corresponding horizontal wind speeds for the two outermost quadrotors and the sonic anemometer at the meteorological mast.

4. Conclusions

Within a two-week campaign in summer 2021, we demonstrated the capability of the SWUF-3D UAS fleet to measure the horizontal wind vector with high temporal resolution at spatially distributed measurement points. The improvement and the extension of the wind algorithm compared to previous versions is demonstrated. Besides the adapted calibration for improvements of variance measurements, the calculation of the lateral wind component is introduced. That enables additional corrections of the wind direction, which particularly improved the dynamic response of the measurement. Overall, the revised algorithm results in an RMSE of $\epsilon_{\overline{u}} =$

0.25 ms^{-1} for the mean wind speed of 119 calibrations flights and $\epsilon_{\sigma^2,u} = 0.16$ m^{2}s^{-2} for the RMSE of the variance. Additionally, a high accuracy for the wind direction is achieved with an RMSE of $\epsilon_{\Phi,w} < 5°$.

The capabilities and limitations of the measurement system for turbulence measurements are demonstrated with four exemplary cases. We show that there is a lower limit of the scales that can be resolved with the SWUF-3D quadrotors. Limitations by sensor noise and rotor induced flow distortion do not allow a good resolution of the turbulence spectrum in conditions with wind speed variances of the order of 0.3 m s^{-1} or smaller and at frequencies higher than 2 Hz. This is especially critical in stable atmospheric conditions where turbulence is generally low and intermittent. For applications which are most relevant for wind energy production, the measurements by the fleet and its resolvable scales can be of great benefit to analyse inflow and wake of WTs. Furthermore, the capability of accurate wind measurements in a broad range of wind velocities during gusty conditions is demonstrated with a horizontal flight pattern during the FESSTVaL campaign. This particularly shows the spatial variability of the flow during such an event, with possible implications for WT loads and control.

Acknowledgments

References

[1] Veers P, Dykes K, Lantz E *et al.* 2019 *Science* **366** eaau2027
[2] Rajewski D A *et al.* 2013 *Bulletin of the American Meteorological Society* **94** 655–672 ISSN 0003-0007
[3] Wildmann N *et al.* 2018 *Atmospheric Measurement Techniques* **11** 3801–3814
[4] Platis A, Siedersleben S K, Bange J, Lampert A, Bärfuss K, Hankers R, Cañadillas B, Foreman R, Schulz-Stellenfleth J, Djath B, Neumann T and Emeis S 2018 *Scientific Reports* **8** 2163
[5] Wildmann N, Hofsäß M, Weimer F, Joos A and Bange J 2014 *Advances in Science and Research* **11** 55–61
[6] Shimura T, Inoue M, Tsujimoto H, Sasaki K and Iguchi M 2018 *Journal of Atmospheric and Oceanic Technology* **35** 1621–1631
[7] Thielicke W, Hübert W, Müller U, Eggert M and Wilhelm P 2021 *Atmospheric Measurement Techniques* **14** 1303–1318
[8] Reuter M, Bovensmann H, Buchwitz M, Borchardt J, Krautwurst S, Gerilowski K, Lindauer M, Kubistin D and Burrows J P 2021 *Atmospheric Measurement Techniques* **14** 153–172
[9] Cuxart J, Wrenger B, Matjacic B and Mahrt L 2019 *Atmosphere* **10** 715
[10] Christian M and Po Wen C 2020 *Journal of Physics: Conference Series* **1618** 032049
[11] Palomaki R T, Rose N T, van den Bossche M, Sherman T J and Wekker S F J D 2017 *Journal of Atmospheric and Oceanic Technology* **34** 1183–1191
[12] Neumann P, Asadi S, Lilienthal A, Bartholmai M and Schiller J 2012 *IEEE Robotics & Automation Magazine* **19** 50–61
[13] González-Rocha J, Woolsey C A, Sultan C and Wekker S F J D 2019 *Journal of Guidance, Control, and Dynamics* **42** 836–852
[14] Brosy C, Krampf K, Zeeman M, Wolf B, Junkermann W, Schäfer K, Emeis S and Kunstmann H 2017 *Atmospheric Measurement Techniques* **10** 2773–2784
[15] Bell T M, Greene B R, Klein P M, Carney M and Chilson P B 2020 *Atmospheric Measurement Techniques* **13** 3855–3872
[16] Wetz T *et al.* 2021 *Atmospheric Measurement Techniques* **14** 3795–3814
[17] Neisser J, Adam W, Beyrich F, Leiterer U and Steinhagen H 2002 *Meteorol. Z. (N.F.)* **11** 241–253
[18] Sun S, De Visser C and Chu Q 2018 *Journal of Aircraft* **56** 1–17

A.3 Analyses of Spatial Correlation and Coherence in ABL flow with a Fleet of UAS

RESEARCH ARTICLE

Analyses of Spatial Correlation and Coherence in ABL Flow with a Fleet of UAS

Tamino Wetz[1] · Josef Zink[1] · Jens Bange[2] · Norman Wildmann[1]

Abstract

The spatial structures of turbulent flow in the atmospheric boundary layer (ABL) are complex and diverse. Multi-point spatial correlation measurements can help improve our understanding of these structures and their statistics. In this context, we investigate Taylor's hypothesis and the statistics of spatial structures on the microscale. For the first time, simultaneous horizontally distributed wind measurements with a fleet of 20 quadrotor UAS (unmanned aerial systems) are realized. The measurements were taken at different heights and under different atmospheric conditions at the boundary layer field site in Falkenberg of the German Meteorological Service (DWD). A horizontal flight pattern has been specifically developed, consisting of measurements distributed along and lateral to the mean flow direction with separation distances of 5 . . . 205 m. The validity of Taylor's hypothesis is studied by examining the cross-correlations of longitudinally distributed UAS and comparing them with the auto-correlations of single UAS. To assess the similarity of flow structures on different scales, the lateral and longitudinal coherence of the streamwise velocity component is examined. Two modeling approaches for the decay of coherence are compared. The experimental results are in good agreement with the model approaches for neutral atmospheric conditions, whereas in stable and convective ABL, the exponential approaches are not unconditionally valid. The validation results and the agreement with the literature on coherence in the ABL underline the potential of the UAS fleet for the purpose of spatial turbulence measurements.

Keywords Coherence · Spatial correlation · Taylor's hypothesis · Turbulence · UAS

Tamino Wetz
tamino.wetz@dlr.de

Norman Wildmann
norman.wildmann@dlr.de

[1] Deutsches Zentrum für Luft- und Raumfahrt e.V., Institut für Physik der Atmosphäre, Oberpfaffenhofen, Germany

[2] Center for Applied Geoscience, Eberhard-Karls-Universitaet Tuebingen, Schnarrenbergstr. 94-96, 72076 Tübingen, Germany

Springer

1 Introduction

The characterization of turbulence is a key aspect of understanding the processes within the atmospheric boundary layer (ABL). The size of turbulent eddies spans a broad range of scales, from millimeters to kilometers - a challenge for experimental research. In order to measure turbulence, various techniques exist in atmospheric science. Most prominently, sonic anemometers allow direct measurement of turbulent fluctuations as point measurements (Rajewski et al. 2013; Mauder and Zeeman 2018). More recently, Doppler wind lidars (DWL) have increasingly been used to derive spatial averages of turbulence parameters (Smalikho et al. 2005; Wildmann et al. 2020). However, for studying spatial structures and their temporal evolution, the techniques are limited in their resolution and rely on assumptions about the state of the atmosphere. To deduce spatial information from point measurements, the frozen turbulence assumption from Taylor is applied (Taylor 1938). This hypothesis states that turbulent eddies remain unchanged in a certain domain or for a certain time and are only advected by the mean wind.

Sonic anemometers and DWL are instruments that can provide long-term observations in the field. For short-term campaigns, airborne in-situ measurements with research aircraft are a way to sample the spatial distribution of turbulence. Within the last two decades, measurements with UAS have become more relevant in ABL research because of their flexible deployment and low cost. For in-situ wind measurements, either fixed-wing (Platis et al. 2018; Wildmann et al. 2015) or rotary-wing UAS—particularly multicopters—are deployed. Multicopters can be equipped with external wind sensors, for example sonic anemometers (Shimura et al. 2018) or hot wire probes (Cuxart et al. 2019). But they can also provide horizontal wind estimates without additional sensors (Neumann and Bartholmai 2015). Fixed-wing UAS have the advantage that larger measurement domains can be studied within the same time period. However, multicopters can be deployed without the necessity of runways or landing strips and can provide stationary measurements at the particular point of interest. A big advantage is that wind measurements can be performed simultaneously at multiple positions when multiple UAS are deployed (Wetz et al. 2021).

Taylor's hypothesis has been tested by various experiments using Doppler wind lidar (Schlipf et al. 2010; Higgins et al. 2012) and arrays of sonic anemometer measurements (e.g., in the HATS field observations, Horst et al. 2004). A fleet of UAS enables additional possibilities with regards to flexibility and simultaneous measurements at multiple points. Mizuno and Panofsky (1975) divided the validity of Taylor's hypothesis into two conditions. First, the similarity within the turbulent flow represented by the coherence along the wind should remain unity, and second, the convection velocity of the eddies should be equal to the local velocity. Particularly the first condition concerning the coherence is analyzed in this study.

For studying turbulent structures, a spanwise array of 10 sonic anemometers was installed at the SLTEST facility in western Utah at a unique site with very low surface roughness over a salt flat. Hutchins and Marusic (2007) examined superstructures (also called very large scale motions), extending over 20 boundary layer depths in length, in high-Reynolds numbers by two-point correlations of laterally distributed, streamwise velocity fluctuation measurements. At the same field site Chauhan et al. (2012) studied the change of the structure's inclination angle under different stability conditions. From a two-point correlation map of vertically separated measurements, an elliptical shape can be derived, with the participial axis representing the structure's inclination angle. The results outline an increasing inclination angle with decreasing stability. Salesky and Anderson (2018) used LES for examining very-large-

82

scale motions and the modulation of near-wall processes in the convective ABL. The increase in the inclination angle with decreasing stability is confirmed by their studies. Building on that study, Salesky and Anderson (2019) found the size of the large-scale motions remain unchanged while the stability decreases. The turbulence organization in stable stratified ABL has recently been examined by Heisel et al. (2022) in LES. The ramp-up structures, with a positive inclination angle, can also be found in stable conditions.

Besides the correlation of the time series as a whole, the similarity of flow structures at different scales can be studied by the coherence between spatially distributed measurements. Mathematically, the coherence can be described as the normalized cross-spectrum (detailed description found in Sect. 3.4). If the turbulence was frozen, the coherence would be unity for all scales (Panofsky and Mizuno 1975). The coherence can be experimentally studied by at least two spatially separated time series of velocity fluctuations. In the early 1960s, Davenport (1961) first formulated a model of coherence for atmospheric boundary layer flows. He proposed an exponential decay function of the coherence with increasing frequency f (decreasing eddy size) of the flow structures. The observations are based on vertically separated, streamwise velocity fluctuation measurements. The model predicts an increase of coherence with decreasing separation distances Δz and decreasing mean wind velocity $\bar{u}$. For the scaling of the exponential function, a dimensionless decay parameter a is defined, so that:

$$\gamma_z(f) = \mathrm{e}^{-a \frac{\Delta z}{\bar{u}} f}. \tag{1}$$

This model is still widely applied for coherence estimations in the ABL. Pielke and Panofsky (1970) confirmed the exponential characteristic of the coherence from Davenport (1961) by studying the streamwise and lateral wind components for vertically separated measurements. Applying the same decay approach, they found an increase in coherence with decreasing atmospheric stability.

Ropelewski et al. (1973) examined horizontal coherence at different measurement sites, including different horizontal separations and various instrument heights. They stated an increase in the decay parameter by turning from longitudinal to lateral wind directions, including a stronger dependency for the lateral coherence on atmospheric stratification than for the longitudinal coherence. They found that for stable stratification, the lateral decay parameter tends to be larger than for unstable conditions. However, they used different approaches for the lateral and longitudinal decay parameters. In addition to Davenport's formulation, the lateral coherence of streamwise velocity fluctuations includes the ratio of the longitudinal to the lateral integral length scale. This ratio itself is a function of stability (Panofsky 1962).

Schlez and Infield (1998) studied longitudinal and lateral coherence at separation distances of 62 m and larger at 18 m height above ground. They focused only on near neutral stratified atmospheric conditions. In addition to the Davenport formulation, the dependency of turbulence intensity is included for the longitudinal and lateral coherence of the streamwise wind component. The model of the lateral coherence is performed without the normalisation of the lateral separation distance Δy with the mean wind speed $\bar{u}$.

Jensen and Kristensen (1979) showed that for isotropic turbulence the lateral coherence does not converge to unity for large scales if the lateral separation Δy exceeds the integral turbulent length scale (ILS) in lateral direction L_y. Furthermore, they proposed a dependence on the ILS if the separation is not small compared to the length scale, this would lead to a maximum coherence of 0.4 for example for the ratio of $\Delta y/L_y = 0.5$. These statements are based on experiments at the Sotra bridge in an altitude of 57 m above water with lateral separations Δy from 5 ... 16 m resulting in a three times lower decay parameter at the bridge

compare to observations over ice in 3 m altitude (Kristensen et al. 1981). Both analyses were limited to neutral stability. They found that the lateral decay parameter is a function of separation distance and altitude, such that the decay parameter c_y increases with increased ratio of $\Delta y / z$.

Knowledge of the coherence in the atmospheric boundary layer is crucial in wind energy science for calculating the aerodynamic loads and further, for estimating the energy production of a wind turbine (WT) (Saranyasoontorn et al. 2004). Therefore, in the Longterm Inflow and Structural Test (LIST) field measurement (Saranyasoontorn et al. 2004) the longitudinal and lateral coherence was studied with multiple anemometers which were laterally separated by 7.7...33 m and vertically separated by 8.5...17 m around a hub height of 23 m. They found an increase in the vertical decay parameter of the streamwise velocity while increasing the vertical distance, based on the original Davenport model. The dependency of the decay parameter on the lateral separation is even greater than on the vertical separation. They also applied a decay model by Thresher et al. (1981) which accounts for the separation distance with an additional term and a scaling parameter in the coherence decay model. Further, comparisons to theoretical models such as the isotropic turbulence model of von Kármán (1948) and the uniform shear turbulence model of Mann (1994) show reasonable agreement with the Mann model, as the von Kármán model generally overestimates the coherence.
In the design process of large suspension bridges and large buildings in industrial aerodynamics, the impact of aerodynamic loads by the coherence is considered as well (Midjiyawa et al. 2021). Cheynet et al. (2016) conducted coherence studies for the structural design of bridges.

Further, the COTUR project studies the offshore turbulence with remote sensing techniques. (Cheynet et al. 2021) measured the lateral coherence using multiple DWL systems with lateral separations of $\Delta y = 21$ m. Extending the Davenport model by combining the lateral and longitudinal coherence resulted in values about $c_y = 15...19$ for the lateral decay parameter.

Simley and Pao (2015) studied the longitudinal coherence of the streamwise wind component in the inflow of a WT using Large Eddy Simulations (LES) and proposed a scan strategy for lidar-based coherence measurements in WT inflow measurements. The time domain is limited to 740 s in their simulation, so that the coherence does not reach unity in every case for the largest resolvable scales. They proposed an approach for the longitudinal coherence which is based on the Davenport model but allows the decay function to converge to smaller vales than unity for low frequencies. Furthermore, Mann (1994) evaluates a turbulence model for spatial coherence within different experiments.

In this study, we deploy the SWUF-3D (Simultaneous Wind measurement with Unmanned Flight systems in 3D) fleet of quadrotors to collect distributed wind measurements in the ABL. This approach was validated in a two-week measurement campaign at the boundary layer field site Falkenberg of the German Meteorological Service (DWD) (Wetz et al. 2021). A dedicated measurement pattern is developed for an examination of Taylor's frozen hypothesis theory by studying horizontal correlations between multiple UAS in different atmospheric conditions. Limits of the frozen turbulence assumption are studied with the spatial cross-correlation function of the wind velocity within the UAS-fleet at the field site. The simultaneous UAS measurements enable extensive coherence studies. We specifically focus on the lateral and longitudinal coherence of the streamwise velocity component for various horizontal separation distances between 5 m and 205 m. We analyze the dependency of the coherence on atmospheric stability and the separation distance by studying the applicability of exponential coherence decay models from Davenport (1961) and Schlez and Infield (1998).

In Sect. 2, the experiment, including the measurement systems and the measurement strategies, is shown. Section 3 explains the wind algorithm used within the fleet. Also, methods are introduced for calculating turbulence quantities, boundary layer characteristics, and correlation analysis, including coherence models. In Sect. 4, the results for turbulence measurements and horizontal correlation analyses of the fleet measurements follow. Additionally, the approximation of coherence with different approaches is examined. The results are discussed in Sect. 5 with regard to the limits of the validity of Taylor's frozen hypothesis and the potential of model approaches for coherence at various separation distances and in different atmospheric conditions.

2 Experimental Setup

2.1 UAS-Fleet

The measurement systems consist of 35 quadrotors of the type Holybro QAV250 with a frame dimension of 0.25 m. Supported by the GNSS and the autopilot, the UAS is able to hover in fixed positions and follow predefined flight paths. The inertial measurement unit (IMU) measures the UAS attitude and its first and second derivatives with a set of sensors, including gyroscopes, accelerometers, and magnetometers. The sensor data are logged to an SD-Card with a temporal resolution between 1 and 250 Hz depending on the sensor type (see also Wildmann and Wetz 2022). With the current system the turbulence can be resolved until 1 Hz (Wetz and Wildmann 2022). Since we do not rely on external wind sensors, the disturbance of the rotors is not crucial for the calculation of turbulence quantities. In smaller scales, the noise level of the sensors and the disturbance by the rotor dominate; therefore, a low-pass filter is used in the data processing so that small scales are neglected. Additionally, a combined temperature and humidity sensor is mounted on each UAS. In the current system, the capacity of the battery was increased compared to a previous measurement campaign (Wetz et al. 2021) so that measurement times of 14 min could be reached.

2.2 Measurement Campaign

In June/July 2021, we participated in the FESSTVaL campaign (Field Experiment on Sub-Mesoscale Spatio-Temporal Variability in Lindenberg) at the Lindenberg Meteorological Observatory - Richard-Aßmann-Observatory (MOL-RAO) operated by the German Meteorological Service (Deutscher Wetterdienst, DWD). In particular, we operated our fleet at the Boundary Layer Field Site (Grenzschichtmessfeld, GM) in Falkenberg, which includes various atmospheric measurement devices at the site. The most relevant for our purpose is the 99 m mast, which is equipped with multiple sensors at different altitudes. At 90 m and 50 m altitudes, sonic anemometers with a temporal resolution of 20 Hz are mounted. The site is located 80 km south-east of Berlin and can be described as having almost flat, heterogeneous terrain. The land use is dominated by grassland and cropland, including some forest 1 km west of the site. In total, during the 2 weeks (June 21–July 2) of the measurement campaign, more than 1000 single UAS flights were realized.

In Fig. 1, the measurement site is shown, including the 99 m mast, the wind rose of 1 year's (2021) mast measurements at 98 m a.g.l. and different measurement patterns of the UAS-fleet. As the wind rose indicates, the site is dominated by westerly winds, which also applies to the two-week measurement campaign, in which most of the flights can be assigned to westerly
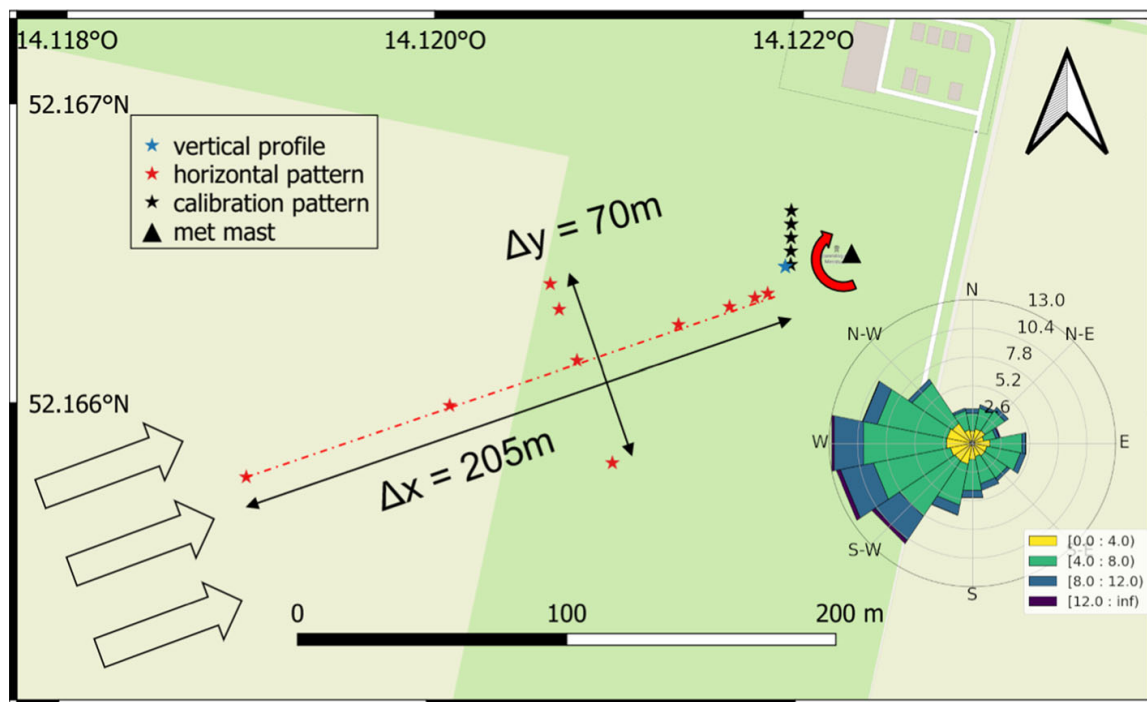
Fig. 1 Map of the field site of GM Falkenberg, including the 99 m meteorological mast and different flight patterns of the UAS-fleet. Each star represents an individual UAS at its measurement position. The dark green area is short cut grass, whereas the light green area was a cornfield in 2021. The arrows on the left side represent the wind direction and the corresponding orientation of the 'horizontal pattern'. Background map ©OpenStreetMap contributors 2022. Distributed under a Creative Commons BY-SA License. The wind rose is extracted from the meteorological mast at 98 m a.g.l

winds. Within the map, the stars represent single UAS in their hover position. The flight 'calibration pattern' indicates multiple UAS in a line in front of the mast at the corresponding sonic measurement heights of 90 m and 50 m. This pattern was mainly used for calibration and validation purposes, as described in Wetz and Wildmann (2022). Further, vertical profiles were measured continuously with a single UAS or with multiple stacked UAS at different altitudes marked with the flight pattern 'vertical profile'. Most relevant for this study is the 'horizontal pattern' which is used for examining turbulence structures in the ABL. In this pattern, multiple UAS are distributed longitudinally and laterally to the mean wind direction at different distances. The pattern was generated semi-automatically in order to adapt the orientation of the pattern to the current wind direction (illustrated by the red curved arrow in Fig. 1), which was observed from the 99 m mast shortly before each flight. The horizontal spacings between the UAS were chosen to allow for a maximum of different separation distances that can be achieved by combining different UAS. The separation distances in longitudinal direction Δx vary from 5 to 205 m and in lateral direction Δy from 10 to 70 m. The shape of the pattern remained similar throughout the campaign and was arranged at different altitudes and for different thermal stratifications: stable (SABL), neutral (NABL), and convective (CABL). This pattern enables horizontal correlation and coherence studies within the ABL.

Table 1 Classification of atmospheric stability adapted from Mohan ([1998](#))

Stability class	Ri_b
Unstable	< -0.011
Near neutral	$-0.011 < \mathrm{Ri}_b < 0.042$
Stable	> 0.042

3 Methodology

3.1 Wind Algorithm

In Wetz and Wildmann ([2022](#)) the calculation of the horizontal wind vector that is used in this study is described in detail. The algorithm is based on the principle of aerodynamic drag and relates the horizontal forces to wind speeds. The forces are derived from the equations of motion in the body frame of the multicopter. Acceleration and attitude data from the inertial measurement unit are used as input data for the wind algorithm. The UAS data are calibrated and validated against the sonic measurements from the 99 m mast. The relation between the wind speed and the horizontal forces is modeled with an exponential function. The calibration result of an independent validation dataset yields a RMSE (root-mean-square error) of 0.25 m s^{-1} for the mean wind speed and 0.16 m^2 s^{-2} for the longitudinal, respectively 0.08 m^{2}s^{-2} for the lateral variance. The accuracy of the wind direction measurement is 4.5°. In Wetz and Wildmann ([2022](#)) we also found that the temporal resolution of wind measurement is limited to 2 Hz due to sensor noise, which dominates at small scales. This is crucial in low turbulence conditions with a low signal-to-noise ratio.

3.2 Atmospheric Conditions

In order to characterize the atmospheric conditions during the analyzed flights, the dynamic stability is determined with the bulk Richardson number:

$$\mathrm{Ri}_b = \frac{|g| \Delta \theta_v \Delta z}{T_v [\Delta u^2 + \Delta v^2]}, \tag{2}$$

which is defined as the ratio of buoyancy energy to shear-kinetic energy (Stull [2016](#)). In Eq. [2](#) the variables $\Delta \theta_v$, Δz, Δu, Δv are the differences over height of virtual potential temperature, altitude, zonal and meridional wind component and T_v is the virtual temperature. The atmosphere is dynamically unstable if the bulk Richardson number is smaller than the critical Richardson number $\mathrm{Ri}_c = 0.25$. During the horizontal flight pattern, additional flights for vertical profiling were performed. From these flights the bulk Richardson number could be calculated. However, we use the data of the sonic measurements from 50 and 90 m altitude to calculate the bulk Richardson number, since vertical profiling flights are not available for every analyzed flight. In order to classify the dynamic stability of the ABL, the Ri_b is used as originally proposed by Mohan ([1998](#)) and also applied by Cantero et al. ([2022](#)). In this study we refer to the original classification for unstable and stable conditions by Mohan ([1998](#)). We define a weakly stratified ('near neutral') class by combining their 'weakly unstable', 'neutral' and 'weakly stable' classes (Table [1](#)).

The height below which the shear production of turbulence exceeds buoyant production is defined by the Obukhov length L_O (Stull 2016):

$$L_O = \frac{- \overline{\theta_v} \, u_\star^3}{k \, |g| \, \overline{(w'\theta_v')}},$$ (3)

where k is the von Kármán constant with a value of 0.4 and g the gravitational acceleration. The turbulent kinematic heat flux $\overline{w'\theta_v'}$ is defined by the fluctuations of the virtual potential temperature θ_v and the vertical velocity w. The friction velocity is defined by $u_\star$. The Obukhov length is calculated at 2 m a.g.l. from sonic anemometer measurements to represent the surface layer characteristics. The surface-layer scaling parameter ζ_O (or Monin-Obukhov stability parameter) is often used for static stability characterizations and is defined as:

$$\zeta_O = \frac{z}{L_O}.$$ (4)

Statically stable conditions are found for positive ζ_O values and unstable conditions for negative ζ_O values, wherein the magnitude defines stronger or weaker stability conditions. For example, large, negative values amplify strong, unstable conditions. The Monin-Obukhov stability parameter is listed in Table 2 as a parameter of surface layer stability. The Brunt–Väisälä frequency N_{BV} sets the upper limit for internal wave frequency in the boundary layer and is defined as:

$$N_{BV}^2 = \frac{g}{\theta_v} \frac{\delta\theta}{\delta z}.$$ (5)

It is only defined for stable stratification. Higher N_{BV} frequencies indicate more stable conditions. In the present study, the Brunt-Väisälä frequency is calculated for the same height as that used for the bulk Richardson number (between 90 m and 50 m). In Table 2, the surface layer parameters based on the Obukhov length in 2 m a.g.l. are listed, as are the Brunt–Väisälä frequency and the bulk Richardson number between 50 and 90 m a.g.l. Due to the different considered altitudes, the derived stability deviates. Particularly, for flight #84 in the early morning hours, the boundary layer between 50 and 90 m according to the Ri_b is still within the nighttime inversion layer, while the parameters at the surface layer in 2 m a.g.l. already indicate buoyant forces close to the ground. Since the lowest altitude of the considered flights is 50 m a.g.l., we refer to the derived Richardson number Ri_b between 90 and 50 m for classification of the flight cases.

Another step of quality control is the stationarity test. This test examines whether the atmospheric conditions can be considered stationary during a flight by comparing the velocity variances of sub-divided time intervals $\overline{\sigma_u^2}_{,SI}$ to the variance of the whole time series $\overline{\sigma_u^2}_{,WI}$. The stationarity is thus quantified by the parameter:

$$St_u = \left| \frac{\overline{\sigma_u^2}_{,SI} - \overline{\sigma_u^2}_{,WI}}{\overline{\sigma_u^2}_{,WI}} \right| \cdot 100\%.$$ (6)

For our study, we subdivided the series into four, five and six time intervals and took the mean value of the different intervals. The test has been carried out for the velocity component in lateral and longitudinal directions. The threshold for assuming stationarity is defined as $St_u < 30\%$ (Foken and Wichura 1996).

3.3 Horizontal Correlations

The cross-correlation function $\rho_{uu_{\Delta x}}(\tau)$ between different UAS measurements of the longitudinal velocity component (Δx meaning the longitudinal separation distance between two UAS) as a function of the time shift τ is defined according to:

$$\rho_{uu_{\Delta x}}(\tau) = \frac{\overline{u'(t)u'_{\Delta x}(t+\tau)}}{\sigma_u \sigma_{u_{\Delta x}}}, \tag{7}$$

as the covariance, normalized by the individual standard deviations σ_u (Pope 2000). The velocity fluctuations u' are derived from the Reynolds decomposition:

$$u' = u - \bar{u}, \tag{8}$$

averaging the velocity u over the time interval of one single flight of 12 min in order to obtain the mean (advection) velocity $\bar{u}$.

The autocorrelation function $\rho_{uu}(t)$ is defined as the correlation of a variable with itself. For the determination of the integral length scale L_x, the autocorrelation function of the streamwise wind velocity is first used to derive the Eulerian turbulent time scale T_x (Lenschow and Stankov 1986). In order to calculate the length scale from the time scale at one measurement point, the frozen turbulence assumption by Taylor is applied (Taylor 1938). The Taylor-Hypothesis states that turbulence remains frozen while passing through the sensor, such that the time scales can be transformed into length scales by multiplication with the advection velocity $\bar{u}$ (Eq. 10). The advection velocity is calculated by the velocity mean of the time interval of one flight (12 min). Following the approach of Lenschow and Stankov (1986), the time scale is calculated by the integral of the autocorrelation function until the first zero crossing (T_0, Eq. 9):

$$T_x = \int_0^{T_0} \rho_{uu}(t)\,d\tau, \tag{9}$$

$$L_x = T_x \bar{u}. \tag{10}$$

Another way to calculate the integral length scale is to use spatial cross-correlations of the streamwise velocity. This approach is examined in Sect. 4.

3.4 Coherence

The coherence between two velocity time series describes the frequency-dependent similarity of the flow structure. The (magnitude-squared) coherence $\gamma^2_{uu_{\Delta x}}(f)$ of two time series $u(t)$ and $u_{\Delta x}(t)$ is defined as the square of the absolute value of the cross-spectrum $S_{uu_{\Delta x}}(f)$ normalized by the individual power spectra $S_{uu}(f)$ and $S_{u_{\Delta x}u_{\Delta x}}(f)$ (see Eq. 15). The cross-spectrum can be calculated by the Fourier transformation of the cross-covariance function $C_{uu_{\Delta x}}(\tau)$, which simply is the cross-correlation function (Eq. 7) without normalization:

$$S_{uu_{\Delta x}}(f) = \int_{-\infty}^{\infty} C_{uu_{\Delta x}}(\tau)\,e^{2\pi i \tau f}\,d\tau \quad . \tag{11}$$

Equivalent to the cross-spectrum, the power spectrum $S_{uu}(f)$ can be calculated by the Fourier transformation of the auto-covariance function. Following Lumley and Panofsky (1964), the cross-spectrum can be decomposed into the cospectrum $Co_{uu_{\Delta x}}(f)$ (real part) and the

quadrature spectrum $Q_{uu_{\Delta x}}(f)$ (imaginary part):

$$S_{uu_{\Delta x}}(f) = \mathrm{Co}_{uu_{\Delta x}}(f) - iQ_{uu_{\Delta x}}(f) \quad . \tag{12}$$

The cospectrum is used, for example, to investigate the spectral distribution of heat flux (Bange et al. 2002). From the cross-spectrum, the phase(-spectrum) can be calculated as the angle between the co- and the quadrature-spectrum:

$$\Phi_{uu_{\Delta x}}(f) = \tan^{-1} \frac{Q_{uu_{\Delta x}}(f)}{\mathrm{Co}_{uu_{\Delta x}}(f)} \quad . \tag{13}$$

The amplitude-spectrum $A_{uu_{\Delta x}}(f)$ refers to the absolute of the complex cross-spectrum:

$$A_{uu_{\Delta x}}(f) = \sqrt{\mathrm{Co}^2_{uu_{\Delta x}}(f) + Q^2_{uu_{\Delta x}}(f)} \quad . \tag{14}$$

Note that in literature also the root-coherence and co-coherence are mentioned (Cheynet et al. 2016). In this study, we refer to the magnitude-squared coherence:

$$\gamma^2_{uu_{\Delta x}}(f) = \frac{A_{uu_{\Delta x}}(f)^2}{S_{uu}(f)S_{u_{\Delta x}u_{\Delta x}}}(f) \quad . \tag{15}$$

That means that the phase is not considered here. The coherence only takes values between zero and unity according to Schwartz's inequality. Unity is only reached when the Fourier components of u and $u_{\Delta x}$ have proportional amplitudes throughout the ensemble (Lumley and Panofsky 1964).

Since in atmospheric sciences we often rely on only one or a few realizations in a limited time frame, the statistical relevance needs to be evaluated. In the case of coherence estimations, the trade-off is between resolvable scales and statistical errors. This balance depends on the so-called degree of freedom M which is defined as the product of the subdivided number of segments and the number of averaged spectral estimates. Assuming that we subdivide a time series into 8 small segments and additionally average over four frequencies, we get a degree of freedom of $M = 8 \cdot 4 = 32$. In order to calculate the coherence between two time series, each series must be subdivided into at least two shorter segments. Kristensen and Kirkegaard (1986) studied the sampling issues with spectral coherence and proposed an error calculation of the sampled coherence depending on M and γ^2. This error calculation reveals that an overestimation of the coherence is always found for a finite value of M. The overestimation and the standard deviation of the coherence estimation reduce with increasing values of M and γ^2.

Carter et al. (1973) proved an increase of the accuracy of sampled coherence by applying an overlapping of the segments by 50 %. Due to the limited measurement time, we are limited in subdividing the time series into smaller series if the larger scales with high coherence should still be resolved. Therefore, we subdivide the large scales with a degree of freedom of $M = 4$ with an overlap of 50 % in order to decrease the error. This results in a time frame of 180 s for the present study, leading to maximum resolvable scale of 1 km, assuming an advection velocity of 6 m s^{-1}. The smaller scales are calculated with up to $M = 32$ in order to increase the statistical accuracy. The spectra are computed using Welch's average periodogram method (Bendat and Piersol 2011).

The error calculation according to Kristensen and Kirkegaard (1986) results for the given value of $M = 4$, assuming $\gamma^2 = 0.4$, in a standard deviation σ of 0.27 (see Eq. 16) and a bias B of 0.09 (see Eq. 17), for $\gamma^2 = 0.9$ the standard deviation results in 0.067 and the bias 0.002. Increasing the degree of freedom to $M = 32$ leads to $\sigma = 0.09$ and $B = 0.011$ for $\gamma^2 = 0.4$. However, these error estimates are only valid if no window function or overlapping

is included in the coherence calculation, since both functions reduce the error, these estimates need to be understood as an upper limit of the error:

$$B_{\gamma^2} = \gamma^2 + \frac{1}{M}(1 - \gamma^2)^2,$$ (16)

$$\sigma_{\gamma^2} = \frac{2}{M}\gamma^2(1 - \gamma^2)^2.$$ (17)

3.5 Coherence Models

According to the theory of Davenport (1961), the coherence of the streamwise velocity fluctuations between vertically separated measurements can be modeled by an exponential function (see Eq. 1). The coherence decreases both with increasing vertical separation Δz and decreasing wavelength $\lambda_x = \bar{u}/f$. The exponential function of the root coherence γ is scaled with a decay constant a in Eq. 1. Note that Davenport uses the root-coherence γ. In order to compare decay parameters resulting from root-coherence γ and magnitude-squared coherence γ^2 the parameter needs to be multiplied by the factor 2 (i.e. $c_i = 2a$ in Eq. 18). Originally, Davenport formulated the model only for vertical separations, but Pielke and Panofsky (1970) also applied this model to horizontal coherence studies, so that it can be applied for all directions and separation distances R (if only the longitudinal direction is considered, $R = \Delta x$):

$$\gamma^2(f) = e^{-c\frac{R}{\bar{u}}f}.$$ (18)

Schlez and Infield (1998) state that the decay of the coherence depends on the turbulence intensity TI and the horizontal distance between the considered points in space. TI is defined as the ratio of the standard deviation σ to the mean wind velocity $\bar{u}$ in:

$$TI = \frac{\sigma_u}{\bar{u}} :$$ (19)

The longitudinal distance Δx is additionally normalized by the mean velocity $\bar{u}$. The rate of decay of the exponential function is defined by the decay parameter α_x in:

$$\gamma_x^2(f) = e^{-\alpha_x\frac{\sigma_u}{\bar{u}}\frac{\Delta x}{\bar{u}}f}.$$ (20)

Schlez and Infield (1998) differentiate between longitudinal and lateral models of the coherence. They state that in the lateral direction the distance Δy between the considered measurements positions should not be normalized by the advection velocity $\bar{u}$ due to the perpendicular orientation of Δy and advection. Thus, the modeled coherence in the lateral direction is:

$$\gamma_y^2(f) = e^{-\alpha_y\frac{\sigma_u}{\bar{u}}\Delta y f}.$$ (21)

As the models of Schlez and Daveport are different, a distinction of the decay parameter is necessary. For clarification we further use the decay parameter c for the Davenport model and α for the Schlez model. The decay parameters of the exponential functions are determined from experimental data through a curve fit using the least squares method as described in Moré (1978). In order to compare the scatter of the decay parameters c and α, resulting from

different coherence approaches, the relative standard deviation d is used:

$$d = \frac{\sigma_c}{\bar{c}}, \tag{22}$$

wherein σ_c represents the standard deviation, normalized by the mean of the decay parameter $\bar{c}$.

3.6 Data Filtering

The 26 available flights of the FESSTVaL campaign with a 'horizontal pattern' are filtered for further processing with respect to two criteria: first, the misalignment β of the flight pattern to the mean wind direction is limited to 30°, so that the assumption of longitudinal and lateral separations is coarsely valid. Second, the stationarity test is applied for the streamwise and lateral wind components, and only flights with ST $<$ 30% are used for the analysis. From 26 flights during the campaign, only 12 remain, which is mainly due to large misalignment angles that occur in low wind conditions. The flights of the 'horizontal pattern' used in further analysis are listed in Table 2.

4 Results

4.1 Validation of Turbulence Measurements

We have previously shown that the calibration results for the mean wind vector and the velocity variance of the UAS measurements are in good agreement with the reference measurements using the calibration pattern close to the 99-m mast (Wetz and Wildmann 2022). The following analyses are based on the 'horizontal pattern' as illustrated in Fig. 1. The capability to measure second order statistics with the UAS is illustrated in Fig. 2a. The amplitude spectra $A_{uu_{\Delta x}}$ of streamwise velocity fluctuations of two UAS with longitudinal distances of $\Delta x = 5$ m and $\Delta x = 205$ m are shown in comparison to the corresponding single-point power spectrum of the sonic anemometer at the mast and a power spectrum of the individual UAS which is closest to the mast. It is evident that, for this neutrally stratified atmosphere, the amplitude spectra and the power-spectrum of the UAS agree well with the reference. Remaining differences can likely be attributed to the fact that the closest UAS is still 30 m away from the sonic. Figure 2b shows the phase-spectra of two UAS combinations with different separation distances ($\Delta x = 5$ m and $\Delta x = 205$ m). Assuming that eddies are transported with the mean advection velocity $\bar{u}$, the wavelengths are defined as:

$$\lambda = \frac{\bar{u}}{f}. \tag{23}$$

We expect to find the maximum of the phase-spectrum (360°) at that wavelength which corresponds to the separation distance $\lambda(\Phi = 360°) = \Delta x$. For larger wavelengths, the theoretical phase-spectrum, expressed in degrees, can be calculated as:

$$\Phi_{uu_{\Delta x}} = \frac{\Delta x}{\lambda} \, 360°. \tag{24}$$

Shorter wavelengths than Δx cannot be adequately represented in the phase-spectrum. The theoretical phase-spectrum is indicated by the dashed lines in Fig. 2b until the separation distances of the considered UAS are reached. The measured phase-spectra in solid lines are

Table 2 Flight protocol of considered flights in Sect. 4 from the 'horizontal pattern'

Date	Time (UTC)	Flight no.	a.g.l. (m)	$\bar{u}$ (m s^{-1})	β (°)	TI (–)	L_x (m)	L_O (z = 2 m) (m)	ζ_O (z = 2 m) (–)	N_{BV} $\Delta z = 90 - 50$ m s^{-1}	Ri_b $\Delta z = 90 - 50$ m (–)	ABL
25.06.2021	12:14	26	50	2.51	24	0.29	108	−4	−0.50	–	−2.427	CABL
25.06.2021	12:40	27	50	1.97	4	0.31	29	−2	−1.00	–	−2.312	CABL
29.06.2021	06:18	87	150	3.71	16	0.162	119	−15	−0.13	–	−0.497	CABL
02.07.2021	12:17	118	90	6.29	1	0.198	329	−40	−0.05	–	−0.137	CABL
02.07.2021	15:12	124	50	6.05	15	0.156	103	−43	−0.05	–	−0.112	CABL
30.06.2021	16:19	101	90	9.26	20	0.209	291	−191	−0.01	–	−0.005	NABL
25.06.2021	15:56	32	50	5.23	27	0.108	143	−29	−0.07	–	−0.001	NABL
30.06.2021	16:52	102	50	8.21	9	0.178	108	−323	−0.01	0.0028	0.006	NABL
30.06.2021	16:05	100	90	8.25	14	0.166	243	−164	−0.01	0.0024	0.01	NABL
30.06.2021	17:05	103	50	7.15	11	0.155	128	−323	−0.01	0.038	0.014	NABL
29.06.2021	03:54	72	90	6.44	17	0.091	87	1	2.00	0.033	0.223	SABL
29.06.2021	05:52	84	150	4.08	20	0.248	153	−20	−0.10	0.01	0.5	SABL

β describes the misalignment of the pattern orientation with the mean wind direction. The flights are grouped into convective (CABL), neutral (NABL) and stable (SABL) ABL

Fig. 2 Power spectrum density $|S_{uu}|$ of sonic anemometer measurements in comparison to UAS measurements **a** power-spectrum $|S_{uu}|$ and amplitude spectra $A_{uu_{\Delta x}}$ and **b** phase-spectra $\Phi_{uu_{\Delta x}}$ with longitudinal separation of $\Delta x = 5$ m and $\Delta x = 205$ m. The thin orange line represents the measured phase for $\lambda < \Delta x$. Dashed lines indicate the theoretical phase resulting from the separation distance Δx and the advection velocity $\bar{u}$ as calculated from Eq. 24 (results from flight no. 100 in Table 2)
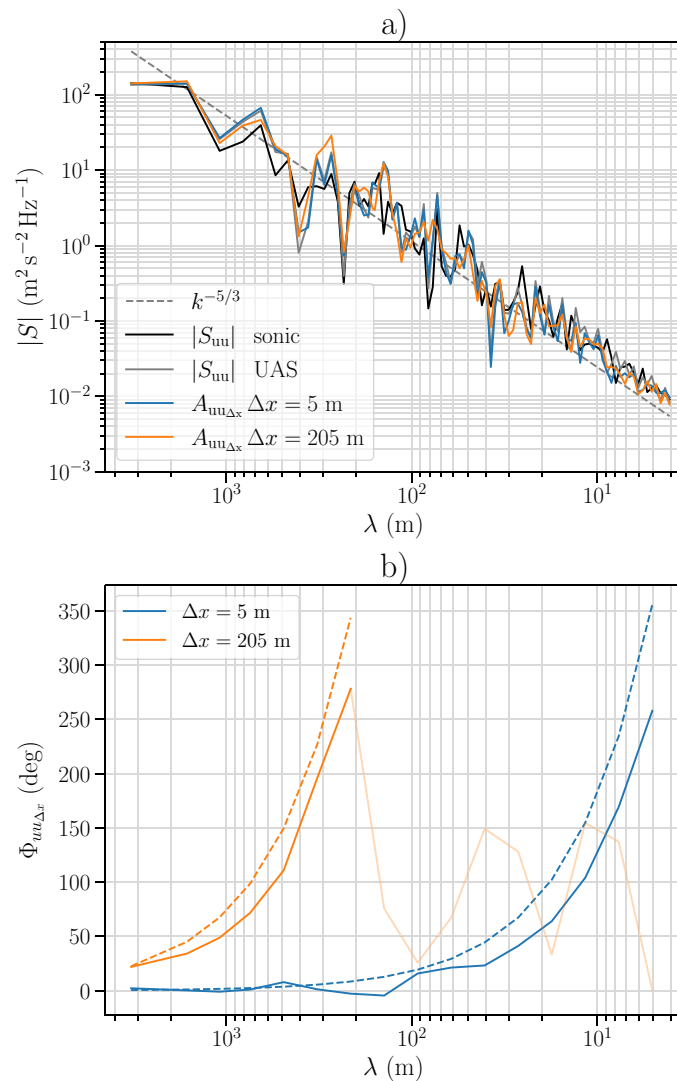
shown in light color if they fall below the separation distances, since reasonable results are only expected in the range larger than the spatial spacing of the considered measurements. The results show that the shape of the measured phase-spectra is in line with the theoretical phase. However, a bias can be seen towards shorter wavelengths, which could be explained by the accuracy of the separation distances estimation or by a slightly faster transport velocity of eddies compared to the calculated advection velocity.

In Fig. 3a the integral length scale L_x in streamwise direction, calculated from UAS measurements, is compared with reference sonic estimates for all flights for which sonic measurements are available in the corresponding flight altitude. The length scale is calculated from the integral over the autocorrelation function as described in Sect. 3, Eq. 10. For the UAS-determined length scale, the median of all ten UAS involved in the flight pattern is calculated. Error bars represent the standard deviation within the fleet. The high R-value of 0.93 confirms the validity of the UAS estimates. Note that the distances between the UAS and the 99 m mast vary in the longitudinal direction from 30 to 235 m and in the lateral direction up to 40 m. For high length scales in the order of $L_x > 400$ m the statistical significance of the measurement decreases due to the limited measurement time and thus the number of measured large eddies in one time series. The stable flight cases are associated with low level jets and a strong inversion in the morning hours. The three stable cases presented are from the same morning and show an increase in the turbulent length scale as the day progresses,
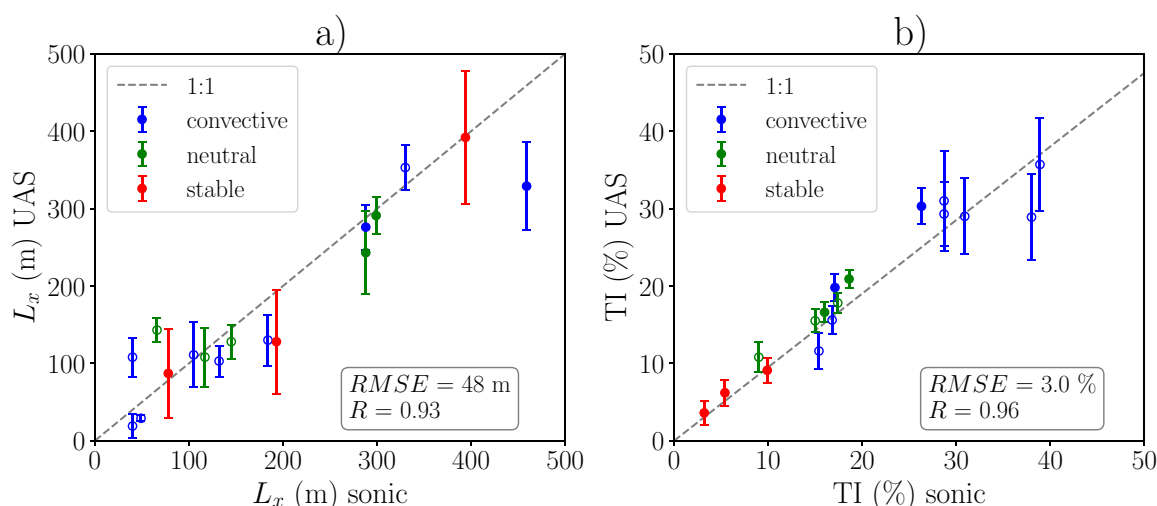
Fig. 3 **a** Integral length scale L_x of UAS measurements in comparison to sonic measurements. L_x for the UAS is calculated by the median of multiple simultaneous measurements. Filled markers are comparisons in 90 m and non filled markers in 50 m a.g.l.. Error bars represent the standard deviation within the fleet. **b** Turbulent intensity TI of UAS measurements in comparison to sonic measurements. The error bars are calculated by the propagation of uncertainty using the accuracy of the mean velocity and standard deviation of the velocity measurement

resulting in increased development of the convective surface boundary layer. This particular situation, combined with the limited measurement time (12 min) for calculating the length scale, could cause high turbulent length scales even in the SABL.

As mentioned in Sect. 3.5, the decay parameter of the coherence can depend on the turbulence intensity (TI). To validate the measurements by the UAS, Fig. 3b shows TI as measured by the UAS in comparison to the sonic. Since a high accuracy was reached for the mean wind speed and the variance measurements (Wetz and Wildmann 2022), TI estimates are also quite accurate, with an RMSE of 3 % and an R-value of 0.96. The comparatively large error bars for high turbulent intensities are due to low wind speeds and the corresponding larger relative wind speed uncertainties, which are present for cases of TI > 0.25.

4.2 Horizontal Correlation

The objective of the analyses of horizontal correlations is to examine the differences between the actual measurements and the theoretical behavior that would be expected for frozen turbulence. Therefore, in Fig. 4 the cross-correlation $\rho_{uu_{\Delta_x}}$ within the fleet in the horizontal pattern in the longitudinal direction is shown. The UAS closest to the tower is cross-correlated with the remaining six UAS in the longitudinal direction, resulting in horizontal separation distances between 5 m and 205 m. The vertical dashed lines mark the theoretical advection time that the flow needs to travel from the upstream UAS to the reference UAS. It is close to the maxima of the cross-correlations for all distances. However, a slightly faster transportation is observed in the cross-correlation maxima compared to the advection velocity, which is in line with the observations that were made in the phase spectrum of the same flight. A detailed comparison between the travel time of the eddies and the advection time using Taylor's hypothesis is given in Fig. 13 in Appendix by the time lag error of the correlation maxima in relation to the theoretical lag.

The cross-correlations of UAS measurements in Fig. 4 are extended by all possible combinations of UAS in the pattern in order to obtain more grid points for the analysis. The decay of the maxima with increasing separation distance is shown in Fig. 5a. The atmosphere during

Fig. 4 Cross-correlation function of streamwise velocity between the longitudinally aligned UAS for flight # 100. Dashed vertical lines are the theoretical time lags of the correlation maxima calculated with Taylor's hypothesis. Colored points mark the intersection between the correlation functions and $\tau = 0$
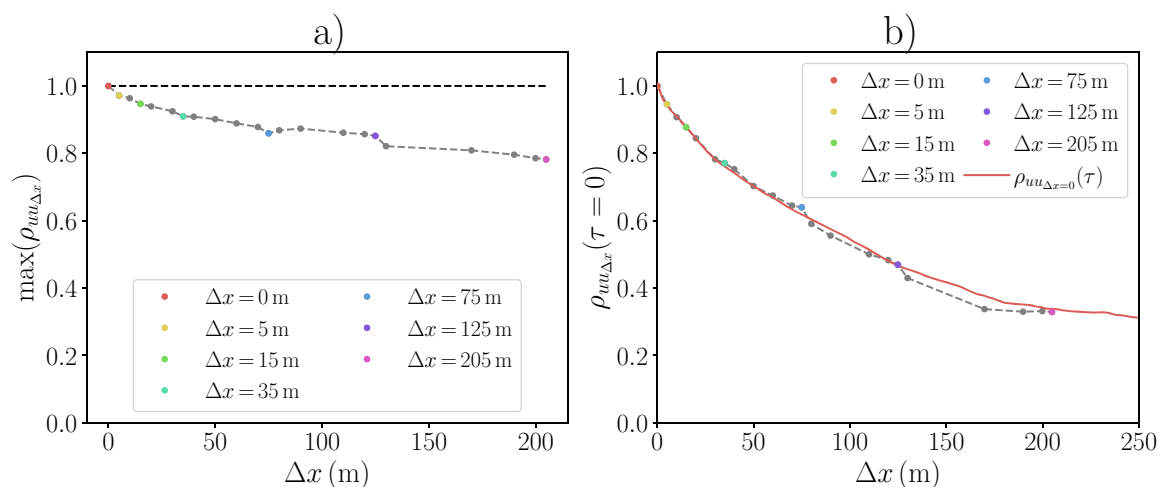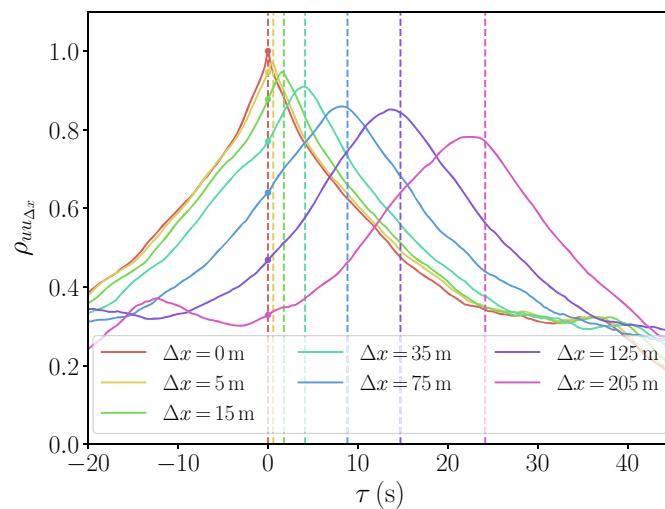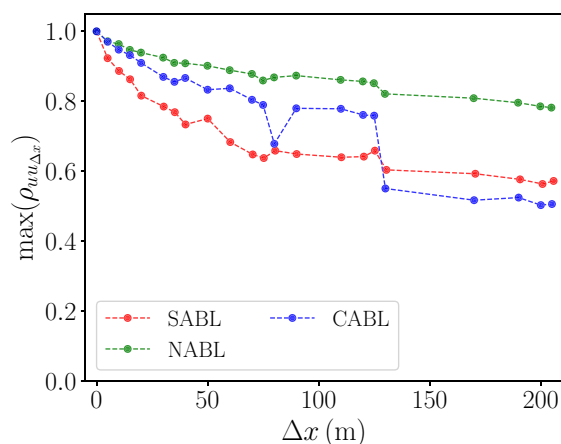

Fig. 5 **a** Cross-correlation function maxima (from Fig. 4) of all longitudinal combination of UAS with corresponding longitudinal separation distances Δx. **b** Autocorrelation $\rho_{uu_{\Delta x=0}}(\tau)$ in comparison to direct spatial cross-correlation using the intersection of the cross-correlation function $\rho_{uu_{\Delta x}}$ and $\tau = 0$, marked as dots in Fig. 4 for flight # 100

the studied flight (# 100 in Table 2) was neutrally stratified with a bulk Richardson number of $\text{Ri}_b = 0.01$. The mean wind speed was $\bar{u} = 8.3 \text{ m s}^{-1}$ with a TI of 0.17 and an integral length scale of $L_x = 245$ m. The fact that the maxima decrease with distance is strictly speaking in disagreement with Taylor's hypothesis, which implies that the maxima of the cross-correlation function should be unity if turbulence is frozen and only advected.

Subsequently, the maxima of the cross-correlation function for different atmospheric conditions are evaluated in Fig. 6. We observe that the maxima decay more strongly in stable and convective conditions compared to neutral conditions. While not explicitly shown here, we also observed stronger decays in lower heights. This means that the frozen turbulence assumption is more valid in neutral stratified boundary layers and in greater distance to the ground.

The autocorrelation of a single point measurement of the wind velocity is frequently used to study horizontal scales of turbulence under the assumption of frozen turbulence. With our data we can compare the single point autocorrelation ρ_{uu} with spatial cross-correlation. For this purpose the intersection of the cross-correlation function with the y-axis (($\rho_{uu_{\Delta x}}(\tau = 0)$)) in Fig. 4, which is equal to the correlation coefficient of two spatially separated measurement points, is determined. Similar to the maxima in Fig. 5a, the correlation coefficients can

Fig. 6 Cross-correlation function maxima (identical derived as Fig. 5a) for CABL(# 118), SABL (# 72) and NABL (# 100) in 90 m a.g.l

be plotted for a multitude of UAS combinations (i.e., different separation distances). This collection of correlation coefficients is compared with the autocorrelation function of the reference UAS in Fig. 5b. The time shift τ of the autocorrelation function is converted to a theoretical spatial shift Δx by the advection velocity $\bar{u}$. In this particular flight, the direct spatial cross-correlation is well approximated by the autocorrelation, thus the assumption of Taylor can be considered to be applicable. Further, the spatial correlation can additionally be used for a direct calculation of the ILS without the need for the frozen turbulence assumption.

In Fig. 7, the spatial cross-correlations are compared to the reference UAS autocorrelation, as in Fig. 5b, but for different atmospheric conditions (Fig. 7a) and measurement heights (Fig. 7b). In the neutrally stratified boundary layer, the autocorrelation is closest to the cross-correlation, thus the estimation of ILS from a single time series can be expected to be in good agreement with an estimation from spatial correlation. The deviation between the curves of the different approaches increases for stable and convective conditions as well as in lower altitudes.

The significant drop of the cross-correlations in convective conditions that can be seen in Fig. 7 and also in Fig. 6 at $\Delta x = 80$ m and $\Delta x > 125$ m is connected to combinations with the UAS in the far west. The decay of the autocorrelation function of this UAS is much steeper than for all other UAS in the pattern, thus the involvement of this UAS leads to smaller cross-correlations. To preclude any technical issues with the particular UAS itself, we checked a calibration flight that was performed in between both convective cases (flight 118 and # 124). The autocorrelations during this calibration flight, where individual UAS are only separated by 5 m each, are in very good agreement throughout the fleet. Therefore, the difference in the correlation of this UAS in the horizontal pattern could well be due to atmospheric features. An explanation could be the different surface land-use at the location of this UAS. As can be seen in Fig. 1 the far west UAS measures over corn fields while the other involved UAS are hovering over grasslands. Particularly in convective conditions, it is conceivable that such a difference in land-use can cause considerable differences in turbulent structures. This result suggests that spatial measurements can reveal atmospheric features that can not easily be observed from single point measurements.

4.3 Horizontal Coherence

The cross-correlation function describes how the time series of horizontally separated UAS measurements are related. The coherence additionally provides information about the simi-
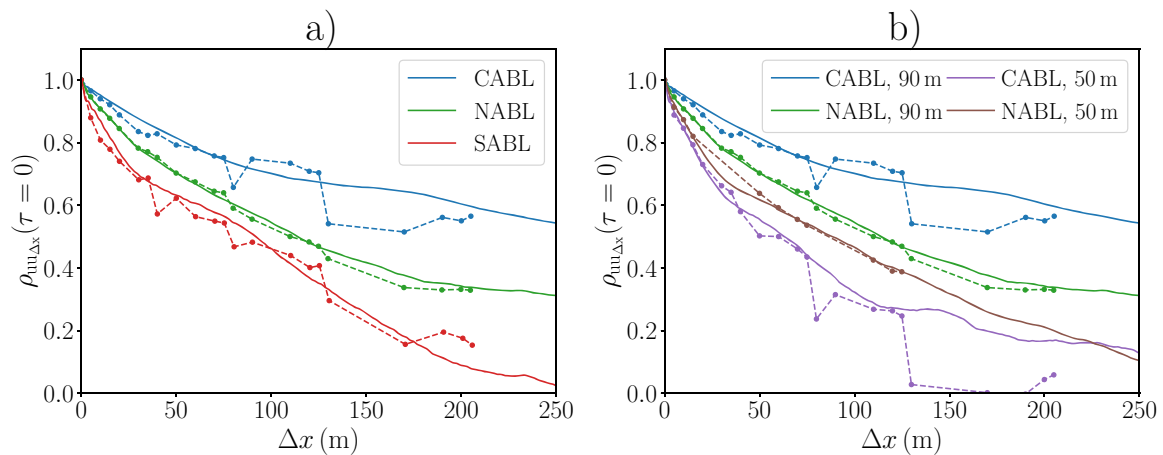
Fig. 7 Cross-correlation within the UAS-fleet of $\tau = 0$, dots and dashed line, in comparison to autocorrelation of single UAS, solid line, for **a** different atmospheric conditions in 90 m a.g.l. and **b** different altitudes (50 m a.g.l. and 90 m a.g.l.). Flight numbers in **a**): 72 (SABL), 100 (NABL), 118 (CABL) and **b**): 100 (90 m, NABL), 102 (50 m, NABL), 118 (90 m, CABL), 124 (50 m, CABL)

larity of flow structures in the frequency space. The intention of this section is to show the capability of the UAS-fleet to determine coherence in the ABL. In the following section, the measurement results are then compared to coherence models to show their applicability and limitations.

Figure 8 shows the longitudinal (a) and lateral (b) coherence of the streamwise velocity fluctuations depending on the frequency for different separation distances Δx and Δy in a neutral ABL. The longitudinal coherence $\gamma^2_{\mathrm{uu}_{\Delta x}}$ is calculated between the closest UAS to the mast and other UAS in longitudinal direction with different separation distances Δx to the reference UAS (see Eq. 15). As expected, the coherence decreases with increasing distance and frequency. The dashed lines outline the corresponding model with an exponential function (see Eq. 18) using individual decay parameters. Additionally, the uncertainties described in Sect. 3 for the chosen degree of freedom M are indicated by the yellow shading for the smallest separation distance of each direction. In lateral direction, only four UAS were aligned. The decay of the lateral coherence is stronger at large scales compared to the longitudinal coherence, but can also be modeled with exponential functions (see Fig. 8). The stronger decay of coherence leads to a smaller frequency range in which flow similarity can be assumed.

4.4 Analysis of Coherence Models

Before we compare the measurement results with coherence models, we need to reduce the dataset for a valid comparison and clarify restrictions, both for the measurements and coherence models.

The coherence at low frequencies does not reach unity if Δx exceeds the integral length scale L_x and the applicability of an exponential decay model is limited in such a case. This is observed at low altitudes and under stable atmospheric conditions, where L_x is typically small. Furthermore, the time of a single hover flight of approximately 12 min is not sufficient for studying the coherence of large separation distances, since the necessary sub-division of the time series only allows an analyzes up to a frequency at whih the coherence has not yet reached its maximum. Due to those restrictions, we only estimate decay parameters for Δx which are small enough to provide solid estimates and compare them for different conditions.
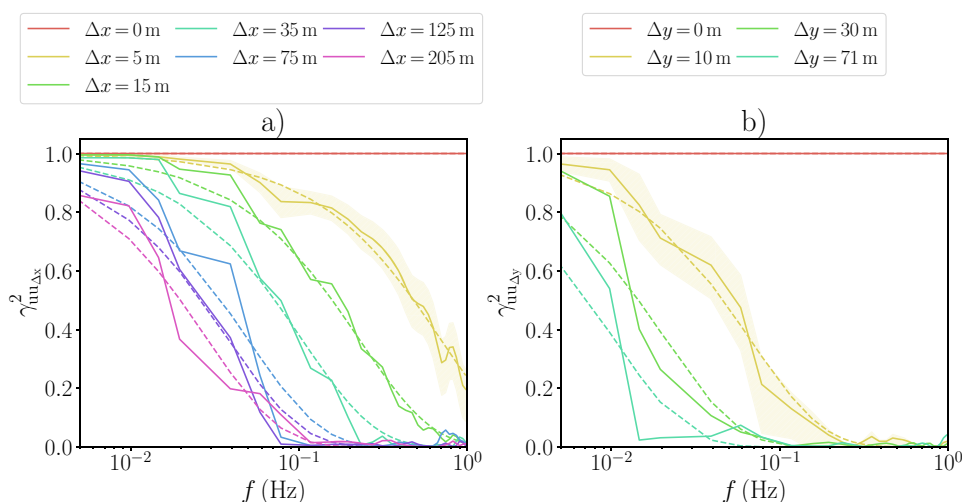
Fig. 8 Coherence of streamwise velocity fluctuations of **a** longitudinally separated UAS measurements and **b** laterally separated measurements on the right side for flight no. 100. In dashed lines, corresponding approximations with exponential decay function (Eq. 18) using individual decay parameters are shown. Uncertainties of the coherence estimation (Sect. 3) are indicated by the yellow shadow for one separation distance of each direction

Longitudinal distances > 35 m and lateral distances > 10 m lead to coherence values which are smaller than unity in the large scales for the current measurement setup. As mentioned in Sect. 3.5, the bias and the uncertainty of the coherence calculation rise with decreasing coherence. Only separation distances smaller than $\Delta x \leq 35$ m and $\Delta y \leq 10$ m are thus considered.

In the following, we compare two of the analytical models for coherence as presented in Sect. 3.5. First, we apply the Davenport (1961) decay model, which is equal in both directions. The coherence model of Schlez and Infield (1998) is then examined, including different models for lateral and longitudinal coherence. The comparison of the models is performed by evaluating the dependency of the decay parameter on the turbulence intensity, since that is the most critical distinction between the two models.

4.4.1 Model Comparison Based on Their Dependency on Turbulence Intensity

The decay parameters for all flights, independent of altitude and atmospheric conditions, are shown in Fig. 9 over turbulent intensity TI for longitudinal (a) and lateral (b) direction. Here, the decay parameters are compared between the Davenport model (blue) and the extended model of Schlez (orange). We observe no clear dependency of the decay parameter c_x and c_y on the turbulent intensity. Despite the fact that Schlez and Infield (1998) (Eq. 20) included the turbulence intensity in their model, the results are not improved compared to Davenport. A universal decay parameter can hardly be used to describe a coherence model for the whole dataset. A wide scatter remains, which is likely due to the wide range of atmospheric conditions in the dataset.

4.4.2 Dependency of Davenports Coherence Model on Atmospheric Conditions

In addition to the question of the dependency on the turbulence intensity, it is examined whether the coherence decay parameter depends on the atmospheric stability. In Fig. 10, the different decay parameters are classified according to the dynamic stability (i.e. bulk
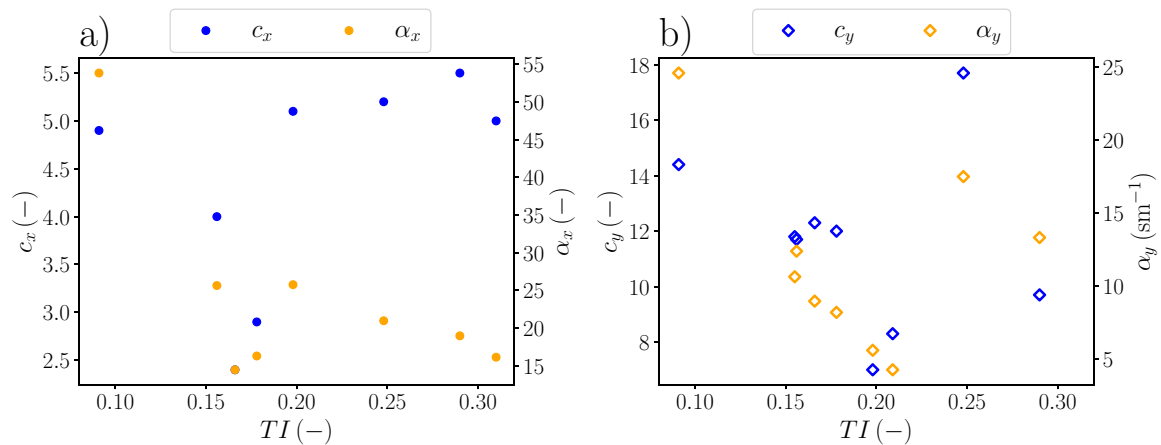
Fig. 9 Coherence decay parameter for Davenport c_x, c_y and for Schlez α_x, α_y approach for **a** longitudinal and **b** lateral direction in dependency of turbulent intensity TI, with separation distances of $\Delta x = 5$ m and $\Delta y = 10$ m

Fig. 10 Coherence decay parameter for the Davenport approach c_x, c_y for longitudinal x and lateral direction y in dependency of the dynamic stability classes defined in Table 1 based on Ri_b, with separation distances of $\Delta x = 5$ m and $\Delta y = 10$ m
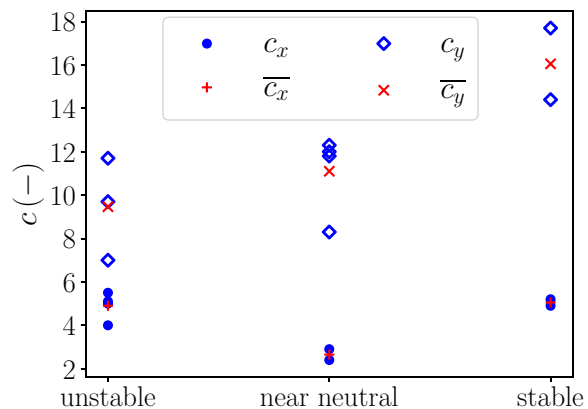
Table 3 Measured mean decay parameters after Davenport model in longitudinal c_x and lateral direction c_y for the 12 considered flights classified by the atmospheric conditions

	CABL	NABL	SABL
$\overline{c_x}$	4.9	2.4	4.8
$\overline{c_y}$	9.5	11.1	16.1

Richardson number Ri_b). In this figure, only the Davenport decay parameters are shown, since the results of the Schlez model do not show clear improvements. Regarding the different directions, it is evident that the decay parameters in the lateral direction c_y take higher values, which indicates less coherence of the flow structure compared to the longitudinal direction(c_x). Considering the lateral direction, the scatter within the different atmospheric conditions is wide. However, regarding the average values, a decrease in coherence could be observed with increasing stability. For clarification, a stronger decrease in coherence leads to a larger decay parameter. In longitudinal direction, the coherence is highest for neutral conditions and decreases in stable and unstable conditions (Table 3). Figure 10 only shows the values for $\Delta x = 5$ m and $\Delta y = 10$ m, which are the smallest separation distances.

Fig. 11 Approximation of the longitudinal coherence of streamwise velocity fluctuations for different atmospheric conditions and separation distances. The coherence is plotted over the wave number k and the separation distance Δx. Dashed lines represent different separation distances Δx of 10, 15, 20, 30, 35 m, the color density decreases with increasing distance
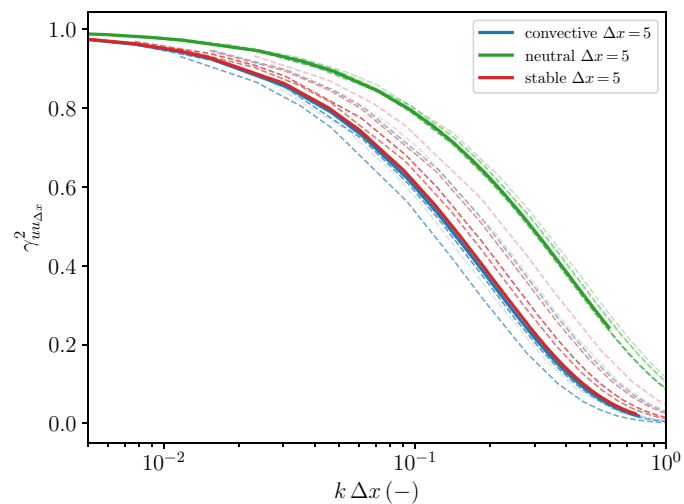
Fig. 12 Decay parameter c_x for different atmospheric conditions in dependency of the longitudinal separation distances Δx. Data from simultaneous flights are connected with dashed lines
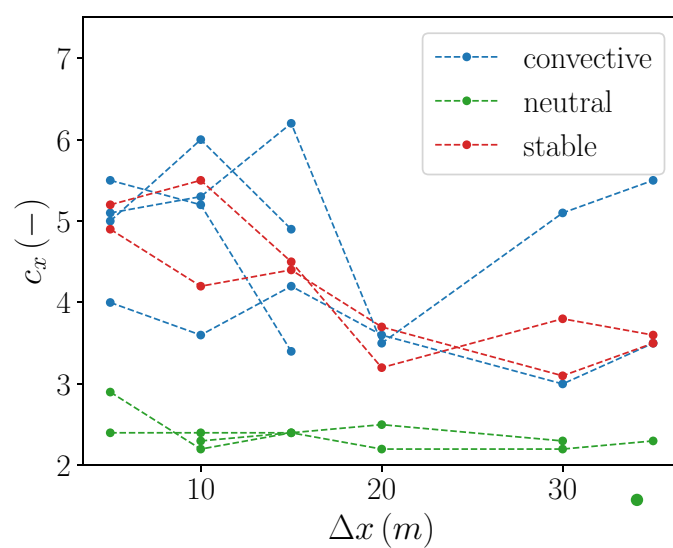
4.4.3 Dependency of Davenports Coherence Model on Separation Distances

As mentioned before, coherence is a function of the separation distance. In the following, we examine whether the dependency on the separation distances proposed by Davenport is generally applicable under different atmospheric conditions. In Fig. 11, longitudinal coherence curves for three cases with different atmospheric stability classes are presented, i.e. stable, neutral and convective. The coherence is plotted against the product of wave number $k = \frac{f}{\bar{u}}$ and separation distance Δx. Following the original Davenport model (Eq. 18), the decay of the coherence should only be a function of $f/\bar{u} \cdot \Delta x$, thus in Fig. 11 the coherence of different separation distances should be equal. However, this only seems to be adequate in neutral conditions. For stable conditions, the decay decreases with increasing separation distances. In convective conditions, the decay parameter is more variable than in the neutral case, but less variable than in the stable case.

In order to examine the capability of the Davenport model to reproduce the dependency of the coherence on the separation distances for different atmospheric conditions for multiple flights, the decay parameter c_x is shown in dependency of the longitudinal separation distance for different atmospheric stability regimes in Fig. 12. During two of the convective cases, the wind velocity was less than 3 m s^{-1} and the integral length scale was too small, so that a determination of c_x for separation distances larger than 15 m was not reasonable. Only very small coherence is observed in the low frequencies in such cases. Due to that, two curves of convective conditions in Fig. 12 end at $\Delta x = 15$ m. For some flights in neutral conditions, the

pattern was incomplete due to technical issues with individual UAS, so that some separation distances are missing. Overall, it can be observed that in neutral conditions c_x is almost constant over distance. For the stable cases, a decrease of the decay parameter with distance is clearly visible. In convective conditions, the scatter is wider and a trend can not be clearly seen.

5 Discussion

5.1 Comparison of the Davenport and Schlez Model

Modeling coherence with an exponential function using the Davenport approach and the further extension by Schlez et al. were originally proposed for neutral atmospheric conditions. The dependency between coherence and separation distance for neutral conditions described in the model is confirmed by Fig. 11. However, in convective and stable conditions, the models are not universally valid. In stable conditions, the decay parameter significantly decreases with increasing distance, although the separation distance is included as a parameter in the model. This dependency of the decay parameter on separation distance in stable conditions is also described by Ropelewski et al. (1973).

In comparison to Davenport, Schlez and Infield (1998) included turbulence intensity into their model, which is a reasonable approach under the assumption that increased statistical turbulence in the flow reduces the coherence. In order to evaluate and compare the scatter of the decay parameters for the Davenport model and the approach by Schlez and Infield (1998), the relative standard deviation d is used. Considering all filtered data, independent of the atmospheric conditions, the deviation for lateral separations ($\Delta y = 10$ m) for Davenport is $d_{D,y} = 0.27$ and for Schlez it is higher with $d_{S,y} = 0.50$. In longitudinal direction, for separation distances of $\Delta x = 5$ m the variation results in $d_{D,x} = 0.26$ and $d_{S,x} = 0.51$ for Davenport and Schlez respectively. The results do not show a reduction of the scatter using the Schlez model. In fact, the Davenport model even shows smaller variation in both directions. The relative standard deviation obviously gets smaller if only flights in a neutrally stratified atmosphere are considered. In these conditions, only small differences between the models are found. It thus seems evident that a simple enhancement of the model with turbulence intensity is not adequate for non-neutral stratification.

5.2 Comparison to Other Studies

To relate the calculated decay parameter c_x and c_y for streamwise velocity component to other studies, we first want to clarify that we are now only referring to the Davenport formulation, and the magnitude-squared coherence γ^2. Shiotani and Iwatani (1980) studied the lateral separation at 40 m height proposing a decay parameter which is a function of the ratio of the separation distance Δy to the height z resulting in $a_y = 14(\Delta y/z)^{0.45}$. Adjusted for the present measurement setup, Shiotani and Iwatani (1980) state a range of $c_y = 10.4 \ldots 13.6$ without distinction of atmospheric stability. The experiment took place at a coast line with high wind speeds of $15 \ldots 40$ m s^{-1}. Schlez and Infield (1998) listed various results from the literature for longitudinal and lateral coherence. The decay parameter in longitudinal direction varies mainly in the range of $c_x = 3 \ldots 8$ and in lateral direction $c_y = 19 \ldots 40$. The experiments that are cited for the lateral direction are not directly comparable due to measurement heights lower than 5 m, separation distances in the range of the integral length

scale, or different surface types such as complex terrain or ice. More relevant for a comparison of lateral coherence is the experiment at the Sotra bridge by Jensen and Kristensen (1979) resulting in $c_y = 14$ for neutral stratification. In comparison, the results of the current study show a range of the decay parameter for lateral separations of $c_y = 9 \ldots 16$ and for longitudinal separations of $c_x = 2 \ldots 5$.

5.3 Coherence of Lateral Separations

In Fig. 10 an increase of the decay parameter with increasing stability is observed for lateral separations of $\Delta y = 10$ m which is in accordance with the study by Ropelewski et al. (1973). For lateral coherence, they found a dependency on the ratio of longitudinal to lateral integral length scales, which itself depends on the atmospheric stratification. The ratio of lateral to longitudinal coherence also increases for stable conditions in comparison to convective ABL. This can be explained by the more narrow shape of turbulent eddies in stable conditions in comparison to a more circular shape in convective conditions. Overall, the results in literature range from $c_x = 3 \ldots 10$ and from $c_y = 9 \ldots 30$, examining various experiments and atmospheric conditions.

For studying the coherence of large separations in the range of the integral length scale, longer measurement times are needed in order to resolve the coherence in larger scales with sufficient accuracy. In particular for stable conditions and for the lateral direction, the coherence is often already very low at comparatively large scales. Theoretically, models can be used that allow for coherence without converging to unity at large scales. However, an additional challenge is that the uncertainty and bias of the coherence calculation are large for small coherence values.

5.4 Implications of Coherence on Taylor's Hypothesis

Mizuno and Panofsky (1975) investigated the limits of Taylor's frozen hypothesis. For that purpose, they proposed a model to estimate the maximum distance at which the hypothesis is still valid. Based on the coherence, which should be close to unity if flow similarity is given, the maximum of the valid spatial separation ΔD is defined as:

$$\Delta D < L_x \frac{2\pi}{c_x}. \tag{25}$$

It depends on the longitudinal integral length scale L_x and the coherence decay parameter c_x. In stable conditions, L_x is typically small due to the damping of vertical motions in the atmosphere, but the coherence decay parameter is typically higher than in convective cases. Both effects decrease the valid distance of Taylor's hypothesis. If we consider a flight in stable conditions during the morning transition of June, 29 (flight number 72) with $L_x = 87$ m and $c_x = 4.5$, the maximum distance for valid Taylor hypothesis results in $\Delta D < 121$ m. Compared to a flight in convective conditions (flight number 118), $L_x = 329$ m and $c_x = 5.5$ lead to a maximum distance of $\Delta D < 376$ m. This information can have implications for the experimental setup and how data from stationary point measurements or aircraft flight legs need to be interpreted.

5.5 ABL Structures Under Different Atmospheric Conditions

In the atmospheric boundary layer, different shapes and characteristics of turbulence are expected for different stratification. The analysis of the longitudinal spatial cross-correlation (see Fig. 6 and Fig. 7) reveals that under neutral conditions frozen turbulence can be assumed, where the spatial development of turbulence is almost negligible in the considered temporal frame. Additionally, the streamwise coherence of longitudinally separated measurements demonstrates high correlations across a wide frequency range in NABL, indicated by small decay parameters (see Fig. 12). If buoyancy terms are significant, either positive (CABL) or negative (SABL), both the coherence and the cross-correlation decrease for increasing longitudinal separation distance. In the NABL coherence scales more uniformly over the separation distance than in SABL and CABL which indicates less spatial variability of the turbulence structures along the considered measurement positions (see Fig. 12). The cross-correlation and coherence of laterally separated measurements, on the other hand, differ significantly between stable and convective stratification. The horizontal shape of flow structures in convective conditions is more circular due to the higher turbulence mixing, which uniforms the turbulence structures. In contrast, in stable conditions and also in neutral conditions, as reported by Hutchins and Marusic (2007), the structures are stretched in the longitudinal direction such that the cross-correlation decays faster in the lateral than in the longitudinal direction (see Fig. 14 in Appendix). In general, the coherence of laterally separated measurements is lower than for longitudinal separations independent of the stratification. However, the ratio between the lateral and longitudinal coherence is largest for neutral and stable conditions (see Fig. 10), which supports the more isotropic shape of the turbulence throughout the observed scales in convective conditions.

For more detailed studies of the shape of turbulent structures, laterally and in particular vertically distributed measurements would be favorable in the future. Vertically distributed measurements would enable an analysis of the vertical shapes of the structures using the presented cross-correlation and coherence methods. These results could be compared with studies from Salesky and Anderson (2018, 2019); Chauhan et al. (2012) who examined the vertical structure of turbulence and the structural steepening under different stratification.

6 Conclusions

During the FESSTVaL campaign, the SWUF-3D fleet of quadrotors was successfully deployed, showing its great potential for studying correlation and coherence with spatially distributed measurements. The turbulent wind measurements were validated to be in good agreement with stationary reference measurements of sonic anemometers at a meteorological mast. We showed with the analyses of cross-spectra, including amplitude and phase, that frequency-resolved processing of data within the fleet is feasible. For the first time, we showed that multicopter UAS can be used for these kinds of measurements. From the presented dataset and results, we can draw multiple conclusions:

1. With a flight pattern of multiple UAS along a horizontal line, the calculation of streamwise ILS using spatial correlation is enabled. The results are in good agreement with the calculation of ILS using the autocorrelation function of the time series of a single UAS when Taylor's hypothesis is valid in neutral atmospheric stratification. In stable and convective conditions, the comparison shows that Taylor's hypothesis is not unconditionally valid in the considered spatial domain.

2. Coherence of the ABL flow is of particular interest for applications where critical wind loads can lead to fatigue and material failure. Measuring coherence is particularly challenging in the field and we showed that a UAS fleet can be a flexible tool to enable such measurements and deepen the understanding. We focused in this study on a demonstration of the feasibility of such measurements and the analysis of the applicability of basic coherence models in different atmospheric conditions at the flat, but heterogeneous field site Falkenberg. Throughout the dataset, the lateral and longitudinal coherence measured with the UAS fleet, show the expected behavior of decreasing coherence with increasing separation distance and smaller frequency scales. The Davenport coherence model shows less scatter than the Schlez-model for all atmospheric conditions. The dependency on turbulence intensity, as proposed by Schlez, could not be confirmed for the decay of coherence with the analyzed flights.

3. We analyzed the decay parameters of the coherence models with respect to the dynamic stability of the ABL. We found that while the Davenport model can be used well to describe coherence for different separation distances with a constant decay parameter in neutral conditions, a high variability arises in stable and convective conditions.

4. The magnitudes of the decay parameters c_x and c_y are in good agreement with other, comparable experiments that are described in literature. For lateral coherence, we found an increase of c_y with increasing stability, which has also been described in the literature before.

5. With L_x and c_x, which can both be determined from the UAS fleet measurements, we also determined the maximum distance of validity for Taylor's hypothesis, which can be of great benefit for future planning of ABL experiments.

6. We could observe that the correlations of one particular UAS, which was furthest away from the other UAS and hovering over a different surface type (cornfield vs. grass), showed significantly different characteristics in convective conditions. This indicates different turbulence structures within a relatively small area and should be investigated in more detail in future.

In future, the results of the coherence can be compared with theoretical models from Mann and von Kármán and with different model approaches that account for coherence only reaching values smaller than one, which are out of scope of this study. With an increased flight time, it will be possible to increase the accuracy of large-scale coherence estimation, which then allows for the analysis of larger separation distances with more robustness. Furthermore, the vertical coherence can also be studied with the UAS-fleet if flight patterns with vertical instead of horizontal alignment of individual UAS are designed. In this context the structural steeping of turbulent structures could be examined by calculating the inclination angle (Chauhan et al. 2012) using vertically distributed measurements. In this study, we only considered the streamwise velocity component, but the component perpendicular to the mean flow is also available and can be analyzed in future. Most recently, we developed new methods to retrieve the vertical wind component as well (Wildmann and Wetz 2022). Using all three wind components, the calculation of the complete coherence tensor becomes possible. Similarly, the calculation of vertical and lateral length scales can be included to gain information about the spatial extent of atmospheric flow structures. Since the fleet of UAS can be deployed most flexibly, we intend to use it in future in more complex terrain, where mast installations are too expensive or impossible. We also see a great potential in the analysis of very instationary turbulent structures such as wind turbine wakes.

of measurement data from the field site of GM Falkenberg. We thank May Bohmann for her assistance with the UAS measurement campaign. Patrick Vrancken internally reviewed the manuscript and we thank him for his valuable comments. We also thank two anonymous reviewers who helped to improve the manuscript.

Data availability The UAS-data are available at Wildmann (2022).

Declarations

Appendix 1: Cross-Correlation Time Lag Error

The lag error, defined as the theoretical lag using Taylor's hypothesis subtracted by the lag of the cross-correlation maxima, is calculated for all flights. This time lag error is shown in Fig. 13a against the cross-correlation maxima for three different atmospheric conditions. Negative lag errors indicate a faster transport of the eddies than the Taylor advection velocity while positive lag errors are related to a slower eddy transport than the advection velocity. For a better relative comparison, the lag error in Fig. 13b is normalized by the theoretical lag. The results show a wide scatter with a tendency towards negative values, which indicates a faster transport of turbulence structures compared to the mean wind speed. However, for this particular case study, the SABL shows a slower eddy transport than the advection velocity. The physical reason for this behavior in this particular flight would require a more detailed analysis which is out of the scope of this paper.
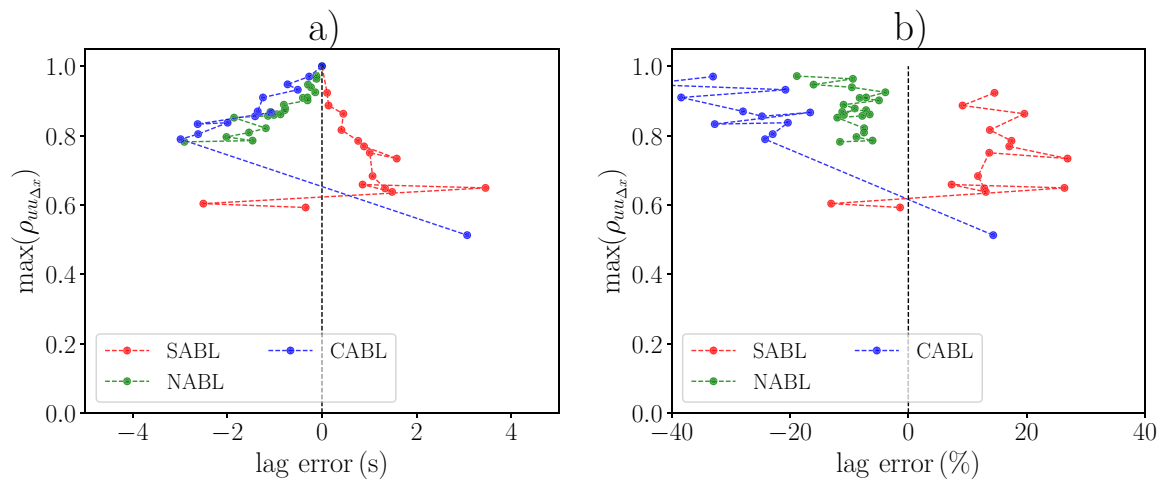
Fig. 13 Lag error of the cross-correlation maxima lag related to theoretic lag by Taylor in dependency of cross-correlation maxima in seconds **a**) and normalized with the theoretical lag in percent **b**) in 90 m a.g.l. for CABL (# 118), SABL (# 72) and NABL (# 100) in b)

Appendix 2: Maxima of Cross-Correlation Function, Lateral vs. Longitudinal Separations

In Fig. 14 the maxima of cross-correlation functions are shown against the separation distances in the longitudinal Δx and the lateral Δy direction. This figure outlines the difference in cross-correlation behavior of longitudinal separations, in comparison to lateral separations under different atmospheric conditions. In convective conditions, the ratio between longitudinal and lateral cross-correlations is small, thus the dependency on spatial correlation is weak, which leads to nearly circular shapes of the turbulence structures. However, under stable and neutral conditions the ratios between longitudinal and lateral correlations are much larger which leads to more narrow, in longitudinal direction stretched, turbulence structures.

Fig. 14 Cross-correlation maxima for longitudinal and lateral distributed measurement against the separation distances Δx and Δy in 90 m a.g.l. for CABL (# 118), SABL (# 72) and NABL (# 100)
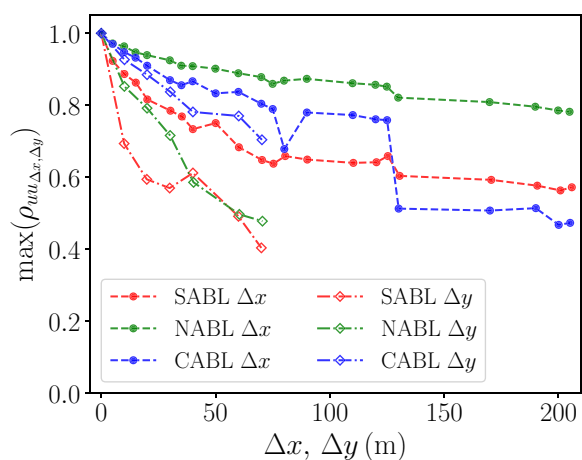
References

Bange J, Beyrich F, Engelbart DAM (2002) Airborne measurements of turbulent fluxes during LITFASS-98: comparison with ground measurements and remote sensing in a case study. Theor Appl Climatol 73(1–2):35–51

Bendat J, Piersol A (2011) Random data: analysis and measurement procedures. Wiley Series in Probability and Statistics, Wiley

Cantero E, Sanz J, Borbón F, Paredes D, García A (2022) On the measurement of stability parameter over complex mountainous terrain. Wind Energy Sci 7(1):221–235

Carter G, Knapp C, Nuttall A (1973) Estimation of the magnitude-squared coherence function via overlapped fast fourier transform processing. IEEE Trans Audio Electroacoust 21(4):337–344

Chauhan K, Hutchins N, Monty J, Marusic I (2012) Structure inclination angles in the convective atmospheric surface layer. Boundary-Layer Meteorol 147(1):41–50

Cheynet E, Jakobsen JB, Snæbjörnsson J, Mikkelsen T, Sjöholm M, Mann J, Hansen P, Angelou N, Svardal B (2016) Application of short-range dual-doppler lidars to evaluate the coherence of turbulence. Exp Fluids 57(12):184

Cheynet E, Flügge M, Reuder J, Jakobsen JB, Heggelund Y, Svardal B, Saavedra Garfias P, Obhrai C, Daniotti N, Berge J, Duscha C, Wildmann N, Onarheim IH, Godvik M (2021) The cotur project: remote sensing of offshore turbulence for wind energy application. Atmos Measure Tech 14(9):6137–6157

Cuxart J, Wrenger B, Matjacic B, Mahrt L (2019) Spatial variability of the lower atmospheric boundary layer over hilly terrain as observed with an rpas. Atmosphere 10(11):715

Davenport AG (1961) The spectrum of horizontal gustiness near the ground in high winds. Q J R Meteorol Soc 87:194–211

Foken T, Wichura B (1996) Tools for quality assessment of surface-based flux measurements. Agric For Meteorol 78(1):83–105

Heisel M, Sullivan PP, Katul GG, Chamecki M (2022) Turbulence organization and mean profile shapes in the stably stratified boundary layer: zones of uniform momentum and air temperature. Boundary-Layer Meteorol

Higgins CW, Froidevaux M, Simeonov V, Vercauteren N, Barry C, Parlange MB (2012) The effect of scale on the applicability of Taylor's frozen turbulence hypothesis in the atmospheric boundary layer. Boundary-Layer Meteorol 143(2):379–391

Horst TW, Kleissl J, Lenschow DH, Meneveau C, Moeng CH, Parlange MB, Sullivan PP, Weil JC (2004) Hats: Field observations to obtain spatially filtered turbulence fields from crosswind arrays of sonic anemometers in the atmospheric surface layer. J Atmos Sci 61(13):1566–1581

Hutchins N, Marusic I (2007) Evidence of very long meandering features in the logarithmic region of turbulent boundary layers. J Fluid Mech 579:1–28

Jensen N, Kristensen L (1979) Lateral coherence in isotropic turbulence and in the natural wind. Boundary-Layer Meteorol 17(3):353–373

Kristensen L, Kirkegaard P (1986) Sampling problems with spectral coherence. No. 526 in Denmark. Forskningscenter Risoe. Risoe-R, Risø National Laboratory

Kristensen L, Panofsky HA, Smith SD (1981) Lateral coherence of longitudinal wind components in strong winds. Boundary-Layer Meteorol 21(2):199–205

Lenschow DH, Stankov BB (1986) Length scales in the convective boundary layer. J Atmos Sci 43(12):1198–1209

Lumley JL, Panofsky HA (1964) The structure of atmospheric turbulence, monographs and texts in physics and astronomy, vol XII. Wiley

Mann J (1994) The spatial structure of neutral atmospheric surface-layer turbulence. J Fluid Mech 273:141–168

Mauder M, Zeeman MJ (2018) Field intercomparison of prevailing sonic anemometers. Atmos Measure Tech 11(1):249–263

Midjiyawa Z, Cheynet E, Reuder J, ágústsson H, Kvamsdal T, (2021) Potential and challenges of wind measurements using met-masts in complex topography for bridge design: Part II - spectral flow characteristics. J Wind Eng Ind Aerodyn 211(104):585

Mizuno T, Panofsky HA (1975) The validity of Taylor's hypothesis in the atmospheric surface layer. Boundary-Layer Meteorol 9(4):375–380

Mohan M (1998) Analysis of various schemes for the estimation of atmospheric stability classification. Atmos Environ 32(21):3775–3781

Moré JJ (1978) The Levenberg–Marquardt algorithm: implementation and theory. In: Watson GA (ed) Numel Anal. Springer, Heidelberg, pp 105–116

Neumann PP, Bartholmai M (2015) Real-time wind estimation on a micro unmanned aerial vehicle using its inertial measurement unit. Sens Actuators A 235:300–310

Panofsky HA (1962) Scale analysis of atmospheric turbulence at 2 m. Q J R Meteorol Soc 88(375):57–69

Panofsky HA, Mizuno T (1975) Horizontal coherence and Pasquill's beta. Boundary-Layer Meteorol 9(3):247–256

Pielke RA, Panofsky HA (1970) Turbulence characteristics along several towers. Boundary-Layer Meteorol 1(2):115–130

Platis A, Siedersleben S, Bange Jea (2018) First in situ evidence of wakes in the far field behind offshore wind farms. Sci Rep 8(2163)

Pope SB (2000) Turbulent flows. Cambridge University Press, Cambridge

Rajewski DA et al (2013) Crop Wind Energy Experiment (CWEX): Observations of Surface-Layer, Boundary Layer, and Mesoscale Interactions with a Wind Farm. Bull Am Meteor Soc 94(5):655–672

Ropelewski CF, Tennekes H, Panofsky HA (1973) Horizontal coherence of wind fluctuations. Boundary-Layer Meteorol 5:353–363

Salesky ST, Anderson W (2018) Buoyancy effects on large-scale motions in convective atmospheric boundary layers: implications for modulation of near-wall processes. J Fluid Mech 856:135–168

Salesky ST, Anderson W (2019) Revisiting inclination of large-scale motions in unstably stratified channel flow. J Fluid Mech 884

Saranyasoontorn K, Manuel L, Veers PS (2004) A Comparison of Standard Coherence Models for Inflow Turbulence With Estimates from Field Measurements. J SolEnergy Eng 126(4):1069–1082

Schlez W, Infield D (1998) Horizontal, two point coherence for separations greater than the measurement height. Boundary-Layer Meteorol 87:459–480

Schlipf D, Trabucchi D, Bischoff O, Hofsäss M, Mann J, Mikkelsen T, Rettenmeier A, Trujillo J, Kühn M (2010) Testing of frozen turbulence hypothesis for wind turbine applications with a scanning lidar system. In: Detaled Program, ISARS. http://www.isars2010.uvsq.fr/

Shimura T, Inoue M, Tsujimoto H, Sasaki K, Iguchi M (2018) Estimation of wind vector profile using a hexarotor unmanned aerial vehicle and its application to meteorological observation up to 1000 m above surface. J Atmos Oceanic Tech 35(8):1621–1631

Shiotani M, Iwatani Y (1980) Gust structures over flat terrains and their modification by a barrier. In: Wind engineering. Elsevier, pp 203–214

Simley E, Pao LY (2015) A longitudinal spatial coherence model for wind evolution based on large-eddy simulation. In: 2015 American Control Conference (ACC), pp 3708–3714

Smalikho I, Köpp F, Rahm S (2005) Measurement of atmospheric turbulence by 2-μm doppler lidar. J Atmos Oceanic Tech 22(11):1733–1747

Stull R (2016) Practical meteorology: an algebra-based survey of atmospheric science. University of British Columbia, AVP International

Taylor GI (1938) The spectrum of turbulence. Proc R Soc Lond Ser 164(919):476–490

Thresher R, Holley W, Smith C, Jafarey N, Lin S (1981) Modeling the response of wind turbines to atmospheric turbulence. Oregon State Univ., Corvallis (USA). Dept. of Mechanical Engineering, Tech rep

von Kármán T (1948) Progress in the statistical theory of turbulence. Proc Natl Acad Sci 34(11):530–539

Wetz T, Wildmann N (2022) Spatially distributed and simultaneous wind measurements with a fleet of small quadrotor UAS. J Phys: Conf Ser 2265(2):022086

Wetz T, Wildmann N, Beyrich F (2021) Distributed wind measurements with multiple quadrotor unmanned aerial vehicles in the atmospheric boundary layer. Atmos Measure Tech 14(5):3795–3814

Wildmann N (2022) Multicopter UAS measurements at GM Falkenberg during FESSTVaL 2021. https://doi.org/10.25592/UHHFDM.10148

Wildmann N, Wetz T (2022) Towards vertical wind and turbulent flux estimation with multicopter UAS. EGUsphere 2022:1–20

Wildmann N, Rau GA, Bange J (2015) Observations of the early morning boundary-layer transition with small remotely-piloted aircraft. Boundary-Layer Meteorol 157(3):345–373

Wildmann N, Päschke E, Roiger A, Mallaun C (2020) Towards improved turbulence estimation with doppler wind lidar velocity-azimuth display (VAD) scans. Atmos Measure Tech 13(8):4141–4158

A.4 Multi-point in situ measurements of turbulent flow in a wind turbine wake and inflow with a fleet of uncrewed aerial systems

Multi-point in situ measurements of turbulent flow in a wind turbine wake and inflow with a fleet of uncrewed aerial systems

Tamino Wetz and Norman Wildmann

Institut für Physik der Atmosphäre, Deutsches Zentrum für Luft- und Raumfahrt e.V.,
Oberpfaffenhofen, Germany

Correspondence: Tamino Wetz (tamino.wetz@dlr.de)

Abstract. The demand on wind energy for power generation will increase significantly in the next decade due to the transformation towards renewable energy production. In order to optimize the power generation of a wind farm, it is crucial to understand the flow in the wind turbine wake. The flow in the near wake close to downstream of the wind turbine (WT) is complex and highly three-dimensional. In the present study, for the first time, the SWUF-3D (Simultaneous Wind measurement with Unmanned Flight Systems in 3D) fleet of multirotor UASs (uncrewed aerial systems) is deployed for field measurements on an operating 2 MW WT in complex terrain. The UAS fleet has the potential to fill the meteorological gap of observations in the near wake with high-temporal- and high-spatial-resolution wind vector measurements plus temperature, humidity and pressure. During the experiment, the flow up- and downstream of the WT is measured simultaneously. Various flight patterns are used to investigate the near wake of the WT. The velocity deficit and the turbulence profile at different downstream distances are measured by distributed UASs which are aligned perpendicular to the flow in the near wake. The results show the expected double-Gaussian shape in the near wake under nearly stable atmospheric conditions. However, measurements in unstable atmospheric conditions with high turbulence intensity levels lead to single-Gaussian-like profiles at equal downstream distances ($< 1\,D$). Additionally, horizontal momentum fluxes and turbulence spectra are analyzed. The turbulence spectra of the wind measurement at the edge of the wake could reveal that tip vortices can be observed with the UASs.

1 Introduction

According to statements by the IEA (2022b), the role of renewable energies in power generation will increase dramatically over the next decade. In the Announced Pledges Scenario (APS), renewable energy will outpace fossil fuels for electricity generation by 2030. This transformation is necessary to achieve the goal of net-zero emissions by 2050. An annual increase of 18 % in wind energy capacity is needed to reach the next milestone in 2030 with global wind power generation of 7300 TWh (IEA, 2022a). On the one hand, an increased demand for wind energy is met by optimizing the power output of an individual turbine, which is mainly achieved with a further enlargement of the wind turbine

(WT) rotors. On the other hand, the power output of entire wind farms must be optimized. The wake that forms behind a wind turbine plays a central role in the optimization of wind farm design and control. The wakes significantly reduce the power output of the downstream turbines when operating in the wake. The increased size of WTs leads to even more pronounced wakes and shorter relative distances between turbines, especially in wind farms that undergo repowering. In order to cover the enormous demand for wind energy, the available space will have to be used as efficiently as possible. This requires closer staggering in wind farms, which in turn leads to more significant wake effects. Veers et al. (2022, 2019) mention the understanding of turbulent flow around WTs in the atmospheric boundary layer as one of

the major challenges in wind energy research, which is supported by Porté-Agel et al. (2019). This need for research is caused by the high complexity of the atmospheric flow and its interaction with the WT. The wake, which forms downstream of a WT, particularly causes losses on the downstream WT in wind parks due to the velocity deficit (Sanderse et al., 2011). Additionally, the increased turbulence can lead to higher fatigue loads on the downstream turbines (Frandsen, 2007).

In order to understand and classify the wake measurements, a brief overview of the flow around a WT is given below. In general, the flow in the atmospheric boundary layer is affected both upstream and downstream of the WT. The induction zone is the area upstream in which the wind speed is reduced due to blockage effects from the WT. The velocity reduction can be estimated depending on the upstream position and the induction factor (Simley et al., 2016). The regime downstream of the turbine is divided into a near wake and a far wake (Vermeer et al., 2003). The near wake is characterized by highly heterogeneous and complex flow distribution and is closely related to the design and operation of the WT. This region extends from the rotor plane to a distance of 2 to 4 D (rotor diameter) downstream (Wu and Porté-Agel, 2012). The flow field of the far wake is less heterogeneous, resulting in a more universal velocity deficit distribution, and is less influenced by the detailed design and operation of the WT. Further downstream, the velocity increases continuously towards freestream velocity while the turbulence intensity decreases (Porté-Agel et al., 2019). The wake recovery is found to be complete at distances of up to 8 D downstream but extends further for large rotor diameters and under stable atmospheric conditions where wakes persist much longer than in unstable conditions (Fuertes et al., 2018). In this study we focus on field experiments in the near wake. The most prominent flow structure in the near wake is the tip vortex helix, besides the root vortex of the blades and the hub vortex. The helical vortex structure results from tip vortices which are induced by the pressure difference of the pressure and the suction side at the rotor blade tips. Various research groups studied the formation and the stability of tip vortices (Sherry et al., 2013; Zhang et al., 2011; Odemark and Fransson, 2013). The formation and the stability of tip vortices are of great interest due to the fact that tip vortices prevent the outer flow entrainment into the near wake (Lignarolo et al., 2014). Therefore, the breakdown of the helix structure enhances turbulent mixing from the outer flow towards the wake center, which leads to wake recovery. This area is typically characterized as the transition between near and far wake, where the mixing from outside towards the center of the wake significantly increases (Wu and Porté-Agel, 2012). The breakdown of the helix usually starts when helix vortex pairing occurs (Odemark and Fransson, 2013). In convective conditions the lifetime of tip vortices is significantly reduced by the high turbulence in the freestream (Lu and Porté-Agel, 2011).

Due to conservation of momentum the rotation of the WT induces a flow deflection in the opposite direction, such that for a clockwise-rotating WT (viewed from upstream towards the WT) the wake rotates counterclockwise (Manwell, 2009). This rotation is distributed over the entire rotor swept area and decreases further downstream. Depending on the yaw misalignment of the WT (Bastankhah and Porté-Agel, 2016), the atmospheric conditions (Abkar and Porté-Agel, 2015) and the direction of WT rotation (Englberger et al., 2020), different wake patterns can develop further downstream.

In the far wake the wind speed deficit is often modeled as a Gaussian distribution around the center, implying the lowest velocity in the center of the WT. However, in the near wake the averaged wind deficit can also be distributed in a double-Gaussian shape in lateral direction indicating high velocities around the center of the wake, while the wake edges are characterized by regions of low velocities. The high-velocity region in the center is due to low momentum extraction by the blades with a small radius (Magnusson, 1999; Crespo et al., 1999; Keane et al., 2016; Bastankhah and Porté-Agel, 2017; Krogstad and Adaramola, 2011; Machefaux et al., 2015). Detailed reviews about wake aerodynamics have been conducted by Porté-Agel et al. (2019) and Vermeer et al. (2003).

In the past, the wake of WTs has been extensively studied using numerical methods, from basic engineering analytic models for single turbines (Jensen, 1983) and wind farm optimization (Bastankhah and Porté-Agel, 2014) towards high-resolution large eddy simulations (LESs) (Mehta et al., 2014). The flow around WTs has been examined in great detail in wind tunnel experiments by many research groups using various flow measurement techniques such as particle image velocimetry (PIV) (Sherry et al., 2013; Bastankhah and Porté-Agel, 2017) or flow visualization with smoke (Hand et al., 2001). In addition to the laboratory flow, the wake has been studied in field campaigns under real atmospheric flow conditions. Most prominent in the last decades are measurements by remote sensing technologies such as Doppler wind lidar. Lidar measurements are carried out both from the ground and directly from the nacelle of a WT. Ground-based lidar measurements are used, for example, to investigate the wake characteristics and development in complex terrain (Wildmann et al., 2020; Menke et al., 2018). They can be used to determine the wake center and track the extension of the wake in the far wake (Wildmann et al., 2018b), analyze turbulence within the wake (Wildmann et al., 2020), or study the wake length dependency on atmospheric conditions (Wildmann et al., 2018a). Nacelle lidars or even spinner-integrated lidars are often used for flow measurements to optimize the active yaw control of the WT (Mikkelsen et al., 2012). In addition, they are deployed for characterizing the WT wake (Aitken and Lundquist, 2014; Brugger et al., 2020; Machefaux et al., 2015; Fuertes et al., 2018) and for model validation (Doubrawa et al., 2020).

More qualitative studies on wake flow characteristics, including coherent structure analysis, have been performed

by Yang et al. (2016), Abraham et al. (2021), and Dasari et al. (2018) using snowflakes to visualize coherent structures. Even PIV was implemented by Abraham et al. (2021) employing snowflakes as a tracer to determine wind speed.

In addition to remote sensing, in situ measurements were carried out to study the flow around WT. Airborne systems that were used for this purpose range from uncrewed flight systems (UASs) in fixed-wing configurations (Kocer et al., 2011; Wildmann et al., 2014; Reuder et al., 2016; Mauz et al., 2019; Alaoui-Sosse et al., 2022) and rotary wing configurations (Thielicke et al., 2021; Li et al., 2022) to crewed measurements around wind parks with a Dornier DO 128 research aircraft (Platis et al., 2021). All the mentioned in situ measurements are based on only one device. This allows only a single time step at a variable spatial position or (for multicopters) a single time series at a fixed spatial position. The approach of using a fleet of multicopters enables highly resolved observations at multiple spatial positions simultaneously. Besides the simultaneous measurement of inflow and wakes, it is possible to conduct multiple time series of the flow at different discrete positions in the wake.

The objective of this work is to examine the near wake of the WT in operational conditions and can be divided into different hypotheses and research questions.

- Can a fleet of UASs measure a double-Gaussian velocity deficit and turbulence intensity profile in the near wake of a WT?

- Do the horizontal momentum fluxes point towards the inner wake at the edge of the wake?

- It is possible to capture the tip vortex with multicopter measurements at the edge of the wake?

- Do the near-wake characteristics significantly change at different downstream distances ($< 2\,D$)?

- What are the influences of atmospheric stability on the near wake regarding the velocity deficit and the turbulence intensity?

The present study is structured as follows: first, in Sect. 2, we describe the experimental setup, including the UAS fleet, the measurement location and the flight strategies. Various methods that are necessary for the evaluation and discussion of the data are then explained in Sect. 3. The results of the field measurements of the UAS fleet on a WT are presented in Sect. 4 and then discussed (Sect. 5). Finally, the results are summarized in a conclusion (Sect. 6).

2 Experiment

2.1 Measurement hardware

The SWUF-3D (Simultaneous Wind measurement with Unmanned Flight Systems in 3D) fleet consists of more than 30 quadrotor UASs. The dimensions of the UASs are relatively small with a distance between two rotor axes of 0.25 m and a take-off weight of 0.645 kg. The UAS is controlled by an autopilot based on inertial measurement unit (IMU) and global navigation satellite system (GNSS) data. The wind speed is measured in hover flight without an additional flow sensor. The wind measurements are carried out by relating the quadrotor movements to the acting wind forces while hovering at a fixed position. With this method accurate wind speed and wind direction measurements can be achieved for the entire fleet (Wetz and Wildmann, 2022). In addition, temperature and humidity are measured by an external sensor. The hardware and the wind algorithm are described in more detail in earlier publications (Wetz et al., 2021; Wetz and Wildmann, 2022). The accuracies (RMSE) of the measurement system are $\epsilon_u = 0.25\,\mathrm{m\,s^{-1}}$ for the mean wind speed, $\epsilon_{\sigma^2} = 0.16\,\mathrm{m^2\,s^{-2}}$ for the wind speed variance and $\epsilon_\Phi < 5°$ for the wind direction. There we showed that turbulent structures can be resolved until a temporal resolution of 1 Hz. Although in previous experiments we have demonstrated the operation of 20 UASs simultaneously with a flight permit in a specific category, in the present study only 5 UASs were operated in the open category of the EASA (European Union Aviation Safety Agency) regulations.
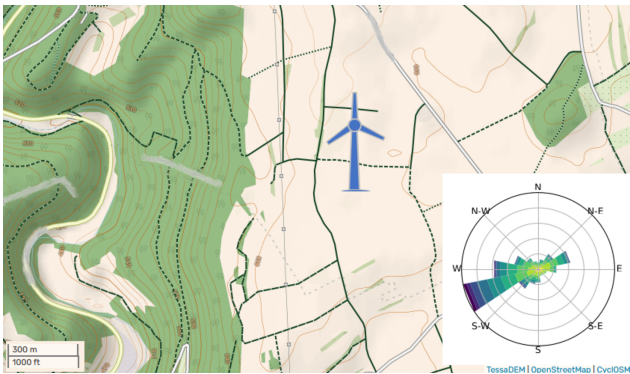
2.2 Measurement site

The measurements were conducted at an Enercon E-82 E2 WT with a rated power of 2 MW, which is reached at a wind speed of $12.5\,\mathrm{m\,s^{-1}}$. The WT is located in complex terrain on an elevated plateau. A prominent slope at 0.5 km to the west with an elevation of about 180 m, resulting from a river valley, dominates the topography (see Fig. 1). The wind direction at the site is dominated by westerly winds (see wind rose in Fig. 1 extracted from the New European Wind Atlas, NEWA). Due to the complex terrain, the WT operates at a comparably high hub height of 138 m with a rotor diameter of $D = 82$ m. The wind direction is measured by a sonic anemometer on the nacelle. Operating data from the WT are available through the SCADA system (Supervisory Control And Data Acquisition system) but are not explicitly presented in this study due to confidentiality agreements.

2.3 Flight strategy

In total, we carried out more than 80 UAS fleet flights on 7 measurement days in 2022. We performed flights both in the early morning under stable atmospheric conditions and under unstable conditions during the day. During the flights, wind speeds between 5 and $13\,\mathrm{m\,s^{-1}}$ were observed from westerly directions in most cases.

Different flight patterns were performed to study the wake of the WT and to measure the free flow at the same time. The measurement time is about 12 min, but only 10 min are considered in order to ensure overlapping time series of the

Figure 1. Topographical map of the measurement site including the location of the WT and the wind rose from the site. © OpenStreetMap contributors 2022. Distributed under the Open Data Commons Open Database License (ODbL) v1.0.

complete UAS fleet and use a standard averaging period in wind energy applications. In the first pattern, referred to as the "longitudinal pattern", the UASs are horizontally distributed in streamwise (longitudinal) direction at an altitude of 120 m a.g.l. (above ground level) downstream of the WT. Note that this height is slightly lower than the hub height which is at 138 m. Due to the operation in the open category, we were limited to flight altitudes of 120 m at distances far from the WT. Multiple UASs are positioned in this horizontal longitudinal line at different distances from the WT (up to $x = 3 D$) with horizontal spacing between the UASs of $x = 0.5 D$. This pattern is illustrated by the blue diamonds in Fig. 2. Additionally to the wake measurement, the inflow is measured at a longitudinal distance of $2 D$ upstream of the WT (illustrated by the green diamond in the "inflow" pattern in Fig. 2). On the UASs' way to the measurement height at 120 m a.g.l. the thermal stratification is measured during the ascent. This means that a vertical profile of the WT inflow is also available at the beginning of each wake measurement. The goal of a second flight pattern in the wake is to measure the horizontal profiles of the wake. In this so-called "lateral pattern", multiple UASs are distributed laterally to the main wind direction in the wake of the WT. The lateral positions of the UASs (relative to the WT nacelle) are chosen so that one UAS measures in the freestream at $y = 1 D$ and the remaining UASs measure inside the WT wake. The lateral spacing within the wake is designed to resolve the edge region of the wake in particular. This pattern is conducted at different longitudinal distances to the WT from $x = 0.5$ to $1.5 D$. The orientation of the pattern was chosen based on the freestream wind direction measured by the UASs and the current orientation of the WT. The most recent orientation of the WT was obtained from SCADA data, and the momentary orientation was additionally estimated visually. Before each launch of the UAS fleet, the orientation of the pattern was updated to ensure alignment to the current wind direction.
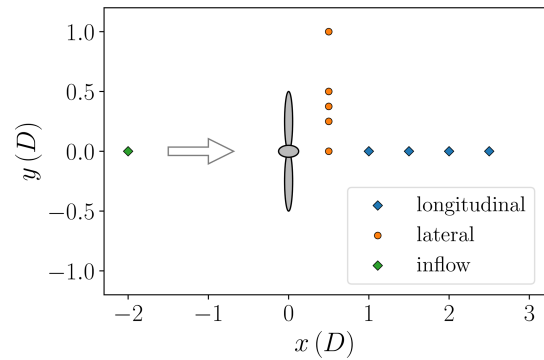
Figure 2. Different flight patterns of the UAS fleet from the top view. The arrow represents the wind direction towards the WT.
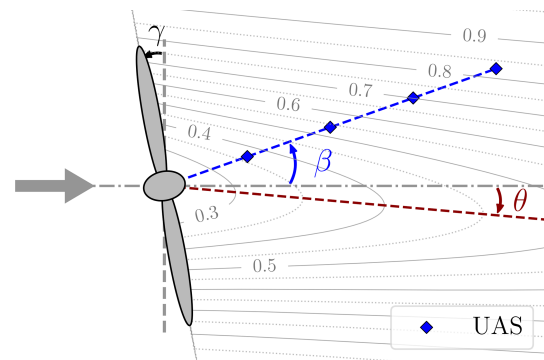
Figure 3. Misalignment of the WT and the UAS fleet from the top view. The reference inflow wind direction is represented by the arrow. γ defines the yaw misalignment of the WT. The deviation of the orientation of the UAS pattern (blue diamonds) is defined by the angle β. The resulting wake deflection, due to the yaw misalignment, is defined by the deflecting angle θ. The velocity deficit in the wake is illustrated by contour lines and extracted from FLORIS (NREL, 2021).

The wind direction and the orientation of the WT in atmospheric boundary layer flows are not stationary and can change frequently. For this reason, misalignment in field measurements of an operational WT cannot be precluded. The definitions of flight pattern alignment and WT misalignment are introduced in Fig. 3. γ is defined as the yaw misalignment of the WT rotor to the incoming flow. Due to a yaw misalignment, the wake is deflected laterally by the deflection angle θ. In addition to the characteristics of the inflow, the deflection angle depends on the thrust coefficient C_T of the WT. A higher thrust coefficient leads to a higher deflection of the wake (Bastankhah and Porté-Agel, 2016). Additionally, the misalignment of the UAS flight pattern with the incoming wind direction is defined as β.

3 Methods

3.1 Characterization of WT inflow

For characterization of the inflow and the atmospheric conditions, various parameters are determined and defined in the following. As mentioned in the Introduction, the inflow significantly influences the characteristics of the WT wake. From the inflow pattern (2 D upstream), the vertical profile is used for thermal stratification classification and a 10 min averaging period at the final measurement position for wind and turbulence properties. First, the mean wind velocity $\overline{u}$ and mean wind direction $\overline{\Phi}$ are calculated for the 10 min hover time in the freestream. From the mean wind direction and the mean orientation angle of the WT, the actual alignment of the orientation of the pattern β and the mean yaw misalignment of the WT γ can be derived (see Fig. 3). Furthermore, the standard deviation of the inflow wind direction σ_Φ is listed as a parameter in Table 1, since it is a measure of the unsteadiness of the flow and influences the accuracy of the relative position of the UAS point measurements in the wake. Since no continuous high-resolution measurement of the wind vector is available, we cannot easily discriminate between turbulence and mesoscale contributions to wind direction changes during our individual 10 min measurement periods. We thus only look at the resulting mean wind and turbulence during the averaging period.

The turbulence intensity I is used as the measure of the turbulence level. I is defined as the standard deviation of the streamwise velocity σ_u normalized by the mean velocity $\overline{u}$:

$$I = \frac{\sigma_u}{\overline{u}}. \tag{1}$$

In the following we refer to the streamwise turbulence intensity I. Additionally, in Table 1 the variance σ_u^2 of the inflow is listed, since it accounts for a significant proportion of the turbulent kinetic energy. The thermal stratification is derived from the lapse rate Γ in the corresponding heights of the WT (from 80 to 120 m). The lapse rate is defined by the gradient of the virtual potential temperature $\Delta\theta_v$ with altitude Δz:

$$\Gamma = \frac{\Delta\theta_v}{\Delta z}. \tag{2}$$

The gradient is calculated using a linear regression within the mentioned height range. The atmospheric boundary layer (ABL) is divided into convective (CABL) for negative lapse rate ($\Gamma < -0.5$ K per 100 m), near-neutral (NABL) for close to zero ($|\Gamma| < 0.5$) and stable (SABL) for positive laps rate ($\Gamma > 0.5$) (Mohan, 1998). Since the wind speed for the rated power is 12.5 m s^{-1} for most of the present flight cases, the WT is operating below rated power. Only for flight no. 206 and no. 207 is the WT operating near the rated power.

3.2 WT wake analysis

In order to analyze the WT wake, more parameters need to be defined in this section. One important parameter for classifying the WT operation point is the tip speed ratio λ. The tip speed ratio (TSR) is defined by the tip speed calculated from the rotor diameter D and the angular velocity ω ($\omega = 2\pi\Omega$) divided by the freestream velocity u_0:

$$\lambda = \frac{\omega D/2}{u_0}. \tag{3}$$

The frequency of occurrence of the tip vortex at a fixed position is called the blade-passing frequency f_{bp}, which is defined by the rotational frequency Ω of the rotor and the number of blades $n_b = 3$:

$$f_{bp} = \Omega n_b. \tag{4}$$

If the rotational speed is presented in revolutions per minute (rpm), it needs to be transformed to revolutions per second. The turbulence intensity which is added to the freestream turbulence by the WT is called *added turbulence intensity* ΔI. It is calculated from the freestream turbulence I_0 and the measured turbulence intensity inside the wake I (Frandsen, 2007):

$$\Delta I = \sqrt{I^2 - I_0^2}. \tag{5}$$

The horizontal momentum flux $\overline{u'v'}$ is defined by the covariance of the horizontal wind components u and v divided by the number of time steps N:

$$\overline{u'v'} = \frac{\sum(u_i - \overline{u})(v_i - \overline{v})}{N}. \tag{6}$$

An analytical estimation of the near-wake length l_{nw} is conducted in order to distinguish whether we are measuring in the near or far wake. The equation is derived from wind tunnel experiments by Bastankhah and Porté-Agel (2016):

$$\frac{l_{nw}}{D} = \frac{\cos\gamma\left(1 + \sqrt{1 - C_T}\right)}{\sqrt{2}\left(c_\alpha I + c_\beta\left(1 - \sqrt{1 - C_T}\right)\right)}, \tag{7}$$

with the constant parameters $c_\beta = 0.154$ and $c_\alpha = 3.6$ (Fuertes et al., 2018). From this equation for an unstable condition with high turbulence intensity (no. 206) the length is $l_{nw} = 1.7\,D$, while for a stable case (no. 604) the near-wake length is $l_{nw} = 2.9\,D$.

In order to estimate the influence of the yaw misalignment on the wake deflection, an analytical dependency is presented. This estimation is based on the conservation of momentum and mass and is a function of the downstream distance x and the yaw misalignment γ (Jiménez et al., 2009):

$$\theta = \frac{\sin\gamma\, C_T}{2\left(1 + \zeta\frac{x}{D}\right)^2}, \tag{8}$$

Table 1. Flight protocol of considered flights in Sect. 4. The first number of the flight number (no.) indicates the flight day (for instance flight 611 is carried out on flight day 6). The variables are calculated from the reference measurement, and the definitions are listed below: γ yaw misalignment; β deviation of pattern orientation; $\overline{u}$ mean velocity; Φ mean wind direction; σ_{Φ} standard deviation of wind direction; I_x streamwise turbulent intensity; σ_u^2 streamwise velocity variance; Γ the lapse rate; and ABL atmospheric boundary layer with convective (CABL), stable (SABL) and neutral (NABL).

Date	Time [UTC]	No.	γ [°]	β [°]	Pattern	$\overline{u}$ [m s^{-1}]	Φ [°]	σ_{Φ} [°]	I_x [–]	σ_u^2 [m^2 s^{-2}]	Γ [K per 100 m]	ABL
18 Feb 2022	11:05	206	7.3	7.1	Lateral ($x = 0.5\,D$)	11.57	242	11	0.214	5.85	−0.511	CABL
18 Feb 2022	11:24	207	6.9	4.1	Lateral ($x = 0.5\,D$)	12.43	239	11	0.216	7.09	–	CABL
28 Apr 2022	10:30	407	21.5	9	Lateral ($x = 0.5\,D$)	6.92	79	11	0.166	1.53	–	CABL
28 Apr 2022	11:26	409	15.5	−15.4	Lateral ($x = 1\,D$)	6.47	75	11	0.144	0.83	−0.522	CABL
28 Apr 2022	11:47	410	21.6	3	Lateral ($x = 1\,D$)	6.42	73	11	0.157	1.2	−0.812	CABL
12 May 2022	04:13	604	20.6	19.2	Longitudinal	6.96	264	4	0.073	0.28	0.067	NABL
12 May 2022	04:34	605	16.2	18.2	Lateral ($x = 0.5\,D$)	6.5	264	5	0.074	0.28	0.253	NABL
12 May 2022	04:53	606	7.6	6.4	Lateral ($x = 0.5\,D$)	6.18	257	8	0.089	0.35	0.76	SABL
12 May 2022	05:14	607	15.7	8.9	Lateral ($x = 1\,D$)	6.08	259	8	0.091	0.34	−0.063	NABL
12 May 2022	05:35	609	20	16.3	Longitudinal	6.04	261	8	0.111	0.49	0.79	SABL
12 May 2022	06:00	611	18.5	12.8	Longitudinal	7.1	263	8	0.112	0.62	−0.109	NABL
12 May 2022	06:20	613	14.1	7.8	Longitudinal	7.05	258	9	0.115	0.96	0.109	NABL
7 Nov 2022	07:10	702	13	4.9	Lateral ($x = 0.5\,D$)	9.04	245	7	0.119	1.14	0.311	NABL
7 Nov 2022	07:31	703	13.9	0.6	Lateral ($x = 1\,D$)	9.17	240	7	0.132	1.43	0.684	SABL
7 Nov 2022	07:53	704	17.7	2.6	Lateral ($x = 1\,D$)	9.29	242	6	0.124	1.55	0.001	NABL
7 Nov 2022	08:20	706	19.5	5.8	Longitudinal	7.48	246	7	0.172	1.7	0.083	NABL
7 Nov 2022	09:06	708	15.2	6.4	Longitudinal	6.97	246	8	0.207	2.15	0.121	NABL
7 Nov 2022	09:25	710	16.2	12.4	Longitudinal	7.77	252	8	0.142	1.19	0.108	NABL
7 Nov 2022	09:50	711	8.9	4.6	Lateral ($x = 0.5\,D$)	8.66	245	8	0.144	1.56	0.031	NABL
7 Nov 2022	10:12	712	10.9	5.2	Lateral ($x = 0.5\,D$)	7.76	245	8	0.124	1.11	0.13	NABL
7 Nov 2022	10:39	713	13.1	8.4	Lateral ($x = 0.5\,D$)	7.74	249	9	0.151	1.44	−0.082	NABL

where ζ is the wake growth rate. Jiménez et al. (2009) defined $\zeta = 0.1$ for yaw misalignments smaller than $\gamma = 20°$. For the considered flights the mean maximal yaw misalignment is about $\gamma = 20°$. Together with an approximate $C_T = 0.7$ the deflection is $\theta = 5.7°$ at a downstream distance of $1\,D$.

4   Results

At the field site we performed multiple flight strategies in different atmospheric conditions over several days. Two flight strategies are considered in detail, namely the longitudinal and lateral patterns. In this section, we first give an overview of all performed flights. This is followed by a detailed analysis of a single flight considering the time series of a lateral pattern and the associated turbulence spectra. The lateral profile of the velocity, the turbulence intensity and the horizontal fluxes for stable to near-neutral atmospheric conditions are examined in the middle section. The downstream evolution of the wake is studied using the longitudinal flight pattern. Finally, the results of the lateral pattern under unstable atmospheric conditions are compared to stable conditions.

4.1   Overview flight data

In Fig. 4 all considered individual UAS flights are shown by a single point at their horizontal measurement position. The coordinate system of UAS locations is aligned with the reference wind direction, and the coordinate origin is locked in the center of the WT but is independent of the orientation of the WT. For example, if the alignment of the longitudinal pattern does not match the reference wind direction measurement, this discrepancy is visible through the angle of the UAS pattern alignment compared to the longitudinal centerline of the wake. The misalignment of the wind turbine to the wind direction is not included in the figure. The normalized wind velocity is indicated by the marker color. Depending on the pattern, the wind velocity is normalized either with UAS measurement upstream ($x = 2\,D$) for the longitudinal pattern or with measurements in the freestream ($y = 1\,D$) for the lateral pattern. Thus, the normalized velocity shows the velocity deficit measurements in the wake. This figure clearly shows qualitatively the wind deficit in the WT wake at different positions. The velocity deficit in longitudinal and lateral directions is examined in more detail in the following sections. The trend in the misalignment between the pattern orientation and the freestream wind direction β is due to the trade-off between wind direction and WT orientation, since

116

the WT orientation shows a clear yaw misalignment throughout the experiment. The different angles are illustrated in Fig. 3, and reasons for the differences are discussed in the following section.

4.2 Reference measurements

On the measurement site only a single WT exists without any further measurement devices, such as meteorological mast or lidars. In order to study the wake of a WT, it is essential to measure the ambient conditions during the wake measurements. Therefore, additionally to each wake measurement, a reference measurement is conducted with the UAS fleet. As already mentioned, the reference is measured either $2 D$ upstream in the inflow or $1 D$ in lateral distance to the side of the WT. After a slow ascent, during which a vertical profile of all thermodynamic variables can be measured, the UAS hovers for 10 min at the top altitude to determine a reference wind direction and wind speed. In Fig. 5 the measured reference wind direction is compared with data from the WT SCADA system. The wind direction measurements of the WT and the UASs are well correlated (correlation coefficient of $R = 0.98$). It is obvious that a systematic bias between the independent measurements exists. Possible reasons are

1. spatial distance between the measurements,

2. imperfect calibration of flow distortions for the sonic anemometer on the WT,

3. errors in northing of either the UAS or WT sonic anemometer,

4. temporal offset between measurements, since WT data are only available as 10 min averages and do not always perfectly align with the UAS flights.

Possibilities 1 and 4 would rather manifest in a random error, while possibilities 2 and 3 can yield a systematic error. The calibration and orientation of the WT sonic are not known to the authors, so it can only be guessed that a combination of all reasons causes the bias and scatter between UAS and WT sonic. Comparing the yaw angles of the WT in Fig. 5 with the UAS measurements, a mean offset throughout all flights can be observed as well. This indicates that the yaw controller is not perfectly adjusted for this specific WT. The trend in the misalignment from the WT leads to the relative position deviations in Fig. 4, since it was attempted to align the UAS pattern with both the turbine orientation and the wind direction. It is worth noting that no systematic error between UAS measurements in the freestream upstream and lateral is observed. Reference measurements with the UAS fleet also did not show systematic errors in any UAS beyond the uncertainties that were previously observed for the system (Wetz and Wildmann, 2022).

4.3 Wake measurements under stable to near-neutral atmospheric conditions

In the following subsection we focus on the lateral and longitudinal flight patterns under stable to near-neutral atmospheric conditions. Details about the considered flights in this section are listed in Table 1.

4.3.1 Analyses of a single lateral flight pattern

The time series of flight no. 606 is shown as an example in Fig. 6. The flight was conducted in the early morning (04:53 UTC) of 12 May 2022, before the nighttime stable ABL was completely eroded by turbulence of the growing mixed layer. As introduced in Sect. 2, the lateral pattern was arranged so that one UAS is located in the freestream, one is placed at the edge of the wake, and the remaining ones are laterally distributed in the WT wake. In Fig. 6a the time series of horizontal velocity clearly show that the outer UAS ($y = 1.05 D$) measures in the freestream, indicated by the highest average velocity, while the inner UASs are placed inside the wake. The innermost UAS ($y = 0.06 D$) behind the nacelle has a considerably lower wind speed deficit than those hovering between $y = 0.2$ and $y = 0.45 D$. This increase in velocity at the center of the wake is already indicative of a double-Gaussian shape of the lateral wake profile. The measurement with the highest velocity fluctuations is located at the edge of the WT wake between $y = 0.5$ and $0.6 D$. In Fig. 6b, the wind direction of the reference UAS shows a strong variation in the inflow ($\sigma_\Phi = 8°$). This variation in inflow wind direction leads to a variation in the relative lateral measurement position with respect to the reference wind direction. These variations in the lateral measurement positions are shown in Fig. 6c. As the velocity series of the inner UAS ($y = 0.3$ and $y = 0.42 D$) already suggests, the relative measuring positions are inside the wake over the entire flight. More interesting is the relative lateral position of the UAS at the edge of the wake. A correlation between the relative lateral position and the velocity deficit can be observed here (with a correlation coefficient of $R = 0.5$). For example, taking the measurement at 04:59 UTC, both the lateral position $y > 0.6 D$ and the velocity imply measurements outside the wake. On the other hand, after the wind direction change at around 05:00 UTC, both the lateral position and the measured velocity indicate measurements within the wake of the WT. This meandering of the wake evidently causes a high turbulence intensity measurement at the edge of the wake. These results show the sensitivity of the relative position of wake measurements in field experiments even and especially in the near-wake region.

In order to understand the distribution of the turbulence energy across the scales, the power spectrum S_u of streamwise wind velocity for the same flight (no. 606) is shown in Fig. 7. Apart from the larger scales ($f < 0.03$ Hz, $l > 200$ m), the measurements inside the wake show in general a higher level
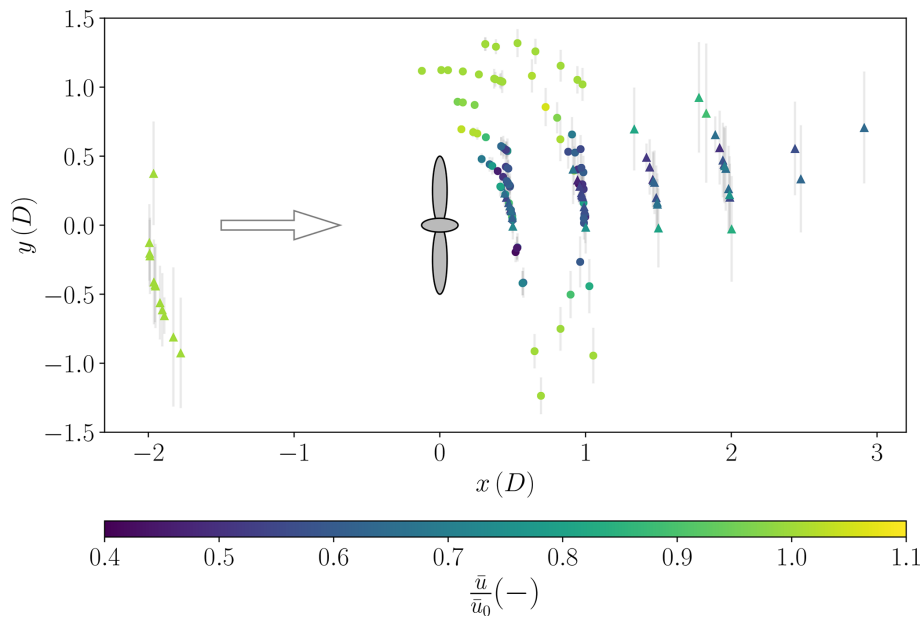
Figure 4. Normalized wind velocity of UAS measurements $\overline{u}/\overline{u}_0$ at locations relative to the reference wind direction. The illustration of the WT defines the position and the lateral dimensions of the WT rotor. Triangle markers represent the longitudinal flight pattern, while circle markers define the lateral flight pattern. The arrow indicates the inflow wind direction. The standard deviation in lateral position is illustrated by the grey vertical lines and is calculated from the standard deviation of the inflow wind direction.
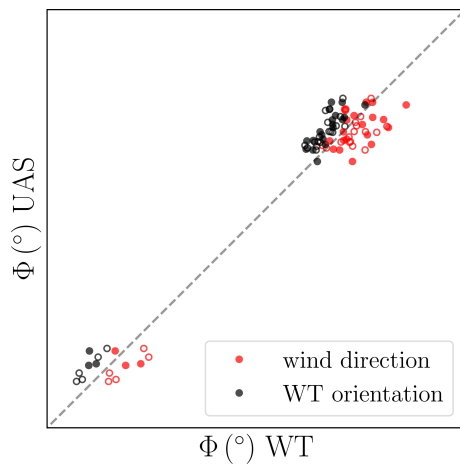
Figure 5. Comparison of WT wind direction and orientation measurements with UAS reference measurements. UAS measurements are conducted in the freestream, either lateral $y = 1\,D$ (empty dots) to or upstream $x = 2\,D$ (filled dots) of the WT. Both the wind direction and the nacelle orientation are measured on the WT nacelle.

of energy compared to the freestream (dashed black line), particularly at the small scales ($f > 0.3\,\mathrm{Hz}$, $l < 20\,\mathrm{m}$). We can assume that the added turbulence in the wake is the main reason for this increase. The measurements at the edge of the wake ($\overline{y} = 0.55$) show the highest turbulence level, especially at the larger scales, but also at smaller scales. This additional variance is caused by the wake meandering, which

itself is mainly caused by the variation in the inflow direction. Another feature that can theoretically be observed at the edge of the wake is the tip vortex. In order to assess whether the tip vortex in the spectrum (Fig. 7) of the UAS measuring at the edge of the wake can be identified, we take the WT rotational speed into account. During the period of the considered flight, the mean rotational speed of the WT is 12 rpm, resulting in a blade-passing frequency (BPF, also known as tip vortex shedding frequency) of $f_{\mathrm{bp}} = 0.6\,\mathrm{Hz}$. In the area of the BPF in Fig. 7 an increase in the spectrum of the UAS at the edge of the wake ($\overline{y} = 0.55$) can be observed. Together with the freestream velocity of $\overline{u}_0 = 6.18$, the tip speed ratio results in $\lambda = 8.36$. Considering the advection velocity at this position of $u_{\mathrm{adv}} = 3.6\,\mathrm{m\,s}^{-1}$, the axial spacing of the helical vortices is about 6 m ($0.07\,D$). In this case we use the mean velocity at the measurement position as advection velocity ($u_{\mathrm{adv}} = \overline{u}$), while in wind tunnel experiments the instantaneous velocity is often used (Zhang et al., 2011; Sherry et al., 2013) resulting in a higher advection velocity compared to the freestream velocity. Taking their ratios of $u_{\mathrm{adv}}/u_0 = 0.8$ into account the vortex spacing would be slightly larger. Porté-Agel et al. (2019) specify a typical range of the normalized mean advection velocity of the tip vortices of $u_{\mathrm{adv}}/u_0 = 0.73\ldots0.78$. However, in our case, assuming a helical vortex spacing of 6 m, at a longitudinal distance of $x = 0.5\,D$, where the measurements are taken, approximately seven tip vortices could theoretically be observed in a snapshot of the wake flow between the measurement position and the WT. Thus, the measured tip vortex
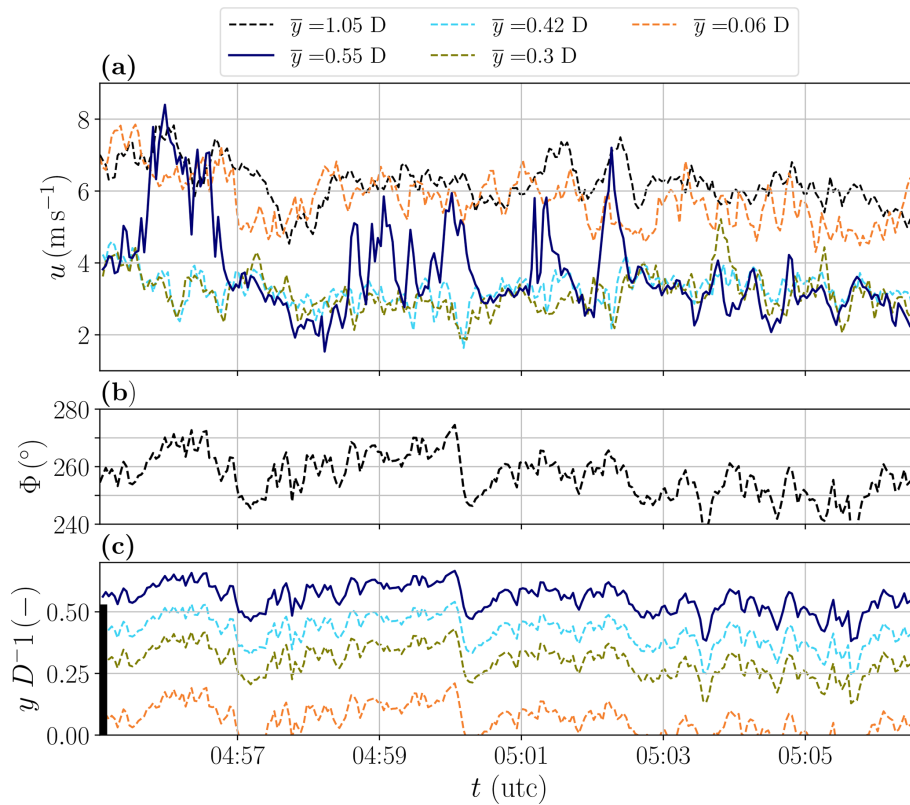
Figure 6. Time series of wind velocity **(a)**, wind direction **(b)** and lateral position **(c)** of a lateral flight pattern in stable conditions (flight no. 606). The lateral positions are calculated using the wind direction of reference UAS measurements, which are shown in the middle figure. The black bar in **(c)** indicates the lateral position of the WT.
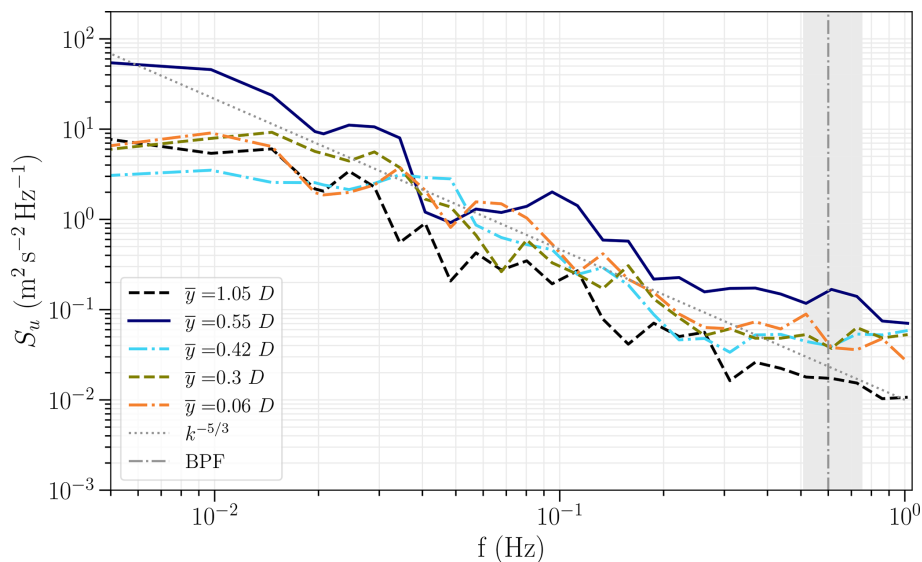
Figure 7. Power spectra of streamwise velocity S_u for flight no. 606 (lateral pattern) at different lateral positions y. The blade-passing frequency (BPF) is indicated by the vertical dashed–dotted line. The grey background around the BPF represents the bandwidth of the BPF based on the extreme values of WT rotation frequency. The spectra are processed with bin averages in the frequency space to decrease the noise.

has a rotation trajectory history of more than two complete WT revolutions. Given such a trajectory history, the peak in the turbulence spectrum is not expected to be very pronounced in the present case due to the dissipation of tip vortices that are diffused over a distance of $0.5\,D$. In addition, the rotational speed of the WT and the wind speed in field operation are not constant, as is mostly the case in wind tunnel experiments, which can also cause some blur in the spectrum. The bandwidth of the expected BPF shown in Fig. 7 is calculated from the maximum and minimum rotation frequencies of the WT measured during the considered time period.

The signature of the tip vortices in a time series of a single point measurement is difficult to capture, since the signature strongly depends on the position relative to the center of the vortices. However, the time series of the lateral velocity v of the relevant UAS ($\overline{y} = 0.55\,D$) shows in some periods the signature of the tip vortex. One segment of the time series of the lateral velocity component v where the signature is clearly visible is shown in Fig. B1a in the Appendix. The signature of the tip vortex at hub height is characterized by a strong increase in lateral velocity followed by an abrupt change towards the opposite lateral direction and ending back at the ambient lateral wind velocity, or, depending on the measurement position relative to the center of the vortex, the vortex can only cause a strong increase or decrease in the streamwise velocity without having a major impact on the lateral velocity.

4.3.2 Horizontal wake profile of velocity deficit and turbulence intensity

For the lateral pattern, the wind velocity deficit is calculated using the reference UAS, which is located at a lateral distance of $y = 1\,D$ to the WT. The pattern is conducted at different longitudinal distances to the WT and in slightly different lateral arrangements. The results in Fig. 8a show the normalized velocity of multiple flights of the lateral pattern on 12 May 2022 under stable to near-neutral and on 7 November 2022 under mostly near-neutral thermal stratification as a function of the lateral distance to the WT hub. The lateral distances differ slightly for identical flight patterns, since we take the misalignment β of the pattern to the wind direction into account. The measuring points of the individual flights, consisting of a maximum of five UASs, are connected in Fig. 8.

The shape of the horizontal velocity profile at a downstream distance of $x = 0.5\,D$ follows an approximate double-Gaussian shape, assuming a nearly symmetrical profile for the remaining parts on the opposite lateral side (see Fig. 8a). A double-Gaussian velocity distribution is characterized by a strong decrease in velocity at the edge of the wake between $y = 0.3$ and $0.6\,D$ followed by an increase in velocity (up to almost freestream velocity) in the center of the wake. This shape is closely connected to the energy that the WT extracts from the wind. The majority of the energy is typically con-

verted at the outer areas in spanwise direction of the rotor, resulting in a comparatively low velocity deficit in the center in the near-wake region. Further downstream, at $x = 1\,D$, the shape differs for the considered flights. The flights on day 7 (no. 7xx) show a less pronounced double-Gaussian shape. This could be explained by the different freestream turbulent intensities and the thermal stratification. On day 6, the turbulence intensity is lower than on day 7, so the turbulence mixing is less pronounced, which leads to a less uniform velocity distribution. At $x = 1\,D$, we still see the same principle shape and relationship between the 2 d, and only small changes in magnitude of the velocity deficit can be observed compared to $x = 0.5\,D$.

Figure 8b shows the added turbulence intensity ΔI over the lateral distance for the same flights. The highest turbulence intensity can clearly be observed at the edge of the wake around $y = 0.5\,D$ due to the tip vortices of the WT blades, the shear layer and the meandering of the wake. At a spatially fixed measurement position at the edge of the WT, the meandering of the WT wake causes high variation in wind velocity due to temporal changes in the relative position from inside to outside of the wake (see Sect. 4.3.1). However, towards the wake center I decreases, showing a double-Gaussian shape similar to the velocity deficit, which has also been reported in the literature (Maeda et al., 2011). On day 6 the freestream turbulence intensity was lower than on day 7, but the magnitude and the basic shape of the added turbulence intensity look similar, so for these cases, the added turbulence intensity does not seem to strongly depend on the freestream velocity. The peak of turbulence intensity further downstream at a distance of $x = 1\,D$ is less pronounced compared to $x = 0.5\,D$.

4.3.3 Streamwise development of the wake

In Fig. 9a the development of the normalized velocity and in Fig. 9b the added turbulence intensity in streamwise direction of the longitudinal pattern are shown. The measurements are normalized with the inflow measurement at an axial distance of $x = 2\,D$ upstream of the WT. Due to the mentioned pronounced double-Gaussian profile of the lateral velocity distribution at $x = 0.5\,D$, the velocity in the center of the wake is comparatively high. As the velocity deficit profile turns into a single-Gaussian shape further downstream (from 0.5 to $1\,D$) due to turbulent mixing, the velocity at the wake center decreases. Even further downstream, the accuracy of the pattern orientation in our experimental setup plays a major role. For example, a pattern misalignment of $\beta = 10°$ indicates a lateral displacement error of $y = 0.35\,D$ at a longitudinal distance of $x = 2\,D$. This displacement leads to measurements towards the lateral edge of the wake, where the velocity increases compared to the center of the wake, assuming a single-Gaussian velocity distribution at these downstream distances. Both effects are most evident for flight no. 604: the turbulence intensity ($I_0 = 0.073$) and
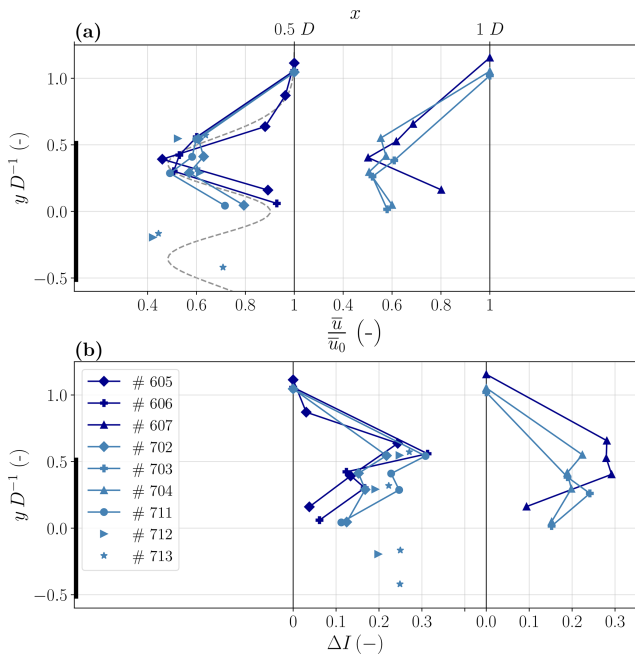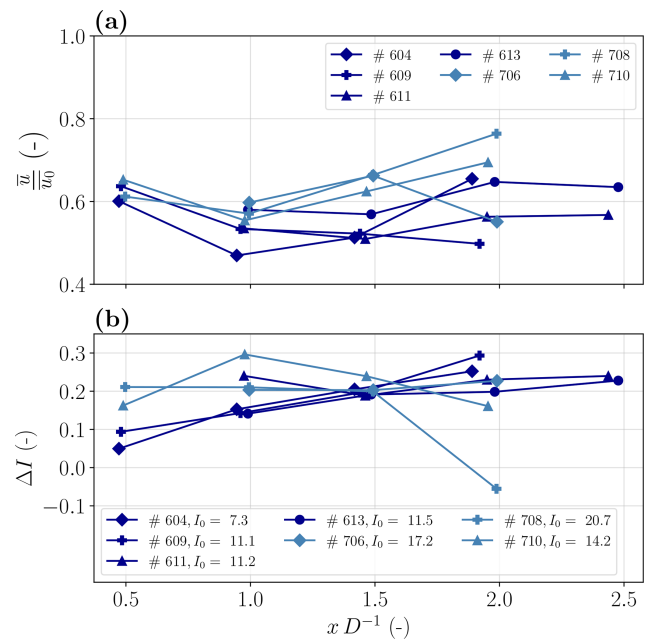
Figure 8. (a) Lateral profile of normalized wind speed $\overline{u}/\overline{u_0}$ in the WT wake at different downstream distances ($x = 0.5$ and $1\,D$). **(b)** Lateral profile of added turbulence intensity ΔI. Different colors indicate different flight days with both stable to near-neutral (dark blue) and mostly near-neutral conditions (light blue). Details about the considered flights are found by the flight number in Table 1. The dashed grey line indicates a mean double-Gaussian symmetric fit of the present data.

Figure 9. (a) Normalized wind speed $\overline{u}/\overline{u_0}$ and **(b)** added turbulence intensity ΔI are shown in the center of WT wake at different downstream distances. Different colors indicate different flight days with both stable to near-neutral (dark blue) and mostly near-neutral conditions (light blue). The reference turbulent intensity I_0 given in the legend is shown in percent.

the standard deviation of the wind direction ($\sigma_\Phi = 4°$) inflow are low compared to the other considered flights, and the misalignment of the pattern is comparable high ($\beta = 19°$). The low level of turbulence intensity and wind direction variation leads to a pronounced double-Gaussian distribution, resulting in a prominent drop in velocity from $x = 0.5$ to $x = 1\,D$ in the wake center. Further downstream, the large misalignment causes a relative measurement location almost outside the wake, which leads to the relatively large increase in velocity of flight no. 604.

Following the same argumentation, the behavior of the added turbulence intensity of flight no. 604 and no. 609 (Fig. 9b) can be explained by the misalignment of the pattern β and the low freestream turbulence intensity I_0. In general, the turbulence intensity increases with downstream distance in the near-wake center. This can be explained by the turbulent mixing of the high turbulence region on the edge of the wake towards the center. For this experiment, the deviation in pattern orientation causes the measurement to be taken outside of the wake center, further towards the edge of the wake, which typically exhibits higher turbulence intensities.

The argumentation about the misalignments and the resulting measurement position outside of the centerline is also valid for flight case no. 708 and its velocity measure-

ments. However, in this case we observe a strong increase in the wind speed towards almost freestream velocity ($0.8u_0$) which can not only be explained by the deviation of the lateral position, since this deviation is also present for other cases which do not show this strong increase in wind speed. The acceleration for this flight case can rather be explained by the decrease in turbulence intensity in Fig. 9b which indicates a wake recovery already starting at the downstream distance of $x = 2\,D$. This is plausible for this case due to the comparably high turbulence intensity (21 %) which enhances the wake recovery. Also, the missing increase in turbulence intensity over longitudinal distance for flight no. 708 can be explained by the high level of turbulence intensity in the freestream. Due to the already high turbulence intensity in the ambient flow, the turbulence induced by the WT plays a minor role in the absolute value of turbulence intensity in the wake. The downstream position of maximum turbulence intensity in the wake center typically occurs at the transition from near wake to far wake. Since the extent of the near wake is larger at low freestream turbulence intensities, the maximum of turbulence intensity will arise further downstream compared to high ambient turbulent intensities (Wu and Porté-Agel, 2012).

Due to the counterclockwise-rotating velocity field (viewed from upstream) in the near wake, a measurable lateral velocity component is expected below the center of the
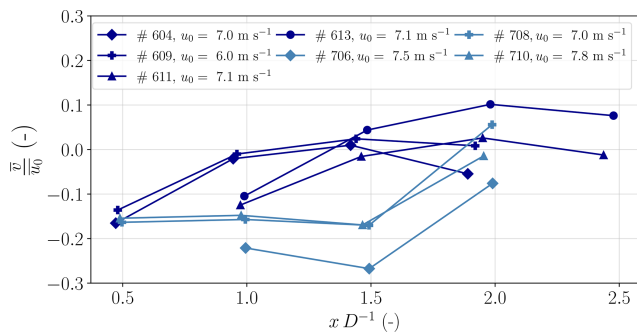
Figure 10. Normalized lateral wind speed $\overline{v}/\overline{u}_0$ in the center of the WT wake at different downstream distances. Different colors indicate different flight days with both stable (dark blue) to near-neutral (light blue) conditions.

Figure 11. Lateral profile of normalized horizontal momentum fluxes $\overline{u'v'}/\overline{u}_0^2$ in the WT wake at different downstream distances ($x = 0.5$ and $1\,D$). Different colors indicate different flight days with both stable (dark blue) to near-neutral conditions (light blue).

wake, where measurements are taken in the longitudinal pattern. Since the lateral velocity is defined positive towards north, the lateral velocity at this position is expected to be negative (for westerly winds). This negative lateral velocity close behind the turbine at a longitudinal distance of $x = 0.5\,D$ and 18 m ($\Delta z = -0.2\,D$) below the center of the wake is observable in Fig. 10 for all cases. Furthermore, the development of the lateral velocity over the longitudinal distance in the wake is shown there. Due to the sensitivity of the exact measurement position to the lateral velocity component, a detailed interpretation is not given at this point. Overall, the velocity field perpendicular to the mean flow is expected to decrease further downstream. In particular at the lower part of the wake, due to strong turbulent mixing, a decrease in the wake rotation is assumed. Zhang et al. (2011) showed in wind tunnel tests that the lateral velocity decreases significantly from $1\,D$ towards $2\,D$ downstream distances. At $x = 5\,D$ the wake rotation is no longer observable.

The analyses of the longitudinal flight pattern show the difficulty in taking in situ measurements of the far wake in a field experiment at a complex site, even with a flexible measurement system like the SWUF-3D fleet. The complex flow with its high variability in the inflow wind direction leads to large lateral deflections of the wake and impedes the positioning of in situ measurements in the wake. The present complex terrain can also cause vertical deflection due to the significant slope west of the WT, which could also affect the vertical position of the WT wake (see for example Wildmann et al., 2017, for flow inclination behind and escarpment and Wildmann et al., 2018a, for vertical wake deflection in complex terrain). Since the lateral velocity components are comparably small, the uncertainty for the velocity measurements are more crucial for this component.
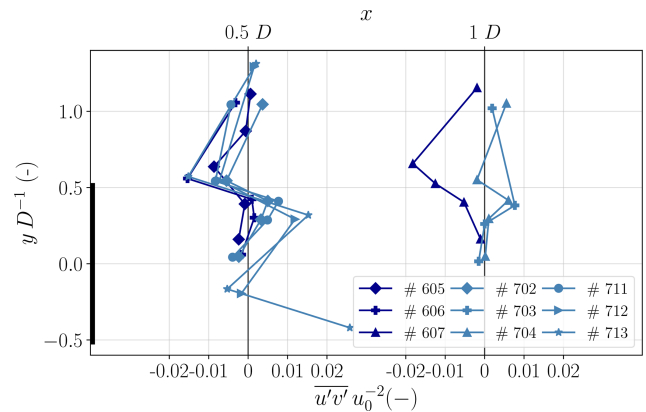
4.3.4 Horizontal momentum fluxes of lateral distributed measurements

In wind energy science, predicting WT wake decay is a key requirement for predicting wind farm efficiency. Turbulent fluxes are a major process that drives the energy transport from the free flow towards the wake of the WT. The turbulent fluxes therefore have a direct impact on the wake recovery. In the following we examine the horizontal momentum fluxes $\overline{u'v'}$ for laterally distributed measurements at two different downstream distances ($x = 0.5$ and $x = 1\,D$), again only for stable to near-neutral atmospheric conditions. In Fig. 11 the horizontal fluxes are normalized by the square of the freestream velocity $\overline{u}_0^2$ comparable to Bastankhah and Porté-Agel (2017). At the edge of the wake at $y = 0.6\,D$ negative fluxes are observed, which lead to an entrainment of energy into the wake. On the other side of the wake, the sign of the fluxes are positive for the same reason. Closer to the center of the wake, the signs of the fluxes are in the opposite direction due to energy transport from the center with high wind speed towards the low-speed area at the edge of the wake. At $1\,D$ distance the momentum fluxes from the inner wake towards the outer wake are less prominent or no longer observable. In the stable case a high momentum flux towards the wake is still present at the edge of the wake.

4.4 Wake measurements in unstable atmospheric conditions

The studied results so far were only based on stable to near-neutral atmospheric conditions where wakes are known to be most critical for wind farm operation. However, unstable, convective conditions occur frequently, particularly at onshore sites. Therefore, in this section we will additionally look at some flights in unstable conditions. In Fig. 12 the unstable flights are added to the previously shown lateral
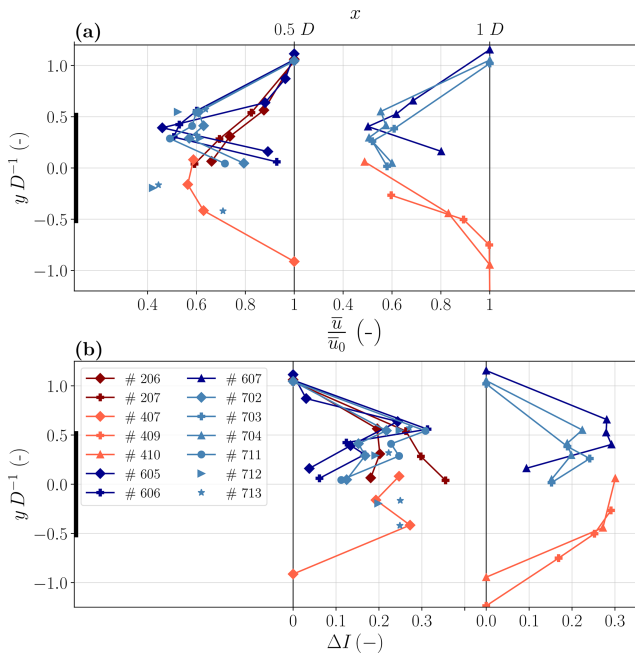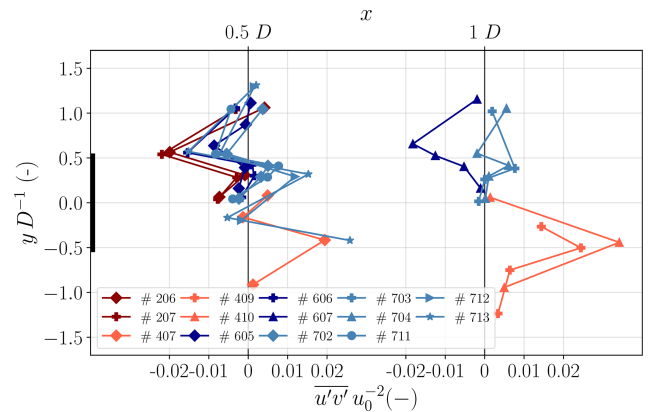
Figure 12. (a) Lateral profile of normalized wind speed $\overline{u}/\overline{u_0}$ in the WT wake at different downstream distances ($x = 0.5$ and $1\,D$). **(b)** Lateral profile of added turbulence intensity ΔI. Different colors indicate different flight days. The blue color represents stable to near-neutral atmospheric conditions, while the red color indicates unstable convective conditions (dark red for highly unstable and light red for less unstable cases).

Figure 13. Lateral profile of normalized horizontal fluxes $\overline{u'v'}/\overline{u_0}^2$ in the WT wake at different downstream distances ($x = 0.5$ and $1\,D$). Different colors indicate different flight days. Blue represents stable to near-neutral atmospheric conditions, while red indicates unstable convective conditions.

profile of the normalized velocity and the added turbulence intensity. It is evident that for unstable conditions the double-Gaussian shape at $x = 0.5$ and $x = 1\,D$ is no longer recognizable for both the velocity and turbulence intensity distribution. The added turbulence intensity supposedly isolates the wake-induced turbulence intensity from the freestream turbulence, making different atmospheric conditions more comparable. The comparison reveals that the amount of added turbulence intensity is about the same at the wake edge in stable and unstable cases. However, in the center region of the wake $y < 0.3\,D$ the added turbulence intensity decreases more significantly under stable conditions, which is a consequence of the double-Gaussian wake shape as presented before. The standard deviation of the incoming wind direction is higher in the unstable cases (approx. $\sigma_\Phi = 11$) than in the stable cases ($\sigma_\Phi = 6\ldots 8$). In addition, the higher turbulence in the ABL leads to a more pronounced turbulence mixing in the near wake and a rapid breakup of tip vortices. All mentioned effects smooth the lateral profile towards a single-Gaussian shape.

Since the double-Gaussian shape is not clearly observable under unstable conditions at the measured distances, it is expected that weaker horizontal fluxes can be observed from the wake center towards the edge of the wake. In Fig. 13, flights under unstable atmospheric conditions are compared

with stable cases. Comparable to the stable conditions, the fluxes towards the wake are observable at the edge of the wake ($y = \pm 0.5\,D$) in the CABL. However, the opposite directions of horizontal fluxes towards the edge of the wake in the center region ($y = \pm 0.3\,D$) are less pronounced. Overall the magnitude of the fluxes slightly increases in unstable conditions due to stronger turbulent mixing.

5 Discussion

5.1 Horizontal velocity deficit distribution

In the present study we observed a double-Gaussian horizontal distribution of the velocity deficit in the near wake under stable atmospheric conditions. In the literature mostly the velocity distributions for distances greater than $1\,D$ are examined; only a few publications exist for measurements close to the rotor plane. Abraham et al. (2019) examined field experiments of the near wake with particle image velocimetry using natural snowfall, outlining a double-Gaussian shape in the vertical direction close to the tower region. A double-Gaussian wake model based on lidar measurements of a 5 MW WT in the wake is proposed by Keane (2021). Menke et al. (2018) observed a double-Gaussian distribution at $1\,D$ even in highly complex terrain using a ground-based wind lidar at the Perdigão site in 2015. Nacelle-based lidars are also often used, for example, by Herges and Keyantuo (2019) for downstream distances of up to $x = 1\,D$, but generally they are mostly conducted for flow field studies further downstream at $x > 2\,D$. Therefore, field data are rarely available especially in the near-wake region as close as $0.5\,D$ downstream.

Krogstad and Adaramola (2011) examined velocity profiles at the near wake in wind tunnel experiments with uniform inflows. They found that the velocity profile is strongly

dependent on the tip speed ratio (TSR). For high tip speed ratios of about $\lambda = 8 \ldots 9$, a double-Gaussian distribution was clearly observed, even with a slightly accelerated region in the center part of the wake. However, if the turbine is operated closer to the design tip speed ratio of $\lambda = 6$, the velocity profile becomes more uniform and could be assumed to be a single-Gaussian distribution. Transferring these results to our study, where the stable and near-neutral cases were conducted at TSRs $\lambda = 7.5 \ldots 9$, the high TSR could also drive the double-Gaussian distribution. Under unstable conditions, the double-Gaussian distribution is not observed in the present study (see Fig. 12). For the flights on day 2 under unstable conditions, the tip speed ratio was closer to the design point at $\lambda = 6$, which could explain the single-Gaussian distribution according to Krogstad and Adaramola (2011). However, the other unstable measurements on day 4 were carried out at TSRs of around $\lambda = 8$ which are comparable to the stable flights. Therefore, the moderate TSR cannot be the only explanation for the single-Gaussian velocity distribution on day 4, but it is rather the unstable atmospheric condition of the inflow which influences the velocity profile in this case. Machefaux et al. (2015) examined the effect of atmospheric stability on WT wakes using a nacelle-based pulsed lidar and LESs. They clearly observed a dependency of atmospheric stability on the velocity deficit distribution. Under stable conditions, the velocity at the wake center increases significantly at a longitudinal distance of $x = 1\,D$, which causes a double-Gaussian distribution, whereas in unstable cases the velocity profile is almost flat with only a slight increase towards the wake center.

5.2   Horizontal fluxes

We have clearly observed lateral turbulent momentum fluxes towards the wake at the edge of the wake (see Fig. 13). These momentum fluxes are in agreement with Bastankhah and Porté-Agel (2017), who performed PIV measurements in wind tunnel experiments for different tip speed ratios. The values for the normalized momentum fluxes $\overline{u'v'}/\overline{u}_0^2$ are of the same magnitude as in the present study. However, the turbulent fluxes from the center wake towards the edge of the wake, which can be seen in Fig. 13, are not observed in their wind tunnel experiments. The PIV measurements were limited to an approximate downstream distance of $x = 0.7\,D$; thus no results are discussed at $x = 0.5\,D$. Furthermore, the velocity distribution at $x = 1\,D$ in their study shows only a weak double-Gaussian distribution, meaning that the lower velocity deficit in the center region is less prominent. Therefore, the velocity gradients within the wake are less strong, which could explain why they did not find significant turbulent transport from the center towards the outer region of the wake.

5.3   Near-wake length

The length of the near wake is defined by the distance downstream from the WT where the transition to the far wake occurs. In Sect. 3 we described an analytical model for estimating the near-wake length. The estimated length for the near wake under stable atmospheric conditions (no. 604) is $l_{\mathrm{nw}} = 2.9\,D$. This length coincides with the development of turbulence intensity in the center of the wake in the downstream direction. The development of the turbulence intensity of the same flight still shows an increase at a distance of $x = 2\,D$, indicating measurements within the near wake, since the downstream position of the turbulence intensity peak is associated with the transition from the near wake into the far wake (Wu and Porté-Agel, 2012). However, due to the deviation in pattern orientation, the increase in I could also be caused by the lateral position outside the wake center. Overall, the estimated wake length for the flights considered is between 1.7 and $2.9\,D$, so it can be assumed that the examined lateral profiles ($x < 1\,D$) are within the near wake. For detailed near-wake length studies, extended simultaneous measurements are needed to capture the entire wake characteristics during the measurements.

6   Conclusions

In the present experiment, for the first time, a fleet of UASs was successfully deployed to measure the wind flow around a WT. The simultaneous up- and downstream measurements show their great potential for detailed WT wake studies, even without any additional instrumentation. The results of velocity and turbulence intensity distributions, as well as turbulence spectra and momentum fluxes, were discussed and compared with the literature. The following statements summarize the study and provide answers to the research questions defined in the Introduction.

– The horizontal velocity deficit and turbulence intensity profile at a downstream distance of $x = 0.5\,D$ under stable to near-neutral conditions clearly outline a double-Gaussian-like distribution, with a lower velocity deficit at the wake center.

– At the edge of the wake, the lateral momentum fluxes point towards the wake center, while in the inner regions of the wake, the fluxes point toward the edge. In general, the turbulent transport takes place towards the low-wind-speed region.

– The blade-passing frequency of the tip vortices can be observed under stable atmospheric conditions in the energy spectra. However the peak of the BPF appears to be quite broad due to the "far" downstream distance ($x = 0.5\,D$), the unsteady rotational speed of the WT and the variation in the inflow wind direction.

– The downstream recovery of the velocity deficit is captured with distributed measurements in the longitudinal direction. In addition, the downstream evolution of the horizontal velocity deficit profile from the prominent double-Gaussian distribution to a single-Gaussian distribution is shown.

– The velocity deficit under unstable atmospheric conditions does not show a double-Gaussian shape at downstream distances of $x = 0.5\,D$. In contrast to stable conditions, no decrease in the added turbulence intensity is observed in the wake center, which is an indication for very fast mixing and tip vortex breakdown.

The relative positioning of single UAS in the wake in continuously varying inflow conditions is a challenging task, particularly in complex terrain where the wake can be deflected horizontally and vertically. The larger the downstream distance is, the more challenging a precise relative positioning is. Therefore, only near-wake measurements are considered. We show in this study that with simultaneous inflow measurements the relative position in the wake can be estimated well. It is a big advantage to operate with multiple UASs simultaneously to capture the spatial extent of the wake. In future field experiments around WTs, the entire fleet of > 20 UASs will be used, allowing us to capture the entire rotor swept area in more detail, making the exact positioning of a single UAS less relevant. With a larger fleet simultaneous wake profile measurements at different downstream distances, both in vertical and lateral directions, will be possible. Additionally, as shown by Wetz et al. (2022), spatial coherence and correlation measurements are possible with the UAS fleet and can be used for detailed studies of the flow around WTs. In the meantime, the wind algorithm is developed towards a full three-dimensional wind vector estimator (Wildmann and Wetz, 2022). It could not be used in this study, as a calibration at high wind speeds as observed in this study has not yet been achieved. In future campaigns, it is the goal to retrieve both the vertical wind component and the vertical momentum fluxes.

Extended experiments are planned in the near future at the Krummendeich Research Wind Farm (WiValdi) owned by the German Aerospace Center (DLR) (https://windenergy-researchfarm.com/, last access: 10 January 2023) (Wildmann et al., 2022). In addition to the three WTs, a variety of meteorological instruments will be installed at the site, such as four meteorological masts (up to 150 m tall) and ground-based and nacelle-based wind lidars. A synthesis of this network of different instruments will enable detailed research on the flow in WT wakes and its interaction with atmospheric turbulence.

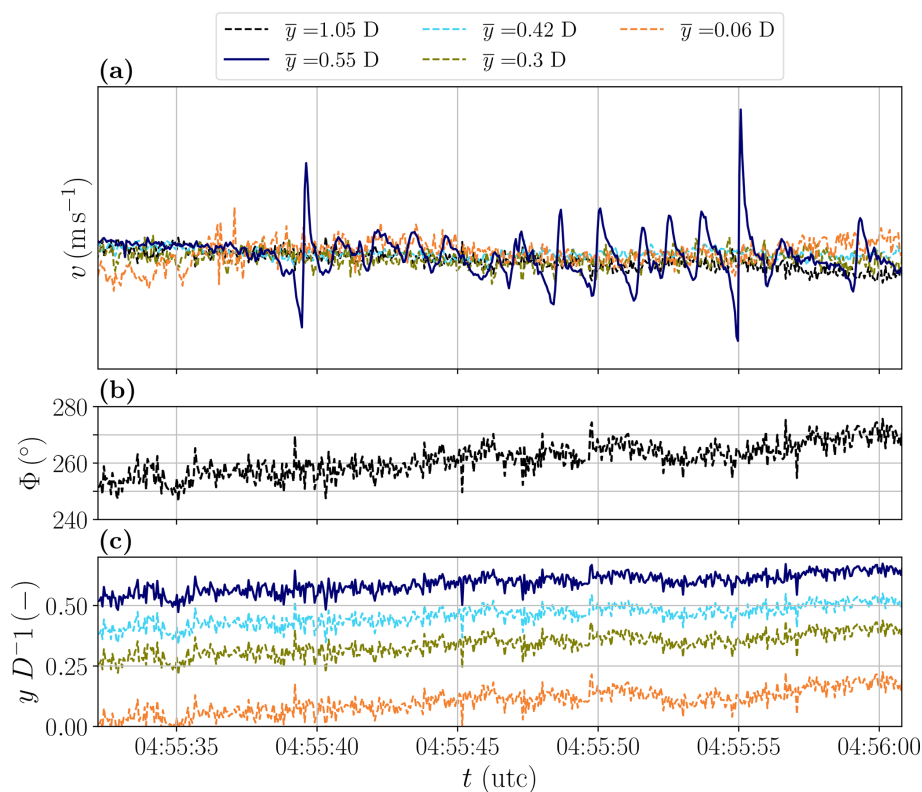## Appendix A: Turbulence intensity overview for all flights

Besides the velocity deficit, the turbulence intensity is an important quantity in WT wake studies. Therefore, in Fig. A1 the added turbulence intensity ΔI (see Eq. 5) is illustrated in the same manner as the overview plot of the velocity deficit in Fig. 4. The increase in turbulence intensity in the wake region is clearly observable. However, the highest I is expected near the edge of the wake due to the tip vortices and the continuously changing deflection of the wake due to the variability in the inflow wind direction.
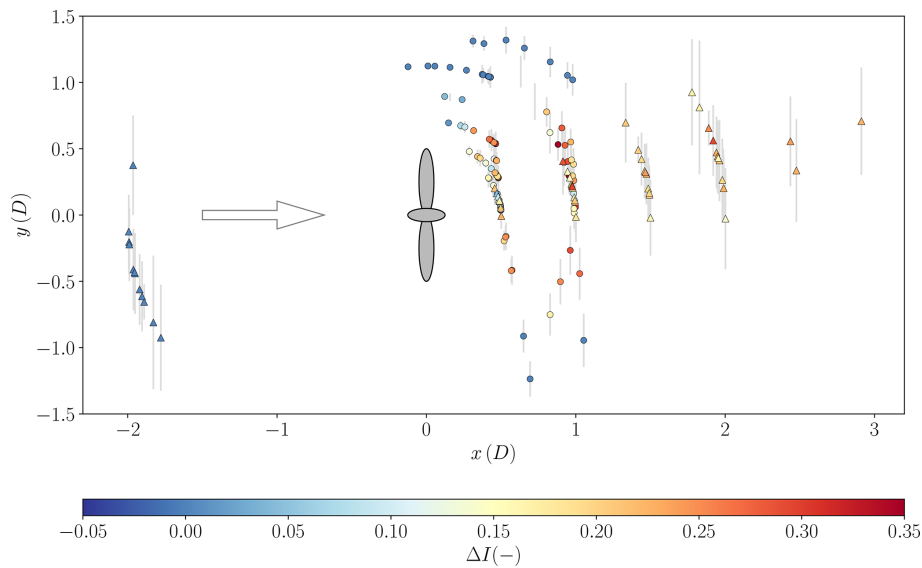
Figure A1. Added turbulence intensity ΔI of UAS measurements at locations relative to the reference wind direction.

Appendix B: Signature of tip vortex in the velocity series

In Fig. B1a the lateral velocity component of a small period of flight no. 606 is shown in the same manner as Fig. 6. The labels on the y axis have been removed for confidentiality reasons. As the measurements are taken at hub height, the tip vortex is expected to rotate almost in the horizontal plane with a rotational axis pointing vertically down towards the earth's surface. The rotational sense of the vortex can be derived from the rotation of the WT blade, which at this position (westerly winds, clockwise-rotating WT, measurement position north, hub height) is moving upwards. This sense of rotation can also be observed in the lateral velocity, with a first strong negative velocity (north wind) followed by a positive velocity (south wind), while the vortex is advected through the measurement point.

Figure B1. Time series of the lateral velocity component **(a)**, wind direction **(b)** and lateral position **(c)** of a lateral flight pattern in stable conditions (flight no. 606). The lateral positions are calculated using the wind direction of reference UAS measurements, which are shown in the middle figure. The black bar in **(c)** indicates the lateral position of the WT.

Author contributions. TW wrote the main manuscript and performed the data analysis. The experiment was conducted by TW. NW was involved in the experiment, contributed to the manuscript and prepared parts of Fig. 1.

Competing interests. The contact author has declared that neither of the authors has any competing interests.

Disclaimer. Publisher's note: Copernicus Publications remains neutral with regard to jurisdictional claims in published maps and institutional affiliations.

Review statement. This paper was edited by Rebecca Barthelmie and reviewed by Stefano Letizia and one anonymous referee.

References

Abkar, M. and Porté-Agel, F.: Influence of atmospheric stability on wind-turbine wakes: A large-eddy simulation study, Phys. Fluids, 27, 035104, https://doi.org/10.1063/1.4913695, 2015.

Abraham, A., Dasari, T., and Hong, J.: Effect of turbine nacelle and tower on the near wake of a utility-scale wind turbine, J. Wind Eng. Indust. Aerodynam., 193, 103981, https://doi.org/10.1016/j.jweia.2019.103981, 2019.

Abraham, A., Martínez-Tossas, L. A., and Hong, J.: Mechanisms of dynamic near-wake modulation of a utility-scale wind turbine, J. Fluid Mech., 926, A29, https://doi.org/10.1017/jfm.2021.737, 2021.

Aitken, M. L. and Lundquist, J. K.: Utility-Scale Wind Turbine Wake Characterization Using Nacelle-Based Long-Range Scanning Lidar, J. Atmos. Ocean. Tech., 31, 1529–1539, https://doi.org/10.1175/jtech-d-13-00218.1, 2014.

Alaoui-Sosse, S., Durand, P., and Médina, P.: In Situ Observations of Wind Turbines Wakes with Unmanned Aerial Vehicle BOREAL within the MOMEMTA Project, Atmosphere, 13, 775, https://doi.org/10.3390/atmos13050775, 2022.

Bastankhah, M. and Porté-Agel, F.: A new analytical model for wind-turbine wakes, Renew. Energy, 70, 116–123, https://doi.org/10.1016/j.renene.2014.01.002, 2014.

Bastankhah, M. and Porté-Agel, F.: Experimental and theoretical study of wind turbine wakes in yawed conditions, J. Fluid Mech., 806, 506–541, https://doi.org/10.1017/jfm.2016.595, 2016.

Bastankhah, M. and Porté-Agel, F.: Wind tunnel study of the wind turbine interaction with a boundary-layer flow: Upwind region, turbine performance, and wake region, Phys. Fluids, 29, 065105, https://doi.org/10.1063/1.4984078, 2017.

Brugger, P., Debnath, M., Scholbrock, A., Fleming, P., Moriarty, P., Simley, E., Jager, D., Roadman, J., Murphy, M., Zong, H., and Porté-Agel, F.: Lidar measurements of yawed-wind-turbine wakes: characterization and validation of analytical models, Wind Energ. Sci., 5, 1253–1272, https://doi.org/10.5194/wes-5-1253-2020, 2020.

Crespo, A., Hernández, J., and Frandsen, S.: Survey of modelling methods for wind turbine wakes and wind farms, Wind Energy, 2, 1–24, https://doi.org/10.1002/(sici)1099-1824(199901/03)2:1<1::aid-we16>3.0.co;2-7, 1999.

Dasari, T., Wu, Y., Liu, Y., and Hong, J.: Near-wake behaviour of a utility-scale wind turbine, J. Fluid Mech., 859, 204–246, https://doi.org/10.1017/jfm.2018.779, 2018.

Doubrawa, P., Quon, E. W., Martinez-Tossas, L. A., Shaler, K., Debnath, M., Hamilton, N., Herges, T. G., Maniaci, D., Kelley, C. L., Hsieh, A. S., Blaylock, M. L., Laan, P., Andersen, S. J., Krueger, S., Cathelain, M., Schlez, W., Jonkman, J., Branlard, E., Steinfeld, G., Schmidt, S., Blondel, F., Lukassen, L. J., and Moriarty, P.: Multimodel validation of single wakes in neutral and stratified atmospheric conditions, Wind Energy, 23, 2027–2055, https://doi.org/10.1002/we.2543, 2020.

Englberger, A., Dörnbrack, A., and Lundquist, J. K.: Does the rotational direction of a wind turbine impact the wake in a stably stratified atmospheric boundary layer?, Wind Energ. Sci., 5, 1359–1374, https://doi.org/10.5194/wes-5-1359-2020, 2020.

Frandsen, S.: Turbulence and turbulence-generated structural loading in wind turbine clusters, PhD thesis, Technical University of Denmark, ISBN 87-550-3458-6, 2007.

Fuertes, F. C., Markfort, C., and Porté-Agel, F.: Wind Turbine Wake Characterization with Nacelle-Mounted Wind Lidars for Analytical Wake Model Validation, Remote Sens., 10, 668, https://doi.org/10.3390/rs10050668, 2018.

Hand, M., Simms, D., Fingersh, L., Jager, D., Cotrell, J., Schreck, S., and Larwood, S.: Unsteady aerodynamics experiment phase vi: Wind tunnel test configurations and available data campaigns, Technical report NREL/TP-500-29955, NREL, https://doi.org/10.2172/15000240, 2001.

Herges, T. G. and Keyantuo, P.: Robust Lidar Data Processing and Quality Control Methods Developed for the SWiFT Wake Steering Experiment, J. Phys.: Conf. Ser., 1256, 012005, https://doi.org/10.1088/1742-6596/1256/1/012005, 2019.

IEA – International Energy Agency: Wind Electricity, https://www.iea.org/reports/wind-electricity (last access: 15 January 2023), 2022a.

IEA – International Energy Agency: World Energy Outlook 2022, https://iea.blob.core.windows.net/assets/830fe099-5530-48f2-a7c1-11f35d510983/WorldEnergyOutlook2022.pdf (last access: 15 January 2023), 2022b.

Jensen, N.: A note on wind generator interaction, no. 2411 in Risø-M, Risø National Laboratory, ISBN 87-550-0971-9, 1983.

Jiménez, Á., Crespo, A., and Migoya, E.: Application of a LES technique to characterize the wake deflection of a wind turbine in yaw, Wind Energy, 13, 559–572, https://doi.org/10.1002/we.380, 2009.

Keane, A.: Advancement of an analytical double-Gaussian full wind turbine wake model, Renew. Energy, 171, 687–708, https://doi.org/10.1016/j.renene.2021.02.078, 2021.

Keane, A., Aguirre, P. E. O., Ferchland, H., Clive, P., and Gallacher, D.: An analytical model for a full wind turbine wake, J. Phys.: Conf. Ser., 753, 032039, https://doi.org/10.1088/1742-6596/753/3/032039, 2016.

Kocer, G., Mansour, M., Chokani, N., Abhari, R., and Müller, M.: Full-Scale Wind Turbine Near-Wake Measurements Using an Instrumented Uninhabited Aerial Vehicle, J. Sol. Energ. Eng., 133, 041011, https://doi.org/10.1115/1.4004707, 2011.

Krogstad, P.-Å. and Adaramola, M. S.: Performance and near wake measurements of a model horizontal axis wind turbine, Wind Energy, 15, 743–756, https://doi.org/10.1002/we.502, 2011.

Li, Z., Pu, O., Pan, Y., Huang, B., Zhao, Z., and Wu, H.: A study on measuring wind turbine wake based on UAV anemometry system, Sustain. Energ. Technol. Assess., 53, 102537, https://doi.org/10.1016/j.seta.2022.102537, 2022.

Lignarolo, L., Ragni, D., Krishnaswami, C., Chen, Q., Ferreira, C. S., and van Bussel, G.: Experimental analysis of the wake of a horizontal-axis wind-turbine model, Renew. Energy, 70, 31–46, https://doi.org/10.1016/j.renene.2014.01.020, 2014.

Lu, H. and Porté-Agel, F.: Large-eddy simulation of a very large wind farm in a stable atmospheric boundary layer, Phys. Fluids, 23, 065101, https://doi.org/10.1063/1.3589857, 2011.

Machefaux, E., Larsen, G. C., Koblitz, T., Troldborg, N., Kelly, M. C., Chougule, A., Hansen, K. S., and Rodrigo, J. S.: An experimental and numerical study of the atmospheric stability impact on wind turbine wakes, Wind Energy, 19, 1785–1805, https://doi.org/10.1002/we.1950, 2015.

Maeda, T., Kamada, Y., Murata, J., Yonekura, S., Ito, T., Okawa, A., and Kogaki, T.: Wind tunnel study on wind and turbulence

intensity profiles in wind turbine wake, J. Therm. Sci., 20, 127–132, https://doi.org/10.1007/s11630-011-0446-9, 2011.

Magnusson, M.: Near-wake behaviour of wind turbines, J. Wind Eng. Indust. Aerodynam., 80, 147–167, https://doi.org/10.1016/s0167-6105(98)00125-1, 1999.

Manwell, J. F.: Wind energy explained, Wiley, ISBN 0470015004, 2009.

Mauz, M., Rautenberg, A., Platis, A., Cormier, M., and Bange, J.: First identification and quantification of detached-tip vortices behind a wind energy converter using fixed-wing unmanned aircraft system, Wind Energ. Sci., 4, 451–463, https://doi.org/10.5194/wes-4-451-2019, 2019.

Mehta, D., van Zuijlen, A., Koren, B., Holierhoek, J., and Bijl, H.: Large Eddy Simulation of wind farm aerodynamics: A review, J. Wind. Eng. Indust. Aerodynam., 133, 1–17, https://doi.org/10.1016/j.jweia.2014.07.002, 2014.

Menke, R., Vasiljević, N., Hansen, K. S., Hahmann, A. N., and Mann, J.: Does the wind turbine wake follow the topography? A multi-lidar study in complex terrain, Wind Energ. Sci., 3, 681–691, https://doi.org/10.5194/wes-3-681-2018, 2018.

Mikkelsen, T., Angelou, N., Hansen, K., Sjöholm, M., Harris, M., Slinger, C., Hadley, P., Scullion, R., Ellis, G., and Vives, G.: A spinner-integrated wind lidar for enhanced wind turbine control, Wind Energy, 16, 625–643, https://doi.org/10.1002/we.1564, 2012.

Mohan, M.: Analysis of various schemes for the estimation of atmospheric stability classification, Atmos. Environ., 32, 3775–3781, https://doi.org/10.1016/s1352-2310(98)00109-5, 1998.

NEWA Consortium: NEWA, https://map.neweuropeanwindatlas.eu, last access: 5 January 2023.

NREL: FLORIS, Version 2.4, Zenodo [code], https://doi.org/10.5281/zenodo.6687458, 2021.

Odemark, Y. and Fransson, J. H. M.: The stability and development of tip and root vortices behind a model wind turbine, Exp. Fluids, 54, 1591, https://doi.org/10.1007/s00348-013-1591-6, 2013.

Platis, A., Hundhausen, M., Lampert, A., Emeis, S., and Bange, J.: The Role of Atmospheric Stability and Turbulence in Offshore Wind-Farm Wakes in the German Bight, Bound.-Lay. Meteorol., 182, 441–469, https://doi.org/10.1007/s10546-021-00668-4, 2021.

Porté-Agel, F., Bastankhah, M., and Shamsoddin, S.: Wind-Turbine and Wind-Farm Flows: A Review, Bound.-Lay. Meteorol., 174, 1–59, https://doi.org/10.1007/s10546-019-00473-0, 2019.

Reuder, J., Båserud, L., Kral, S., Kumer, V., Wagenaar, J. W., and Knauer, A.: Proof of Concept for Wind Turbine Wake Investigations with the RPAS SUMO, Energ. Proced., 94, 452–461, https://doi.org/10.1016/j.egypro.2016.09.215, 2016.

Sanderse, B., Pijl, S., and Koren, B.: Review of computational fluid dynamics for wind turbine wake aerodynamics, Wind Energy, 14, 799–819, https://doi.org/10.1002/we.458, 2011.

Sherry, M., Nemes, A., Jacono, D. L., Blackburn, H. M., and Sheridan, J.: The interaction of helical tip and root vortices in a wind turbine wake, Phys. Fluids, 25, 117102, https://doi.org/10.1063/1.4824734, 2013.

Simley, E., Angelou, N., Mikkelsen, T., Sjöholm, M., Mann, J., and Pao, L. Y.: Characterization of wind velocities in the upstream induction zone of a wind turbine using scanning continuous-wave lidars, J. Renew. Sustain. Energ., 8, 013301, https://doi.org/10.1063/1.4940025, 2016.

Thielicke, W., Hübert, W., Müller, U., Eggert, M., and Wilhelm, P.: Towards accurate and practical drone-based wind measurements with an ultrasonic anemometer, Atmos. Meas. Tech., 14, 1303–1318, https://doi.org/10.5194/amt-14-1303-2021, 2021.

Veers, P., Dykes, K., Lantz, E., Barth, S., Bottasso, C. L., Carlson, O., Clifton, A., Green, J., Green, P., Holttinen, H., Laird, D., Lehtomäki, V., Lundquist, J. K., Manwell, J., Marquis, M., Meneveau, C., Moriarty, P., Munduate, X., Muskulus, M., Naughton, J., Pao, L., Paquette, J., Peinke, J., Robertson, A., Sanz Rodrigo, J., Sempreviva, A. M., Smith, J. C., Tuohy, A., and Wiser, R.: Grand challenges in the science of wind energy, Science, 366, eaau2027, https://doi.org/10.1126/science.aau2027, 2019.

Veers, P., Dykes, K., Basu, S., Bianchini, A., Clifton, A., Green, P., Holttinen, H., Kitzing, L., Kosovic, B., Lundquist, J. K., Meyers, J., O'Malley, M., Shaw, W. J., and Straw, B.: Grand Challenges: wind energy research needs for a global energy transition, Wind Energ. Sci., 7, 2491–2496, https://doi.org/10.5194/wes-7-2491-2022, 2022.

Vermeer, L., Sørensen, J., and Crespo, A.: Wind turbine wake aerodynamics, Prog. Aerosp. Sci., 39, 467–510, https://doi.org/10.1016/s0376-0421(03)00078-2, 2003.

Wetz, T. and Wildmann, N.: Spatially distributed and simultaneous wind measurements with a fleet of small quadrotor UAS, J. Phys.: Conf. Ser., 2265, 022086, https://doi.org/10.1088/1742-6596/2265/2/022086, 2022.

Wetz, T., Wildmann, N., and Beyrich, F.: Distributed wind measurements with multiple quadrotor unmanned aerial vehicles in the atmospheric boundary layer, Atmos. Meas. Tech., 14, 3795–3814, https://doi.org/10.5194/amt-14-3795-2021, 2021.

Wetz, T., Zink, J., Bange, J., and Wildmann, N.: Analyses of Spatial Correlation and Coherence in ABL flow with a Fleet of UAS, Research Square, https://doi.org/10.21203/rs.3.rs-2033943/v1, 2022.

Wildmann, N. and Wetz, T.: Towards vertical wind and turbulent flux estimation with multicopter uncrewed aircraft systems, Atmos. Meas. Tech., 15, 5465–5477, https://doi.org/10.5194/amt-15-5465-2022, 2022.

Wildmann, N., Hofsäß, M., Weimer, F., Joos, A., and Bange, J.: MASC – a small Remotely Piloted Aircraft (RPA) for wind energy research, Adv. Sci. Res., 11, 55–61, https://doi.org/10.5194/asr-11-55-2014, 2014.

Wildmann, N., Bernard, S., and Bange, J.: Measuring the local wind field at an escarpment using small remotely-piloted aircraft, Renew. Energy, 103, 613–619, https://doi.org/10.1016/j.renene.2016.10.073, 2017.

Wildmann, N., Kigle, S., and Gerz, T.: Coplanar lidar measurement of a single wind energy converter wake in distinct atmospheric stability regimes at the Perdigão 2017 experiment, J. Phys.: Conf. Ser., 1037, 052006, https://doi.org/10.1088/1742-6596/1037/5/052006, 2018a.

Wildmann, N., Vasiljevic, N., and Gerz, T.: Wind turbine wake measurements with automatically adjusting scanning trajectories in a multi-Doppler lidar setup, Atmos. Meas. Tech., 11, 3801–3814, https://doi.org/10.5194/amt-11-3801-2018, 2018b.

Wildmann, N., Gerz, T., and Lundquist, J. K.: Long-range Doppler lidar measurements of wind turbine wakes and their interaction with turbulent atmospheric boundary-layer flow at Perdigao 2017, J. Phys.: Conf. Ser., 1618, 032034, https://doi.org/10.1088/1742-6596/1618/3/032034, 2020.

Wildmann, N., Hagen, M., and Gerz, T.: Enhanced resource assessment and atmospheric monitoring of the research wind farm WiValdi, J. Phys.: Conf. Ser., 2265, 022029, https://doi.org/10.1088/1742-6596/2265/2/022029, 2022.

Wu, Y.-T. and Porté-Agel, F.: Atmospheric Turbulence Effects on Wind-Turbine Wakes: An LES Study, Energies, 5, 5340–5362, https://doi.org/10.3390/en5125340, 2012.

Yang, X., Hong, J., Barone, M., and Sotiropoulos, F.: Coherent dynamics in the rotor tip shear layer of utility-scale wind turbines, J. Fluid Mech., 804, 90–115, https://doi.org/10.1017/jfm.2016.503, 2016.

Zhang, W., Markfort, C. D., and Porté-Agel, F.: Near-wake flow structure downwind of a wind turbine in a turbulent boundary layer, Exp. Fluids, 52, 1219–1235, https://doi.org/10.1007/s00348-011-1250-8, 2011.